A Rotating Disc Gauge For Absolute Total Pressure Measurement in High Vacuum

by

Andrew David Chew

A Thesis Submitted for the Degree of
Doctor of Philosophy

University of York
Department of Physics
February 1993

ABSTRACT

A new rotating disc absolute vacuum gauge has been built. The characteristics of a rotating disc gauge have been determined for the first time and are reported. The geometrical edge effect and the high speed loss of molecular torque have been measured and agree with theoretical predictions. The rotating disc has been shown to operate in the high vacuum region with an associated uncertainty in absolute measurement of less than ± 3% at 1×10^{-5} mbar. Reproducibility of measurements of better than ± 1% is reported. The rotating disc gauge developed has a lower pressure measurement limit of 1×10^{-7} mbar with an associated uncertainty of ± 11%. A modification to the rotating disc gauge should enable pressure measurements in the 10^{-9} mbar range.

The experimental comparisons of the rotating disc gauge with a spinning rotor gauge gave values of the tangential momentum accommodation coefficient of unity for hydrogen, helium, methane, water vapour, nitrogen, air, carbon dioxide and krypton on a highly ordered, smooth, flat and adsorbate covered silicon (111) surface. The values of tangential momentum accommodation coefficients measured on rough silicon and titanium surfaces were a few percent above unity for hydrogen, helium, water vapour, nitrogen and air. The sensitivity of the rotating disc gauge was found to be proportional to the square root of the relative molecular mass of a gas, as is expected from theory.

It is shown that the rotating disc gauge can be used as a *universal absolute* total pressure gauge for high vacuum.

CONTENTS

	Page
ABSTRACT	2
CONTENTS	3
LIST OF TABLES	7
LIST OF FIGURES	9
PREFACE	13
ACKNOWLEDGEMENTS	15
DECLARATION AND OTHER PUBLICATIONS	16
CHAPTER 1 GENERAL INTRODUCTION	17
1.1 INTRODUCTION	17
1.2 VACUUM CONCEPTS	17
1.2.1 Results From Kinetic Theory	19
1.2.2 Other Vacuum Equations	21
1.3 GAS FLOW	21
1.4 GAS-SURFACE INTERACTIONS	22
1.5 TRANSPORT PHENOMENA AND MOLECULAR DRAG	25
1.6 PRESSURE MEASUREMENT	26
1.7 GAUGE CALIBRATION	34
1.8 VISCOSITY GAUGES	36
1.9 SPINNING ROTOR GAUGE	37
1.9.1 Details and Principle of Measurement	37
1.9.2 Measurement Range and Uncertainties	40
1.10 THE ROTATING DISC GAUGE	41
1.10.1 Details and Principle of Measurement	42
1.10.2 Experimental Observations	44
1.10.3 Conclusions	44
CHAPTER 2 ROTATING DISC GAUGE THEORY	46
2.1 INTRODUCTION	46
2.2 MOLECULAR TRAJECTORIES	48
2.3 ANALYSIS	53

2.4 ANALYTICAL TREATMENT OF THE EDGE EFFECT 56
2.5 ALLOWANCE FOR MORE THAN ONE GAS SPECIES 58
2.6 ROTATING DISC GAUGE SENSITIVITY 59
2.7 MOTION OF THE HARMONIC RECEIVER SUBJECTED TO A STEADY TORQUE 59
2.8 CENTRIFUGAL EFFECTS 62
2.9 AIMS OF THE PROJECT 62

CHAPTER 3 APPARATUS AND EXPERIMENTAL PROCEDURE 64
3.1 INTRODUCTION 64
3.2 VACUUM CHAMBER 64
3.3 PUMPING ARRANGEMENT 69
3.4 PRESSURE REGULATION AND THE INTRODUCTION OF GASES 73
3.5 PRESSURE GAUGES 75
3.5.1 Spinning Rotor Gauge 76
3.6 RESIDUAL GAS ANALYSIS 78
3.7 HIGH SPEED ROTOR 80
3.8 RECEIVER SUSPENSION 85
3.9 SHUTTER MECHANISM 100
3.10 MEASUREMENT OF DEFLECTIONS 106
3.11 EXPERIMENTAL PROCEDURE 109
3.12 SUMMARY 112

CHAPTER 4 PRELIMINARY RESULTS AND ROTATING DISC GAUGE CHARACTERISTICS 113
4.1 INTRODUCTION 113
4.2 ROTATING DISC GAUGE AND IONIZATION GAUGE COMPARISONS 113
4.2.1 Conclusions 118
4.3 EDGE EFFECT LOSSES 121
4.3.1 Preliminary Pressure Measurements 123
4.3.2 Further Edge Effect Investigations 125
4.3.3 Conclusions 130
4.4 ROTATING DISC GAUGE PERFORMANCE UNDER VARIABLE SENDER SPEED 131
4.4.1 Effect of Disc-Separation on the High Speed Loss Effect 138
4.4.2 High Speed Fall Off Effect in Other Gases 139
4.4.3 Conclusions 139

4.5 REPRODUCIBILITY OF MEASUREMENTS 142
4.6 CONCLUSIONS 144

CHAPTER 5 PRESSURE MEASUREMENT USING THE ROTATING DISC GAUGE 146
5.1 INTRODUCTION 146
5.2 ROTATING DISC GAUGE COMPARISON WITH A SPINNING ROTOR GAUGE 146
5.2.1 Experimental 147
5.2.2 Results and Discussion 147
5.2.3 Conclusions 153
5.3 UNCERTAINTIES IN ROTATING DISC GAUGE MEASUREMENTS 154
5.3.1 Uncertainties from the Rotating Disc Gauge Operating Equation 154
5.3.2 Additional Uncertainties 156
5.3.3 Conclusions 160
5.4 RANGE OF ROTATING DISC GAUGE MEASUREMENTS 160
5.4.1 Conclusions 162
5.5 GENERAL CONCLUSIONS 162

CHAPTER 6 ROTATING DISC GAUGE PERFORMANCE IN VARIOUS GAS ATMOSPHERES 163
6.1 INTRODUCTION 163
6.2 EXPERIMENTAL 163
6.3 PROCEDURE 164
6.4 RESULTS AND DISCUSSION 165
6.5 ROTATING DISC GAUGE SENSITIVITY 170
6.5.1 Rough Surfaces 172
6.6 CONCLUSIONS 173
6.7 ROTATING DISC GAUGE AND IONIZATION GAUGE COMPARISONS 174
6.7.1 Results and Discussion 174
6.8 GENERAL CONCLUSIONS 177

CHAPTER 7 ROTATING DISC GAUGE CHARACTERISTICS FOR VARIOUS GEOMETRIES 179
7.1 INTRODUCTION 179
7.2 THEORY 179
7.3 EXPERIMENTAL 181
7.4 ROTATING DISC GAUGE AND IONIZATION GAUGE COMPARISONS 182

7.5 EDGE EFFECT CHARACTERISTICS 182
7.6 PERFORMANCE UNDER VARIABLE SENDER SPEED 191
7.7 CONCLUSIONS 195

CHAPTER 8 CONCLUSIONS AND FUTURE WORK 197
8.1 CONCLUSIONS 197
8.2 FUTURE WORK 201

APPENDIX 1 TORQUE FREE SUSPENSION 205

REFERENCES 207

List of Tables

Table	Title	Page
Chapter 1		
1.1	Values of various vacuum parameters for nitrogen at different pressures and 0 °C	20
Chapter 2		
2.1	Values of μ for various molecular mass and sender speed combinations	57
Chapter 3		
3.1	Residual gas analyser sensitivity factors	79
3.2	Voltage and current settings for different rotor speeds	83
3.3	Tachometer measurements of rotor speeds	85
3.4	Specifications of the standard moment of inertia pieces	96
3.5	The torsion constants of the calibrated fibres	98
3.6	Periods of the suspensions used	99
Chapter 4		
4.1	The vacuum composition at an indicated pressure P_{IG} of 6.0×10^{-6} mbar	123
4.2	P_{RDG} and P_{IG} values corrected for vacuum composition	124
4.3	Experimentally and analytically determined values of the edge effect loss factor	126
4.4	Values of ν at various pressures and a constant sender-receiver separation	134
4.5	Values of ν for two sender-receiver separations and a constant pressure	135
4.6	The vacuum composition for typical high speed fall off data	136
4.7	Values of the high speed fall off at various disc-separations	138

4.8 The effect of increasing relative molecular mass on the magnitude of the high speed fall off 139
4.9 Measurements of deflection under constant conditions at a pressure of 3.5×10^{-6} mbar 143
4.10 Measurements of deflection under constant conditions at a pressure of 3.5×10^{-7} mbar 144

Chapter 5

5.1 Data of simultaneous RDG, SRG and IG pressure measurements 149
5.2 RDG, SRG and IG pressure values corrected for vacuum composition 152
5.3 Uncertainties in RDG pressure measurements for various deflections 156

Chapter 6

6.1 A typical data set for simultaneous RDG and SRG pressure measurements in nitrogen 166
6.2 σ_{RDG} values for various gases on different RDG receiver surfaces 168
6.3 Expected and measured RDG sensitivities for various gases on a smooth silicon receiver surface 170
6.4 Values of σ_{RDG} for two rough receiver surfaces relative to those of the smooth silicon receiver surface 173
6.5 Data set of simultaneous P_{IG} and P_{RDG} measurements for nitrogen 175
6.6 IG sensitivity factors relative to nitrogen 177

Chapter 7

7.1 P_{RDG} and P_{IG} values for various diameter receiver discs 187
7.2 Edge effect loss factors for different diameter receiver discs 190
7.3 Measurements of the fall off of deflection at high sender speeds 195

List of Figures

Figure	Title	Page
Chapter 1		
1.1	The reflection of a molecule from a surface	23
1.2	A plate P moving with velocity u in a gas G between walls W	27
1.3	Measuring ranges of vacuum gauges	29
1.4	Operating principle of the thermionic ionization gauge	31
1.5	Uncertainty of measurement as a function of pressure for various absolute primary pressure gauges	35
1.6	The spinning rotor gauge	38
1.7	The original rotating disc gauge	43
Chapter 2		
2.1	Schematic of the basic rotating disc gauge apparatus	47
2.2	Basic geometry of the rotating disc gauge	49
2.3	Detailed views of the rotating disc gauge geometry	51
2.4	Response of the receiver to a step function of molecular torque	61
Chapter 3		
3.1	Schematic of the rotating disc gauge system	65
3.2	Side view of the system	66
3.3	Front view of the system	67
3.4	Chamber specifications	68
3.5	The pumping arrangement shown in standard symbols	69
3.6	The turbomolecular pumping system	71
3.7	Schematic of the turbomolecular pump automatic control and interlock system	72
3.8	The gas line	73
3.9	View of the system from the front right side showing the gas line	74
3.10	End view into the chamber showing the rotating disc gauge and the spinning rotor gauge	77
3.11	A typical residual gas analyser output	80

3.12	The adapted structure of the high speed rotor	81
3.13	The rotor shaft arrangement	82
3.14	Schematic of the receiver suspension	86
3.15	Receiver shaft and discs	87
3.16	Centring jigs and standard inertia pieces	87
3.17	SEM picture of the smooth surface of a silicon (111) wafer	88
3.18	SEM picture of the rough side of a silicon (111) wafer	89
3.19	SEM picture of the surface of 500 nm of titanium grown on a silicon (111) surface	89
3.20	The shaft of the receiver suspension	91
3.21	The mirror piece	92
3.22	Details of the mirror piece	92
3.23	The phosphor-bronze torsion fibre and vices for its attachment	93
3.24	Details of the lower vice	94
3.25	Details of the upper vice	95
3.26	Details of the standard moment of inertia pieces	97
3.27	The shutter mechanism and internal supports	100
3.28	Front view and details of the shutter mechanism	101
3.29	Details of the hook mechanism	102
3.30	View looking down on the shutter	103
3.31	Side view of the damping posts	105
3.32	The laser and scale arrangement	107
3.33	View looking down on the apparatus for measuring deflections	108
3.34	Response of the receiver to a step function of molecular torque	110
3.35	A typical log book record for nitrogen on a 92 mm smooth silicon receiver surface	111

Chapter 4

4.1	Deflection versus indicated ionization gauge pressure for air at various disc-separations	114
4.2	Deflection versus indicated ionization gauge pressure for nitrogen	116
4.3	Deflection versus P_{IG} for helium	117
4.4	Deflection versus P_{IG} in the low 10^{-5} mbar range	119

4.5 Deflection versus P_{IG} in the 10^{-7} mbar range 120
4.6 Deflection versus disc-separation in air at different pressures 122
4.7 Deflection versus disc-separation for nitrogen at two different pressures 127
4.8 Deflection versus disc-separation in pure nitrogen at two set pressures 128
4.9 Deflection versus disc-separation in pure helium at two set pressures 129
4.10 Deflection versus variable sender speed in air at three set pressures 132
4.11 Deflection versus sender speed at two set disc-separations 133
4.12 Deflection versus sender speed in nitrogen for a fixed disc-separation and a fixed pressure 137
4.13 Deflection versus sender speed for helium at two set pressures 140
4.14 Deflection versus sender speed for helium at two set disc-separations 141

Chapter 5

5.1 P_{SRG} versus P_{IG}. 148
5.2 P_{RDG} versus P_{SRG} for the experimentally determined value of ε 150
5.3 P_{RDG} versus P_{SRG} for the analytically determined value of ε 151

Chapter 6

6.1 A plot of typical P_{RDG} versus P_{SRG} values for nitrogen 167
6.2 RDG sensitivity versus (relative molecular mass)$^{1/2}$ for the smooth silicon receiver surface 171
6.3 A typical P_{IG} versus P_{RDG} plot for nitrogen 176

Chapter 7

7.1 Rotating disc gauge configuration for the case of a smaller receiver disc 180

7.2 Deflection versus P_{IG} for the 84.64 mm diameter receiver disc 183
7.3 Deflection versus P_{IG} for the 78.04 mm diameter receiver disc 184
7.4 Deflection versus P_{IG} for the 70.00 mm diameter receiver disc 185
7.5 Deflection versus disc-separation for the 84.64 mm diameter receiver disc 186
7.6 Deflection versus disc-separation for the 78.04 mm diameter receiver disc 188
7.7 Deflection versus disc-separation for the 70.00 mm diameter receiver disc 189
7.8 Deflection versus sender speed for the 84.64 mm diameter receiver disc 192
7.9 Deflection versus sender speed for the 78.04 mm diameter receiver disc 193
7.10 Deflection versus sender speed for the 70.00 mm diameter receiver disc 194

Chapter 8

8.1 Possible rotating disc gauge geometrical variations 203

List of Symbols

c	Torsion constant of the fibre
f	Sender frequency
G	Torque
I	Moment of Inertia
J	Impingement rate
l	Length of the torsion fibre
L	Mirror-scale distance
m	Molecular mass
M	Relative molecular mass
n	Gas number density
P	Total pressure
P_i	Partial pressure of a gas species
r	Radius of the rotor of the spinning rotor gauge
r_i	Amount of a gas relative to nitrogen
R	Disc radius
R_o	Gas constant
S	Relative sensitivity of an ionization gauge
S_{RDG}	Rotating disc gauge sensitivity
t	Disc-separation
T	Absolute temperature
$\bar{v}$	Mean thermal velocity
v_b	Bias velocity
y_o	Measured deflection
α	Energy accommodation coefficient
ε	Edge effect correction factor for equal sized discs
ε'	Edge effect correction factor for unequal sized discs
η	Coefficient of viscosity
λ	Mean free path
ν	Coefficient of high speed fall off
σ_{RDG}	Tangential momentum accommodation coefficient of a gas on the receiver surface
σ_{SRG}	Tangential momentum accommodation coefficient of a gas on the rotor of the spinning rotor gauge
ϕ	Angular deflection
ω	Radian frequency of the sender
$-\dot{\omega}/\omega$	Relative deceleration rate of the spinning rotor gauge

PREFACE

The use of absolute pressure gauges which can be calibrated from their own physical properties is an important and convenient way of calibrating vacuum gauges. Currently the lower limit of absolute, or primary, gauges is about 1×10^{-5} mbar. At lower pressures complex methods are used to create a known pressure. Viscosity gauges, which exploit the phenomenon of molecular drag, offer a means for absolute pressure measurement. Most of these gauges are decrement type where the rate of decrease of amplitude of oscillation of an object is used for pressure measurement. The spinning rotor gauge (SRG) is the only widely used viscosity gauge of this type but can only be considered as a calibration transfer standard since it has to be calibrated itself. Currently no viscosity gauge is used as an absolute pressure standard.

The rotating disc gauge (RDG) first suggested by Langmuir (1913) and developed by Dushman (1915) has the advantage of being a static viscosity gauge in which a surface is deflected from rest and has a shorter measurement time than decrement gauges. In the RDG the molecular torque developed by a gas desorbing from a high speed disc is communicated to another disc in close proximity to it by molecular drag. The resulting deflection is used to give a measurement of pressure. The early promise of the RDG has not been pursued.

The author started work on building an RDG in October 1989 with Dr.A. Chambers of the University of York and in collaboration with Dr.A.P. Troup of Edwards High Vacuum International, Crawley. Modern day technology was applied to the original design of Dushman (1915). The ultimate aim of the author's work was to assess and realise the potential of the RDG for absolute pressure measurement.

Chapter 1 gives an introduction to the subject of vacuum and a review of common and viscosity vacuum gauges.

The theory of the RDG is given in detail in Chapter 2. This includes an analytical description of the edge effect which was derived by Prof.G.J.Pert of the University of York.

Chapter 3 describes the RDG built and the experimental procedures involved in operating it.

Chapter 4 gives an account of experiments performed to determine the characteristics of the RDG. Data of the geometrical and high speed edge effects are given and compared to theoretical predictions. Data assessing the reproducibility of RDG readings is also presented.

Chapter 5 describes an experimental comparison of the RDG with an SRG to determine the tangential momentum accommodation coefficient σ_{RDG} of the RDG receiver surface. The associated uncertainties and range of measurements of the RDG are discussed.

Chapter 6 describes experimental comparisons of the RDG with the same SRG in a range of gases to determine their σ_{RDG} values on smooth and rough surfaces. The sensitivity of the RDG for different gases is also discussed. Experimental comparisons of the RDG with a Bayard-Alpert ionization gauge (IG) are reported and the relative sensitivity factors of the IG for various gases are determined.

Chapter 7 describes experiments in which the RDG geometry is changed. Here data of characteristics of the RDG for several receiver discs all smaller than the sender disc are presented.

Finally Chapter 8 summarises this thesis and gives plans for future work.

ACKNOWLEDGEMENTS

I am pleased to be able to acknowledge the help and support given to me during the course of my work.

I would first like to thank Dr.A.Chambers for originally stimulating my interest in vacuum technology and for giving me the opportunity to pursue research in this field. His supervision, help and friendship during the course of my work has been of the greatest value and I am indebted to him for this. I would also like to thank him for proof reading this thesis.

I would like to thank Dr.A.P.Troup of Edwards High Vacuum International (EHVI) for his help and collaboration in setting up the project as one of the Science and Engineering Research Council's (SERC) Cooperative Awards in Science and Engineering. Financial support from the SERC and EHVI is gratefully acknowledged. The provision of equipment from EHVI and the technical assistance of their employees, particularly Mr.S.Fox and Mr.S.Ormrod, is gratefully recorded.

I would like to thank the following for their technical help. Mr.B.Wilkinson who made the chamber, Mr.P.Durkin who made the receiver shaft assembly, Mr.S.Moehr who ground the silicon wafers and the Wacker Chemical Company which donated them. I would like to thank Mr.C.Ovenden and Mr.M.Peters for their general technical assistance and advice. I would like to thank Mr.J.C.Dee for the scanning electron microscope plates and Mr.D.S.Schmool for the auger electron spectroscopy and reflection high energy electron diffraction studies of the receiver discs. I would also like to thank Mr.A.B.Gebbie for the preparation of photographs of the apparatus.

I am very grateful to Prof.G.J.Pert for his work in the theoretical and computational modeling related to the project.

Finally I would like to thank all my family and friends for their help and understanding.

DECLARATION AND OTHER PUBLICATIONS

The work presented in this thesis is that of the author except where the contributions of others have been acknowledged explicitly in the main text or by the means of references. A list of other publications arising from this work is shown below.

1. A.Chambers, A.D.Chew and A.P.Troup (1992)
   'Preliminary observations of the behaviour of an absolute gauge of the rotating disc type in high vacuum'
   Vacuum, 43, p9.

2. A.Chambers, A.D.Chew and A.P.Troup (1992)
   'Rotating disc gauge for absolute total pressure measurement in high vacuum'
   Journal of Vacuum Science and Technology, A10, p2655.

3. A.D.Chew, A.Chambers and A.P.Troup (1993)
   'The gas species dependence of the performance of a rotating disc gauge in high vacuum'
   Vacuum (in press).

CHAPTER 1

GENERAL INTRODUCTION

1.1 INTRODUCTION

The subject of vacuum has occupied many great minds for many centuries (Saunders and Brown, 1991). Aristotle's view that 'nature abhors a vacuum' and that vacuum was a logical impossibility was widely held until the 17th century (Madey, 1984). Berti around 1640 produced the first verifiable vacuum. Since then the scope and importance of vacuum has increased so that vacuum technology plays a critical role in everyday modern life. Industries ranging from semiconductor processing to freeze drying and research methods from surface physics to particle accelerators rely on vacuum (Wutz et.al., 1989). Measurement of vacua has itself become a major industry and a subject of intellectual endeavour and achievement.

This chapter gives an overview of important vacuum concepts, useful formulae and a review of vacuum gauges and calibration procedures. Viscosity gauges are then described in particular the spinning rotor gauge (SRG) which is a widely used viscosity gauge and the rotating disc gauge (RDG); the subject of the author's work. The RDG theory is given in detail in Chapter 2.

The breadth of the subject is such that the reader is in some places directed to other sources for a full description. There are many texts on vacuum theory, pumps, gauges and practices. Chambers et.al. (1989) gives a basic text and Wutz et.al. (1989), Dushman and Lafferty (1962) and Weston (1985) give complete and sophisticated treatments.

1.2 VACUUM CONCEPTS

A vacuum is defined as a space in which the pressure is below atmospheric pressure. In a gas the total pressure is defined as the rate of transfer of the normal component of momentum of the molecules to the plane divided by the area of the plane. The SI unit of pressure is the Pascal (Pa) which is defined as that pressure exerted by a force of 1 Newton perpendicular to a plane surface of area 1 m^2.

A more commonly used unit is the mbar such that 1000 mbar = 10^5 Pa. The unit Torr is still sometimes used. Chew (1992) gives a comprehensive review of many pressure units.

The standard atmosphere is the pressure for the normal state of a gas at a temperature of 0 °C. By definition (Wutz et.al., 1989)

$$\begin{aligned} 1 \text{ standard atmosphere} &= 1.01325 \times 10^5 \text{ Pa} \\ &= 1013.25 \text{ mbar} \\ &= 760 \text{ Torr} \end{aligned} \tag{1.1}$$

The ranges of vacuum are (Wutz et.al., 1989)

Low or Rough Vacuum (LV)	Atmosphere to 1 mbar
Medium or Fine Vacuum (MV)	1 to 10^{-3} mbar
High Vacuum (HV)	10^{-3} mbar to 10^{-7} mbar
Ultra High Vacuum (UHV)	10^{-7} mbar to 10^{-11} mbar and below

The vacuum environment is a gas at a reduced pressure. Theories of vacuum must therefore account for the laws which have been shown to hold true for gases. One form of the equation of state of ideal gases is

$$P = n\,k\,T \tag{1.2}$$

where P is the pressure, n is the number of gas molecules per unit volume, k is Boltzmann's constant and T is the absolute thermodynamic temperature. The number density n is therefore

$$n = 2.5 \times 10^{22} \times P \quad m^{-3} \tag{1.3}$$

at 20 °C where P is in mbar, see table 1.1.

The total pressure of a gas is the sum of the partial pressures from each of n gas species i.e.

$$P_{TOTAL} = \sum_{i=1}^{n} P_i \tag{1.4}$$

1.2.1 Results From Kinetic Theory

The law according to which molecular velocities are distributed at any given temperature is such that the *mean thermal velocity* is

$$\bar{v} = \left(\frac{8kT}{\pi\ m} \right)^{1/2} \tag{1.5}$$

a thorough derivation of this is given by Dushman and Lafferty (1962).

For a Maxwellian distribution of velocities the *mean kinetic energy* $\bar{E}$ per degree of freedom of a molecule is

$$\bar{E} = \frac{1}{2}\ k\ T \tag{1.6}$$

The *impingement rate* is the strike rate of molecules on a vacuum surface. It is given by

$$J = \frac{1}{4}\ n\ \bar{v} \tag{1.7}$$

and can be expressed in an alternative form where

$$J = \frac{P}{\left(2\ \pi\ m\ k\ T \right)^{1/2}} \tag{1.8}$$

Typical values are given in table 1.1.

The random motion of molecules means that collisions will occur between them and the *mean free path* λ is defined as the mean distance travelled by the molecules between collisions such that (Dushman and Lafferty, 1962)

$$\lambda = \frac{1}{n\ \pi\ d^2\ 2^{1/2}} \tag{1.9}$$

where d is the diameter of the sphere representing the molecule. For

nitrogen at room temperature

$$\lambda = \frac{6.6 \times 10^{-3}}{P} \text{ cm} \qquad (1.10)$$

where P is in mbar. Typical values are given in table 1.1.

The *monolayer formation time* t_{mono} is the time for the formation of an adsorbed monolayer of gas on a surface. It can be shown (Wutz et.al., 1989) that at 300 K

$$t_{mono} = \frac{3.6 \times 10^{-6}}{P} \text{ secs} \qquad (1.11)$$

where P is in mbar. Typical values are given in table 1.1.

The *sojourn time* τ is the mean lifetime of an adsorbed molecule remaining on a surface. The simple model of de Boer (1968) says that

$$\tau = \tau_o \exp(q/kT) \qquad (1.12)$$

where q is the molecule-surface binding energy and τ_o has a typical value of 10^{-13} secs. Typical values are given in table 1.1.

Pressure / mbar	n / cm^{-3}	J / cm^{-2} s^{-1}	λ / cm	t_{mono}
10^{3}	2.7×10^{19}	2.8×10^{23}	6×10^{-6}	3 ns
1	2.7×10^{16}	2.8×10^{20}	6×10^{-3}	3 μs
10^{-3}	2.7×10^{13}	2.8×10^{17}	6	3 ms
10^{-6}	2.7×10^{10}	2.8×10^{14}	60 m	3 s
10^{-10}	2.7×10^{6}	2.8×10^{10}	600 km	8 h

Table 1.1 Values of various vacuum parameters for nitrogen at different pressures and 0 °C. See text for meaning of symbols (Weston, 1985).

1.2.2 Other Vacuum Equations

The *throughput* Q of a gas is defined (Dushman and Lafferty, 1962) by

$$Q = P \dot{V} \text{ mbar l } s^{-1} \tag{1.13}$$

where $\dot{V}$ is the volumetric flow rate (or speed) of a gas at a pressure P. The conductance C measures ease of flow and is defined by

$$C = Q / \Delta P \tag{1.14}$$

where ΔP is the pressure difference between two regions. Dushman and Lafferty (1962) gave a complete account of the conductance of various orifices and tubes.

For a volume V and a pumping speed S the pressure in a vacuum falls to a pressure P from a pressure P_o after a time t such that

$$P = P_o \exp(-t / (V/S)) \tag{1.15}$$

1.3 GAS FLOW

The *Knudsen number*

$$K_n = \lambda / D \tag{1.16}$$

may be used to characterize flow regions.

From table 1.1 it can be seen that from atmospheric pressure to 10^{-2} mbar λ is much less than typical pipe diameters D i.e. $\lambda \ll D$. Here molecule-molecule collisions dominate gas behaviour and the gas behaves as a fluid. This is called viscous flow which obeys the laws of fluid mechanics and occurs when $K_n < 10^{-2}$.

In high vacuum and UHV λ is much greater than typical vessel dimensions. For $K_n > 1$ there is molecular flow where molecule-wall collisions dominate gas behaviour and surface processes become important. An adsorbed molecule retains no memory of its original direction of arrival and molecules desorb from a surface in a random manner according to the Knudsen cosine law of diffuse emission which

is discussed below.

The transition regime of gas flow for which $10^{-2} < K_n < 1$ is difficult to analyse and is usually described by a combination of viscous and molecular flow.

1.4 GAS-SURFACE INTERACTIONS

The nature of the interaction of a gas and a surface is of prime importance in vacuum. Molecules impinging on a solid surface immersed in a gas have a Maxwell-Boltzmann distribution at the temperature of the gas. In this case the energy carried to the surface can be determined from kinetic theory. In general molecules do not actually reach thermal equilibrium with the surface i.e. they are not completely thermally accommodated. The *energy accommodation coefficient* α takes this into account (Knudsen, 1946) where

$$\alpha = \frac{E_i - E_r}{E_i - E_T} \qquad (1.17)$$

and E_i is the incident energy of molecules, E_r is the energy of reflected molecules and E_T is the energy of reflected molecules which are in equilibrium with the surface. A value of $\alpha = 1$ indicates complete thermal accommodation. Thomas (1981) comprehensively reviewed the subject of thermal accommodation of molecules on controlled surfaces. In general the value of α increases as the adsorbate coverage of a surface increases.

In figure 1.1a a molecule is shown impinging on a surface at an angle ϑ to the normal. The molecule may become adsorbed on the surface either by physical sorption or chemisorption. See for example de Boer (1968). After a limited lifetime of adsorption the molecule will desorb. In figures 1.1b, 1.1c and 1.1d the forces on the surface derived from the change in momentum of the molecule are shown. If the molecule leaves the surface specularly (figure 1.1b) there is no net tangential force on the surface. If it leaves in a direction normal (figure 1.1c) to the surface then there is complete transference of tangential momentum and there is a net tangential force on the surface derived from the loss of the molecule's tangential momentum. If the molecule leaves in a direction to the left of the normal direction

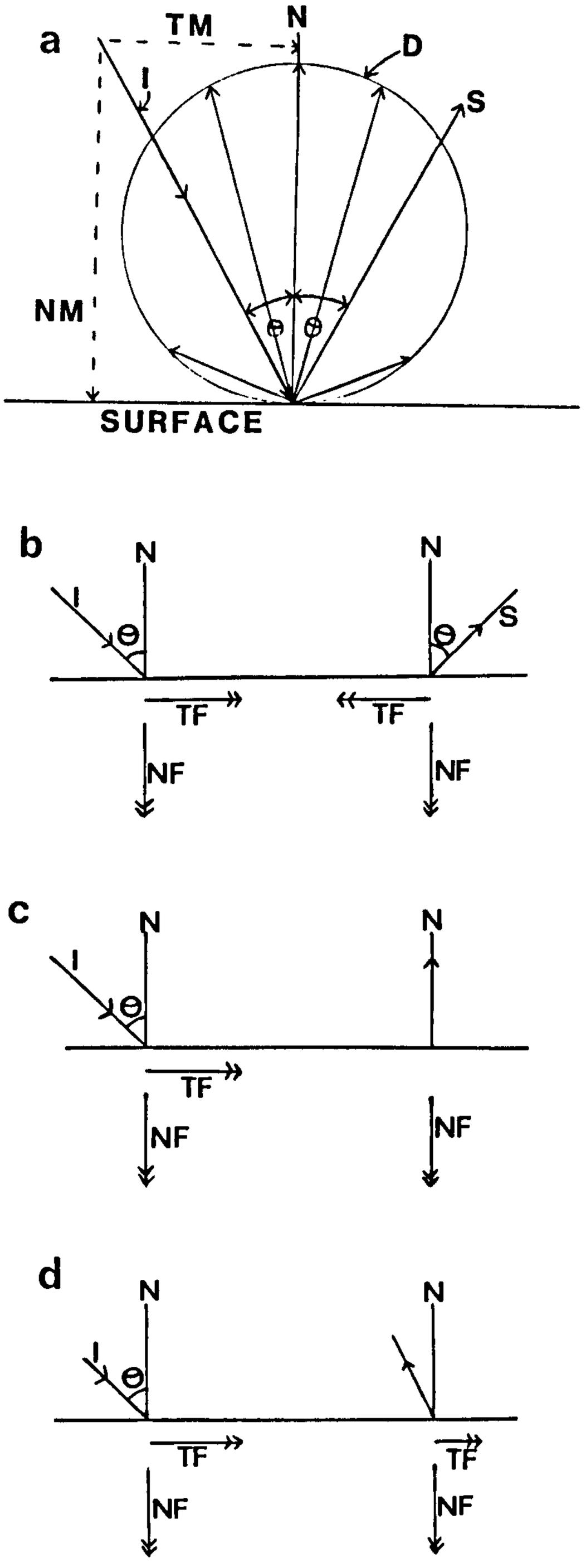

Figure 1.1 The reflection of a molecule from a surface. (a) Molecule impinging on a surface: NM Normal component of momentum and TM Tangential component of momentum. (b) Specular reflection. (c) Reflection normal to surface. (d) 'Reverse' reflection. TF Force tangential to surface and NF Force normal to surface are the forces on the surface derived from the change in momentum. D Diffuse reflection; I Incoming molecule; N Normal to the surface; S Specular reflection.

then there is 'increased' tangential momentum transfer.

The *Knudsen cosine law* of diffuse emission (Knudsen, 1946) relates the number of molecules dn emitted by an area ds of a diffusely reflecting surface within the solid angle dw which makes an angle ϑ with the normal to the surface thus

$$dn = \frac{n}{\pi} \cos\vartheta \, dw \qquad (1.18)$$

That is, the probability of a molecule leaving at an angle ϑ to the normal is proportional to $\cos\vartheta$ regardless of the angle of incidence, see figure 1.1a. On average molecules therefore leave in a direction normal to the surface, as in figure 1.1c. Complete transference of tangential momentum occurs and there is a net tangential force on the surface derived from the loss of the tangential momentum. The Knudsen cosine law of diffuse scattering is empirical in nature and does not require a condition of equilibrium. Wenaas (1971) described a derivation of the equilibrium cosine law which specifies the flux distribution of all molecules scattered from a surface resulting from the equilibrium distribution of incident molecules.

There are occasions on which molecules may be specularly reflected from the surface (see Steckelmacher, 1966 and Carter, 1972). Maxwell proposed that a fraction 1-f (where f is called Maxwell's coefficient of diffuse reflection) of incident molecules were specularly reflected with the remainder reflected diffusely. A value of f = 1 would correspond to zero specular reflection and therefore complete transference of tangential momentum. A value of f < 1 indicates some specular reflection. This is now usually described by the *tangential momentum accommodation coefficient* σ (Comsa et.al.,1977) such that

$$\sigma = \left(\frac{v_i - v_r}{v_i} \right)_{AVERAGE} \qquad (1.19)$$

where v_i is the tangential velocity (with respect to the macroscopic surface) of a molecule impinging on the surface, v_r is the tangential velocity of the same molecule after its reemission. A value of σ of unity indicates that v_r is zero and corresponds to perfect transference of tangential momentum.

Much work has been done on the measurement of σ (or f). Millikan (1923) measured f values which varied with the surface from 0.79 for air on fresh shellac to 1.00 for air on mercury. Van Dyke (1923) found values of f below unity for various gas-surface combinations whereas Blankenstein (1923) measured values of f near unity for various other combinations. Recent work on the subject of σ values has been done mainly with regard to the calibration of spinning rotor gauges. Fremerey (1980) developed a theoretical model for the calculation of the molecular drag on a tangentially moving surface. A quantitative prediction of the effective tangential momentum transfer between gas molecules and a tangentially moving rough surface in molecular flow was given.

An important conclusion from the widespread experimental work is that for a highly ordered, smooth, flat and adsorbate covered surface the value of σ is unity for all gases and is independent of the value of α, see Comsa et.al. (1981) and Thomas (1981). For bare surfaces values of σ as low as 0.20 were found by Lord (1977) and Lord and Thomas (1977). For rough surfaces values of σ above unity have been widely observed (see Thomas and Lord, 1974 and Comsa et.al., 1981). Fremerey (1982) comprehensively reviewed the subject of σ values on rough surfaces. His theoretical treatment of the subject led to the conclusion that

$$0 \leq \sigma \leq 4/\pi \qquad (1.20)$$

where a value of σ below unity is consistent with specular reflections or a deformation of the Knudsen and Maxwell-Boltzmann distributions. A σ value above unity occurs when momentum is exchanged on elements of a rough surface which are inclined to the average tangential surface.

1.5 TRANSPORT PHENOMENA AND MOLECULAR DRAG

A gas which streams through a pipe with a narrow bore has a resistance to its flow so that the velocity decreases uniformly in the direction of flow from the axis until it reaches zero at the walls. The internal viscosity of a gas means that each layer of gas parallel to the direction of motion exerts a tangential force on the adjacent layers. The coefficient of viscosity η is defined (Dushman and

Lafferty, 1962) as being the tangential force per unit velocity gradient. In viscous flow

$$\eta = \frac{1}{3} n m \bar{v} \lambda \qquad (1.21)$$

A plate moving at velocity u through a gas needs energy to be supplied to it otherwise its velocity would decrease due to the friction between the plate and gas molecules, see figure 1.2. It can be shown (Dushman and Lafferty, 1962) that the rate of transference of momentum from the plate per unit area in viscous flow is

$$B = \eta \frac{u}{d} \qquad (1.22)$$

where d is the distance from the plate.

The rate of transference of momentum per unit area from the moving plate in the molecular flow regime is (Dushman and Lafferty, 1962)

$$B = k u P \left(\frac{M}{T} \right)^{1/2} \qquad (1.23)$$

where k is a constant. This result is important since it describes the phenomenon of molecular drag or momentum transfer (Roth, 1976). This means that if a surface is in motion it can transfer a velocity component to a molecule.

Viscosity, or molecular, gauges exploit this principle by providing an imposed motion relative to the average motion of undisturbed gas molecules. A surface is either set into oscillation and molecular drag causes its amplitude of oscillation to decrease or a surface in continuous rotation imparts a molecular torque by molecular drag to a surface which is then displaced from its original position.

1.6 PRESSURE MEASUREMENT

The measurement of vacuum pressures is needed in order to characterize a vacuum environment. This is especially the case in industrial processing (English, 1984) where measurement and control of vacuum is essential. Partial pressure gauges are designed to identify and

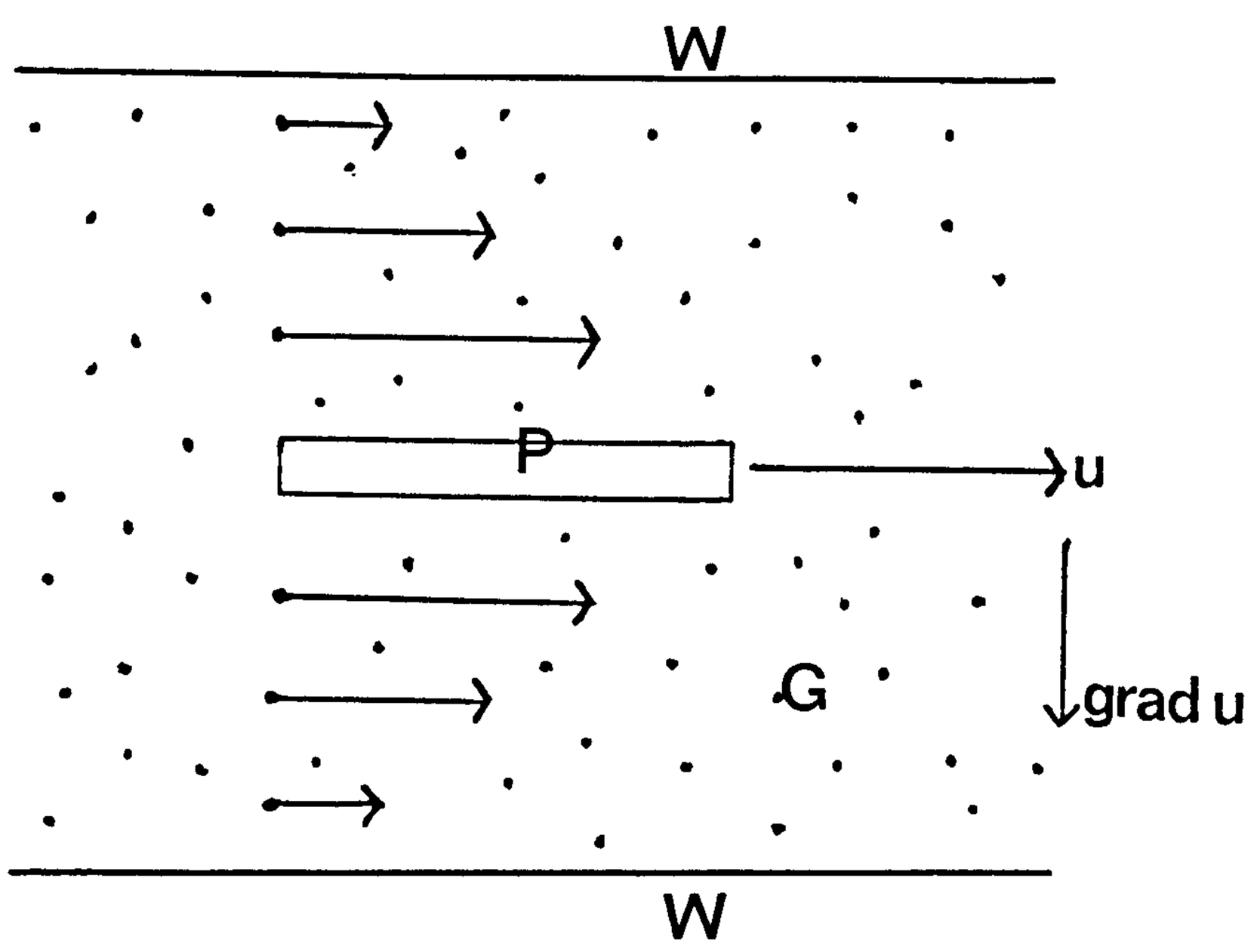

Figure 1.2 A plate P moving with velocity u in a gas G between walls W.

quantify each gas species in a vacuum. This is a highly specialised subject in itself and was reviewed comprehensively by Lichtman (1984) and Leck (1989). Total pressure gauges measure the total pressure of all the gases in the vacuum. The discussion here is limited to total pressure gauges. The total range of pressures to be measured for vacuum technological applications extends from 10^{3} to 10^{-12} mbar and can not be covered by any single gauge. In this section the classification of total pressure gauges is given and the most common gauges and calibration procedures are described. Viscosity gauges are then discussed.

Gauges are *absolute* if they can be calibrated from their own physical properties in terms of the fundamental units otherwise they are *non-absolute*. Additionally they can be classified as being *direct* if they measure actual force per unit area or *indirect* if they measure the particle number density n or a physical quantity proportional to n (Wutz et.al., 1989). Only direct gauges give pressure measurements that are independent of gas species.

Commonly used gauges were reviewed by Weston (1979), Fitch (1987) and Leck (1989). Figure 1.3 shows the operating ranges of the most common vacuum gauges (Wutz et.al, 1989).

The simplest vacuum gauge is the glass U-tube containing mercury or some other low vapour pressure liquid (Wutz et.al, 1989). One limb of the tube is connected to the vacuum chamber. Usually a low pressure is held above the other limb so that the unknown pressure is given directly by the difference in the levels of the two liquid columns. The usual lower limit due to the precision at which the height of the two levels can be measured by these absolute gauges is about 1 mbar. Interferometric techniques enable lower and high accuracy ($\pm 10^{-5}$%) measurements (Truffier and Choumoff, 1974). In the McLeod absolute gauge a gas is confined to a known volume and compressed by a rising column of mercury so that the original pressure is increased to an extent where it can be measured by a U-tube manometer. This gauge was comprehensively reviewed by Thomas and Leyniers (1974) and can measure absolutely pressures of order 10^{-4} or 10^{-6} mbar with an uncertainty at best below ± 1% (Leck, 1989).

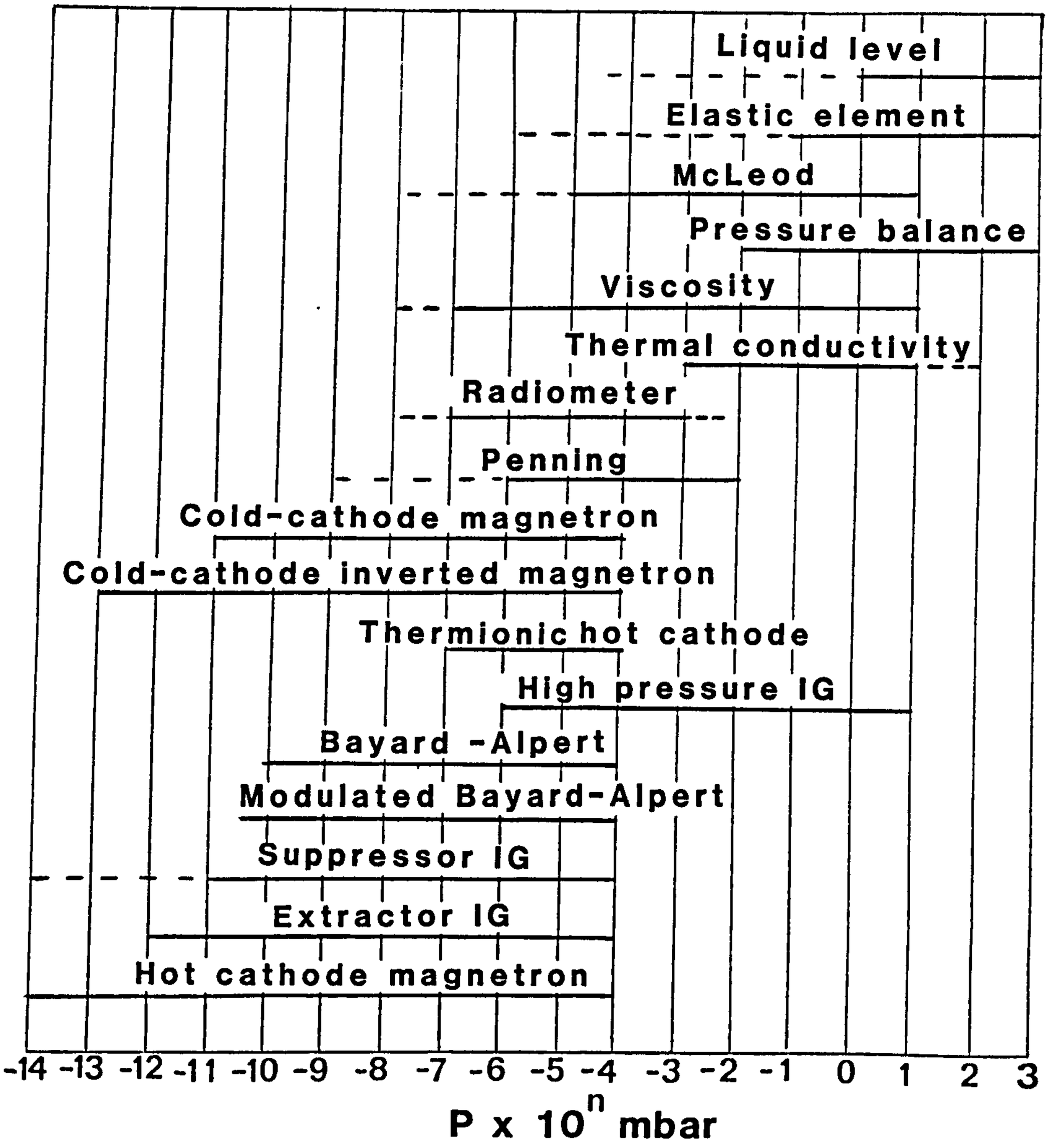

Figure 1.3 Measuring ranges of vacuum gauges. The dashed lines show the range for special constructions or particular operating conditions. Wutz et.al. (1989).

Elastic element absolute gauges have a membrane which separates two volumes one of which is at a known pressure and the other is open to the vacuum to be measured. The differential pressure across the membrane gives rise to a force which deflects the membrane and is related to give a measurement of pressure. In the Bourdon gauge (1013 - 10 mbar ± 1%) the atmospheric pressure squeezes a tube which is connected to the vacuum and causes the movement of a dial, see Jitschin (1990). A diaphragm gauge (1013 - 1 mbar) employs a useful technique of variable membrane stiffness to lower the operating range with an uncertainty of ± 1% (Wutz et.al., 1989). Capacitance type transducers enable measurements of membrane deflections of 1 nm and can measure a differential pressure of 10^{-6} mbar. They are used as commercial (non-absolute) instruments with uncertainties of ± 0.4% and below (Jitschin, 1990).

Thermal conductivity gauges are non-absolute gauges in which the gauge head contains a fine wire filament which is heated by passing an electric current through it and is exposed to the vacuum to be measured. The heat loss from the wire is proportional to the gas pressure. A change in pressure causes a change in temperature of the filament and hence a change in its resistivity. A Pirani gauge is one in which the heated filament forms one branch of a Wheatstone bridge; the changing bridge current enables a measurement of pressure. The operating range is 100 - 10^{-3} mbar with an uncertainty of ± 6 - 20% (Jitschin, 1990 and Harris, 1989). Thermocouple gauges operate in a similar manner except the change in temperature of the filament is monitored by a thermocouple and they operate in the range 5 - 10^{-3} mbar ± 10% (Harris, 1989).

The sensor of quartz friction non-absolute gauges is an oscillating piece of quartz in the shape of a tuning fork. The electrically driven forced oscillation is damped by gas friction and pressure is measured from changes of the resonance impedance (Ono et.al., 1986). The reported uncertainties are ± 10% in the range 10^{3} to 10^{-3} mbar (Jitschin, 1990). The spinning rotor viscosity gauge (SRG) has attained a position of great importance in vacuum metrology in the range 10^{-2} to 10^{-6} mbar and is discussed fully below.

Ionization gauges (IG) are very important low pressure gauges in which non-absolute measurements are made by an indirect method in which the

gas is partly ionized. Depending upon the method of ionization used the measured electrical parameter is either a pure ion current or a gas discharge current. An ionization gauge using the former method is shown in figure 1.4. In it a thermionic cathode K is surrounded by a positive grid anode A.

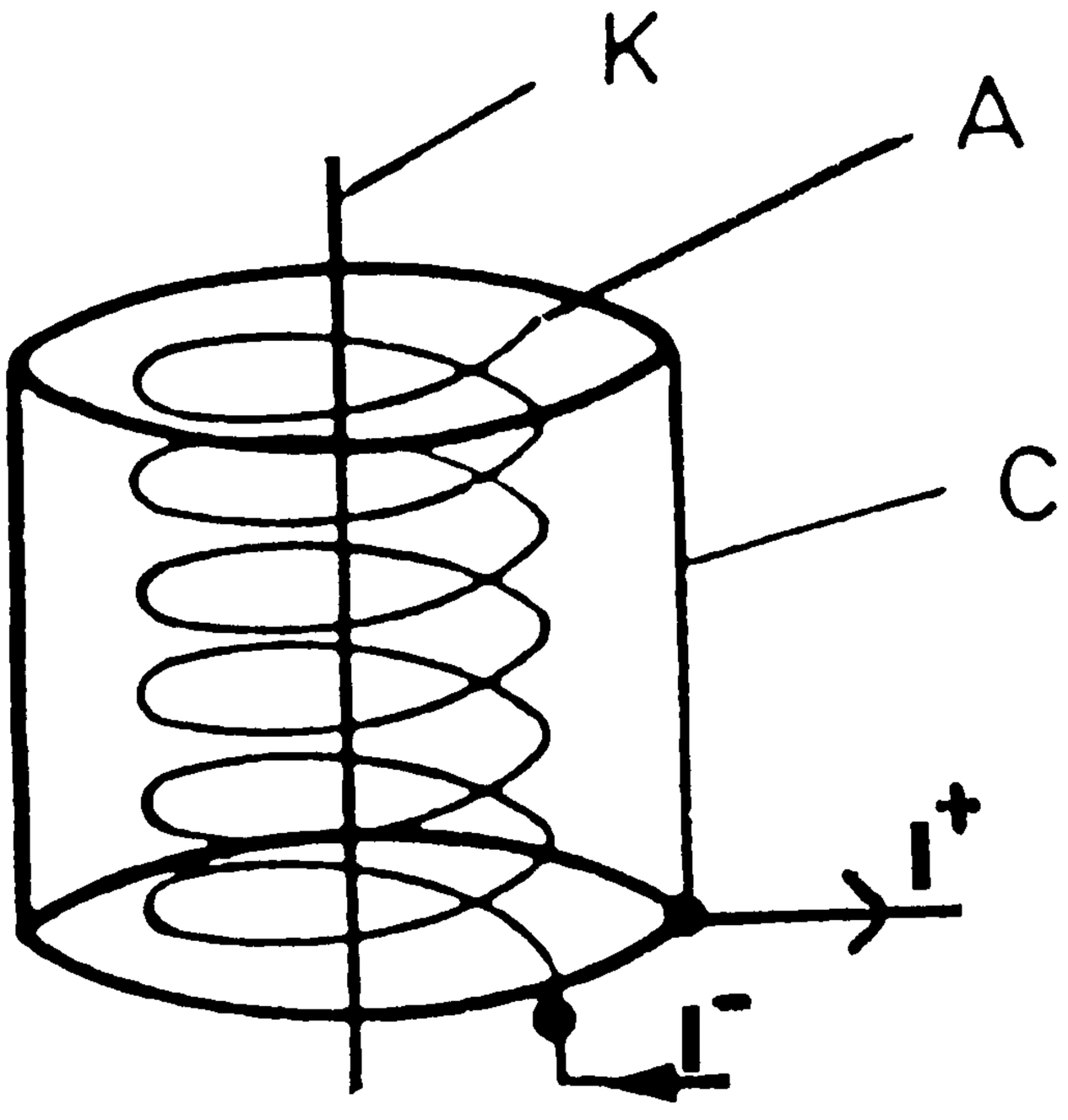

Figure 1.4 Operating principle of the thermionic ionization gauge. A Anode; C Ion collector and K Thermionic Cathode .

Again concentric to this is an ion collector C which is at a more negative potential than the potentials of the other electrodes. Electrons emitted from K with current I^- are attracted to the anode. They collide with gas molecules which are ionized in the process. Positive ions are created which are attracted to C. There they are measured as an ion current I^+ where

$$I^+ = n\ l\ \nu\ I^- \qquad (1.24)$$

where n is the molecular number density, l is the average electron path length and ν is the ionization cross-section. Since at low pressures ν and l are constant the sensitivity of an ionization gauge is

$$K = \frac{I^+}{I^-} \times \frac{1}{P} \quad mbar^{-1} \qquad (1.25)$$

where P is the pressure in mbar.

The above equation shows that the ion current I^+ is proportional to pressure. The electron current I^- is usually kept constant because it would otherwise change with pressure due to gas coverage and work function effects. There are several types of thermionic ionization gauge (Wutz et.al, 1989) each having a different configuration of electrodes. The concentric triode gauge was the first ionization gauge based on thermionic triode valves. It measures in the range 10^{-2} to 10^{-7} mbar and its configuration is shown in figure 1.4. Medium vacuum ionization gauges operate at high pressures (1 to 10^{-6} mbar) by interchanging the anode and ion collector functions and by reducing the separating distances between electrodes.

The lower limit of ionization gauges is determined by the residual ion current at the ion collector due to the 'X-ray effect'. The number of photons created when electrons collide with matter is proportional to I^-. These photons give rise to a photoelectron current emitted by the ion collector which gives rise to an apparent increase in the positive ion current measured at the ion collector. This limits the previously discussed IGs to 10^{-7} mbar. The Bayard-Alpert gauge (BAG), (see Wutz et.al., 1989) is an IG in which the ion collector surface area is considerably reduced. The central ion collector is a very thin wire

surrounded by a coaxial anode grid with the cathode outside of it. These gauges are very popular and measure in the range 10^{-4} to 10^{-10} mbar with an uncertainty at best of about ± 20% (Jitschin, 1990).

In extractor gauges the X-ray limit of the BAG is reduced by a complex change of configuration such that the solid angle within which X-ray photons produced at the anode can strike the collector is much smaller than in the BAG. The lower measurement limit is 10^{-12} mbar, see Wutz et.al. (1989).

The main cold cathode ionization gauge is the Penning gauge where a gas discharge is established between an anode and a cathode by a high d.c. voltage. The gas discharge current is pressure dependent. A strong magnetic field is used so that it is possible to create long spiral path lengths of electrons from the cathode to the anode. This enables a rough indication (typically with an uncertainty of ± 100%) to be made in the range 10^{-2} to 10^{-7} mbar, see Wutz et.al. (1989).

There have been many gauges developed which at best attained temporary use. The radiometer gauge was first developed by Crookes (Dushman and Lafferty, 1962) in 1873 and became common in the Knudsen radiometer gauge form. This absolute gauge consists of two parallel plates one of which is heated and the other supported on a sensitive suspension so that the small radiometric force acting upon it causes it to move. This can be used to give pressure measurements from 10^{-3} to 10^{-7} mbar. Wu (1966) reviewed the Knudsen gauge which have declined in popularity and Beavitt et.al. (1968) and Bialas (1984) described modified radiometer type gauges capable of measurements of much lower pressures.

Other gauges such as a microweighing system (Zamojski, 1982) and an absolute thermodynamic manometer (Taborek and Goodstein, 1979) in the suggested range 10^{-1} to 10^{-20} mbar have been developed. A gauge counting ultra-violet photons from an electron bombarded gas was suggested to have a lower limit of 10^{-13} mbar (Alexeff, 1961). An absolute gauge employing the spectral analysis of the Brownian motion of a suspended mirror was said to give absolute measurements of pressure at 10^{-3} mbar (Morimura et.al., 1974). None of these gauges have found widespread acceptability.

1.7 GAUGE CALIBRATION

Like any other instruments vacuum gauges need to be calibrated. All calibration procedures establish the connection between the final gauge head readings and the calibration pressures which are determined by some other method. There are three methods to produce a known pressure (Wutz et.al., 1989):

(i) By the measurement of pressure using an absolute pressure gauge as a primary standard.

(ii) By the establishment of a well-defined expansion of a gas at a known pressure as measured in (i).

(iii) By the determination of pressure via the molecular beam principle, here the reference pressure is determined by using a gauge calibrated by (i) or (ii).

Additionally a secondary gauge, or transfer standard, may be used as a reference gauge. These are gauges which are not absolute but have been calibrated by one of the first two methods above and are used as a reference to check other gauges. All types of gauges can in principle be used as a transfer standard.

Figure 1.5 shows the uncertainties of primary pressure gauges (Poulter, 1977) used for calibration by direct comparison. The McLeod and the U-tube manometers are most widely used as primary standards. It is interesting to note that the best uncertainty of these absolute gauges at 10^{-5} mbar is about ± 5%.

In the static expansion method the test gas is initially filled into a vessel of small volume and then isothermally expanded into an evacuated vessel of large volume (Jitschin et.al., 1990). The resulting pressure is then calculated from the initial high pressure and from the volume ratio by using Boyle's law. The established pressure has a best uncertainty below ± 1.0% in the range 10 to 10^{-7} mbar.

Dynamic expander devices pass a gas at a known rate through a known conductance to generate a known pressure in the range 10^{-5} (± 1%) to

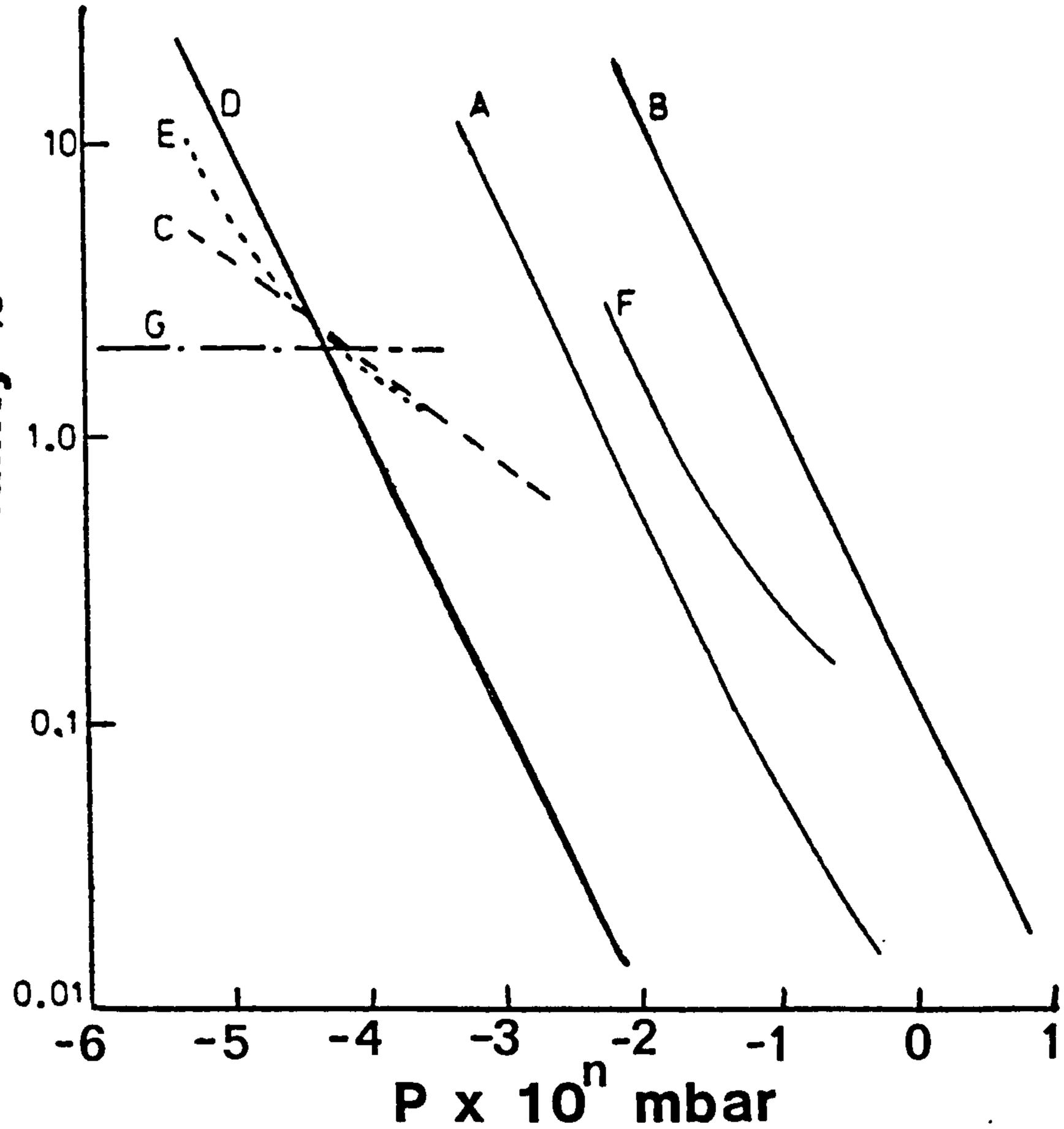

Figure 1.5 Uncertainty of measurement as a function of pressure for various absolute primary pressure gauges (Poulter, 1977).
A Oil U-tube gauge; B Mercury U-tube gauge; C McLeod gauge; D Interferometric oil gauge; E Piston gauge (low range); F Piston gauge (high range) and G Levitation gauge.

10^{-9} (± 5%) mbar. See Wutz et.al. (1989) and Steckelmacher (1987).

In the molecular beam method a molecular flux is established using a Knudsen cell to produce a measurably very low pressure in an opposite cell. This is described in detail by Wutz et.al. (1989) and can be used to establish pressures from 10^{-8} (± 7%) to 10^{-12} (± 30%) mbar.

The most commonly used secondary (or transfer) standards are capacitance manometers (10^{3} to 10^{-3} mbar), spinning rotor gauges (10^{-2} to 10^{-6} mbar) and thermionic ionization gauges which are used for the lowest vacuum pressures.

It is clear that absolute gauges offer the most convenient means of gauge calibration.

1.8 VISCOSITY GAUGES

Viscosity gauges, which are also called momentum transfer, friction or molecular gauges, operate using the principle of molecular drag and are absolute. There are basically two types of viscosity gauge: those in which a surface is set into oscillation and the decrement of its amplitude used as a measurement of pressure and those in which a rotating surface causes the deflection of another surface by providing a molecular torque.

In over a century many decrement type gauges have been developed including many designs of oscillating discs, vanes and fibres. These were comprehensively reviewed by Dushman and Lafferty (1962) and Drawin (1965). They are susceptible to vibrations and the lowest measured pressures were of the order 10^{-5} mbar (Roberts, 1970). An oscillating vane viscosity gauges was developed (Christian and Leck, 1966) which enabled measurements in the range 10^{-3} to 10^{-6} mbar with an uncertainty of ± 4% (Austin and Leck, 1972). The diamagnetic levitation gauge had a disc which was magnetically levitated and set into rotation. The decrement rate of the disc gave an absolute measurement of pressure in the range 10^{-3} to 10^{-7} mbar and had the potential to measure 10^{-10} mbar (Evrard and Boutry, 1969). Indeed this gauge found (limited) use as a primary standard. Recently an electrostatic levitation gauge where the damping of an oscillating electroactively levitated microscopic particle gives a measurement of

pressure in the range 10^{-2} to 10^{-8} mbar has been developed (Hinkle and Kendall, 1990). The quartz friction gauge which is non-absolute was described earlier. This and the SRG are the only viscosity gauges to be used commercially. The SRG and the rotating disc viscosity gauges are now described in detail.

1.9 SPINNING ROTOR GAUGE

The spinning rotor gauge (SRG) has become in the last decade an important transfer standard for high vacuum. Basically it measures the frequency decrement of a magnetically suspended freely rotating sphere which is used to give a measurement of pressure. The SRG has a long history. Epstein (1924) considered the case of the molecular drag on a freely rotating sphere. This idea was taken up by Beams et.al, (1946) who developed a magnetic suspension for a small sphere and ultimately made an actual SRG using magnetically suspended solid spheres and cylinders (Beams et.al., 1962) capable of pressure measurements in the range 10^{-4} to 5×10^{-8} mbar. Further theoretical work was done on this technique by Bowden and Lord (1963) and Keith (1963) who considered coriolis effects. Nixon and Kenney (1964) developed an electronic damping system for the magnetic suspension and Harbour and Lord (1965) developed an SRG which had an uncertainty of ± 3%. Interest in SRGs was then taken up by Fremerey (1971) who proposed an SRG capable of measurements of 10^{-9} mbar (Fremerey, 1972) and succeeded in producing a commercial SRG (Fremerey, 1985).

1.9.1 Details and Principle of Measurement

The basic configuration of an SRG is shown in figure 1.6. The spherical rotor R is typically a 4.5 mm diameter steel ball bearing which is magnetically suspended on the axis of a non-magnetic stainless steel tube connected to the vacuum system. The suspension is achieved by the magnetic force between two mutually attracting permanent magnets M which cancels the gravitational force on the rotor. Two electromagnetic coils A act as vertical stabilization coils to bind the rotor in a central equilibrium position. Lateral damping coils L damp out lateral oscillations. Drive coils D provide a rotating magnetic field for spinning the rotor about the vertical axis. A rotation speed of about 400 Hz is created beyond which the drive is cut and the rotor is allowed to coast. The slowing down of

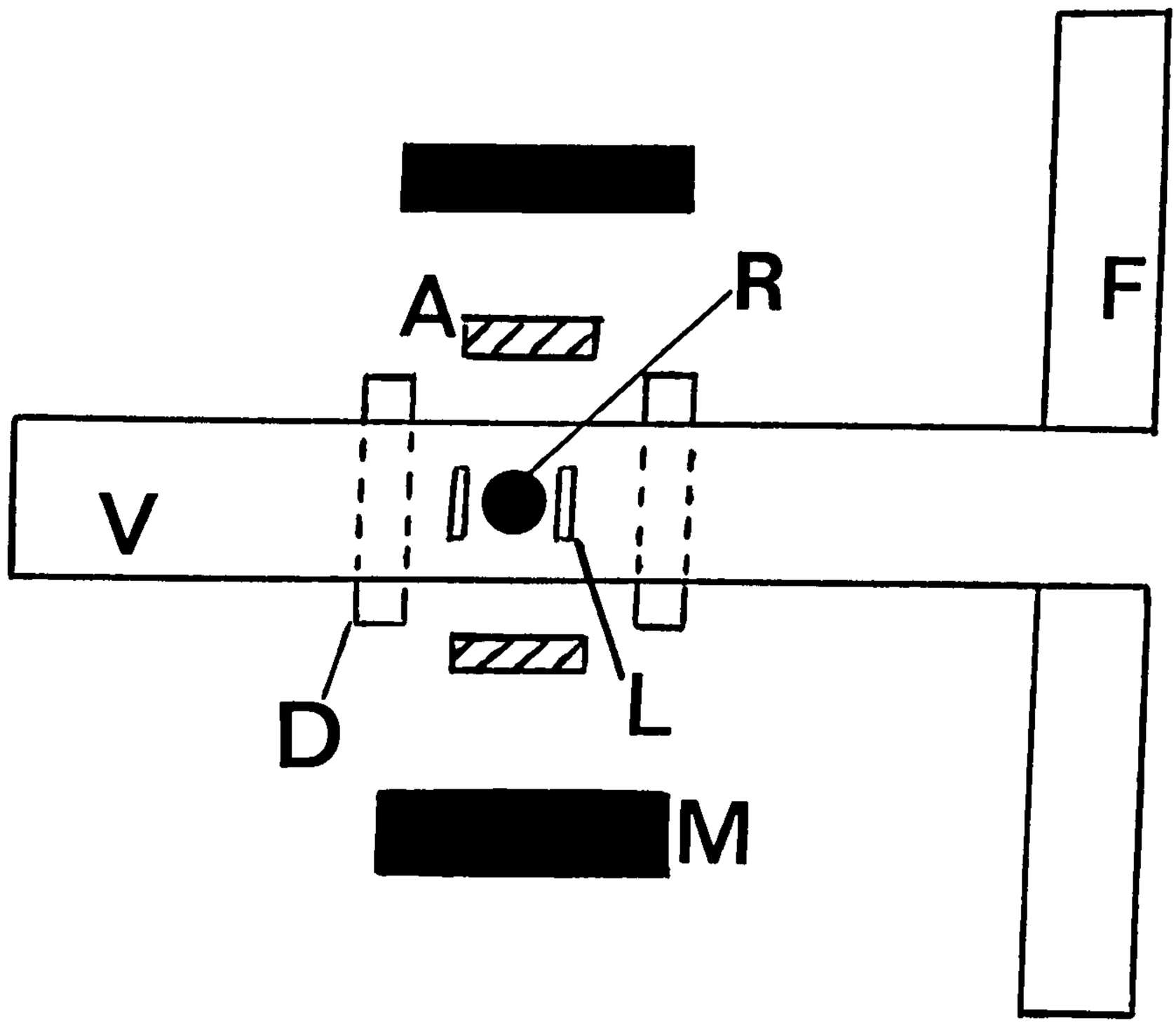

Figure 1.6 The spinning rotor gauge.
A Vertical stabilization coils; D Drive coils; F Flange; L Lateral damping coils; M Attracting magnets; P Pick-up coils (in front of rotor-not shown); R Rotor and V Vacuum enclosure.

the rotor by the molecular drag of molecules is measured by the relative deceleration rate $-\dot{\omega} / \omega$ of the rotor radian frequency ω. The pick-up coils P measure the inductive signal generated by the rotating component of the rotor magnetization and give a measurement of the deceleration rate.

By considering the transfer of tangential momentum to the rotor from the gas molecules it can be shown (Fremerey, 1985) that

$$-\frac{\dot{\omega}}{\omega} = \frac{10\ \sigma_{EFF}\ P}{\pi\ \rho\ r\ \bar{v}} \qquad (1.26)$$

where ρ is the density and r is the radius of the rotor. P is the pressure, $\bar{v}$ is the mean molecular velocity and σ_{EFF} is the effective tangential momentum accommodation coefficient of the rotor and gauge head combination.

To measure the deceleration rate a fixed number of rotations N is used and the sequence of timing intervals $\tau_i < \tau_{i+1} < \tau_n$ which elapse for N rotations is measured (Wutz et.al., 1989) whence

$$-\frac{\dot{\omega}}{\omega} = \frac{\tau_{i+1} - \tau_i}{\tau_i . \tau_{i+1}} \ . \qquad (1.27)$$

There are other contributions to the deceleration of the rotor other than from molecular drag. The residual magnetic drag on the rotor is pressure independent and is of the order of 10^{-5} to 10^{-6} mbar nitrogen equivalent (McCulloh et.al., 1985). It is mainly due to eddy currents induced in the rotor by asymmetries in the suspension field and eddy currents induced by the rotating components of the rotor's magnetic moment in surrounding metallic components. A change in temperature of the rotor causes a change in its moment of inertia via expansion or contraction. By the conservation of angular momentum this results in changes in the rotation frequency ω. The magnitude of this depends on the rate of change of the rotor temperature dT/dt and the thermal expansion coefficient α of the rotor. Random noise (RN) in the timing circuitry also causes a deceleration of the rotor.

Equation 1.26 therefore becomes (McCulloh et.al., 1985)

$$-\frac{\dot{\omega}}{\omega} = \frac{10\ \sigma_{EFF}\ P}{\pi\ \rho\ r\ \bar{v}} + 2\ \alpha\ \dot{T} + \frac{\dot{\omega}}{\omega}_{(RESIDUAL\ DRAG)} + \frac{\dot{\omega}}{\omega}_{(RANDOM\ NOISE)} \qquad (1.28)$$

Clearly to be able to measure pressure the three last terms of this operating equation must be evaluated. Lindenau (1988) showed that a temperature drift of 1 K hour^{-1} has an equivalent nitrogen pressure of about 1.5×10^{-7} mbar. By allowing at least 5 hours after rotor spin-up for the rotor to reach equilibrium the temperature stability has an equivalent nitrogen pressure of 10^{-8} mbar (McCulloh et.al., 1985). With an optimized gauge head and a temperature stability of $\pm$ 0.05 K hour^{-1} an equivalent nitrogen pressure of $\pm 4 \times 10^{-9}$ mbar is possible (Setina, 1990). The random noise effects were investigated by Hirata et.al. (1986) who concluded that vibrations, especially those below 100 Hz and at the rotational frequency of the rotor (400 Hz), should be eliminated as far as possible to below 0.03g (where $g \simeq 9.8$ ms^{-2}). The residual drag is the largest contribution of the non-molecular decelerating effects.

The limits of stability and the lower limit of the SRG is determined by the residual drag. Redgrave and Downes (1988) measured an amplitude of variation of about 5% in the value of residual drag in one hour after the rotor had reached thermal equilibrium. The residual drag value needs to be measured regularly and by definition means that the SRG can not be regarded as an absolute gauge.

1.9.2 Measurement Range and Uncertainties

The lower limit of SRG measurement is determined by the frequency measurement instrumentation and the residual drag. It is usually in the 10^{-7} mbar range (Reich, 1982). The upper limit is defined by it being operational in the molecular flow regime i.e. to about 10^{-2} mbar (Wutz et.al., 1989). Recent work (Lindenau and Fremerey, 1991) has been conducted on the linearization and temperature compensation of the SRG up to one atmosphere so that its operating range is from 10^{3} to 10^{-8} mbar. The SRG is usually used as a transfer standard in the range 10^{-2} to 10^{-6} mbar.

There are several contributions to the uncertainty of SRG measurements. The uncertainty in the measurement of the diameter and density of the rotor is about $\pm$ 0.12% (Wutz et.al., 1989) and that in

the timing circuitry is about ± 0.5% (American Vacuum Society (AVS), 1989). The lowest temperature drift gives an uncertainty of about ±0.4% and the best uncertainty in the measured temperature is about ±0.08% (AVS, 1989). The uncertainty in the residual drag is at best ± 0.1% (AVS, 1989). The uncertainty in the calibration of the coefficient σ_{EFF} of the rotor is about ± 1.5% with a drift in value of ± 0.6 to 1.5% in two years, see Redgrave and Downes (1988) and Dittmann et.al (1989). Effects such as rotor contamination, baking and exposure to air can effect this value.

The total uncertainty is therefore about ± 100% at 1×10^{-7} mbar and ±12 to 15% at 1×10^{-6} mbar, see AVS (1989) and Wutz et.al. (1989). At 1×10^{-5} mbar the uncertainty is $\simeq$ ± 5% (AVS, 1989). Reproducibilities of the order of ± 1% have though been reported (McCulloh, 1983) and with careful calibration and use an uncertainty of ± 2% is possible (Leck, 1989). This gives the SRG a great application as a transfer standard for high vacuum.

1.10 THE ROTATING DISC GAUGE

The rotating disc gauge (RDG) design was first suggested by Langmuir in 1913 and Dushman constructed one in 1915. In it a thin disc is suspended by a fine fibre above a disc rotating at high speed. A molecular torque is developed by the molecules desorbing from the lower disc which is transmitted to the upper disc by molecular drag and causes the latter to deflect against the torsion constant of the suspension fibre. This deflection can be measured to give a measurement of pressure. Langmuir (1913) suggested that a lower operational limit of 10^{-7} mbar might be achievable. The RDG built by Dushman (1915), and shown in figure 1.7, is described below. The only similar device to be built since was by Briggs (1954) who used a high speed cylinder to deflect a concentric outer cylinder by molecular drag. This was capable of measurements in the range 20 to 10^{-6} mbar although a commercial instrument measured to 10^{-3} mbar. No other RDG has been made in the same configuration as that of Dushman (1915), see Dushman (1922), Dushman (1949), Drawin (1965) and Wutz et.al. (1989).

1.10.1 Details and Principle of Measurement

In the original RDG shown in figure 1.7 a glass bulb B contains a rotating disc A of thin aluminium about 35 mm in diameter which is attached to a rotor capable of speeds up to 10 krpm. Above this disc at a distance of less than 10 mm is a thin mica disc C 25 μm thick and about 30 mm in diameter which is held by a 150 mm long quartz fibre 20 μm in diameter. A mirror M is attached to the mica disc for optical monitoring of the deflection of the upper disc.

A simple theory for the RDG's operation was developed which did not account for edge effects. A complete theoretical treatment of the RDG is given in the next chapter. The deflection α of the upper disc was calculated to be

$$\alpha = \frac{k\ t^2\ r^4\ P\ \omega}{2\ \pi\ K} \left(\frac{M}{R_o T} \right)^{1/2} \qquad (1.29)$$

where t is the period of the upper disc, r is the radius of the lower disc, P is the pressure, ω is the angular velocity of the rotating disc, M is the molecular mass, R_o is the gas constant, T is the thermodynamic temperature, K is the moment of inertia of the upper disc and mirror and k is a constant incorporating the tangential momentum accommodation coefficient of the surface of the upper disc.

A sensitivity of $\alpha = 150^{\circ} / 10^{-3}$ mbar was predicted which corresponds to a deflection of 1 mm at a distance of 50 cm at 8×10^{-7} mbar in nitrogen.

Several correction factors were identified the main one being due to eddy currents in the metal framework holding the mirror onto the upper disc. These were caused by the rotating magnetic field of the rotor. A torque was set up due to these eddy currents such that equation 1.29 becomes

$$\alpha = \frac{k\ t^2\ r^4\ P\ \omega}{2\ \pi\ K} \left(\frac{M}{R_o T} \right)^{1/2} + k_1\ i^2\ \omega \qquad (1.30)$$

where the torque produced by the eddy currents is $k_1 i^2 \omega$; k_1 is a

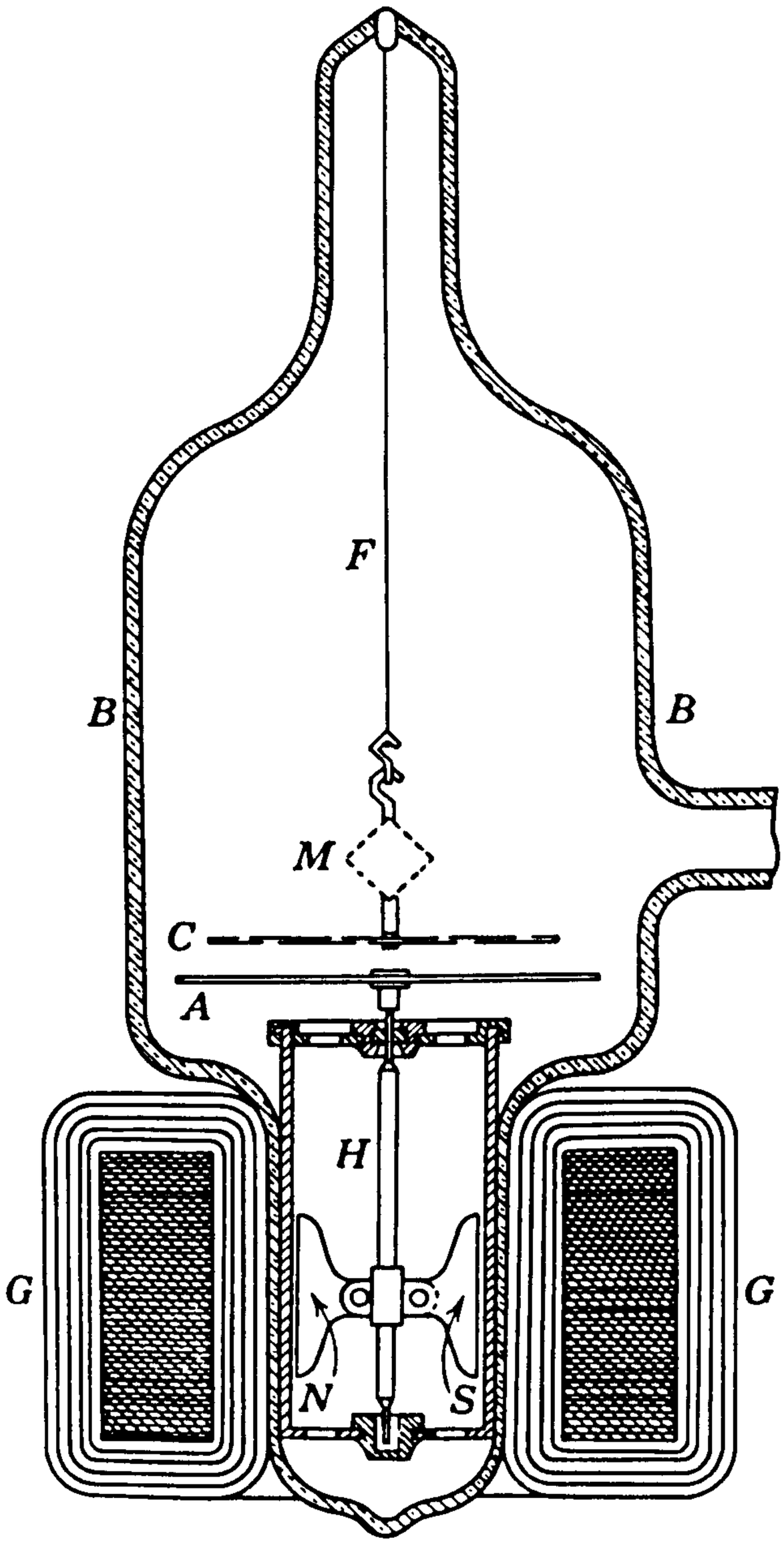

Figure 1.7 The original rotating disc gauge (Dushman, 1915).
A High speed aluminium disc; B Glass bulb; C Thin mica disc; F Quartz torsion fibre; G Gramme ring; H Steel or tungsten shaft and M Mirror.

constant, i is the current in the commutator and Gramme ring of the rotor and ω is the angular velocity of the rotor. The eddy current torque contributed an equivalent nitrogen pressure of about 10^{-6} mbar.

The upper disc was prone to swing which necessitated great care in the alignment and introduced an unknown uncertainty. The edge effect loss of molecules from between the discs arising from the Knudsen cosine law of emission of molecules from the lower disc was thought to be negligible if the upper disc was much smaller than the lower one.

1.10.2 Experimental Observations

Only very limited data was gathered by Dushman (1915). It was observed that the deflection of the upper disc was proportional to rotor speed up to 2 krpm at a pressure of about 10^{-3} mbar of air. Deflections were also seen to be proportional to the pressure measured on a McLeod gauge in the 10^{-2} to 10^{-3} mbar range. Experiments with air and hydrogen showed that the deflection at a set pressure varied with the square root of the molecular mass as predicted in the theory. Other experiments were conducted to measure the vapour pressures of mercury and ice and to measure the pressure and 'clean-up' effect in a tungsten lamp. RDG measurements also showed that the vacuum created by a Gaede molecular pump was below 7×10^{-7} mbar.

1.10.3 Conclusions

The RDG built by Dushman (1915) measured pressure down to about 10^{-6} mbar. Only very limited data on the RDG's characteristics were obtained. In particular no edge effects were measured and the maximum rotor speed was only 2 krpm. Dushman recognised the potential that the RDG had for absolute pressure measurement and for measuring the values of tangential momentum accommodation coefficients. He was limited in his work by the technology of the day. Drawin (1965) suggested using the RDG in a constant deflection mode. In this case the rotor speed needed to produce a constant deflection of the upper disc is measured to give a measurement of pressure.

The RDG has great potential as an absolute gauge for the high vacuum region. The actual RDG measurement time is determined by the period of the upper disc which is very much shorter than that associated with

decrement type viscosity gauges. The calibration of the RDG from its own properties is also very much simpler than for the decrement gauges. Langmuir (1913) suggested a lower limit of 10^{-7} mbar for the RDG. This would considerably extend the range of operation of primary gauges (currently at about 10^{-5} mbar) and an RDG was constructed for this reason.

CHAPTER 2

ROTATING DISC GAUGE THEORY

2.1 INTRODUCTION

The first operating equation for the rotating disc gauge (RDG) was derived by Dushman who considered a simple treatment without correcting for edge effects (Dushman, 1915). In this chapter a complete theoretical analysis of the RDG is presented and the aims of the author's work are given.

The basic geometry of the RDG is shown in figure 2.1. It has a disc of radius R, the 'sender', which rotates at radian frequency ω. Above this disc, at a sender-receiver separation t, is another disc of matching size, the 'receiver', which is suspended by one means or another.

In the viscous regime of gas flow where the mean free path λ in the gas is such that $\lambda \leq t$ the device would be a viscometer being dependent upon viscous forces for its operation. In this classical situation (Newman and Searle, 1965) the total torque G_v developed by molecules which attain the speed of the sender and impact upon the receiver is

$$G_v = \frac{R^4 \pi \eta \omega}{2 t} \qquad (2.1)$$

where R is the radius of the discs, η is the coefficient of viscosity and ω is the radian frequency (speed) of the sender. This torque can be measured against a torsion fibre of torsion constant c such that

$$G_v = c \phi \qquad (2.2)$$

where the angular deflection ϕ produced is the measurable quantity.

In the RDG developed (see Chapter 3) t is typically 5 mm. By inspection of table 1.1 which gives values of λ at different pressures, it can be seen that for low pressures ($< 10^{-3}$ mbar), the regime of interest in this work, $\lambda \gg t$. Here molecular flow

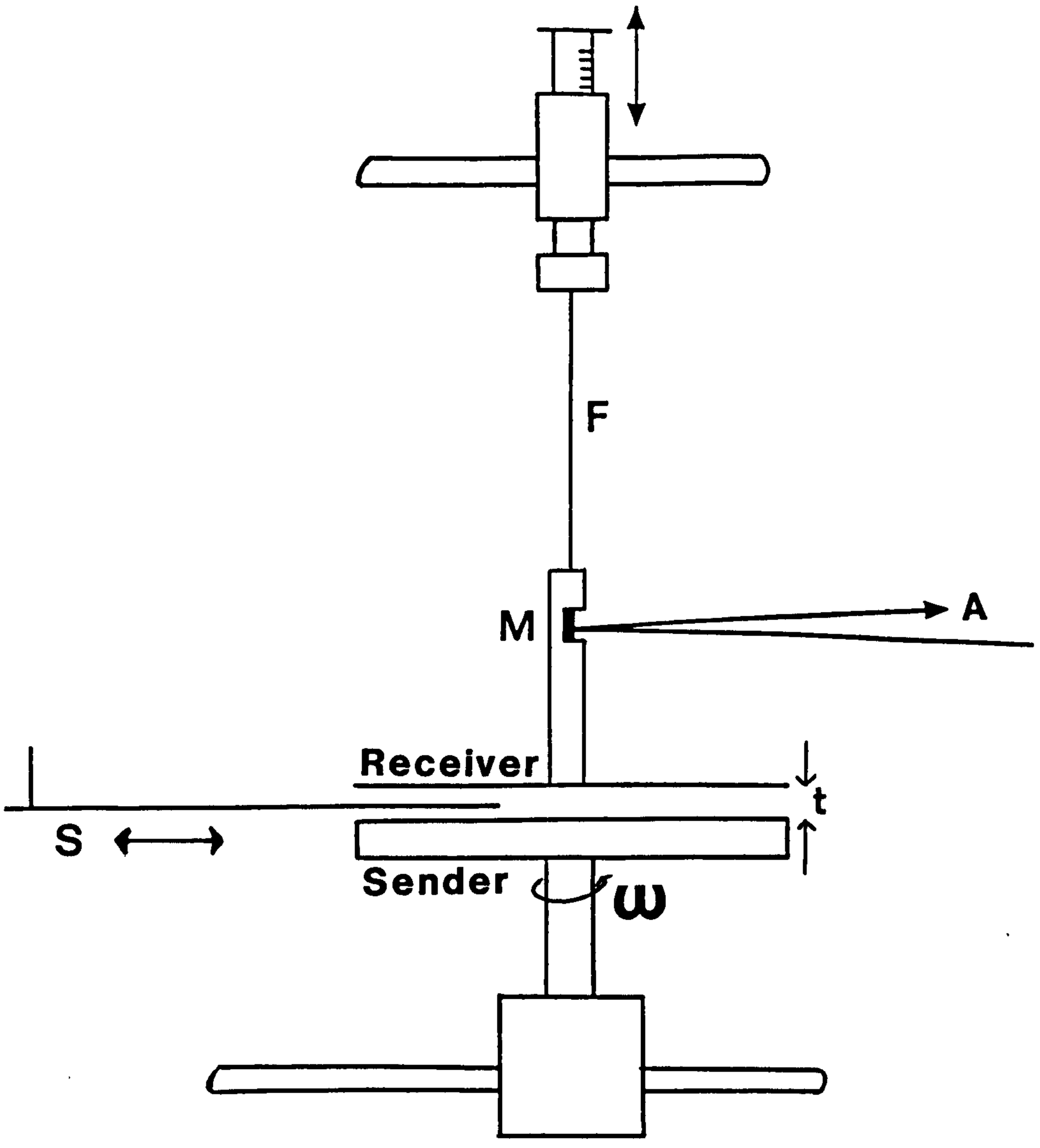

Figure 2.1 Schematic of the basic rotating disc gauge apparatus. A Reflected beam to external scale; F Torsion fibre; M Mirror; S Shutter - withdrawn to create a step function of molecular torque.

conditions operate i.e. molecule-surface collisions dominate gas behaviour and the coupling between the discs is by molecular drag.

Consider the rotor constituting the high speed sender. It has a surface with an imposed motion relative to the gas molecules. The rotor is therefore subject to a retarding force due to molecular impacts which increases with speed and as the number density n of molecules increases. It is assumed here (as was the case in practice) that the rotor was able to regulate its power supply to overcome the variable retarding force and to keep at a constant speed.

2.2 MOLECULAR TRAJECTORIES

Consider molecular trajectories within the RDG. With reference to figure 2.2 it can be seen that in the laboratory reference frame molecules of mass m desorb from a locality P at radial distance r on the sender. They do so with a bias velocity v_b, and correspondingly an imposed momentum mv_b, which is parallel to the discs and tangential to the circular motion, superimposed on their thermal velocity where

$$\underline{v}_b = \underline{r} \times \underline{\omega} \qquad (2.3)$$

The mean thermal velocity from the Maxwell-Boltzmann distribution is

$$\bar{v} = \left(\frac{8\ k\ T}{\pi\ m} \right)^{1/2} \qquad (2.4)$$

where k is the Boltzmann constant, T is the absolute thermodynamic temperature of the system and m is the molecular mass.

In the rotating reference frame of the sender molecules leave the surface of this disc in all directions distributed in a solid angle according to the Knudsen cosine law of diffuse emission. The Knudsen distribution sphere is represented in figures 2.2a, 2.3a and 2.3c by the circle K. A molecule leaving the sender at position P in the direction PN normal to the plane of the disc will travel unhindered (in the molecular flow pressure regime) across the discs' interspace. The superimposed bias velocity means that the molecule will travel forward to point P_1 on the underside of the receiver, as shown in figure 2.2b, a plan view of the discs in which the receiver disc is

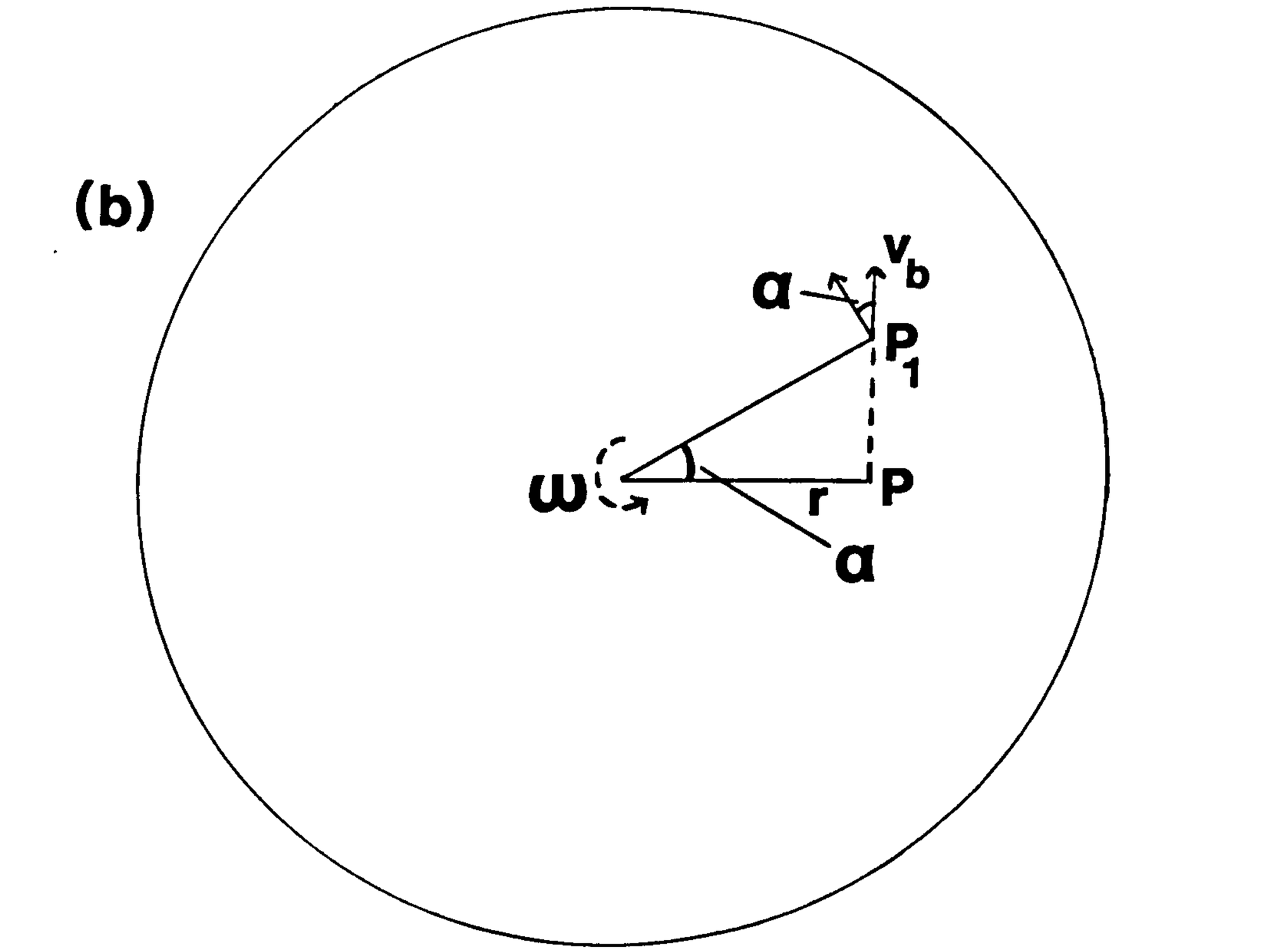

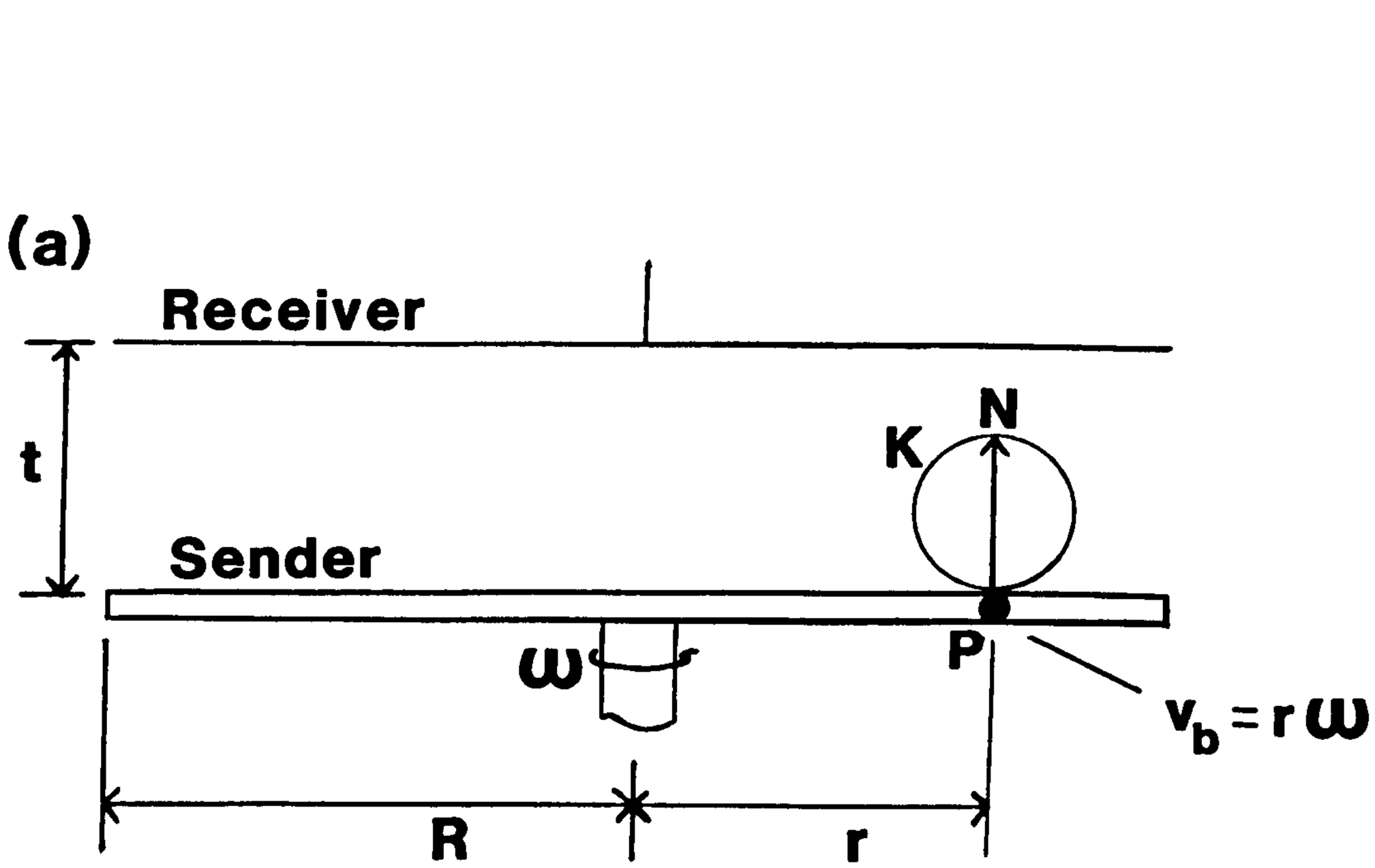

Figure 2.2 Basic geometry of the rotating disc gauge.
(a) View along direction of velocity bias and (b) Plan view. See text for meaning of symbols.

imagined to be transparent and to be at rest. At P_1 momentum $\sigma.m.v_b$ is given up to the receiver where σ is the tangential momentum accommodation coefficient of molecules on the receiver surface and $\sigma = 1$ represents complete transference of tangential momentum which is the case for a flat, smooth and adsorbate covered surface.

From figure 2.2b it can be seen that an impulsive torque

$$\sigma\ m\ v_b\ \cos\alpha\ \frac{r}{\cos\alpha} = \sigma\ m\ v_b\ r \qquad (2.5)$$

is created about the centre of the receiver.

For molecules which do not leave position P in a normal direction there are several possible cases which may apply. Between certain limits symmetrical effects operate whereas asymmetrical effects operate outside of them. Figure 2.3a, showing a detailed diametral section in which all parts of the sender to the right hand side of the centre O move into the page and those to the left move out of it, illustrates this.

A flux of molecules in direction PM at an angle γ clockwise from PN arrives at the receiver with a momentum mv_b at a torque arm greater than r about the centre. However, in the direction PL at an angle γ anticlockwise to PN an equal flux arrives at the receiver at a torque arm less than r by the same amount. The combination of these effects is the same as if both fluxes left P in a direction normal to the surface and delivered a torque of $\sigma mv_b r$ per molecule (i.e. at a torque arm of r) to the receiver where $v_b = r\omega$.

Molecules leaving the sender at anticlockwise angles up to the direction PO arrive at the receiver to create a torque promoting rotation in the same direction as that of the sender, the torque reducing to zero for molecules arriving at O. For anticlockwise angles beyond PO where molecules 'cross the centre' the torque produced will oppose the receiver's rotation. The effect of these molecules which cross the centre from right to left are exactly compensated for by those which cross the centre from left to right from a position Q at a radial distance r on the left hand side of the sender. By similar reasoning it can be seen that the loss of molecules out of the interspace at anticlockwise angles greater than

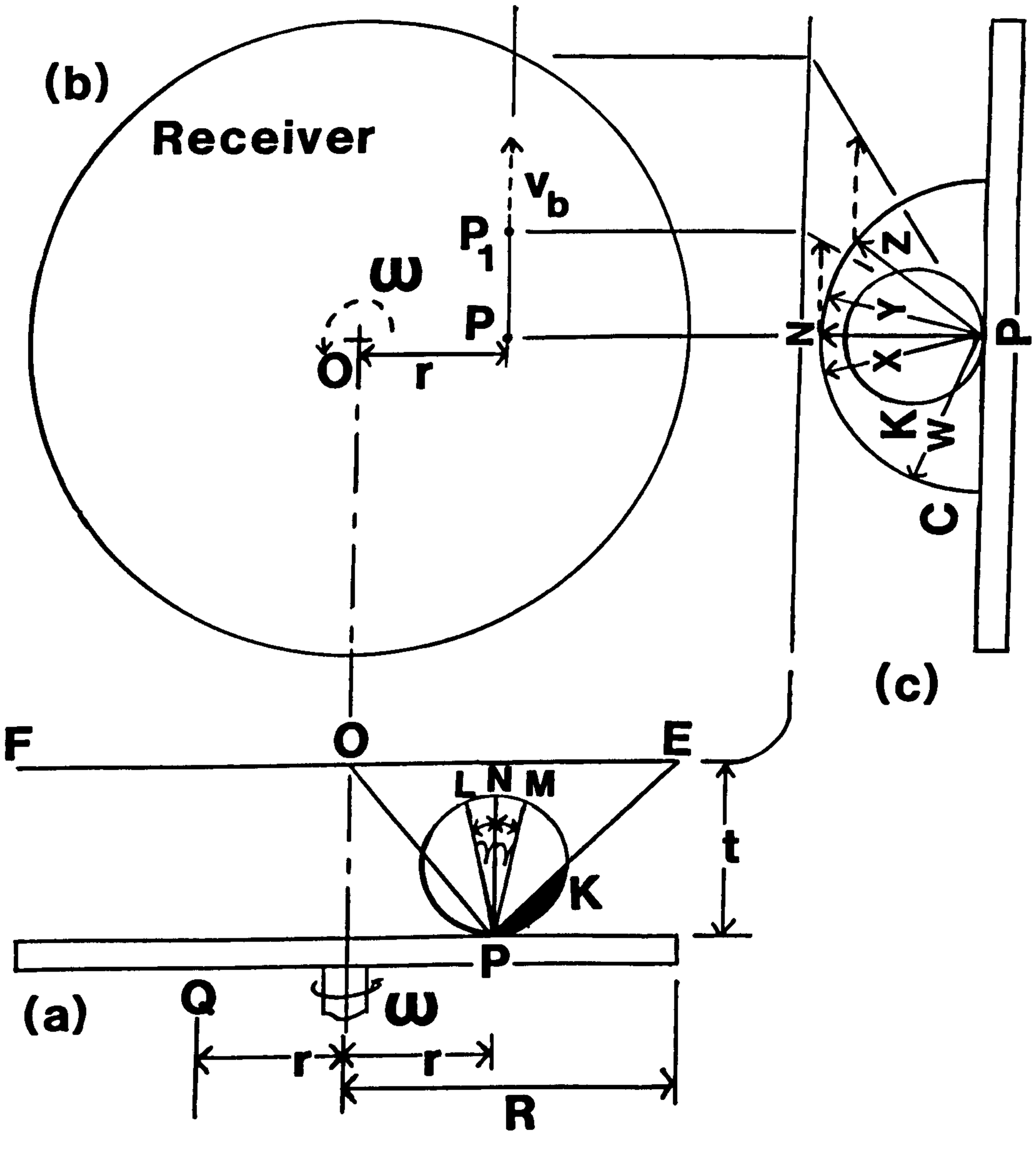

Figure 2.3 Detailed views of the rotating disc gauge geometry.
(a) Diametral section, (b) Plan view and (c) Side view. See text for meaning of symbols.

that defined by PF may be discounted. This is because even if there had had been a receiver surface at this radius to receive these molecules the torque they would have produced would have been cancelled by a torque of equal magnitude, but in the opposite direction, due to the flux from the other side.

Of prime importance is the loss from the interspace of molecules into solid angle at clockwise angles greater than that specified by PE. This flux is indicated by the shaded part of the Knudsen sphere K. Molecules near and at the edge of the disc have the largest bias velocity and since an appreciable fraction of them will be lost there is an appreciable loss of torque. This 'edge effect' is a characteristic of the RDG which has not been discussed before.

In the work of Dushman (1915) this effect was recognised but thought to be negligible for the case where the diameter of the rotating (sender) disc is very large compared with that of the upper (receiver) disc and where the disc-separation was < 10 mm. The validity of this approximation is discussed later.

Figure 2.3c shows a side view of the discs arrangement at a section containing the point P. C is a velocity semicircle, of which there is a complete family, representing the range of molecular velocities. In any direction the distribution in velocity is governed by the Maxwell-Boltzmann distribution. The tips of vectors drawn from P to C represent molecules which desorb with velocity $\bar{v}$ into the half space. The flux in a given direction is determined by the intersections with K. The dashed vectors show the imposed velocity bias.

With the same arguments as those above it can be seen that molecules which leave the sender in a normal direction PN impart momentum $\sigma\ m\ v_b$ to the receiver. Symmetry arguments can be used again to show that molecules in directions PX and PY combine to give the same effect as though all molecules leave in the normal direction PN. The symmetry again only operates within certain limits. The velocities of molecules at an angle represented by PZ are combined with the bias velocity so that they just reach the edge of the receiver. Molecules desorbing at angles greater than that represented at PZ are lost from the interspace. This loss is partly, but not equally, offset by the gain of flux which would otherwise be lost for large anticlockwise

desorption angles. Thus molecules desorbing in the direction W just reach the receiver because of the imposed velocity bias. This loss effect is due partly to the Knudsen distribution and partly to the bias velocity.

A straightforward analysis of the edge effect loss is not possible because of the geometrical complexities of the situation. An analytical treatment and computational modeling was undertaken during the course of the project by Pert (1993) and will be referred to in due course.

Empirically the edge effect is allowed for by introducing the quantity ε where $0 < \varepsilon < 1$ and

$$\varepsilon = \varepsilon(t/R) \qquad (2.6)$$

$\varepsilon \longrightarrow 1$ for $t \ll R$ and $\varepsilon \longrightarrow 0$ for $t \gg R$. That is, as the separation of the discs increases the greater is the loss of molecules from the discs' interspace and hence of molecular torque. The approach which follows is based upon an analysis with an empirical edge effect correction factor introduced to take account of molecules lost from the interspace.

2.3 ANALYSIS

Consider an annulus of width dr and an area $2\pi r.dr$ at a radial distance r on the sender. Because of the symmetries discussed above and because of the fact that desorption, on average, is in a direction normal to the sender surface then the desorption of molecules at all points on the sender can be treated as being in a normal direction. With this assumption edge effect losses do not arise.

It has been shown that for this case a single molecule of mass m at radial distance r creates an impulsive torque of $\sigma m v_b r$ about the centre of the receiver. For the annular ring the contribution to the total torque transferred to the receiver by molecules desorbing from the sender is

$$dG = 2\pi r.dr.J.\sigma m v_b.r \qquad (2.7)$$

where J is the impingement rate of molecules onto the receiver

corresponding to the number density n in the interspace.

The results of kinetic theory show that

$$J = \frac{1}{4} n \bar{v} \tag{2.8}$$

and

$$n = \frac{P}{k T} \tag{2.9}$$

where P is the pressure, k is the Boltzmann constant and T is the absolute thermodynamic temperature. The mean thermal velocity $\bar{v}$ is given in equation 2.4.

Substituting for the bias velocity, $v_b = \omega r$ and integrating from r = 0 to r = R over the whole area gives the total torque

$$G = \int_0^R 2\pi \sigma J m \omega r^3 dr \tag{2.10}$$

$$= \frac{\pi}{2} J \sigma m \omega R^4 \tag{2.11}$$

The coefficient ε is introduced to account for the edge effect loss of molecular torque such that

$$G = \varepsilon \left[\frac{\pi}{2} J \sigma m \omega R^4 \right] \tag{2.12}$$

Substituting the results from kinetic theory gives

$$G = \varepsilon \frac{\pi}{8} \frac{P}{k T} \left(\frac{8 k T}{\pi m} \right)^{1/2} \sigma m \omega R^4 \tag{2.13}$$

$$= \varepsilon \left(\frac{\pi m}{8 k T} \right)^{1/2} P \sigma \omega R^4 \tag{2.14}$$

Since $k = \frac{R_o}{N_A}$ (2.15)

where R_0 is the universal gas constant and N_A is the Avogadro number then

$$G = \varepsilon \left(\frac{\pi}{8000\ R_0} \right)^{1/2} \frac{M^{1/2}}{T^{1/2}}\ P\ \sigma\ \omega\ R^4 \qquad (2.16)$$

where M is the relative molecular mass and $\omega = 2\ \pi\ f$ where f is the sender frequency.

For nitrogen (M = 28.013) at 20 °C, with ε and σ assumed to be unity, and for R = 46 mm (the actual value of the RDG constructed: see Chapter 3) then

$$G \simeq 6 \times 10^{-6}\ P\ f \qquad (2.17)$$

where P is in mbar and G is in Nm. Hence for 850 Hz (maximum sender speed, see Chapter 3) at 10^{-6} mbar, $G \simeq 5 \times 10^{-9}$ Nm.

In the case where the torque is measured statically against a torsion fibre of torsion constant c then

$$G = c\ \phi \qquad (2.18)$$

where ϕ is the angular deflection produced at equilibrium.

The deflection is evaluated by measuring the change in position y of a spot of light which is reflected by a mirror set at the centre of the receiver suspension (see figure 2.1) on a scale of radius of curvature L set at a distance L from the centre of the suspension.

Here $$\phi = \frac{y}{2L} \qquad (2.19)$$

thus $$G = c\ \frac{y}{2L} \qquad (2.20)$$

substituting this in equation 2.16 and rearranging for P gives the operating equation of the RDG thus

$$P_{RDG} = \frac{\frac{c}{2L}}{\varepsilon\ \sigma_{RDG}\ \omega\ R^4 \left(\frac{\pi}{8000\ R_o} \right)^{1/2}} \cdot \frac{T^{1/2}}{M^{1/2}} \cdot y \qquad (2.21)$$

where P_{RDG} is the pressure measured with the RDG. The dependence of P_{RDG} upon $T^{1/2}/ M^{1/2}$ is characteristic of viscosity type gauges.

It should be noted that the only non-directly measurable quantities in the RDG's operating equation are σ_{RDG} and ε. The value of σ_{RDG} the tangential momentum accommodation coefficient of molecules on the receiver surface, can range from $0 \leq \sigma \leq 4/\pi$. For a smooth, flat and adsorbate covered surface it is well established that σ is unity for all gases, see Chapter 1. In early work the value of ε was determined empirically and later analytically so that the RDG is in theory an absolute gauge capable of primary measurements of pressure of $\leq 10^{-3}$ mbar.

2.4 ANALYTICAL TREATMENT OF THE EDGE EFFECT

The value of ε was originally determined empirically and then analytically. The analytical derivation was performed by Prof.G.J. Pert and is reported by Pert (1993). He considered the case of equal sized discs of radius R at a separation t and assumed a Knudsen cosine distribution of molecular effusion from the sender with a Maxwell-Boltzmann velocity distribution. The probability of a molecule leaving the sender and reaching the receiver was derived. From this the proportion of lost torque was derived where

$$\varepsilon\left(\frac{t}{R} \right) = \left[\left(1 + \left(\frac{t}{2R} \right)^2 \right)^{1/2} - \frac{t}{2R} \right]^4 \qquad (2.22)$$

This expression for the edge effect loss due to the Knudsen distribution is valid only for low sender speeds where $\mu \ll 1$ and

$$\mu = \frac{\omega\ t}{\bar{v}} \qquad (2.23)$$

ω is the radian frequency of the sender.

Table 2.1 shows values of μ for t = 5 mm (typical), at different sender speeds and a range of molecular masses at 20 °C. It can be seen that for nitrogen residual gas with a value of t = 5 mm then the expression for ε will hold up to a sender speed of 35 krpm.

Sender speed / krpm	Relative Molecular Mass 2	28	84
7	0.002	0.008	0.013
10	0.003	0.011	0.019
20	0.006	0.022	0.038
30	0.009	0.033	0.058
40	0.012	0.044	0.077
50	0.015	0.056	0.096
100	0.030	0.111	0.192

Table 2.1 Values of μ for various molecular mass and sender speed combinations.

At high sender speeds there is a loss of torque due to the velocity bias from the sender and the expression for ε becomes invalid. A comparison of the expression for ε with experimental results is given in Chapter 4.

In the work of Dushman the maximum sender speed was 10 krpm. The sender was of diameter 35 mm (Dushman, 1915), thus loss from the velocity bias would have been negligible. Although the discs were kept at a separation of 10 mm or less there would still have been a loss of torque due to the Knudsen cosine distribution. The analysis would have been complicated by the discs being of different sizes but an edge effect loss of torque would still have been present which was not accounted for. The results of experimental investigations of the edge effect of the different sized discs configuration are given in Chapter 7.

2.5 ALLOWANCE FOR MORE THAN ONE GAS SPECIES

If there are N gas species making up the vacuum then

$$P_{RDG} = \sum_{i=1}^{N} p_i \tag{2.24}$$

where p_i is the partial pressure of each gas. Assuming that each gas has the same (unity) value of σ_{RDG} then the torque

$$G = \sum_{i=1}^{N} G_i \tag{2.25}$$

By using the substitution for β where

$$\beta = \frac{\frac{c}{2L} \qquad T^{1/2}}{\varepsilon\ \sigma_{RDG}\ \omega\ R^4 \left(\frac{\pi}{8000\ R_0} \right)^{1/2}} \tag{2.26}$$

and since

$$y = \sum_{i=1}^{N} y_i \tag{2.27}$$

by rearranging equation 2.21 for y and substituting for β then

$$y = \frac{1}{\beta} \sum_{i=1}^{N} M_i^{1/2} . P_i \tag{2.28}$$

where

$$P_i = r_i . P_{N_2} \tag{2.29}$$

i.e. r_i is the amount of each gas species relative to that of nitrogen (P_{N_2}). Thus

$$y = \frac{1}{\beta} \sum_{i=1}^{N} M_i^{1/2} . r_i\ P_{N_2} \tag{2.30}$$

combining equations 2.24 and 2.29 and substituting for P_{N_2} in equation 2.30 gives

$$y = \frac{P_{RDG}}{\beta} \quad \frac{\sum_{i=1}^{N} M_i^{1/2} . r_i}{\sum_{i=1}^{N} r_i} \tag{2.31}$$

rearranging this for P_{RDG} gives

$$P_{RDG} = \beta\ y \quad \frac{\sum_{i=1}^{N} r_i}{\sum_{i=1}^{N} M_i^{1/2} . r_i} \tag{2.32}$$

2.6 ROTATING DISC GAUGE SENSITIVITY

For a single gas equation 2.21 can be rearranged to express an RDG sensitivity, S_{RDG} thus

$$S_{RDG} = \frac{\beta\ y}{P\ \ M^{1/2}} \tag{2.33}$$

with working units of mm $mbar^{-1}$ where M is the relative molecular mass.

2.7 MOTION OF THE HARMONIC RECEIVER SUBJECTED TO A STEADY TORQUE

The angular motion of the receiver disc's response to a step function of torque G at time t = 0 can be expressed by the familiar differential equation below. The situation is shown in figure 2.4.

$$I\ \ddot{u} = G - f\ \dot{u} - c\ u \tag{2.34}$$

where u is the angular deflection ($u = \phi = y / 2L$), I is the moment of inertia of the receiver, f is the damping constant from friction at the point at which the fibre is held, internal friction of the fibre and from molecular impacts on the receiver and c is the torsion constant of the fibre.

Let $G_o = G/I$ (2.35)

$2k = f/I$ (2.36)

and $\omega_o^2 = c/I$ (2.37)

then using these substitutions in equation 2.34 gives

$$\ddot{u} + 2 k \dot{u} + \omega_o^2 u = G_o \quad (2.38)$$

This is a well known equation with solution

$$u = u_o \left(1 - \frac{1}{\cos(\varepsilon)} \exp(-kt) \cos(vt-\varepsilon) \right) \quad (2.39)$$

where

$$\varepsilon = \arctan(k/v) \quad (2.40)$$

and

$$v = (\omega_o^2 - k^2)^{1/2} \quad (2.41)$$

The period of the induced oscillation is

$$T = \frac{2\pi}{\left(\frac{c}{I} - \frac{f^2}{4I^2} \right)^{1/2}} \quad (2.42)$$

for the case of light damping $\omega_o^2 \gg k^2$

and $$T = 2\pi \left(\frac{I}{c} \right)^{1/2} \quad (2.43)$$

In this case the amplitude of the induced oscillation is, to an excellent approximation, unchanged over the course of several oscillations as is indicated in figure 2.4. The displacement y_o (the measured quantity) which corresponds to eventual steady state deflection is easily determined since it is the centre of the induced oscillation.

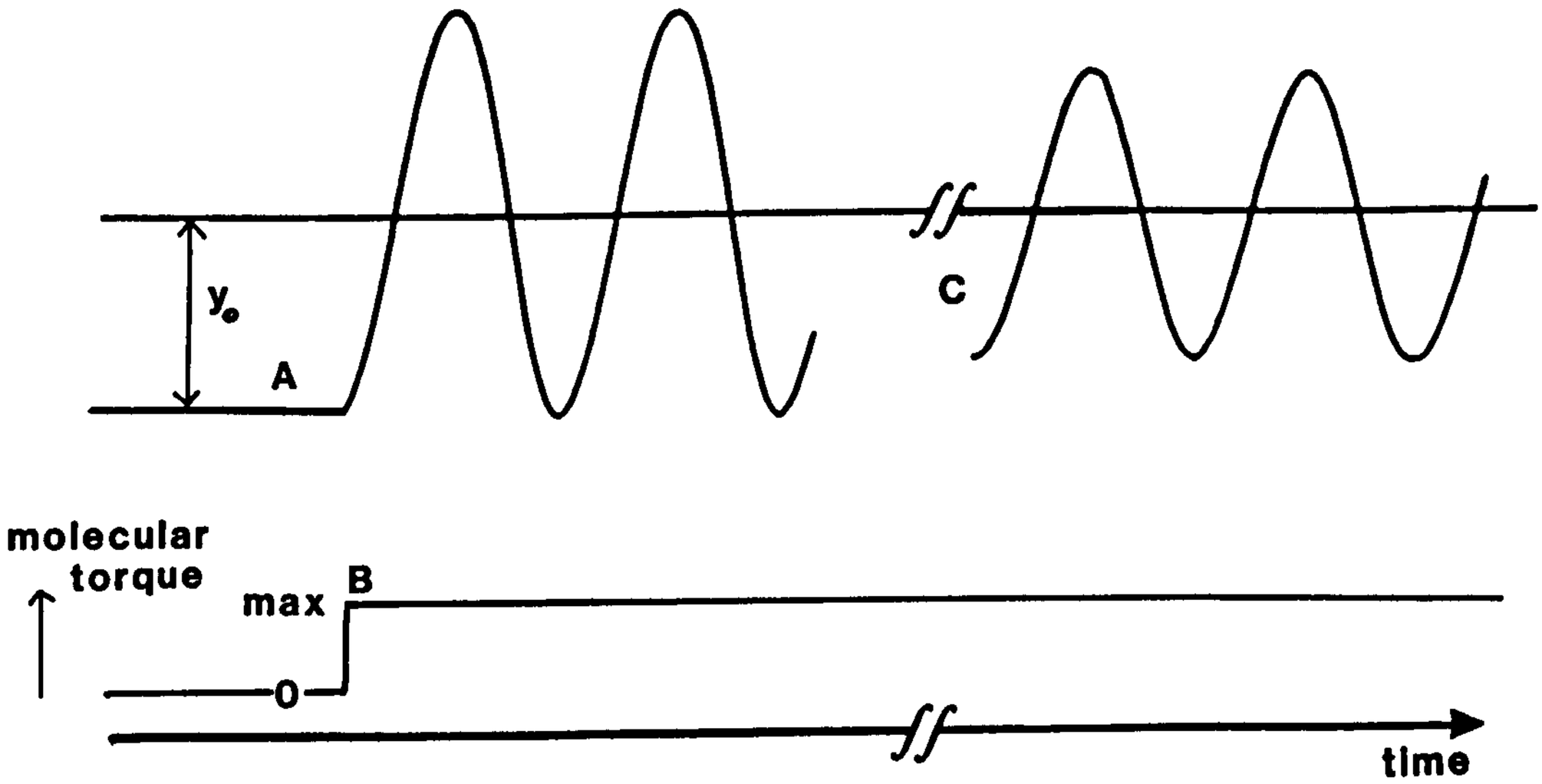

Figure 2.4 Response of the receiver to a step function of molecular torque.
A Sender quiescent before torque applied; B Step function of torque applied; C Amplitude constant over an interval of a few periods.

By using a long period of suspension (the lowest actually used was 23.4 secs, see Chapter 3) then the maximum speed of rotation of the receiver for its greatest deflection (250 mm) will be negligible compared to even the lowest sender speed.

2.8 CENTRIFUGAL EFFECTS

Consider a molecule of nitrogen bound to the surface at the edge of the 46 mm radius (r) sender. The centrifugal force it is subjected to is

$$F_c = m \omega^2 r \tag{2.44}$$

where $\omega = 2\pi f$. The maximum value of the sender frequency f is 850 Hz, see Chapter 3, whence $F_c = 6 \times 10^{-20}$ N for nitrogen.

The magnitude of the binding force (Eisberg and Resnick, 1985) is

$$F_b = \frac{dU}{dr} \tag{2.45}$$

If the molecule is in its least bound state before desorption r is a few molecular radii. If the binding potential U is taken as the energy kT (at room temperature) of desorption then $F_b \propto 4 \times 10^{-12}$ N. Thus the weakest binding force is still very much larger than the largest centrifugal force. There is therefore a negligible centrifugal effect on the Knudsen and Maxwell-Boltzmann distributions of desorbing molecules and the assumption that molecules leave the surface normally is valid.

2.9 AIMS OF THE PROJECT

In Chapter 1 it was shown that the RDG held out considerable promise as a means of absolute pressure measurement for high and ultra-high vacuum. Although other hybrid gauges have been developed, most notably the spinning rotor gauge (SRG) and the rotating cylinder gauge, the RDG has not been pursued in its original form since the work of Dushman (1915). Many decrement type viscosity gauges, have been developed with the aim of extending the lower limit of primary

pressure measurement, a need which was shown to clearly exist. The RDG is unique in its operation from a static position and it was the author's aim to develop and investigate the performance of an RDG and to establish its position in the pressure gauge hierarchy.

The distinct aims of the authors work were:

(1) To build an RDG based on the design of that built by Dushman (1915) using modern day vacuum technology.

(2) To investigate the edge effect characteristics of the (equal sized discs) RDG and its performance at high sender speed. To then contrast these findings with theoretical and computational predictions.

(3) To compare measurements of pressure made using the RDG with those made simultaneously by an externally available SRG transfer standard.

(4) To determine the uncertainties associated with the RDG pressure measurements and to establish the range of pressure measurements possible using the RDG.

(5) For a range of gas species to investigate the predicted $M^{1/2}$ dependence of the sensitivity of the RDG (see equation 2.33) and to establish the universality of the RDG for different gases.

(6) With the above aim in mind and since the RDG's operating equation (2.21) clearly illustrates the potential of the RDG for measuring values of the tangential momentum accommodation coefficient σ, which was noted but not investigated by Dushman (1915), the author aimed to measure the values of σ for various gases on different surfaces exploiting the externally available transfer standard.

(7) To investigate the characteristics of an RDG for various sized receiver discs which were all smaller than the sender disc.

CHAPTER 3

APPARATUS AND EXPERIMENTAL PROCEDURE

3.1 INTRODUCTION

In this chapter the design, technical details and construction of the rotating disc gauge (RDG) apparatus are described. The construction of all apparatus was undertaken in the departmental workshop unless stated. A schematic diagram of the system is shown in figure 3.1 and photographs in figures 3.2 and 3.3. Details of individual parts of the apparatus and the procedure for using the RDG are then described.

3.2 VACUUM CHAMBER

The chamber was a tube of 150 mm internal diameter terminated in DN150CF flanges, see figure 3.4, and was originally mounted on an ion pump. It was made from 3.175 mm stainless steel (ports of 1.59 mm) bakeable to 350 °C. The length and T shape of the chamber was determined by the need to avoid interference between the ionization gauges and the RDG. It was also designed to have a large enough volume (17 l) to ensure pressure equalization and to accommodate the RDG and its shutter mechanism.

Ports were incorporated for reference pressure gauges, gas entry, a roughing line, a deposition source and for general access. The chamber was mounted via supports (see figure 3.1) on a frame to avoid over-stressing the neck of the ion pump. Supports at the end of the chamber ensured equal distribution of weight and facilitated alignment of the chamber. The frame was held on adjustable feet which enabled alignment, and located on 4 mm deep steel plates to minimise vibrations and to avoid movement.

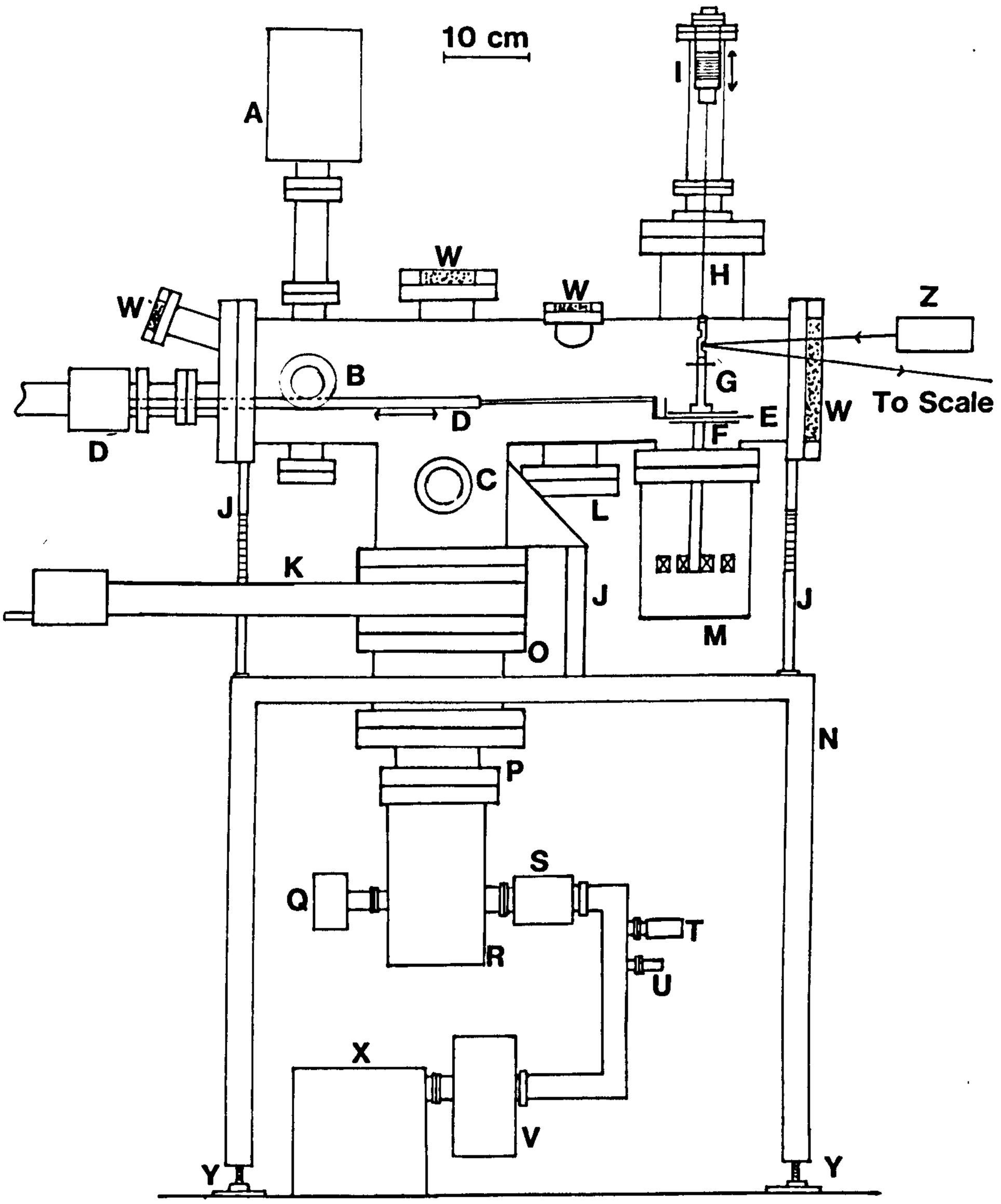

Figure 3.1 Schematic of the rotating disc gauge system.
A Residual gas analyser; B Hot cathode ionization gauge; C Fine-leak valve; D Drive for shutter; E Shutter; F High speed disc; G Receiver suspension; H Torsion fibre; I Vertical drive for suspension; J Supports; K Gate valve; L Deposition source (not used); M High speed rotor; N Frame (960 mm high); O Collar; P Stepper flange; Q Automatic vent valve; R Turbomolecular pump (in position of original ion pump); S Isolation valve; T Pirani gauge; U Vent valve; V Fore-line trap; W Window view ports; X Rotary (backing) pump; Y Adjustable feet on base plates and Z Lamp and scale arrangement.

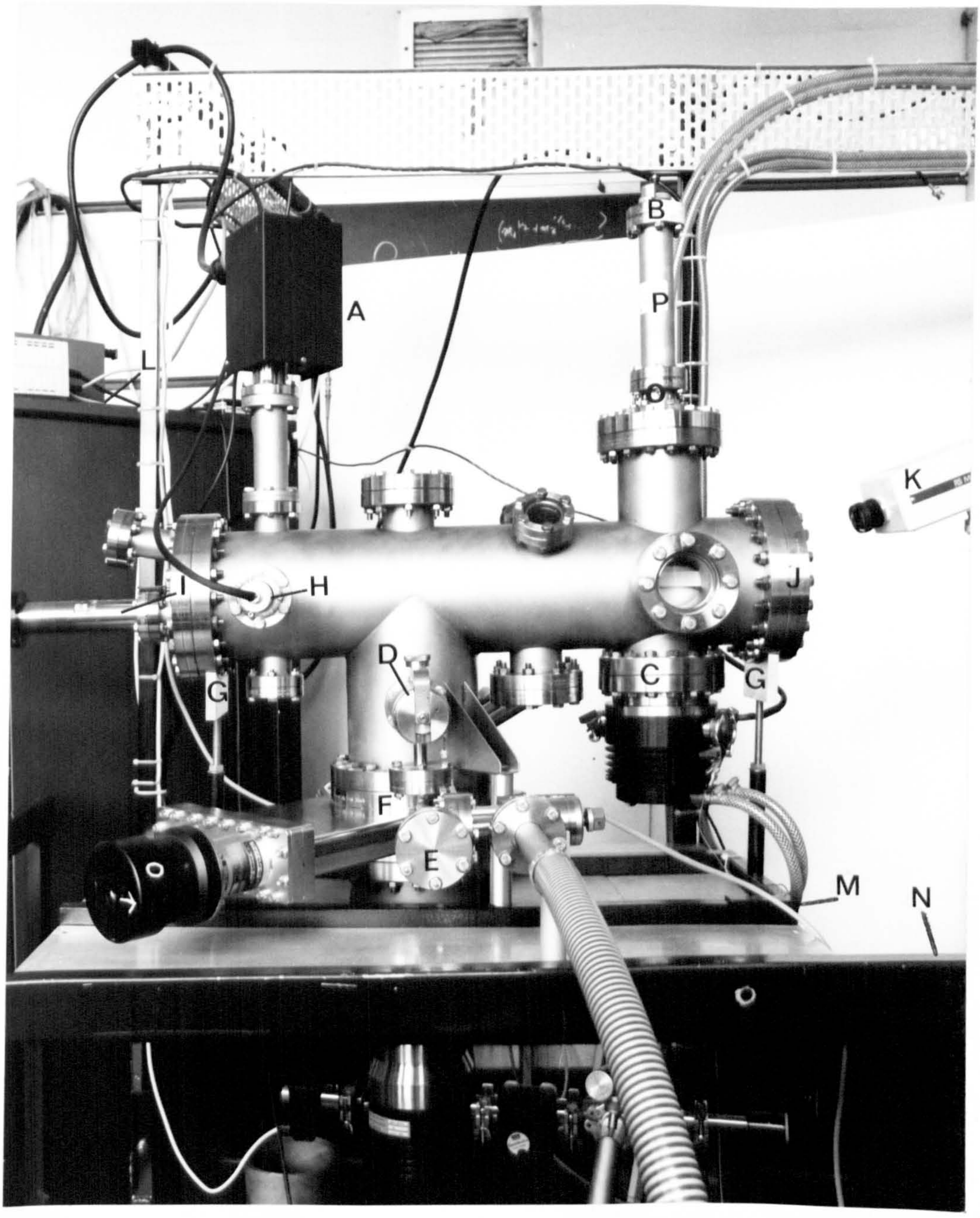

Figure 3.2 Side view of the system.

A Residual gas analyser; B Vertical drive and fibre; C High speed rotor; D Fine-leak valve; E Gas line; F Gate valve; G Supports; H Hot cathode ionization gauge; I Drive for shutter manipulation; J View port; K Camera; L Instrument control rack; M Frame for chamber mounting; N Barrier; O Rotatable flange and P Tube for longer fibre.

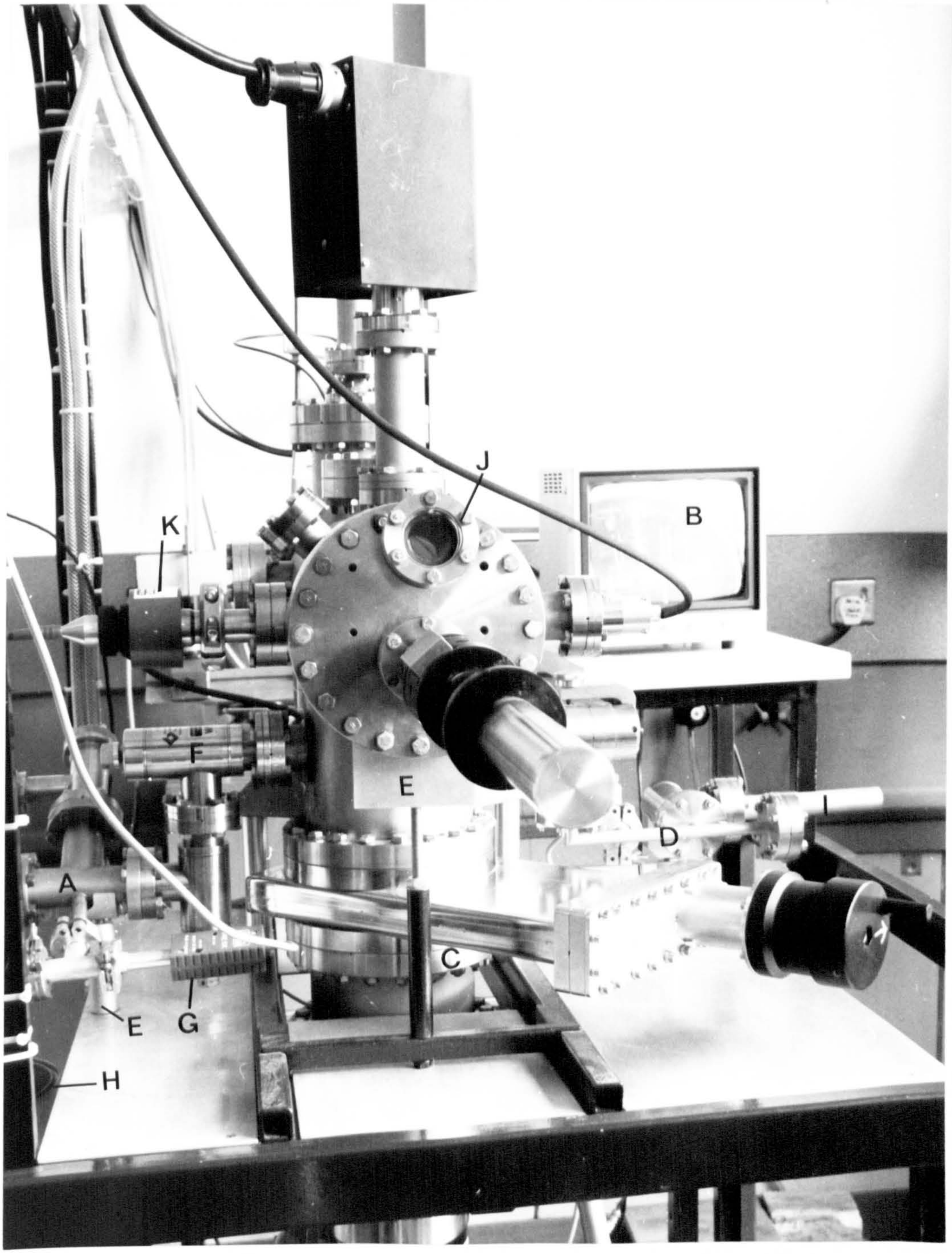

Figure 3.3 Front view of the system.

A Roughing line; B Camera monitor; C Collar; D Gas line; E Support; F Isolation valve; G Pirani gauge; H Adsorption pump; I To rotary pump; J Viewport and K Penning gauge.

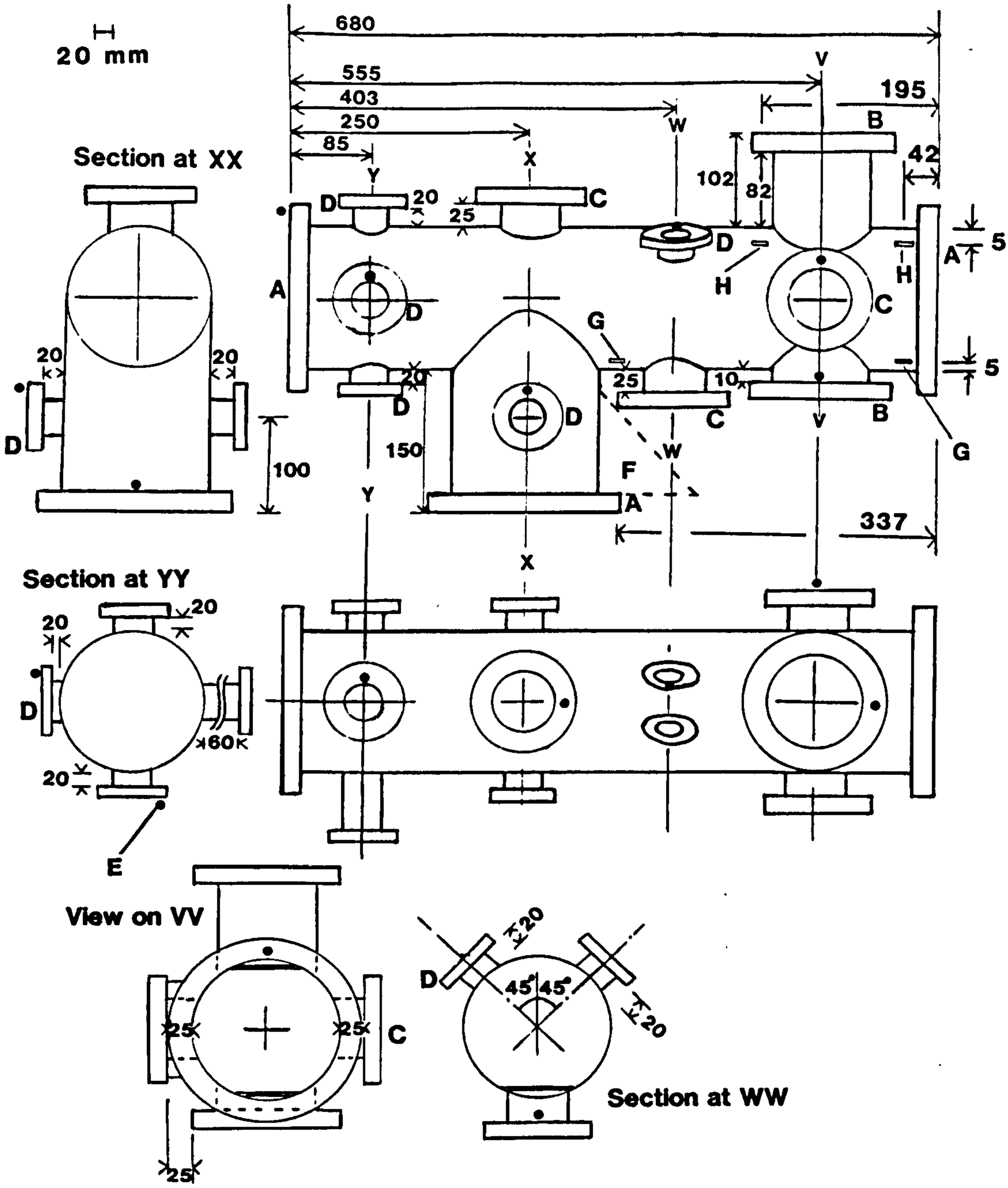

Figure 3.4 Chamber specifications.
A DN150CF flange; B DN100CF flange; C DN63CF flange; D DN35CF flange; E Flange hole alignment; F Support welded to chamber; G Internal support (3.52 mm deep) and H Internal support (1.36 mm deep).

3.3 PUMPING ARRANGEMENT

The pumping arrangement of the system is shown in standard graphic symbols in figure 3.5.

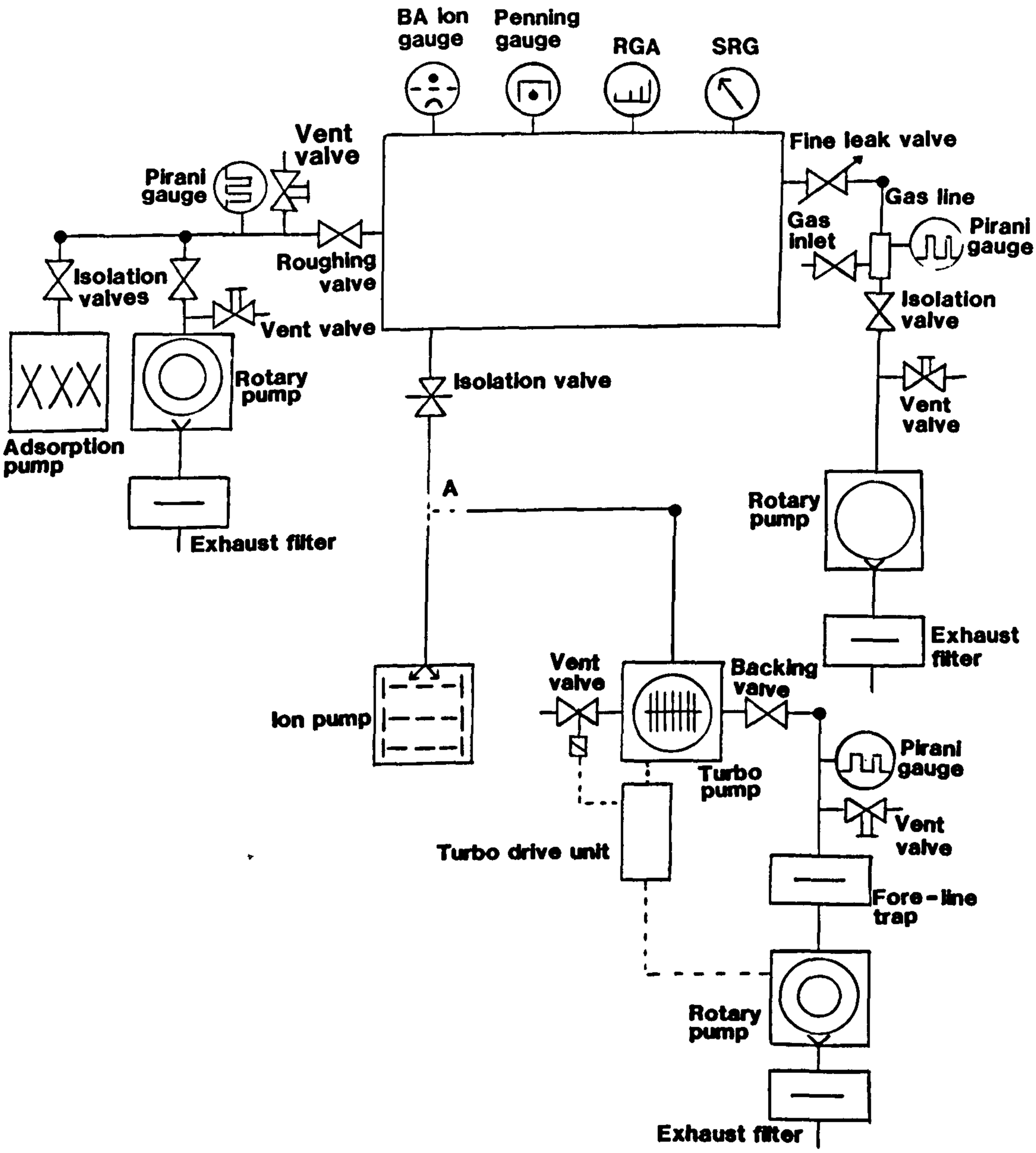

Figure 3.5 The pumping arrangement shown in standard symbols.
A - Turbomolecular pump superseded ion pump.

The roughing line was supported to relieve stress on the chamber's flange, see figure 3.3. An Edwards High Vacuum International (EHVI) E2M5 two stage rotary pump (Edwards, 1989) of speed 5 $m^3 hour^{-1}$ was used to achieve a vacuum of 10^{-1} mbar in a few minutes from atmosphere. A cryogenic adsorption pump was then used to take the system to below 10^{-3} mbar in about 30 minutes.

A Mullard VKP500 cold cathode magnetron sputter ion pump (Mullard, 1965) was used for the achievement of high vacuum. It had a pumping speed for nitrogen of 200 ls^{-1} and was powered by a Mullard KPS500 5 kV power supply. Pressures of 1×10^{-7} mbar were routinely achieved. A Caburn GV6000M gate valve, bakeable to 200 °C (Caburn-MDC, 1990) was used to isolate the ion pump from the rest of the chamber. This enabled the ion pump to operate continuously when the chamber was at atmospheric pressure. The ion pump's performance was limited by the backstreaming of vapour from the bearing grease of the high speed rotor. A 115 mm long collar was fitted to the ion pump's flange to raise the chamber to a height to fit in the high speed rotor and to avoid interference by the magnetic fields of the ion pump. Adjustable feet on the ion pump enabled alignment and were located on 4 mm deep steel base plates to suppress vibration and movement.

The ultimate pressure in the system was 9×10^{-8} mbar and consequently to operate in pure gas atmospheres the pressure had to be raised above 10^{-5} mbar. Since the ion pump was unreliable at these pressures and to increase pump down times an EHVI EXT200 turbomolecular pump (Edwards, 1992) on a DN100CF flange was installed, see figure 3.6. It was operated by an EXC200 controller and had a pumping speed for nitrogen of 200 ls^{-1}. The turbomolecular pump was installed vertically. An ISX 100/6 inlet screen was fitted to stop debris falling into the pump and reduced the pumping speed by 15 %.

The turbomolecular pump was continuously water cooled at 20 $lhour^{-1}$ and backed to 10^{-3} mbar by an EHVI E2M5 two stage rotary pump. A molecular sieve fore-line trap was fitted between the turbomolecular pump exhaust and the rotary pump to avoid back streaming from the rotary. An EHVI TAV10EK (Edwards, 1992) automatic vent valve was fitted to vent the system in the event of pump failure to avoid migration of oil into the vacuum system when the turbomolecular pump

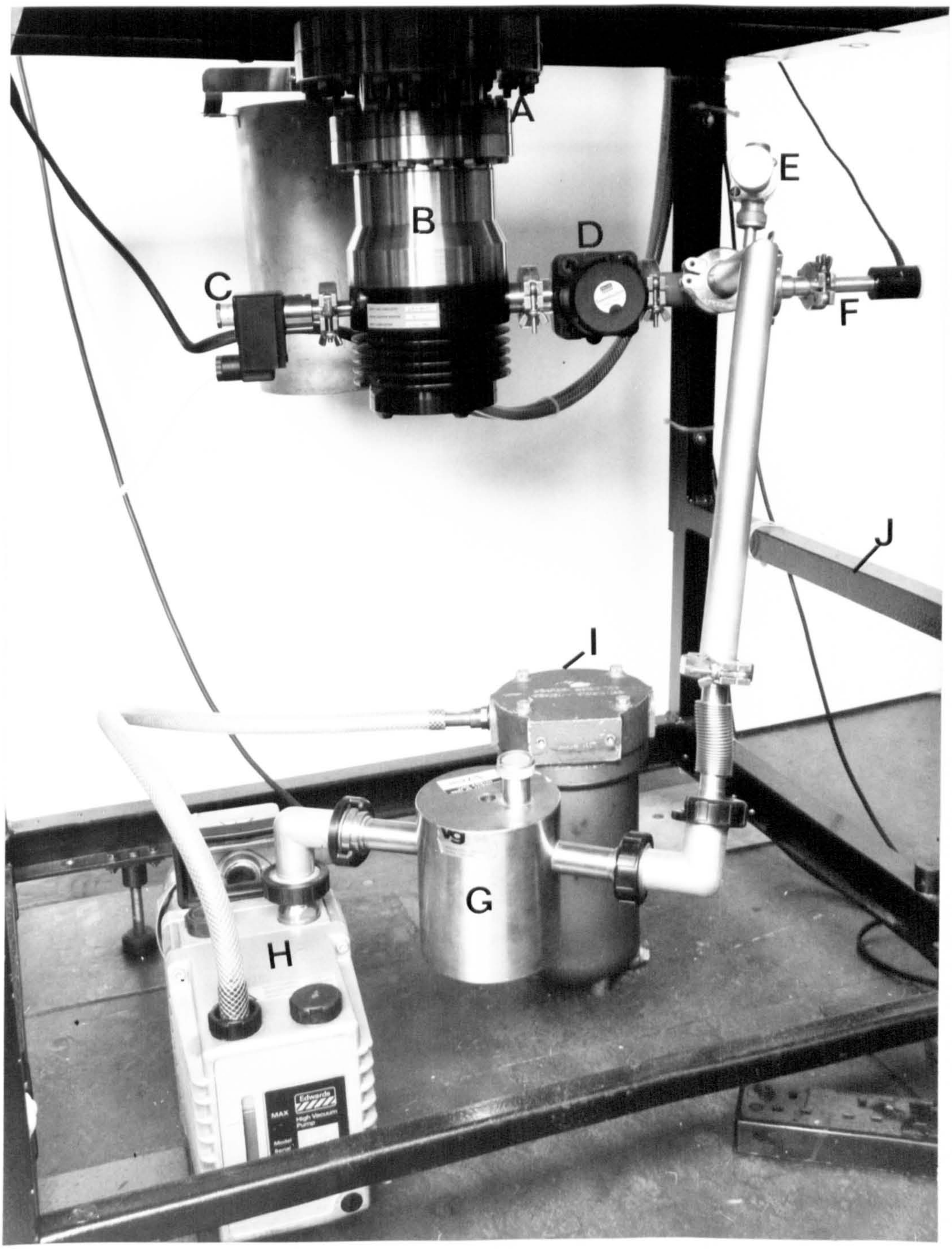

Figure 3.6 The turbomolecular pumping system.
A Stepper flange; B Turbomolecular pump; C Automatic vent valve; D Backing valve; E Vent valve; F Pirani gauge; G Fore-line trap; H Rotary pump; I Exhaust filter and J Frame for mounting the chamber.

was off.

The system was automatically interlocked so that the turbomolecular pumping cycle was controlled by the EXC200 controller, see figure 3.7. When the controller was activated the vent valve closed and the rotary ran for a preset time of 90 secs, before the turbomolecular pump was started. This ensured that the backing pressure was below the maximum (0.2 mbar) for the turbomolecular pump to operate. Pressures below 10^{-6} mbar were achieved from atmosphere in 12 hours. The ultimate pressure after bakeout was 9×10^{-8} mbar of dominantly water vapour back streaming from the rotor.

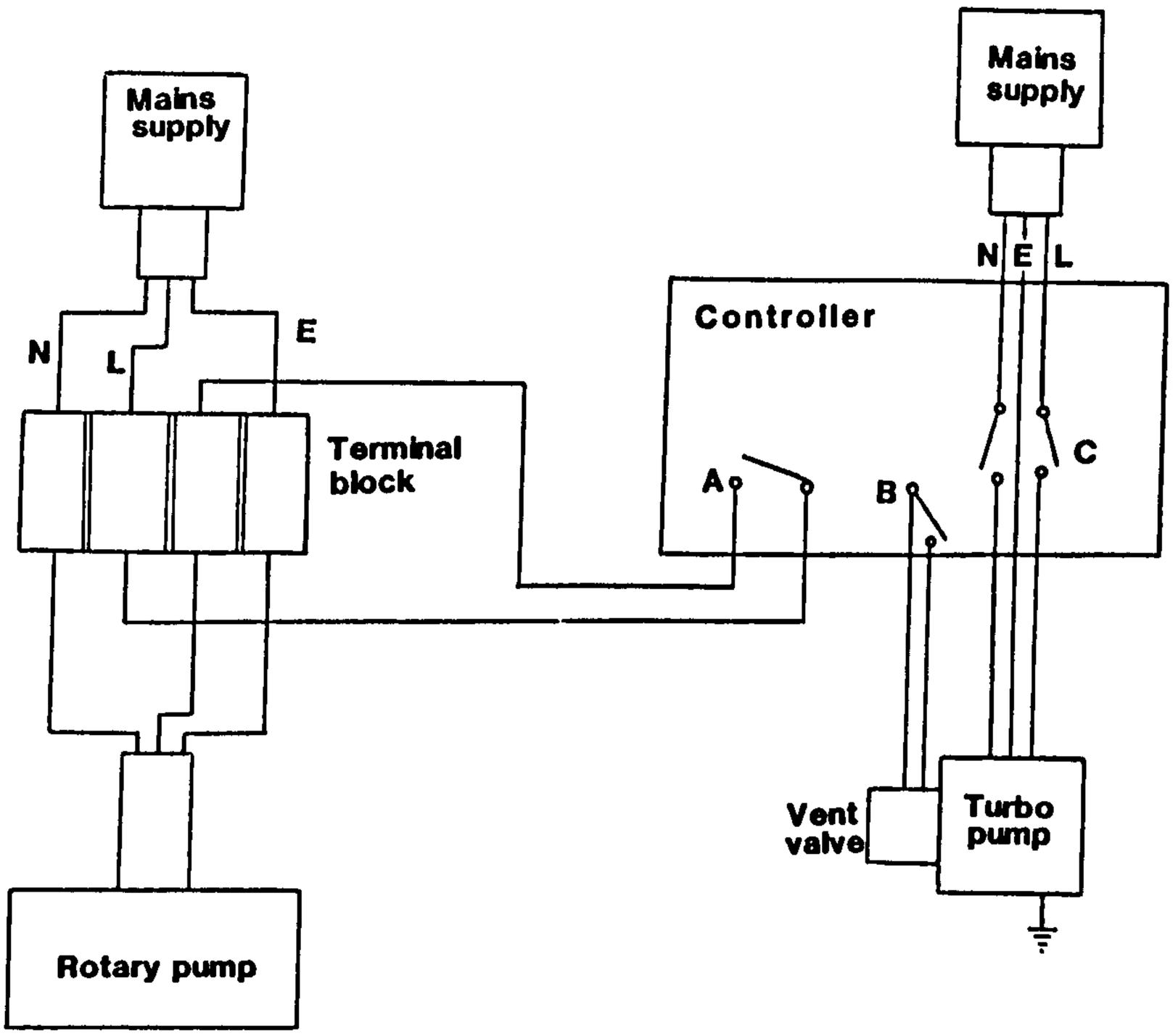

Figure 3.7 Schematic of the turbomolecular pump automatic control and interlock system.
Relay switches A (backing rotary pump), B (vent valve) and C (turbomolecular pump) operated by the controller.

The system was leak tested (to 10^{-11} mbar ls^{-1}) and baked for 2 days. Nickel chrome alloy heating element tapes were used (Hotfoil, 1991) with aluminium foil covering insulation. A maximum of 200 °C was achieved.

3.4 PRESSURE REGULATION AND THE INTRODUCTION OF GASES

To raise the pressure in the system a single gas or air was introduced via a high precision Vacuum Generators (VG) MD series fine-leak valve (Vacuum Generators, 1989) with an open conductance of 0.1 ls^{-1}. It was mounted on a DN35CF flange on the pump section of the chamber to avoid gas beaming effects at the gauges. A 0.05 l volume gas line was constructed, see figures 3.8 and 3.9, and connected to the fine-leak valve. This line was pumped by an EHVI E2M5 single stage rotary pump (Edwards, 1989) and 1 and 2 litre gas bottles (Masonlite, 1992) were used to introduce pure gases into the line and thence the chamber. A support piece was used to relieve the stress from the gas line on the fine-leak valve.

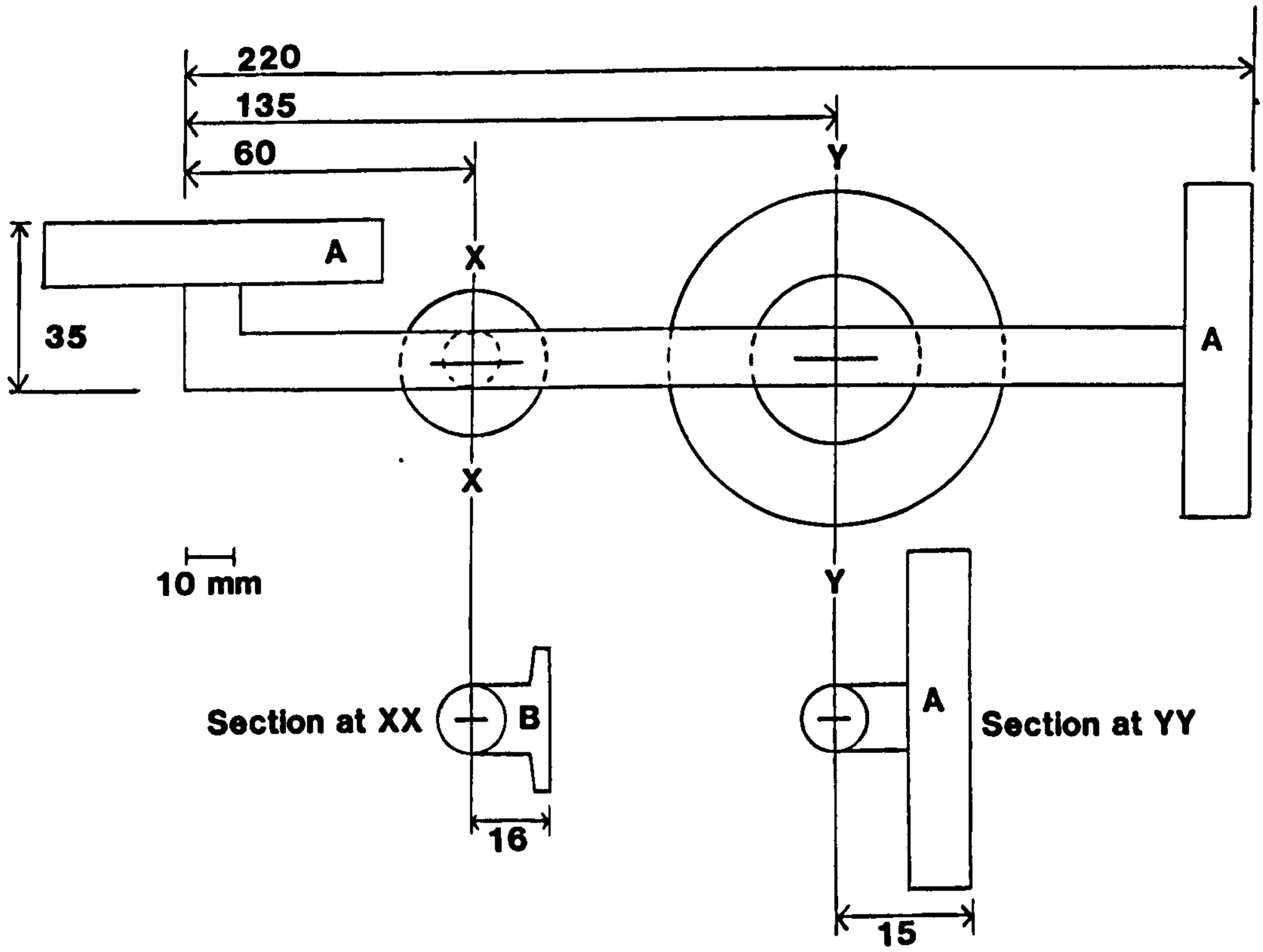

Figure 3.8 The gas line.
A DN35CF flange and B NW10 flange.

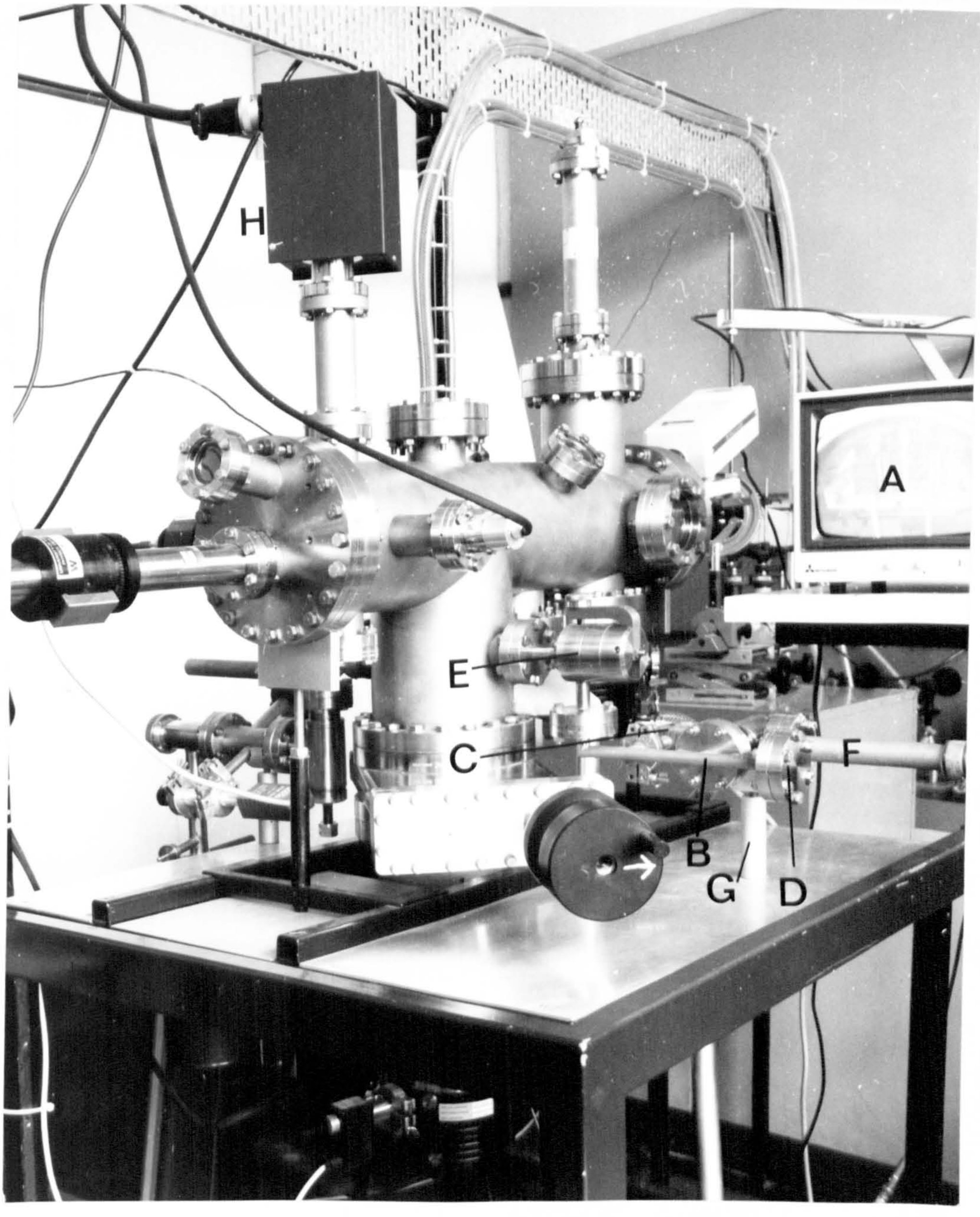

Figure 3.9 View of the system from the front right side showing the gas line.
A Monitor for camera and RGA display; B Gas line; C Pirani gauge; D Position of gas bottles; E Fine leak valve; F To rotary pump; G Support and H Residual Gas Analyser (RGA).

3.5 PRESSURE GAUGES

Several gauges were used on the chamber and pumping system for pressure measurement and control. A Bayard-Alpert (BAG) thermionic ionization nude gauge which was controlled by a Millennia series (Vacuum Generators, 1989) Intelligent Pressure Gauge Controller (IPGC) was used. The BAG had twin tungsten helical filaments with a sensitivity of 19 $mbar^{-1}$ (see Chapter 1) and was used to measure pressures below 10^{-4} mbar. It was operated at 1 mA emission and had a variable preset automatic overpressure trip. It was mounted on a DN35CF flange in tubulation so that it did not protrude into the chamber but with sufficient clearage to avoid conduction effects. The gauge head and leads were bakeable to 250 $^{\circ}C$ and was used to monitor the pressure during bake out. A + 0.25 V/decade output signal (+ 2.5 V at 10^{-4} mbar) was provided from the BAG to enable remote monitoring on a chart recorder and an IBM compatible PC. A relay operated by the BAG was used as a pressure protection interlock for the residual gas analyser.

The BAG had a digital display to one decimal point and was used to monitor pressure stability and as a reference gauge.

An EHVI CP25EK Penning cold cathode ionization gauge (see Chapter 1) with a 505 controller (Edwards, 1989) was installed on a NW25 flange with a aluminium UHV seal fitting to an NW25 to DN35CF converter. It gave an analog display of pressure in the range 10^{-2} to 10^{-7} mbar and was used primarily to monitor conditions with its 0 to + 10 V output signal during pump down. The Penning gauge was not bakeable and had to be kept below 70 $^{\circ}C$. A pressure rise was created when the gauge was turned on at low pressures and the system took 15-30 minutes to return to base pressure.

In the range 5 to 10^{-3} mbar three Pirani gauges were used to monitor pressure. A VG P30 (Vacuum Generators, 1989) was on the backing line of the turbomolecular pump to monitor the backing pressure (figure 3.6) and was controlled by the IPGC. Two EHVI PRE10K Pirani gauges both operated by a 502 controller were also used (Edwards, 1989). One was on the roughing line, see figure 3.3, to measure pressure during pump down and one on the gas line, see figure 3.9. The Pirani gauges had NW10 fittings and were not bakeable.

3.5.1 Spinning Rotor Gauge

A spinning rotor gauge (SRG), see Chapter 1, was used as a transfer standard for comparisons of pressure measurements made with the RDG.

The SRG was an MKS Second Generation Spinning Rotor Gas Friction Vacuum Gauge type SRG-2 (MKS Instruments, 1989). It had a magnetically suspended 4.5 mm diameter steel (100Cr6) ball rotor of density 7.790 gcm^{-3} held in a non-magnetic stainless steel chamber on a DN35CF flange. The ball, chamber and control unit were calibrated together, for nitrogen, by the National Physical Laboratory (NPL) high-vacuum series expansion apparatus. The effective tangential momentum accommodation coefficient of the ball was determined to be 1.024 for nitrogen (National Physical Laboratory, 1990).

To ensure reproducible positioning of the cylindrical gauge head the axis of the counter flange was located within $\pm 1^{\circ}$ of the horizontal and the rotor chamber was adjusted so that the guide bar was placed vertically within $\pm 1^{\circ}$ underneath the upper guide bar. The SRG was located in the near vicinity of the RDG, see figure 3.10. Interference from magnetic fields and low frequency electrical noise was avoided by the correct positioning of the SRG and its cables.

The SRG was operated in accordance with NPL procedures (National Physical Laboratory, 1990). First this required the rotor and chamber to be baked to 200. $^{\circ}C$ to degas the ball. The SRG's operating equation shows that the offset of the SRG must be measured to allow accurate measurements of pressure, see Chapter 1. There were three contributions to the offset; the residual magnetic drag, the thermal drift and random noise.

Random noise problems were indicated by a departure from the normal 415 Hz operating frequency of the ball. The only noise problem encountered when the system was ion pumped was if the chamber was knocked. When the turbomolecular pump was used the vibrations from it combined with those from the high speed rotor so that the SRG was inoperable at rotor speeds between 15 and 35 krpm. At other rotor speeds no noise problems were encountered by the SRG.

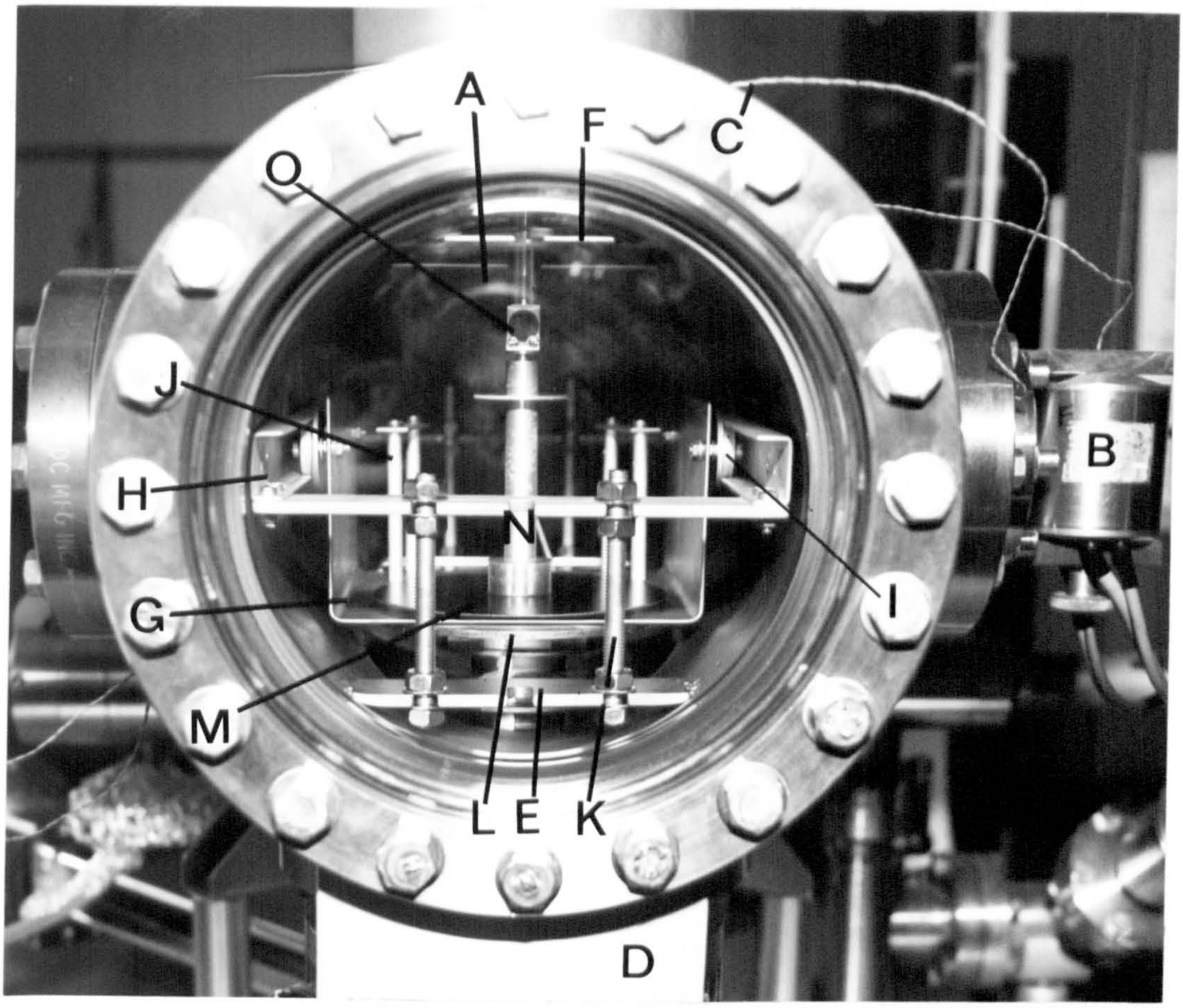

Figure 3.10 End view into the chamber showing the rotating disc gauge and the spinning rotor gauge.

A DN150CF window; B SRG; C Thermocouples; D Support; E Chamber internal support (3.52 mm deep); F Chamber internal support (1.36 mm deep); G Shutter; H Rails; I Shutter wheels; J Damping posts; K M6 rod for rail fixture; L High speed sender disc; M Silicon receiver disc; N shaft and O Mirror.

The thermal drift contribution was made negligible by running the SRG for over 5 hours before measuring the offset, this ensured that the ball reached a stable temperature (T). This and stabilizing laboratory conditions ensured the value of dT/dt was negligible.

When the environmental conditions above were achieved the residual magnetic drag of the SRG was measured. The system was lowered to base pressure so that the molecular drag was negligible and the pressure reading of the SRG (P_{SRG}) was due only to the residual magnetic drag. The relative molecular mass of the gas to be used in the experiment and the temperature were entered into the SRG controller. A sampling interval of 25 secs was used as in the NPL calibration procedure. The residual drag was the mean value of 20 or more consecutive, undisturbed, measurements. The nitrogen equivalent value of the residual drag was typically 1.8×10^{-5} mbar (c.f. 1.74×10^{-5} to 2.39×10^{-5} mbar measured by the NPL).

The residual drag was entered into the SRG controller and the system's pressure increased. The mean of 5 consecutive measurements was used to give the value of P_{SRG}. A sampling interval of 25 seconds was used and the temperature was updated regularly. The SRG measurements of pressure were taken simultaneously with those of the RDG. The offset was measured regularly, typically every 60 minutes.

By minimizing thermal drifts and random noise the offset value was highly stable. The sources of uncertainty in the SRG measurements were due to contamination of the ball after or in the absence of baking, drift in the calibration of the ball, a general uncertainty in P_{SRG} measurements and an uncertainty in calibration of the SRG in gases other than nitrogen. These are discussed fully in Chapters 1 and 6.

3.6 RESIDUAL GAS ANALYSIS

For a determination of pressure by the RDG the gas composition of the vacuum must be known. A Hiden HAL I 100 quadrupole, residual gas analyser (RGA), was used to give quantitative measurements of residual gases (Hiden Analytical, 1991) in the range 2 - 100 atomic mass units. The RGA had a printer and remote monitor output (see figure 3.9). It was mounted inside a 35 mm i.d. tube on a DN35CF flange with 150 mm

internal axial clearance so that it did not protrude into the chamber. The RGA was over pressure protected via a relay interlock with the BAG IPGC controller so that it was not exposed to pressures above 10^{-4} mbar. With the electronics head removed it was bakeable to 350°C.

The RGA was used in its bar mode to identify the gases in the system with partial pressures in the range 10^{-4} to 10^{-11} mbar. The 15 most dominant gases and their RGA sensitivity factors, see table 3.1, were then programmed into the RGA.

Gas	Relative molecular mass	Major peak	Relative sensitivity
Air	28	28	1.00
Argon	40	40	1.20
Carbon dioxide	44	44	1.40
Carbon monoxide	28	28	1.05
Helium	4	4	0.14
Hydrogen	2	2	0.44
Krypton	84	84	1.70
Methane	16	16	1.60
Neon	20	20	0.23
Nitrogen	28	28	1.00
Oxygen	32	32	0.86
Propene	42	41	1.00
Rotary pump oil	500	57	1.00
Turbo pump oil	71	43	1.00
Water vapour	18	18	0.90

Table 3.1 Residual gas analyser sensitivity factors.

Partial pressures of each gas were given to two decimal places and updated every 60 seconds. A typical RGA output is shown in figure 3.11. On the manufacturers recommendation the data was not used as absolute partial pressure values but as accurate values of the amount of each gas relative to nitrogen (r_i).

Print number 00001 13:36:45 14 APR 1992

MASS	17	2	18	28	40	4	32	16	44	41	43	20	4	14	57	TOTAL
RANGE	-8	-8	-7	-6	-9	-10	-7	-8	-8	-10	-10	-8	-10	-7	-10	-6
REL SENS	0.90	0.44	0.90	1.00	1.00	0.14	0.86	1.60	1.40	1.00	1.00	0.23	1.00	1.00	1.00	1.00
00:00:00	1.95	3.56	0.56	7.26	10.05	10.05	1.63	1.44	0.38	1.62	2.71	4.04	2.11	8.94	0.33	10.05
RANGE	-8	-8	-8	-6	-8	-9	-7	-8	-9	-10	-10	-8	-10	-7	-10	-5
00:01:02	2.04	3.82	6.81	8.12	3.09	1.58	1.67	1.46	3.80	1.54	2.97	4.00	2.10	8.94	0.36	1.06
00:02:06	2.03	3.77	6.74	8.11	3.07	1.53	1.69	1.46	3.82	1.43	3.07	4.01	2.34	8.93	0.30	1.06
00:03:10	2.02	3.72	6.68	8.10	3.06	1.59	1.66	1.45	3.86	1.48	3.09	3.99	2.00	8.94	0.31	1.05
00:04:13	1.99	3.67	6.63	8.08	3.05	1.60	1.68	1.45	3.80	1.42	3.22	3.96	2.09	8.90	0.16	1.05

Figure 3.11 A typical residual gas analyser output.

3.7 HIGH SPEED ROTOR

A unique adaptation to a turbomolecular pump was made in collaboration with EHVI to provide an RDG sender disc with a maximum tip speed of 246 ms^{-1} (Edwards, 1989) which is of the same order as molecular velocities (471 ms^{-1} for nitrogen at 20 $^{\circ}C$).

The blades of an EHVI EXT200 turbomolecular pump of the same type used to pump the system were removed and a 92 mm diameter flat disc, the sender, affixed to the 24 mm diameter drive shaft. This is shown in figure 3.12. Smaller discs were located lower down the shaft to provide stability. The outer casing of the turbomolecular pump was cut away to allow the sender disc to protrude 62 mm above the pump's DN100CF flange and 32 mm into the chamber. The sender disc was made of a 7075 Peruval 215 aluminium alloy and was smooth (to 0.8 μm) to ensure diffuse molecular desorption. It was bakeable at rest to 120 $^{\circ}C$ and was installed so that the top disc was perfectly horizontal.

The shaft of the rotor was surrounded by copper rods as shown in figure 3.13, and three coils were set external to the shaft and rods. A rotating magnetic field was established in each coil each with a different phase. A current was induced in the copper rods and the shaft was dragged in an anticlockwise direction by the coils.

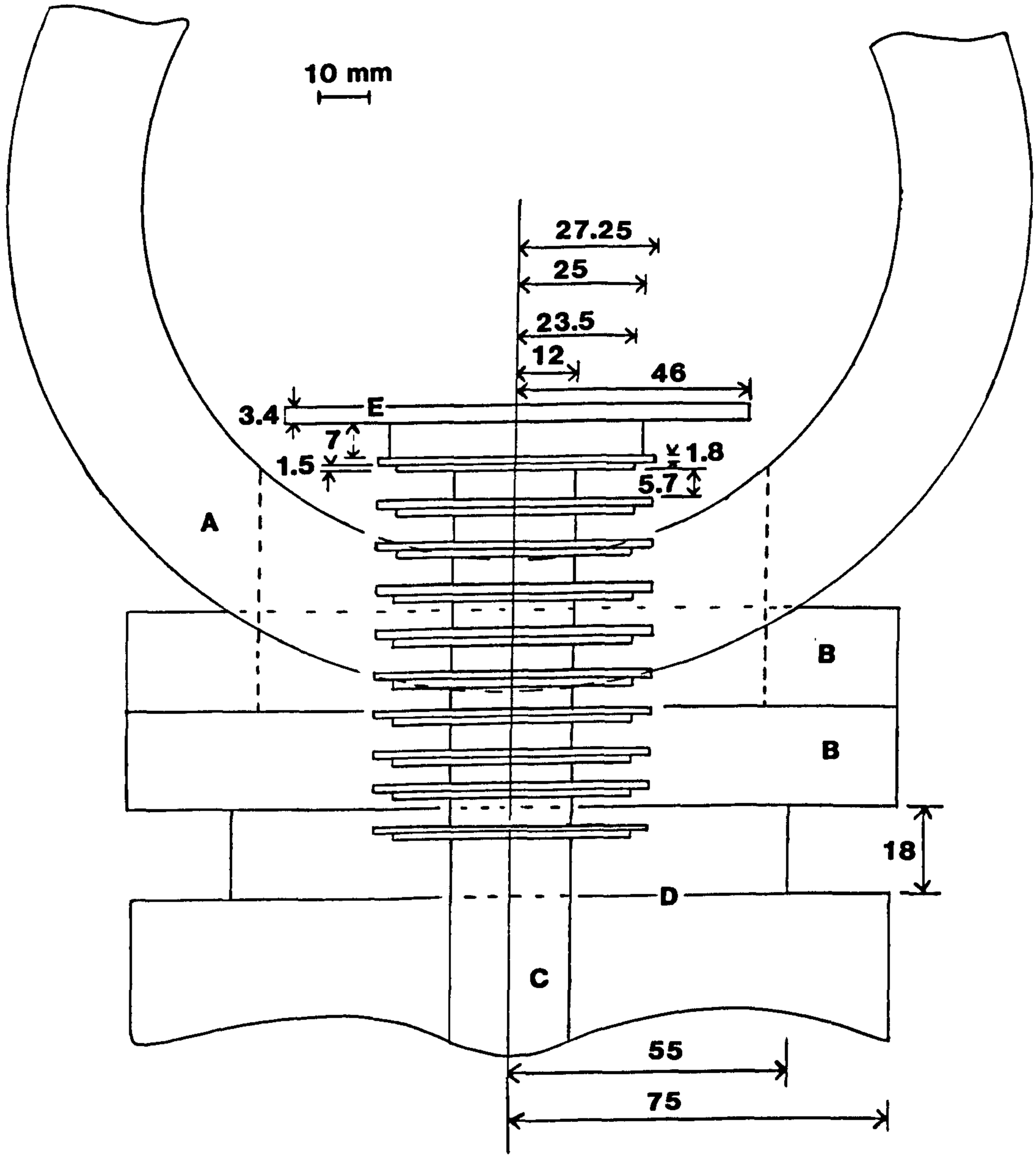

Figure 3.12 The adapted structure of the high speed rotor.
A DN150CF window; B DN100CF flange; C Rotor shaft; D Rotor body and E Sender disc: reflective tape affixed at its edge.

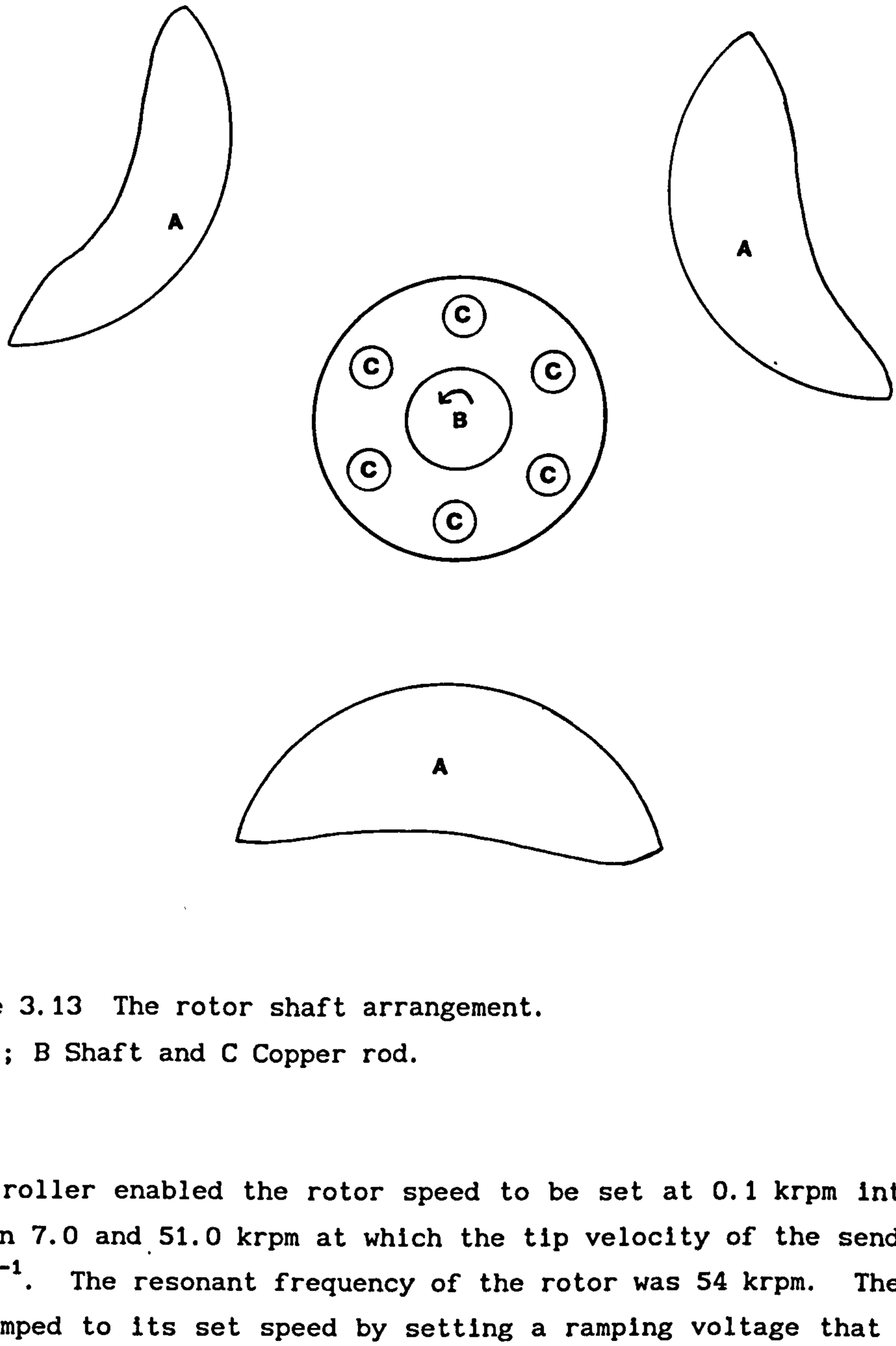

Figure 3.13 The rotor shaft arrangement.
A Coil; B Shaft and C Copper rod.

A controller enabled the rotor speed to be set at 0.1 krpm intervals between 7.0 and 51.0 krpm at which the tip velocity of the sender was 246 ms^{-1}. The resonant frequency of the rotor was 54 krpm. The rotor was ramped to its set speed by setting a ramping voltage that varied with the speed of the rotor, see table 3.2. The maximum current drawn by the rotor was 1.2 A above which the rotor could be overloaded. The rotor was only operated below 10^{-3} mbar to avoid overheating by viscous drag on the discs and shaft.

An important consideration was the 'slip' in the rotor which was the difference between the frequency of the rotor and the drive frequency of the rotating magnetic field. This effect was only seen when running the rotor at a speed of 7.5 krpm (4 V) which was actually measured as 7.1 krpm, see Chapter 6, at higher running speeds the

voltage was high enough to avoid slip.

Speed[a] / k rpm	Ramp voltage / V	Running voltage / V	Current drawn / A
7.5	7-8	4	1.1-1.2
10	8-10	6-8	1.2
15	15	15	1.0-1.1
20	20	20	0.9
25	25	25	0.9
30	30	30	0.9
35	40	40	0.9
40	45	45	0.9
45	50	50	1.0
50	50	50	0.9

Table 3.2 Voltage and current settings for different rotor speeds.
[a]All speeds had a preset ramp time of 2 minutes although the actual time to ramp varied between 1/2 and 2 minutes depending upon the speed and the 'run in' time.

Since the adapted turbomolecular pump was unbladed there was no compression ratio provided to avoid backstreaming of vapour from the Apiezon lubricating oil of its bearings. After exposure to the atmosphere the oil became saturated with water vapour. When the rotor was running the oil was heated to above 100 $^{\circ}$C and this caused a large pressure rise, typically to above 10^{-5} mbar from mainly water vapour. To overcome this problem and to reduce the base pressure of the system when the rotor was at rest the rotor had to be 'run in' and continuously water cooled at 20 lhour^{-1}. To do this the rotor was run at 50 krpm for 12 to 16 hours to accelerate the outgassing of the water vapour. This procedure also ensured that the lubricating oil was evenly spread around the bearings which gave consistency in the speed of the rotor and minimised vibrations. The 'run in' time was minimised by venting the system with nitrogen. After 'run in' and baking the base pressure was 9×10^{-8} mbar and running the rotor increased the pressure negligibly except at 50 krpm when the running pressure was 2×10^{-7} mbar.

To avoid overheating effects from currents induced when the rotor's discs cut magnetic field lines the rotor had to be positioned away from fields greater than 7 mT. The location and shield of the ion pump, the location of the SRG and the choice of non-magnetic materials for the receiver suspension and shutter mechanisms ensured that no such interference occurred. The measured field at the turbomolecular pump was 20 μT.

At high speed the shaft of the rotor bent from its vertical axis by up to 1 μm and the surface of the sender disc deviated from the horizontal plane by up to 40 μm. This caused the edge of the sender to be 0.1 mm above the horizontal but only at the highest speed (50 krpm). At the centre of the sender disc was a small indentation of 1 mm diameter. These effects are further discussed in terms of the uncertainties they introduce into the measurement of pressure with the RDG in Chapter 5.

The rotor was aligned by adjusting the supports on the chamber and its horizontal level was checked repeatedly by a spirit level.

The vibrations from the rotor were small (0.5 g at 850 Hz) and did not cause interference with the receiver's fibre suspension when the ion pump was used. When the turbomolecular pump was used there were some instances of interference between the vibrations from it and the rotor. On a few occasions a small driving force was set up at the fibre suspension which caused a problem in damping the receiver disc of the fibre suspension. The effects of vibrations on the spinning rotor gauge were discussed earlier.

The rotor controller established rotor speeds with an uncertainty of ±0.1 krpm. A commercial Radio Spares Microprocessor 622-543 infra-red tachometer (Radio Spares, 1991) was used to measure the rotor speeds to ± 1 rpm. Two 25 mm length strips of reflective tape were set symmetrically at the edge of the sender disc, see figure 3.12, and the beam of the tachometer was shone onto it and reflected back through the window, see figure 3.10. Only rotor speeds, under vacuum, up to 35 krpm could be measured in this way, see table 3.3, because the centrifugal force on the tape above this speed caused the tape to come off. For this reason the rotor could not be properly 'run in', when measuring the speeds with the tachometer. As a result the measurement

of the lowest rotor speed (7.5 krpm) by the tachometer was unreliable as discussed in Chapter 6.

Set rotor speed / krpm	Speed measured with tachometer / krpm
7.5	7.42[a] ± 0.01
10	9.975 ± 0.001
15	14.982 ± 0.001
20	20.117 ± 0.006
25	25.141[b]
30	30.04 ± 0.03
35	35.03 ± 0.05

Table 3.3 Tachometer measurements of rotor speeds.
[a]Unreliable measurement due to rotor not being run in.
[b]Single measurement.

3.8 RECEIVER SUSPENSION

The receiver suspension mechanism is shown in figures 3.1, 3.10 and 3.14. It was designed and constructed to enable ease of manipulation and to have the sensitivity to measure the molecular torque provided by the high speed sender disc in high vacuum i.e. so that deflections were of the right order in the range 10^{-5} to 10^{-7} mbar.

The smooth side of a 0.5 mm thick, 4 inch diameter, silicon (111) wafer was used as the original receiver surface (Wacker Chemical Co., 1990), see figure 3.15. It was ground down to a 92 mm diameter to match the sender disc by using a mounting jig, see figure 3.16, and weighed 8.05 g. It was flat to < 0.5 μm and scanning electron microscope (SEM) studies showed it to be smooth to better than 1 μm though with small chips at the edges due to the grinding process, see figure 3.17. Reflection high energy electron diffraction (RHEED) studies showed that the it was a highly ordered (111) surface.

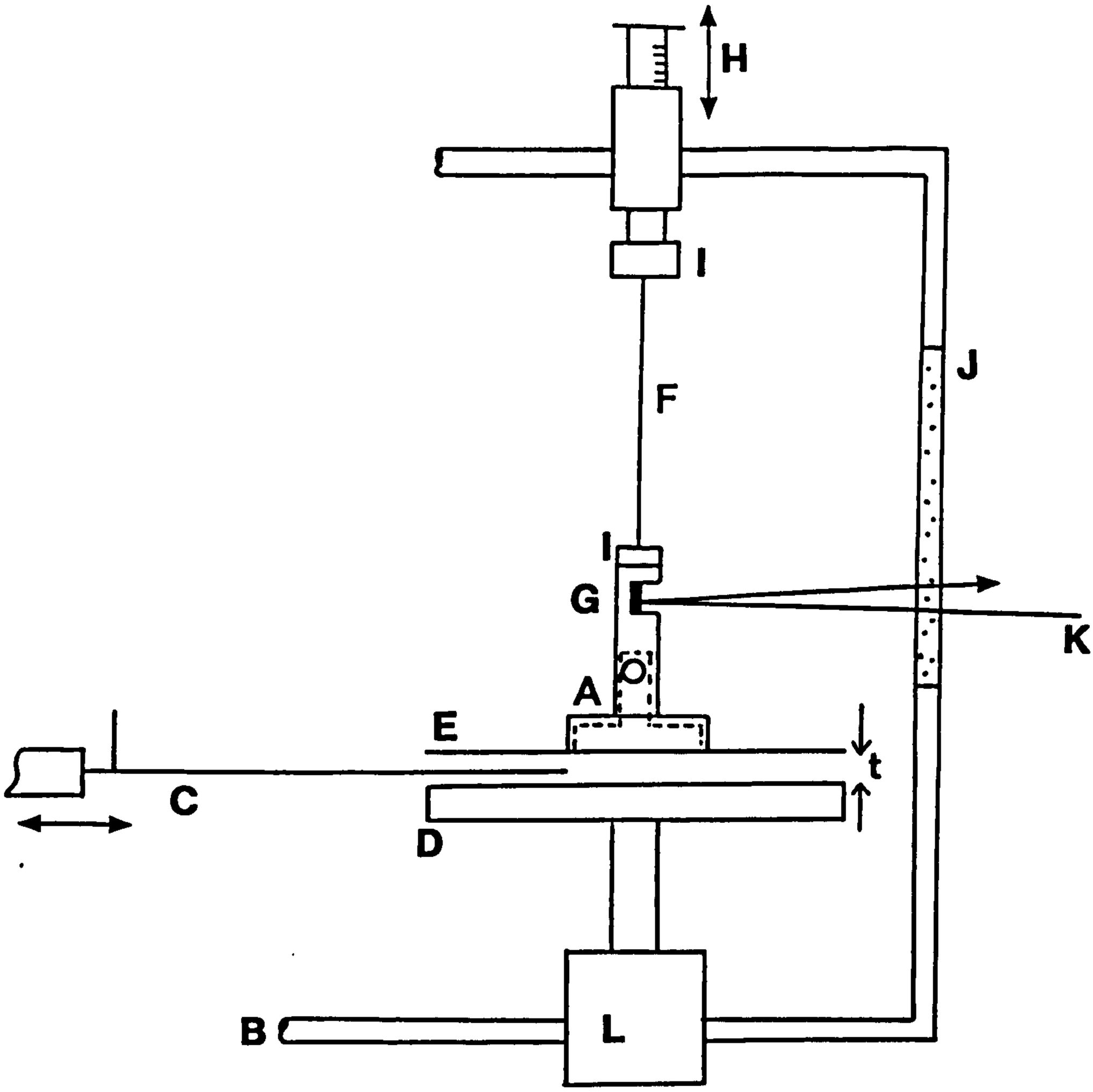

Figure 3.14 Schematic of the receiver suspension.
A Shaft; B Vacuum wall; C Shutter; D High speed sender disc; E Receiver disc; F Torsion fibre; G Mirror; H Vertical drive for receiver; I Vice; J Window; K Laser beam reflected to scale; L High speed rotor and t Disc-separation.

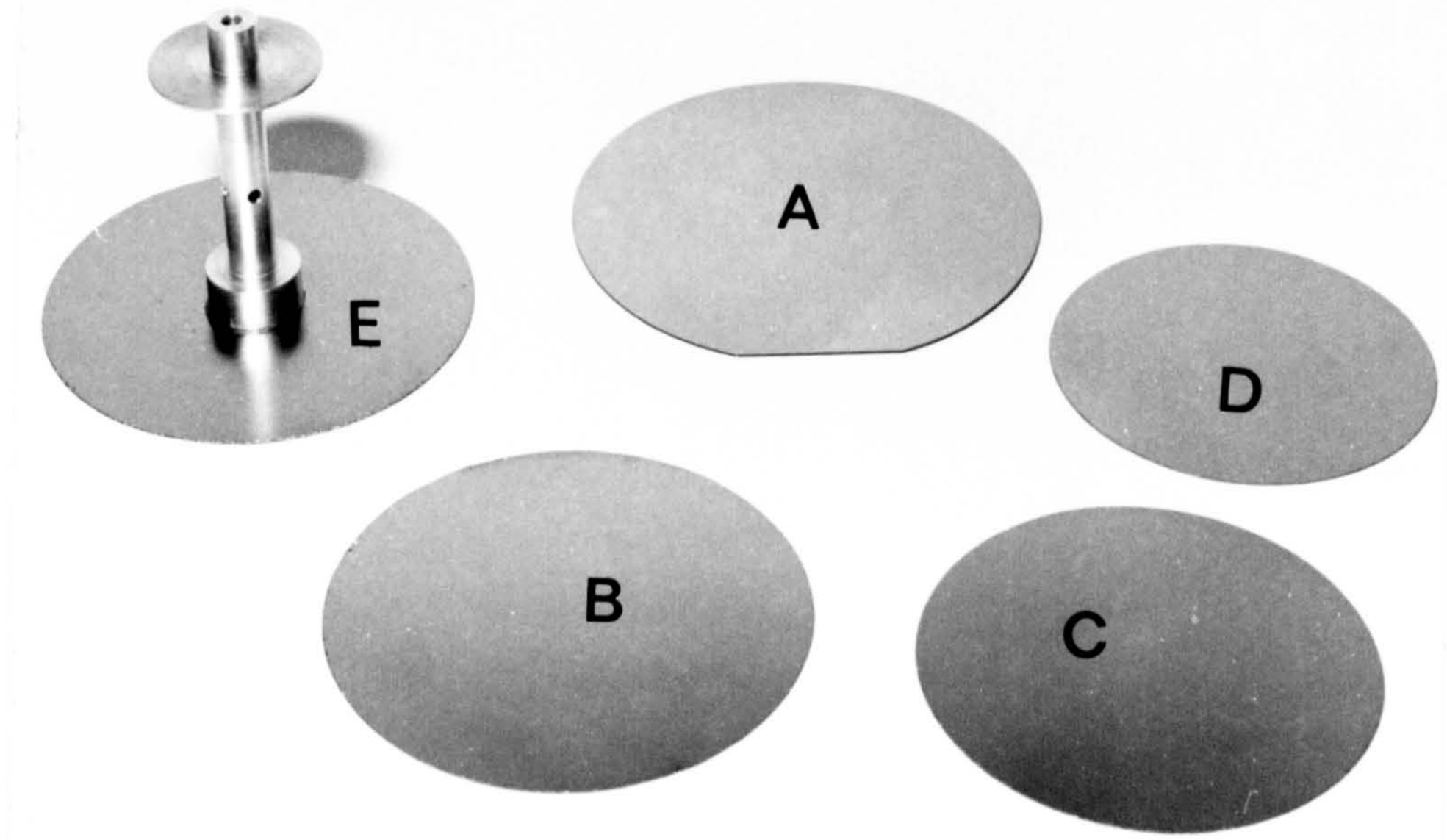

Figure 3.15 Receiver shaft and discs.
A Unground 4 inch diameter silicon wafer; B 92 mm diameter ground disc; C 84.64 mm diameter ground disc; D 78.04 mm diameter ground disc and E Receiver suspension shaft fixed to a receiver disc. N.B. all discs shown with rough side upwards.

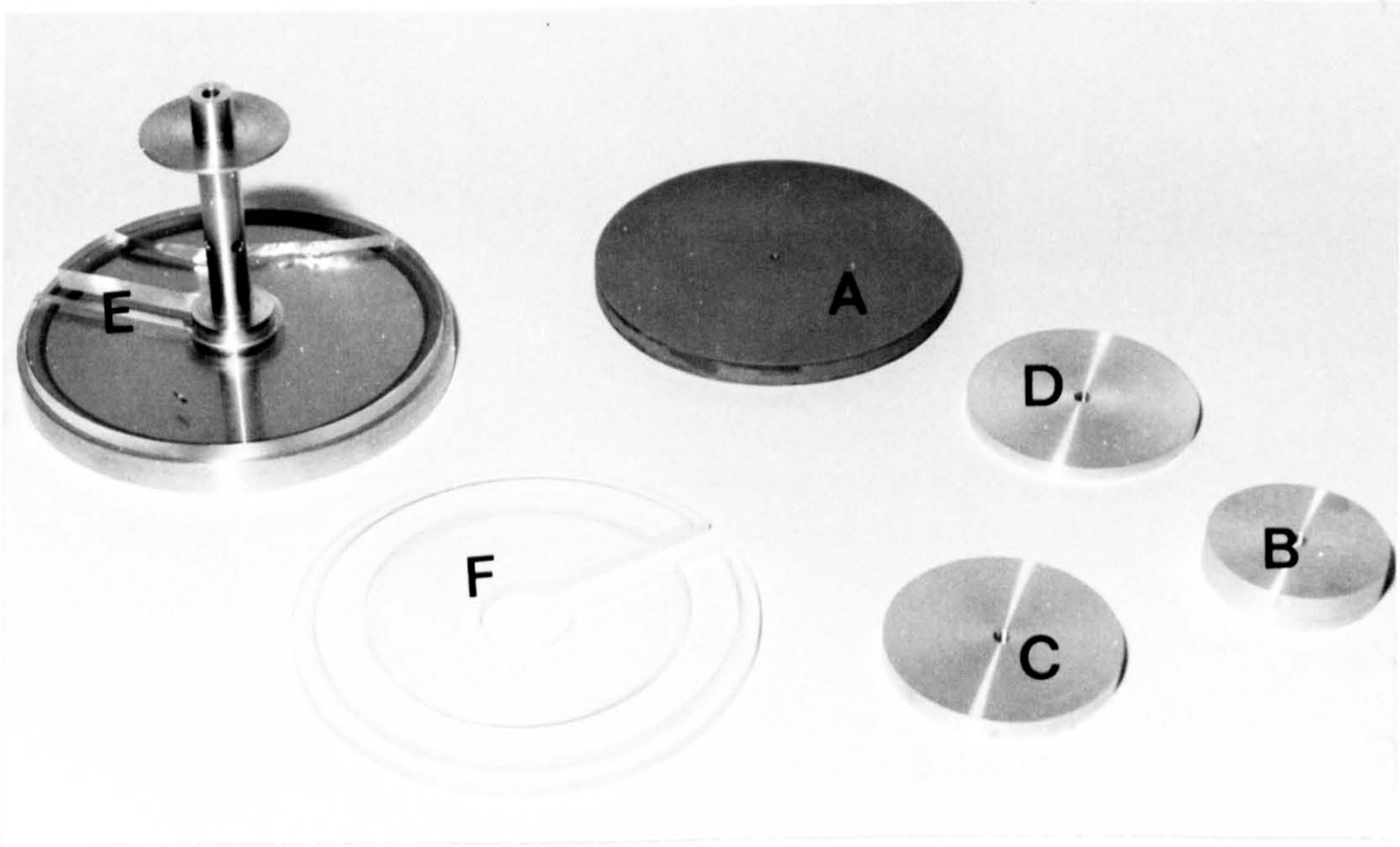

Figure 3.16 Centring jigs and standard inertia pieces.
A Mounting jig; B Inertia standard 1; C Inertia standard 2; D Inertia standard 3; E Centring jig for central location of shaft onto 92 mm diameter disc and F Centring jig for smaller discs.

Figure 3.17 SEM picture of the smooth surface of a silicon (111) wafer.

The rough side of a silicon wafer was also used as a 92 mm diameter receiver surface. SEM studies (figure 3.18) showed there to be uniform protrusions of the order of 10 μm on this surface. A 92 mm receiver surface of 500 nm of titanium grown on the smooth side of a silicon (111) wafer was also used, see Chapter 6. SEM studies (figure 3.19) showed this surface to be featureless in parts and in others to have island growths of the order of 10 μm. These islands were due to localised heating during deposition and a non uniform deposition rate.

In chapter 7 receiver discs of diameter 84.64 mm, 78.04 mm and 70.00 mm were used, see figure 3.15, weighing 6.79 g, 5.75 g and 3.32 g respectively. The 84.64 mm diameter disc was ground from a 4 inch diameter silicon (111) wafer and the smooth side used as above. The two smallest discs were ground from 3 inch diameter silicon (100) wafer with again the smooth side used.

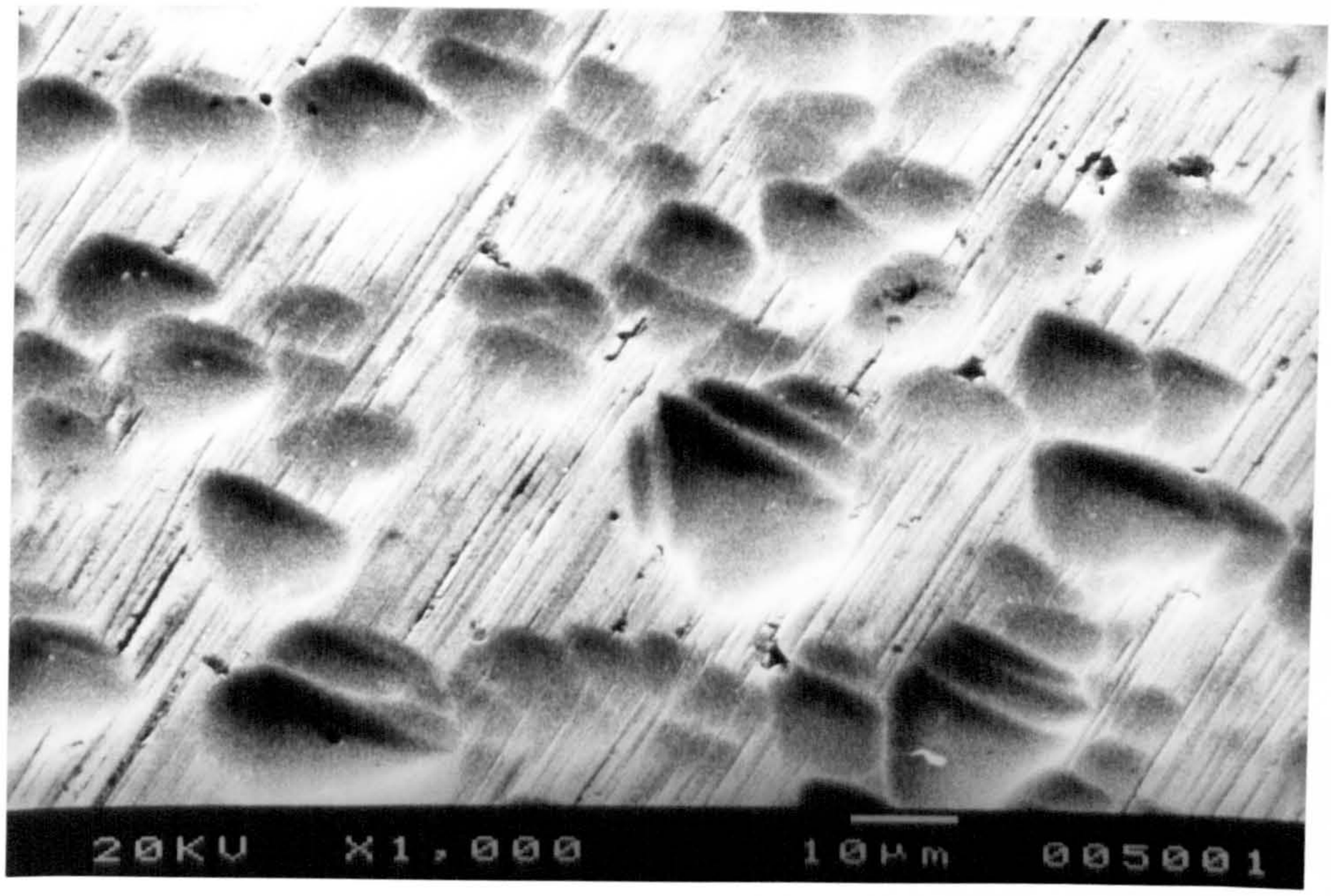

Figure 3.18 SEM picture of the rough side of a silicon (111) wafer.

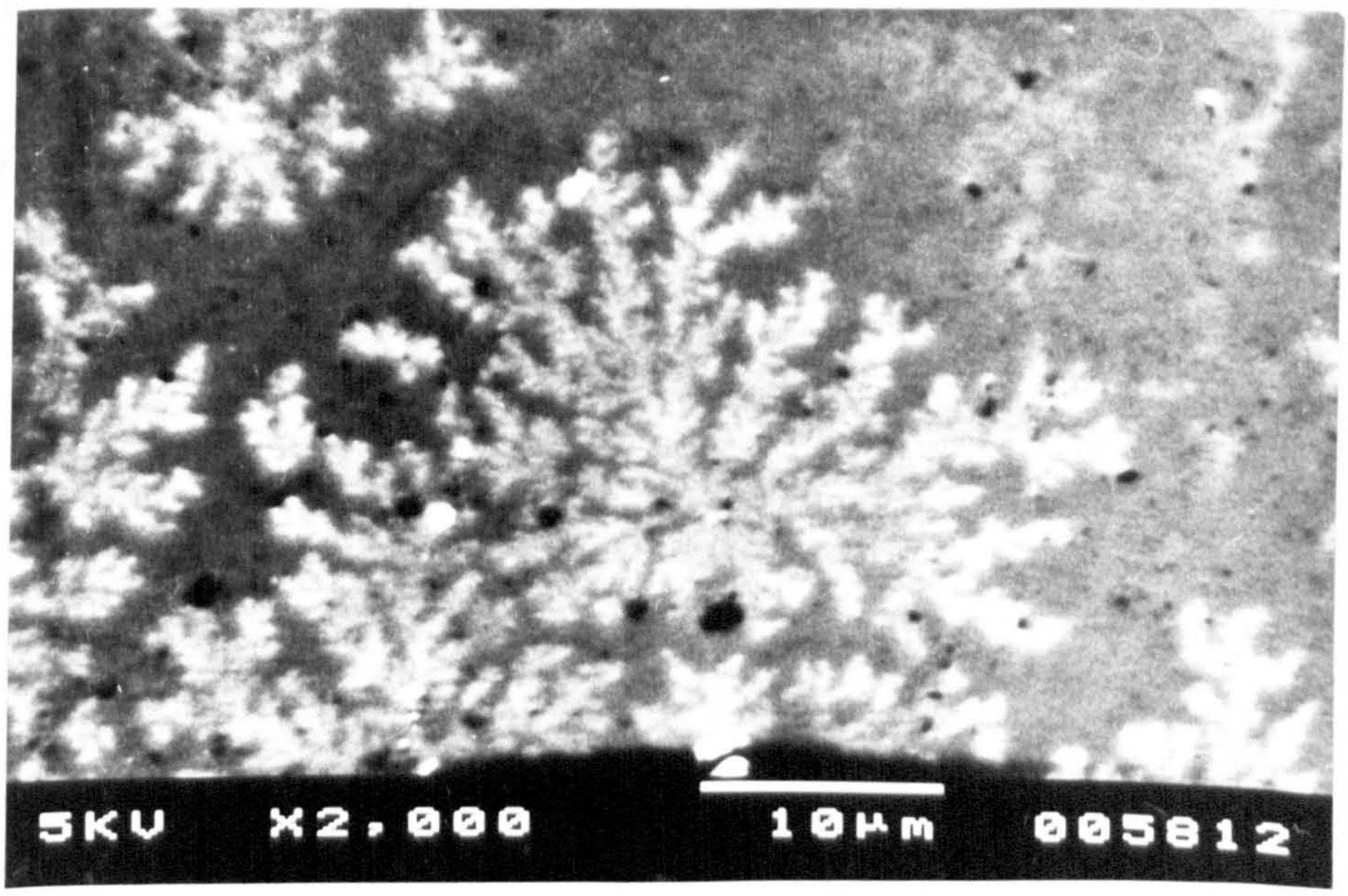

Figure 3.19 SEM picture of the surface of 500 nm of titanium grown on a silicon (111) surface.

Auger electron spectroscopy (AES) studies showed that the smooth and rough silicon surfaces were covered in an adsorbed layer of carbon and oxygen. Additionally AES studies confirmed that the surface of titanium grown on silicon was fully covered by titanium and that itself was covered by an adsorbed layer of carbon and oxygen.

Centring jigs were made, see figure 3.16, to locate the aluminium shaft centrally on the discs. The discs were fastened to the shaft by a small amount of epoxy resin (Ciba-Geigy, 1990) with a low outgassing rate.

The receiver discs were fastened to the aluminium (dural) alloy receiver shaft shown in figures 3.10 and 3.20. The shaft was hollowed out to be as light as possible (11.06 g) but large enough to manipulate easily. The ledge at the top of the shaft allowed for the possibility of eddy current damping and the lower ledge ensured a perfect fixture to the receiver disc. The shaft was M4 tapped to fasten the mirror piece shown in figures 3.21 and 3.22. The symmetrical mirror piece was made from dural and designed to locate the mirrors exactly at the centre of the suspension. The mirrors were made by depositing 10 nm of alumina on 0.22 mm thick and 10 mm diameter flat microscope cover slips. The mirror piece weighed 5.14 g and was M4 tapped to fasten it to the fibre vice described below.

For ease of attachment rectangular section torsion fibres were used. They were held at both ends in between the two half cylinders of the vices shown in figure 3.23. The smaller vice (figure 3.24) with the fibre held centrally in it was fastened to the mirror piece and held the shaft. It weighed 2.41 g. The large vice (figure 3.25) fastened the top of the fibre to the suspension's vertical motion drive. This vice was large enough to allow 6 mm variable horizontal positioning of the fibre so that the receiver disc could be aligned coaxial to better than 0.1 mm to the sender. The sharp top edges of the half cylinders of both vices were sanded down to prevent them cutting through the fibres. Great care was taken to ensure that the fibres were located centrally in the small vice and to avoid any kinks in them.

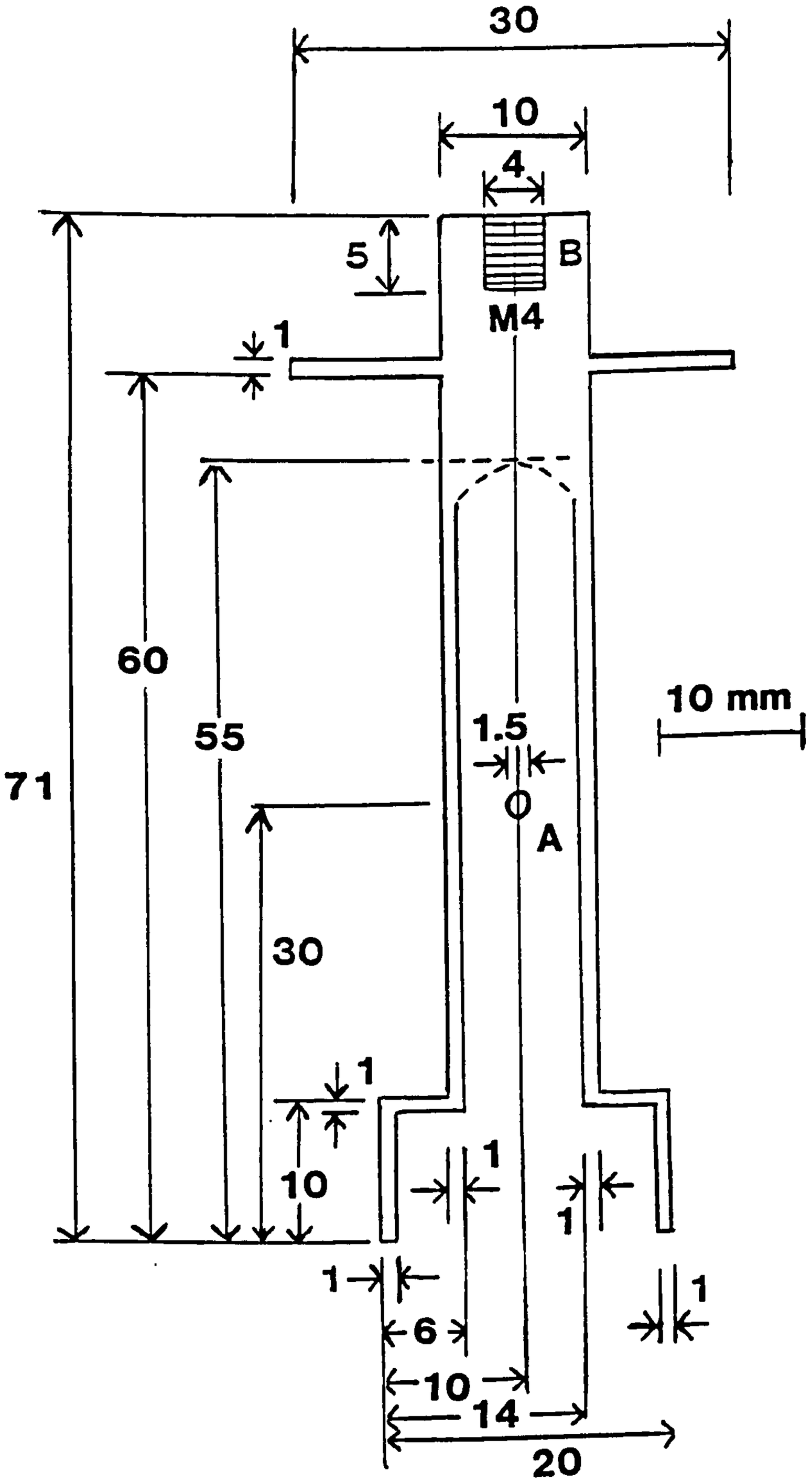

Figure 3.20 The shaft of the receiver suspension.
A Vacuum relief and B M4 tapped hole for connection to the mirror piece.

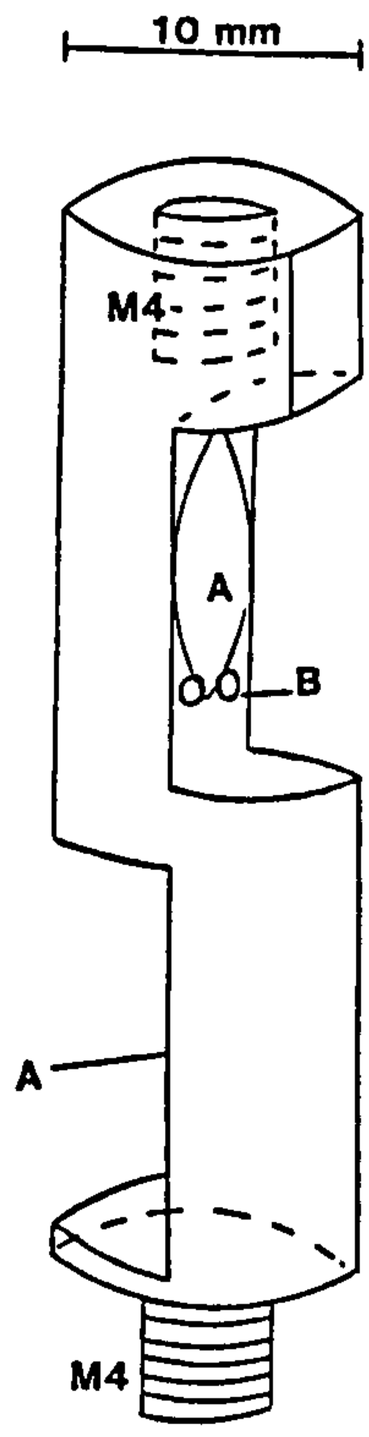

Figure 3.21 The mirror piece.
A Position of mirrors and B M1.6 washers to hold mirrors flat.

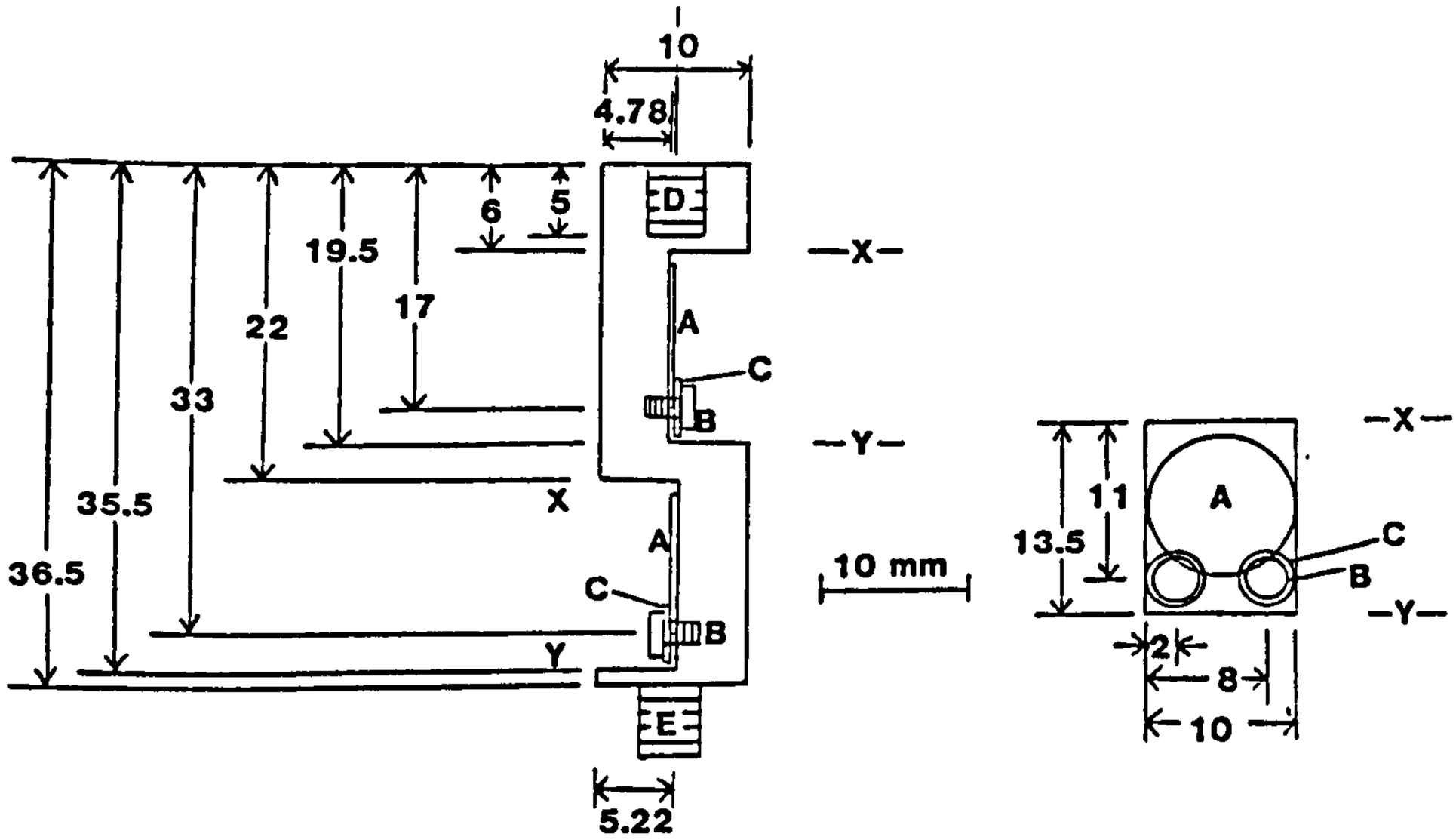

Figure 3.22 Details of the mirror piece.
A Mirror (silvered at front); B M1.6 screw; C Washer to hold mirror flat; D M4 tapped to connect to the lower vice and E M4 thread to connect to the shaft.

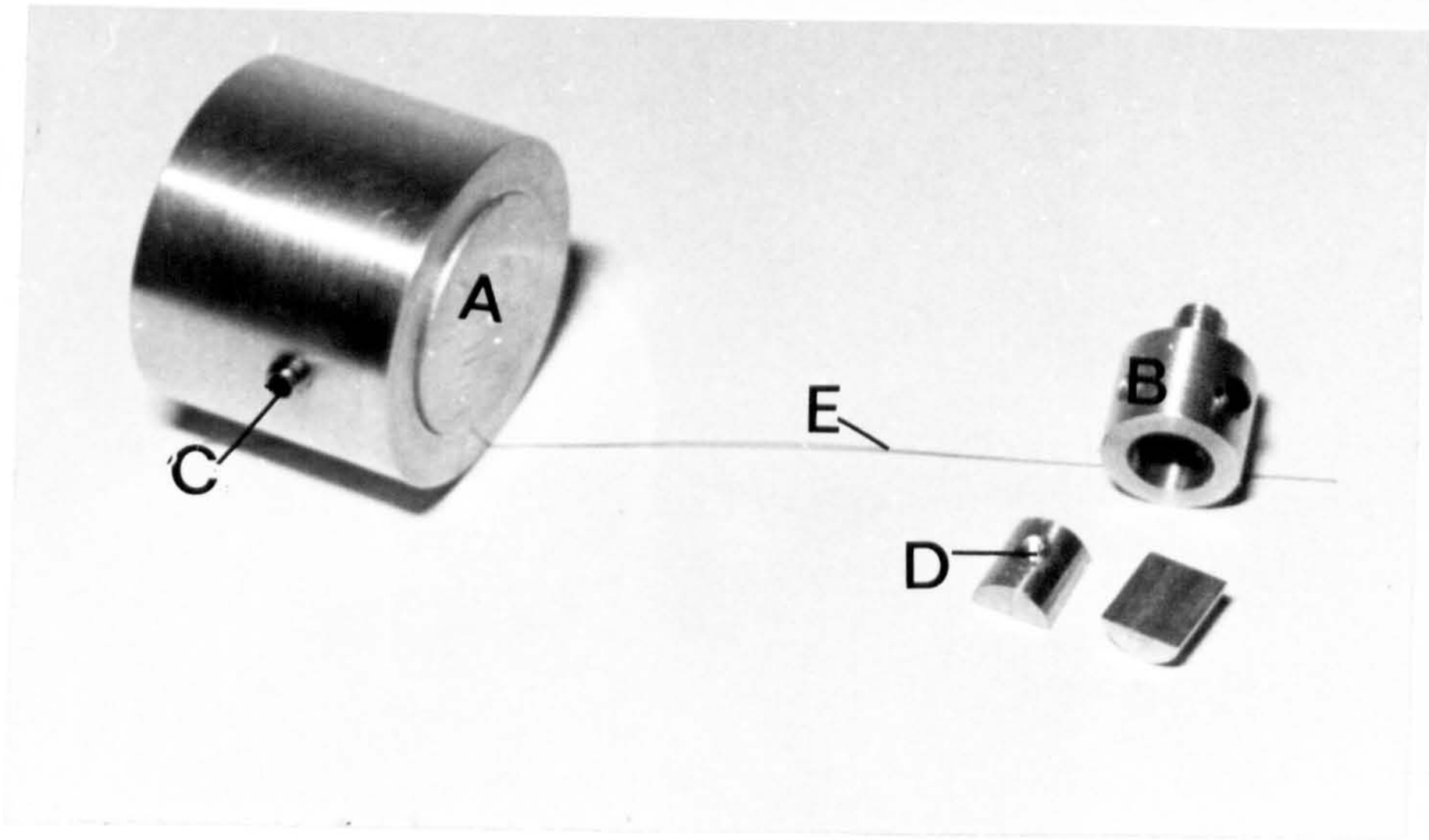

Figure 3.23 The phosphor-bronze torsion fibre and vices for its attachment.
A Upper vice; B Lower vice; C Grub screw; D Half cylinder with recess for grub screw and E Phosphor-bronze torsion fibre.

For a rectangular cross section fibre the torsional rigidity C is

$$C = \frac{1}{3} (w - 0.63\ t)\ t^3\ \mu \qquad (3.1)$$

where μ is the shear modulus, w is the fibre width and t the thickness such that $w > 5t$ (Condon and Odishaw, 1967). The torsion constant of a fibre of length l is

$$c = \frac{C}{l} \qquad (3.2)$$

such that for a torque G and an angular deflection ϕ

$$G = c\ \phi \qquad (3.3)$$

A 7% Cam Metric phosphor-bronze fibre (figure 3.23) of width 0.17 mm and thickness 0.03 mm rolled from a 0.003 inch diameter cylindrical wire was used (Cam Metric, 1990). The cross-sectional area of the fibre was 5.1×10^{-9} m^2 and the total mass of the suspension was 26.66 g. This produced a stress of 5.1×10^7 Pa to be compared with

the fibre's yield stress of 1.3×10^8 Pa (Gray, 1982). The fibre had a shear modulus of 4.4×10^{10} Pa and a Young's modulus of 12×10^{10} Pa (Anderson, 1981). The extension / unit length produced by the suspension was 0.04%.

The expected torsion constants of the fibres used of lengths 58.4 mm and 262 mm were 1×10^{-6} Nm and 2×10^{-7} Nm respectively.

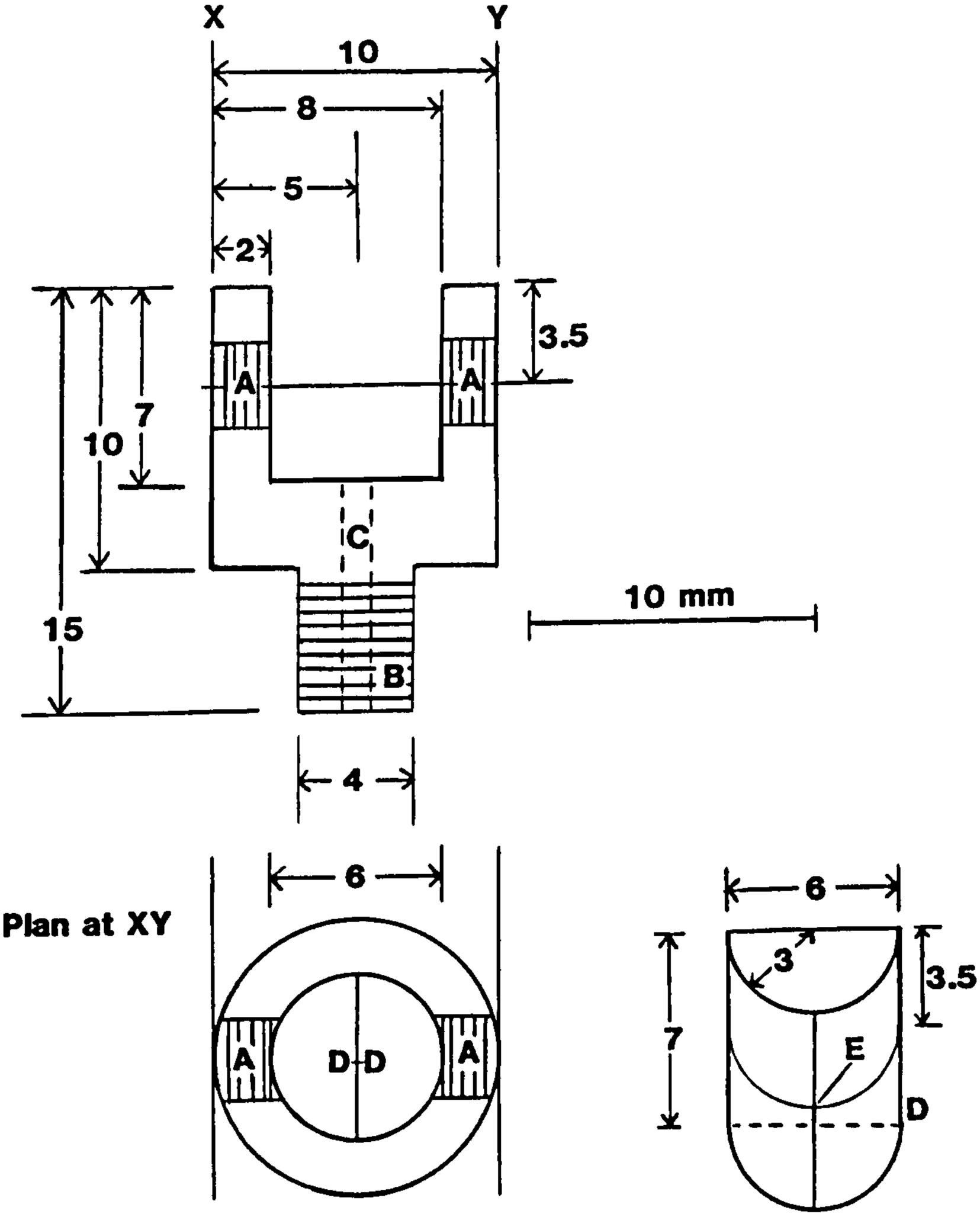

Figure 3.24 Details of the lower vice.
A M3 hexagonal grub screw; B M4; C Vacuum relief; D Half cylinders and E Location of recess for the grub screw.

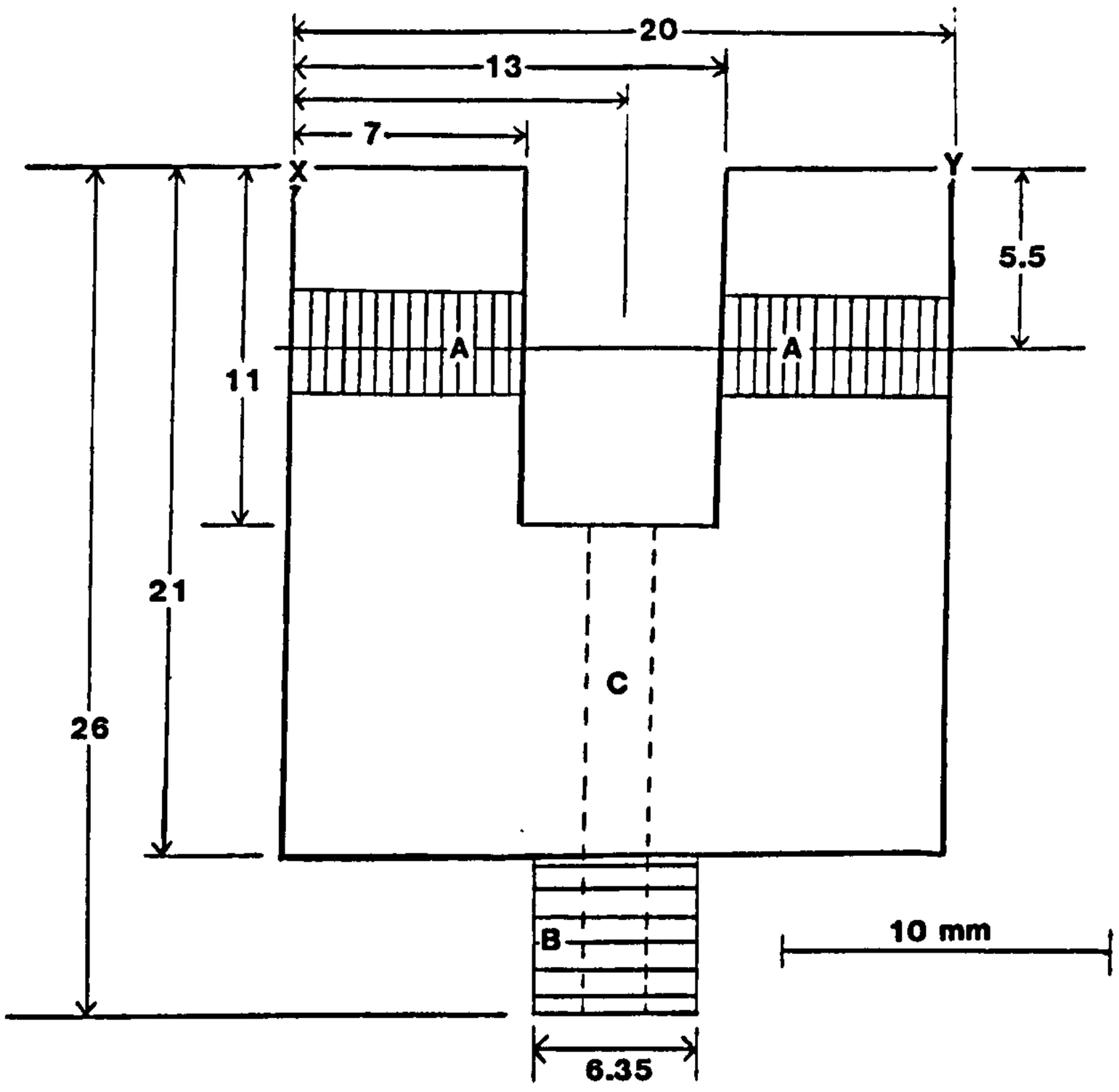

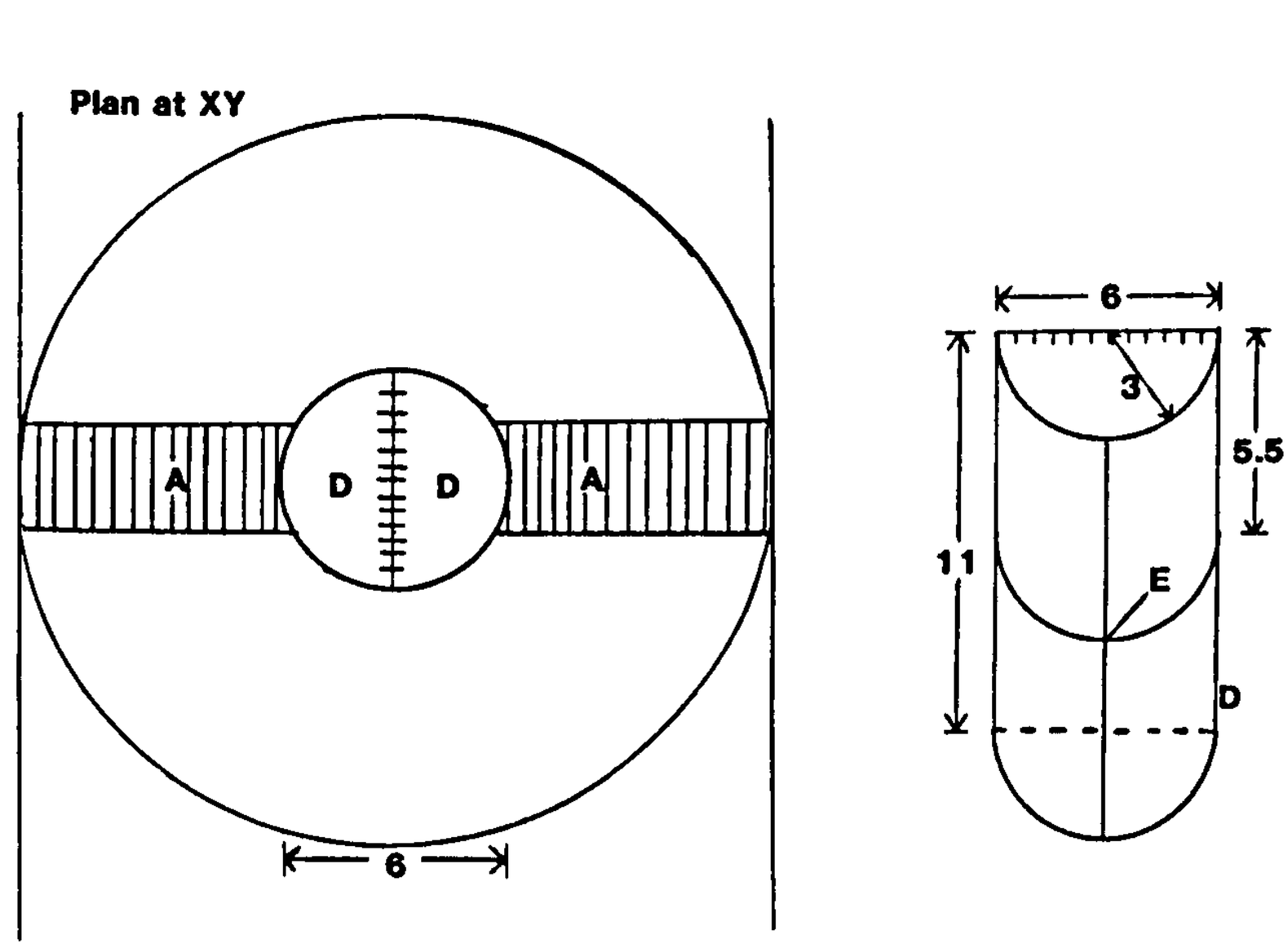

Figure 3.25 Details of the upper vice.
A M3 hexagonal grub screw; B 0.25 inch thread; C Vacuum relief; D Half cylinders with positioning marks and E Location of the recess for the grub screw.

To accurately determine the torsion constant of a fibre three standard moment of inertia pieces, shown in figure 3.16, were used. For a circular disc of mass m and radius r the moment of inertia about an axis through the centre of the disc and normal to the plane faces is

$$I = \frac{1}{2} m r^2 \qquad (3.4)$$

These discs were made to match the total mass (26.66 g) and calculated moment of inertia (9.134×10^{-6} kgm^2) of the suspension. They were M4 centrally tapped and their sharp edges were not deburred, see figure 3.26. They were fastened to the fibre's lower vice in place of the mirror piece, shaft and disc. The total moments of inertia of these discs and the vice were calculated to include the threads and the vice's grub screws. The specifications are given in table 3.4.

Inertia standard	Radius / mm ± 0.02	Mass / g ± 0.001	Mass including vice / g ± 0.001	Moment of inertia / $\times 10^{-6}$ Nm
1	19.88	31.381	33.791	6.23 ± 0.01
2	25.65	27.793	30.203	9.17 ± 0.01
3	27.45	24.423	26.833	9.23 ± 0.01

Table 3.4 Specifications of the standard moment of inertia pieces.

The uncertainty, ΔI, in I was calculated using the standard expression (Squires, 1985) below

$$\Delta I = I \left(\left(\frac{2\Delta r}{r} \right)^2 + \left(\frac{\Delta m}{m} \right)^2 \right)^{1/2} \qquad (3.5)$$

The difference between the mass of the suspensions and those of the standard inertias produced a difference in the extension of a fibre and hence changed the value of c (see equation 3.2). The magnitude of this effect though is negligible as discussed in Chapter 5.

To measure the torsion constant of the fibre the periods T for each standard inertia piece was measured and the results used to calculate

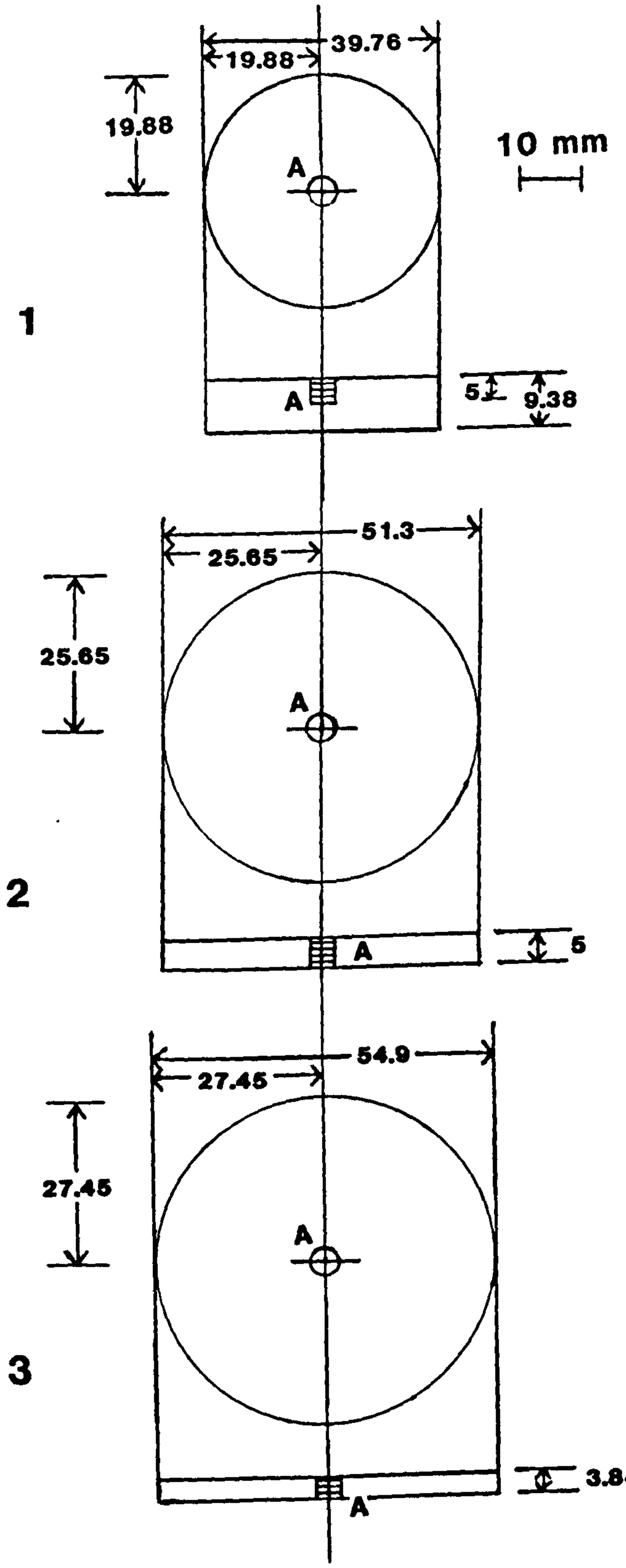

Figure 3.26 Details of the standard moment of inertia pieces.
A M4 thread.

the (mean) torsion constant as below

$$c = 4\pi^2 \frac{I}{T^2} \tag{3.6}$$

The results of the calibrations are shown in table 3.5

Fibre length / mm	Torsion constant / $\times 10^{-7}$ Nm
58.44	6.614 ± 0.015
262.25	1.465 ± 0.003
262.25[a]	1.470 ± 0.001

Table 3.5 The torsion constants of the calibrated fibres.
[a]Fibre adjusted slightly and recalibrated.

The uncertainty Δc of the calibration was calculated from

$$\Delta c = c \left[\left(\frac{2\Delta T}{T} \right)^2 + \left(\frac{\Delta I}{I} \right)^2 \right]^{1/2} \tag{3.7}$$

By timing the period of the receiver suspension T_{sus} when it was held by the calibrated fibres the moment of inertia of the suspension I_{sus} was measured from

$$I_{sus} = \frac{c}{4\pi^2} T_{sus}^2 \tag{3.8}$$

and the uncertainty from

$$\Delta I_{sus} = I_{sus} \left[\left(\frac{2\Delta T_{sus}}{T_{sus}} \right)^2 + \left(\frac{\Delta c}{c} \right)^2 \right]^{1/2} \tag{3.9}$$

such that $I_{sus} = 9.15 \pm 0.02 \times 10^{-6}$ kgm^2. The periods of the various

suspensions used are shown in table 3.6. They were checked regularly to ensure that the fibres' constant had not changed.

Fibre length / mm	Radius of disc used on suspension / mm	Suspension period / secs
58.44	92	23.38
262.25	92	49.62
262.25[a]	92	49.54
262.25	84.64	42.38
262.25	78.04	36.57
262.25	70	26.70

Table 3.6 Periods of the suspensions used.
[a]Fibre adjusted slightly.

The fibre was fastened via the upper vice to a VG linear motion drive (Vacuum Generators, 1989). The drive was mounted centrally in DN35CF tubulation on the top receiver flange, see figures 3.1 and 3.2. The tubulation had a rotatable flange for alignment so that the lower mirror could be positioned parallel to the window. A 199 mm extra length tube was installed to accommodate the longer fibre.

The drive provided 26.2 mm of travel in 26 turns of 50 graduations. It was calibrated in terms of extension from its fully compressed state at each full turn. With the suspension attached and the drive fully compressed, the separation of the sender and receiver discs was measured with vernier callipers. This enabled an accurate (± 0.4 mm) determination of the variable disc-separation (t) at each calibrated position of the drive. The sender and receiver discs were measured by vernier callipers to be parallel to better than 0.1 mm at a separation of 24 mm.

The full extension of the drive was not used since the lengths of the fibres were chosen to ensure that the suspension could rest on the shutter (see below) with the fibre slack and also to allow the discs to theoretically touch.

3.9 SHUTTER MECHANISM

A shutter mechanism was constructed to shield the receiver disc from the sender disc, to damp the motion of the receiver suspension and to 'park' the suspension during non-operation.

The shutter was constructed so that it could be rapidly withdrawn so as to create a step function of molecular torque from the sender disc for the receiver to sense. A square U-shaped 'trolley' shutter made from non-magnetic stainless steel 110 mm wide and 108 mm long was used, see figures 3.1, 3.10 and 3.27. It ran on aluminium wheels inside aluminium rails of length 330 mm, see figure 3.28. The rails were supported on M6 posts onto the secure fixtures welded inside the chamber, see figures 3.27 and 3.4.

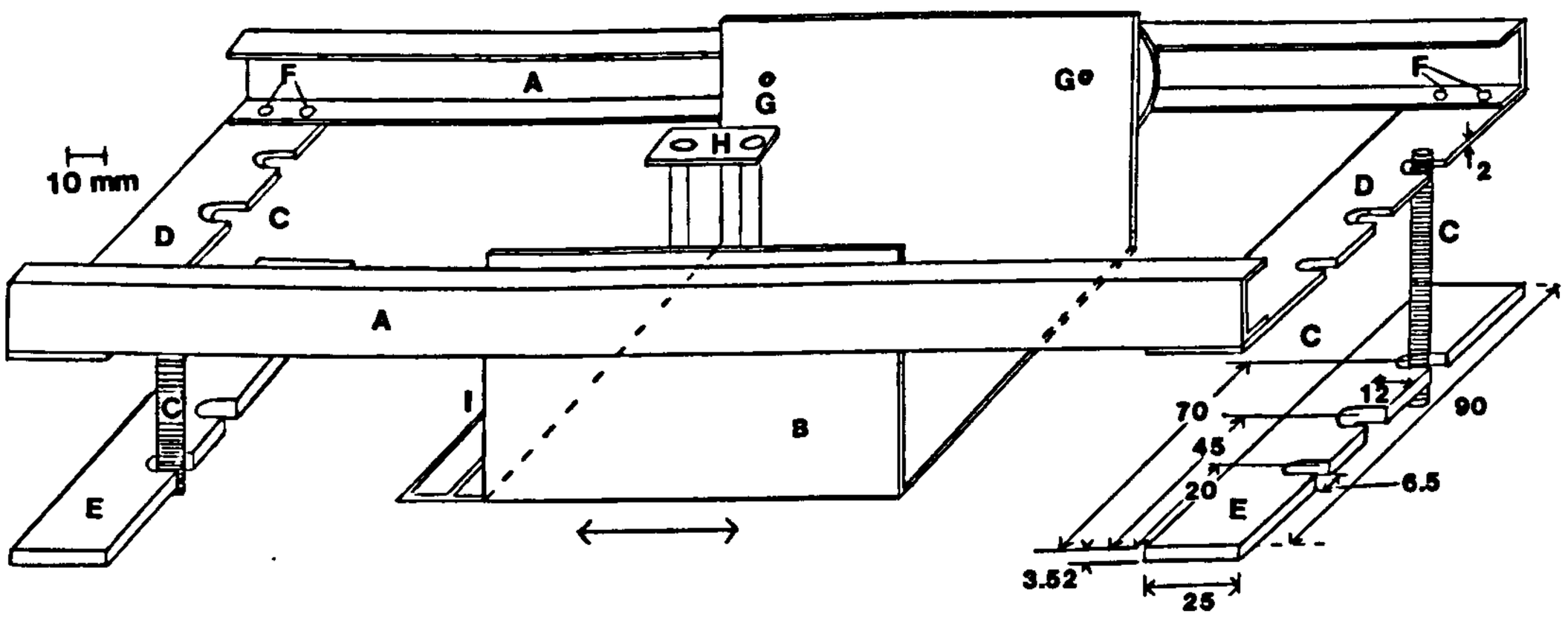

Figure 3.27 The shutter mechanism and internal supports.
A Rails; B Shutter; C M6 posts; D Support for attachment to chamber; E Internal chamber support; F M3 screws; G M3 screws for attachment of wheels to shutter (15 mm from end of shutter); H Damping post and I Bars for siting of hook of linear transporter.

The shutter was withdrawn and inserted by a Caburn-MDC MT-12 magnetically coupled linear transporter (Caburn-MDC, 1990) providing 350 mm of travel and bakeable to 200°C. It was held on a DN35CF flange fitting to the DN150CF front end flange, see figure 3.1. A view port above the drive enabled the operator to observe the suspension and shutter mechanism, see figure 3.3. An M6 aluminium rod

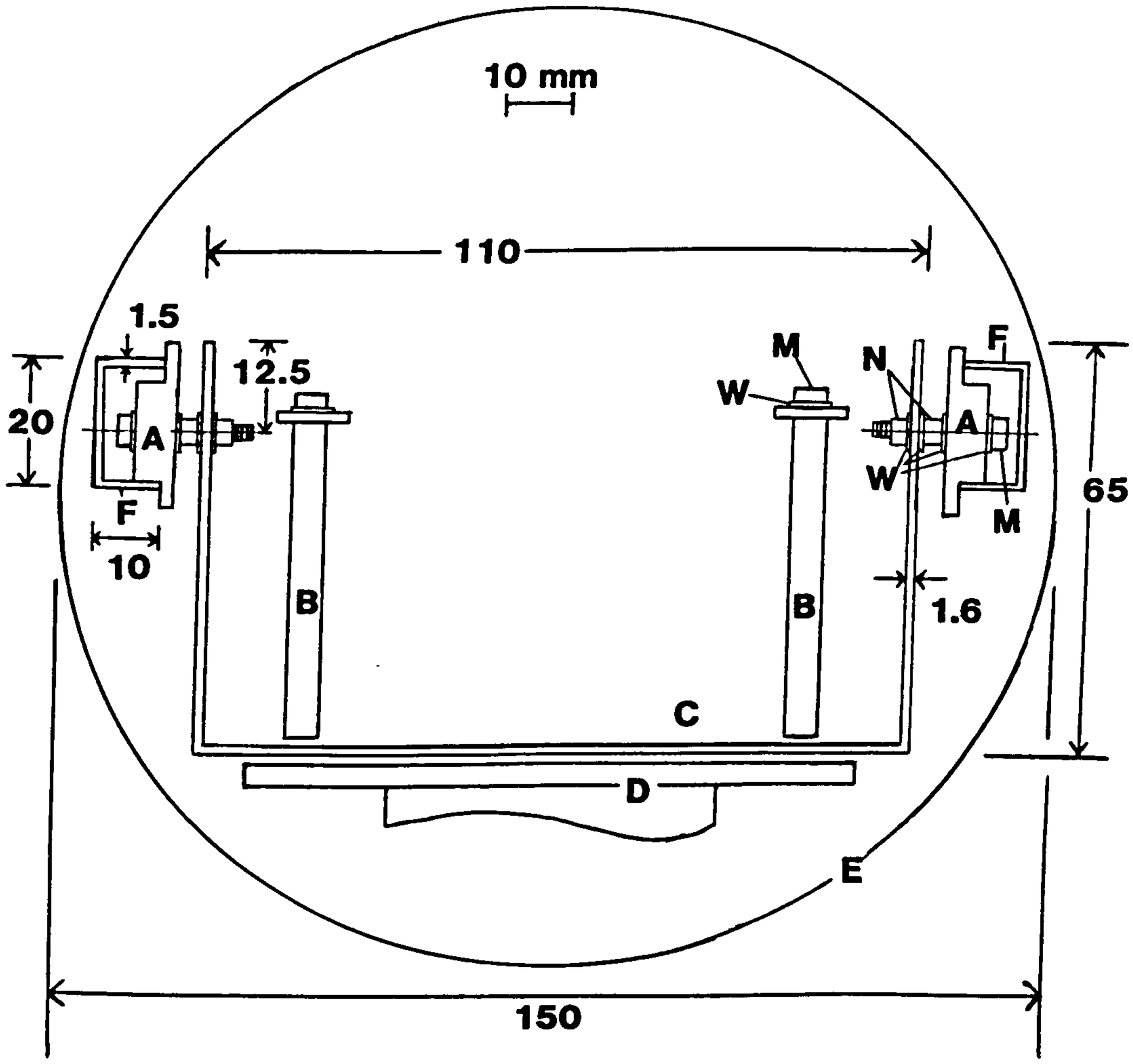

Figure 3.28 Front view and details of the shutter mechanism.
A Wheel; B Damping post; C Shutter; D High speed sender; E Chamber wall; F Rail; M M3 screw; N Nut and W Washer

mechanism (figure 3.29) was attached to the linear transporter and had an M3 hook which was manipulated to fit between the bars on the shutter hence providing contact for withdrawal and reinsertion of the shutter. Trapped volumes were avoided by filing threads and providing vacuum relief where necessary. The hook mechanism gave approximately 1/2 of the maximum (0.96 Nm) torque allowed on the transporter.

The shutter was withdrawn from a position fully covering the discs to one completely clear of them in ≤ 0.5 secs. A comparison of this withdrawal time with the smallest period of all the suspensions, 23.4 secs (table 3.6), indicates that to an excellent approximation the shutter mechanism could be withdrawn to create a step function of torque from the sender. The configuration of the shutter mechanism in relation to the suspension and high speed rotor is shown in figure 3.30.

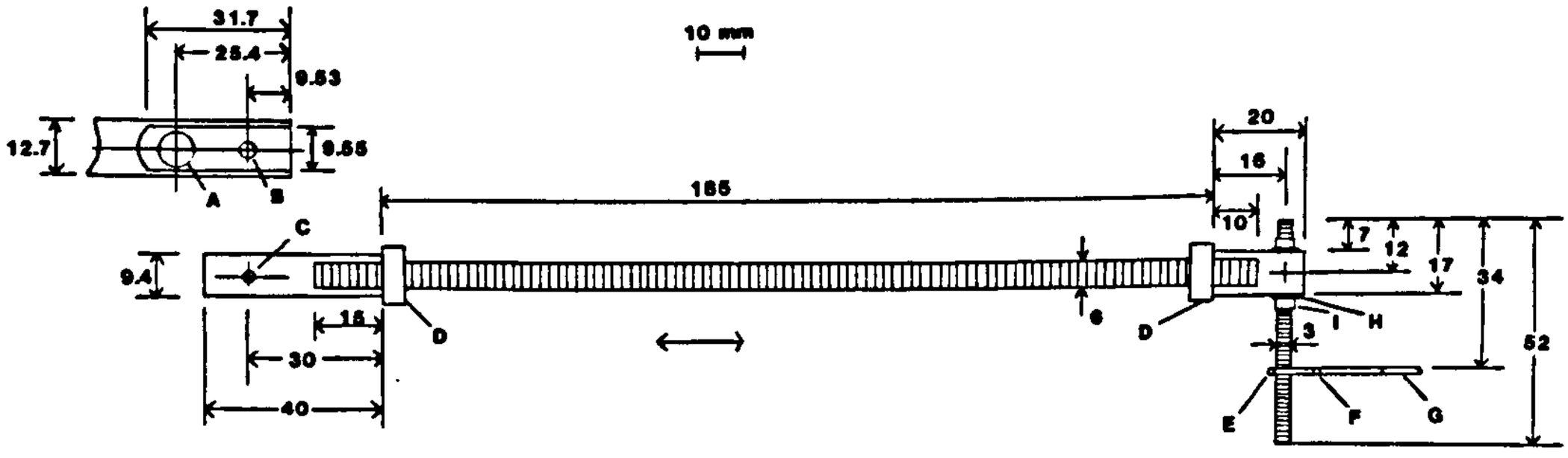

Figure 3.29 Details of the hook mechanism.
A 7.94 mm hole; B 3.57 mm hole (A and B on end of transporter); C M3 tapped; D M6 nut; E Bar for shutter withdrawal; F Bar for shutter insertion; G Shutter; H M3 washer and nut and I Hook.

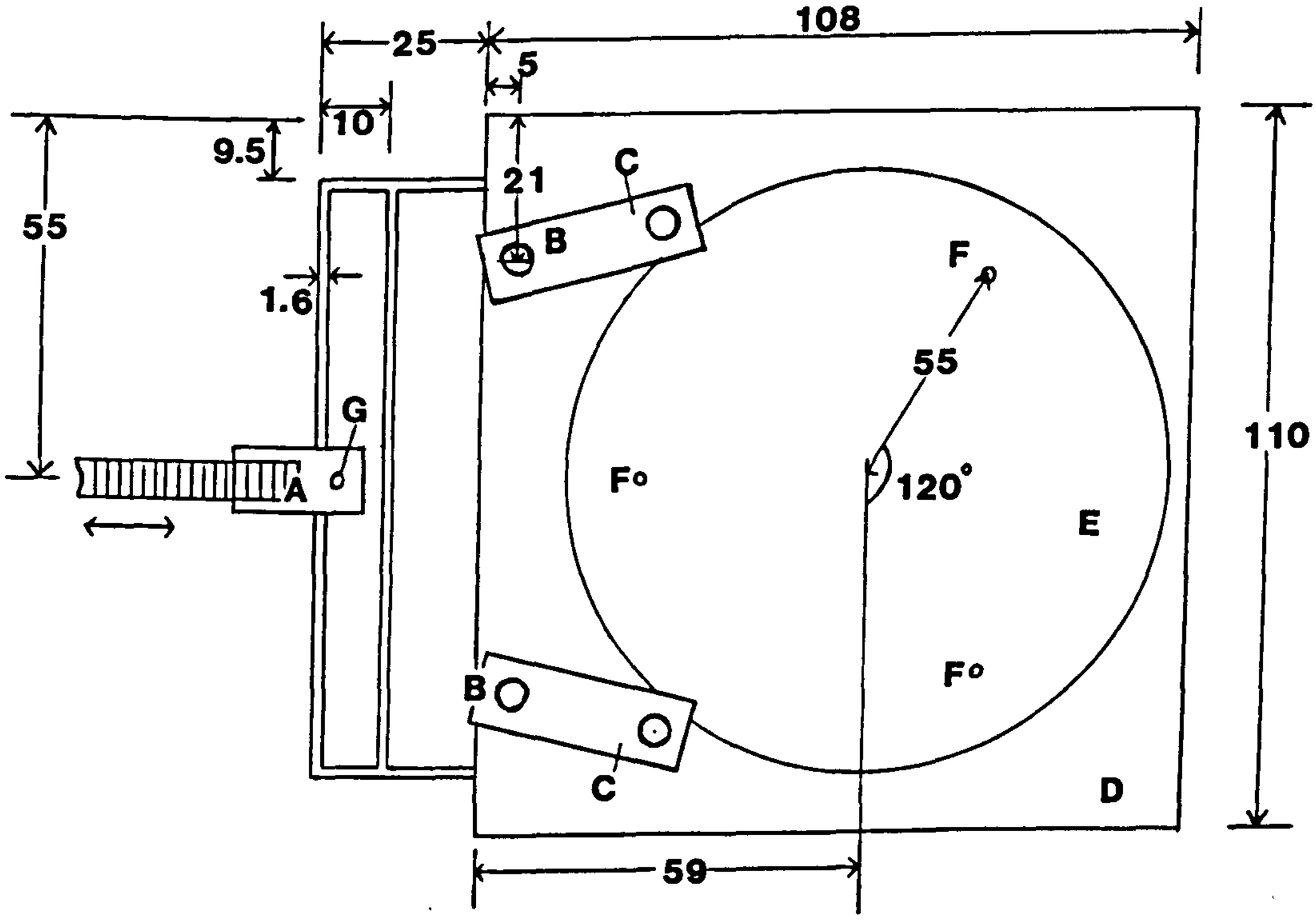

Figure 3.30 View looking down on the shutter,
A Hook mechanism manipulated by the transporter; B Rod fixing the damping post mechanism to the shutter; C Aluminium piece holding damping post; D Shutter; E Position of sender and receiver discs; F Supports and G M3 hook.

Posts were fixed to the shutter to allow damping of the receiver disc at all sender-receiver separations, see figures 3.10, 3.28 and 3.31. Great care was taken to ensure that the posts were vertical and that they touched the receiver disc simultaneously.

From a position where the posts were just short of the receiver disc the shutter and posts were moved forward to touch it and stop its motion. The posts were then slowly withdrawn to leave the receiver disc quiescent with the shutter still covering the discs, ready to be withdrawn.

After this procedure the receiver would sometimes still have a small horizontal oscillation. This was measured by the reflected light spot on the external scale which was 1088 mm from the mirror. A typical horizontal oscillation had an amplitude of 4 mm. The measured deflection y_o was then determined by the change in the centre of the initial and induced oscillations, see figure 3.34.

There was sometimes a residual swinging motion which had a typical vertical amplitude of 0.5 mm on the external scale. This meant that the edge of the receiver disc was displaced by 0.02 mm from the horizontal. This effect is further discussed in terms of the uncertainty it introduces into the measurement of pressure with the RDG in Chapter 5.

At rest the suspension was lowered onto the shutter so that the fibre was slack. This prevented any accidental damage to the fibre and suspension especially during work on the chamber when vibrations would have caused the suspension to swing violently.

The adhesion between the disc and the shutter was great enough to break the fibre if the suspension was raised with the receiver disc in contact with the shutter. To avoid this three M2 steel bearing supports were secured to the shutter, see figures 3.30 and 3.31, in positions to allow the receiver to rest upon all of them. The suspension could then be raised from its resting position without affecting the fibre.

For experiments when the chamber was turbomolecular pumped the vibrations were such that the suspension could not always be damped by

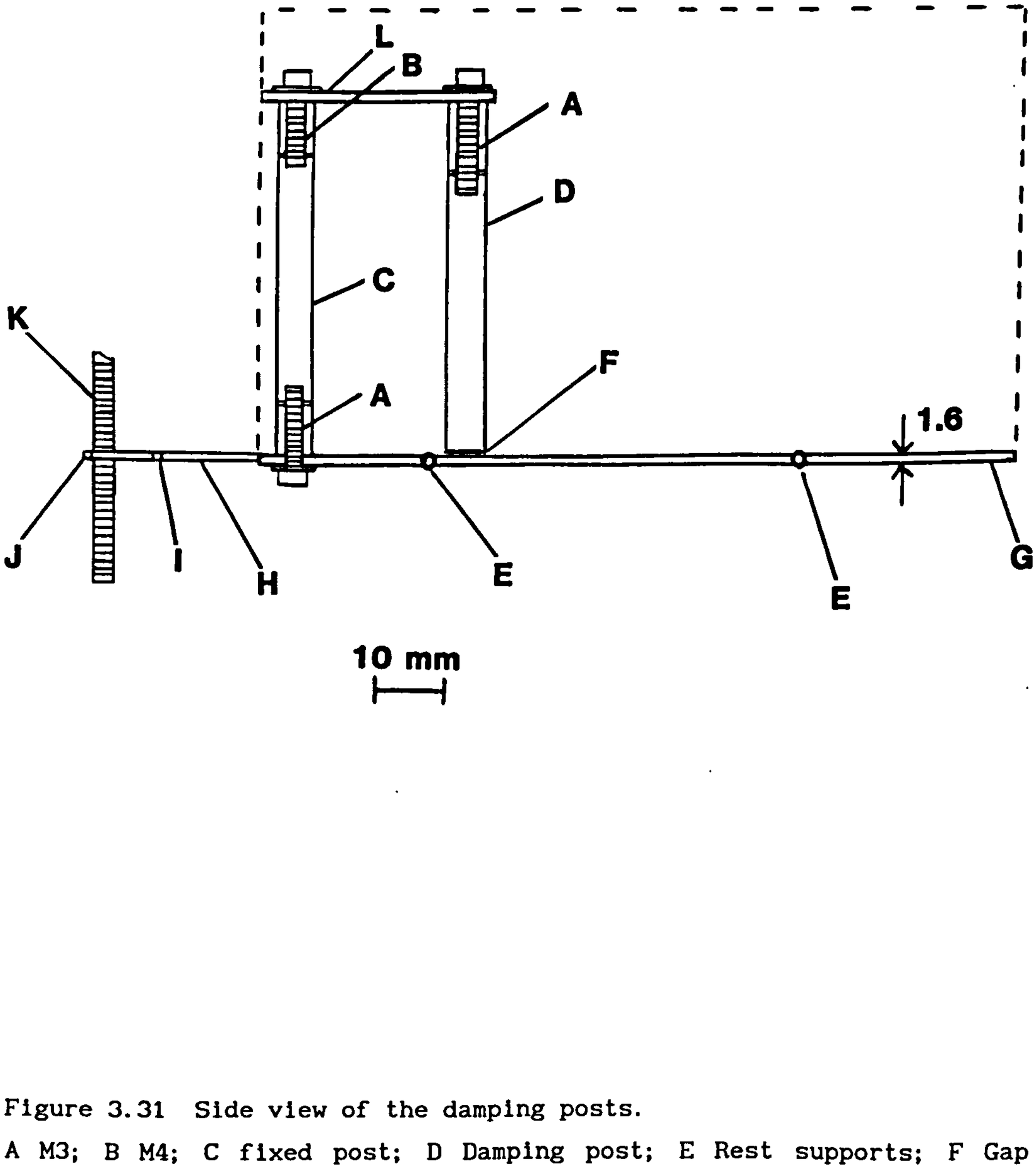

Figure 3.31 Side view of the damping posts.
A M3; B M4; C fixed post; D Damping post; E Rest supports; F Gap between post and shutter allowing variable positioning; G Shutter; H Bar structure; I Bar to insert shutter; J Bar to withdraw shutter and K Hook.

the damping posts. In these cases the suspension was damped by slowly raising the receiver disc from the bearings. This method was not as effective for the largest sender-receiver separations.

The positioning of the shutter meant that there was a minimum disc-separation at which the receiver was clear of the shutter. The minimum value at which the shutter could be safely removed without touching the receiver was 3 mm.

The effect of vibrations introduced by withdrawing the shutter was measured by observing the vertical and horizontal movements of the suspension. This was done by monitoring the reflected light spot from the suspension onto the external scale, see below. Many tests of withdrawal and insertion of the shutter were performed without vibrations affecting the suspension in any way.

3.10 MEASUREMENT OF DEFLECTIONS

A simple laser and scale mechanism was used to enable the deflection of the receiver disc to be measured, see figures 3.32 and 3.33. A Model 155 Class 2 laser (Spectra-Physics, 1978) was used as a monochromatic light source and was focused through the end DN150CF view port onto the lower mirror of the suspension. The light was reflected to produce a 1 mm diameter spot on a 1 mm graduated scale. The radius of curvature of the scale was 1088 mm and it was positioned 1088 mm from the mirror. The laser could be moved vertically and horizontally to enable the light to strike the mirror at all disc-separations. The scale was moved vertically to ensure correct alignment.

The position of the mirror inside the chamber meant that as the disc-separation was increased, and thus the mirror raised, the visibility was reduced, see figure 3.10. For the lowest separations the maximum measurable deflection was 250 mm, corresponding to a swing of 500 mm on the scale. Deflections greater than this caused the spot to be thrown beyond the window and lost.

The suspension used enabled disc-separations up to 30 mm to be viewed, for greater separations the mirror would have had to be lowered on an adapted shaft.

For remote viewing an MLV 81 Video Camera (Radio Spares, 1991) was positioned to view the discs. The picture was shown on a monitor so that the operator could view the shutter whilst it was being manipulated, see figures 3.9 and 3.32. The monitor also provided remote viewing of the RGA output.

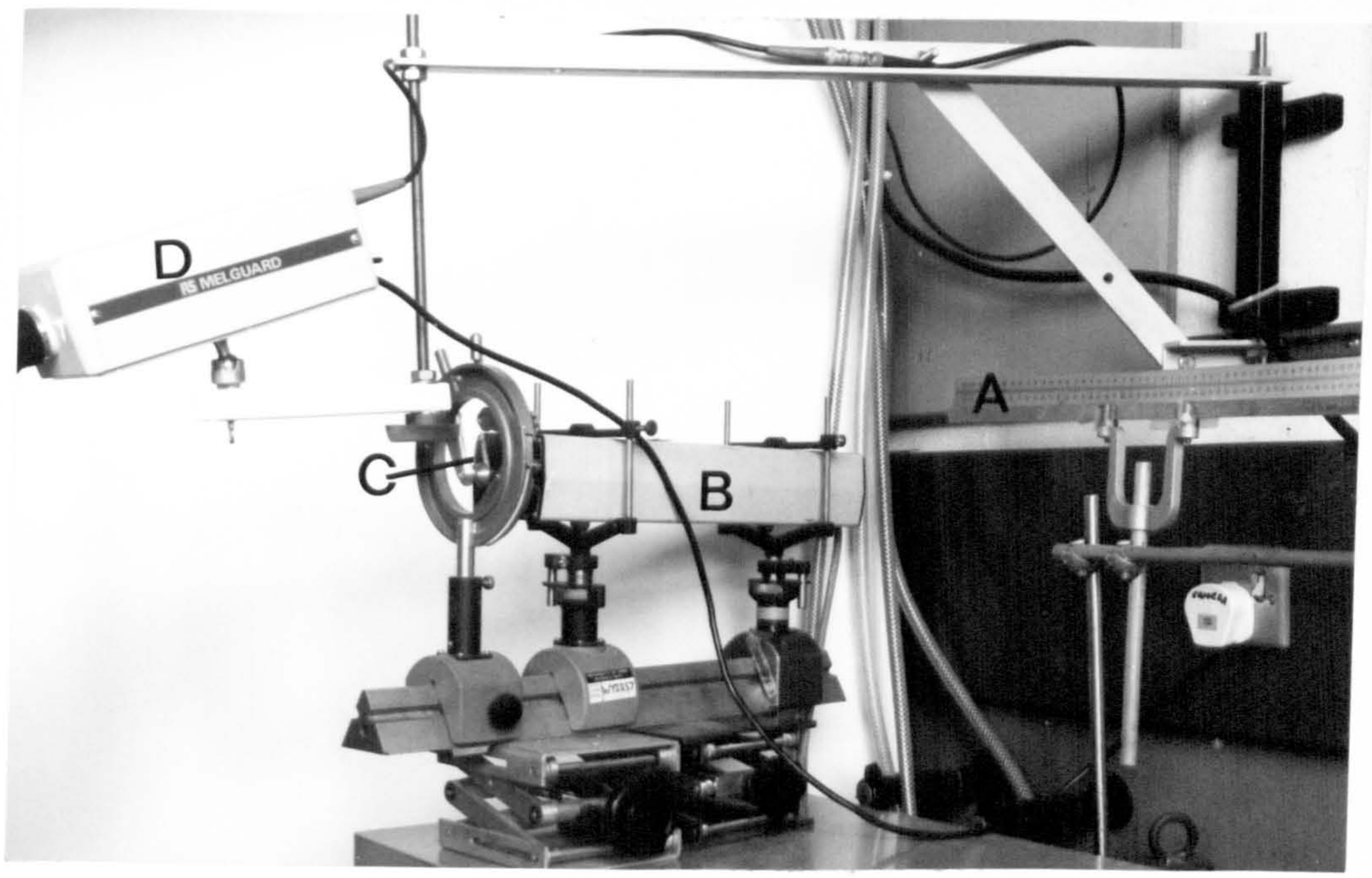

Figure 3.32 The laser and scale arrangement.
A Scale; B Laser (variable position); C Lens and D Camera.

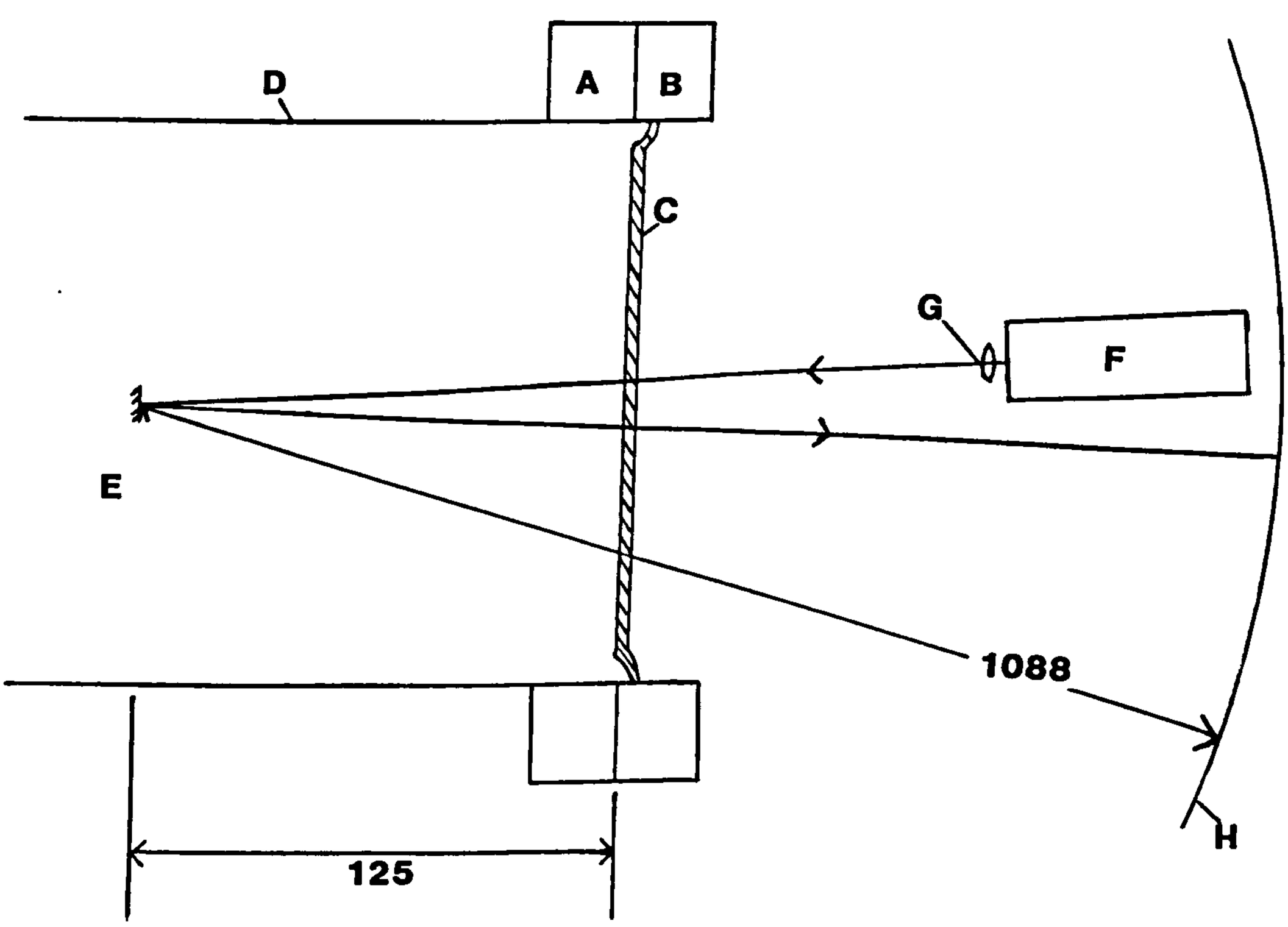

Figure 3.33 View looking down on the apparatus for measuring deflections. Dimensions in mm.
A DN150CF end chamber flange; B DN150CF view port flange; C Window; D Chamber wall; E Mirror at centre of suspension; F Laser; G Lens and H Scale.

3.11 EXPERIMENTAL PROCEDURE

The procedure for taking data using the RDG is described with reference to its operating equation below where the symbols have their usual meanings, see Chapter 2.

$$P_{RDG} = \frac{\frac{c}{2L}}{\varepsilon\ \sigma_{RDG}\ \omega\ R^4 \left[\frac{\pi}{8000\ R_o}\right]^{1/2}} \cdot \frac{T^{1/2}}{\sum M_i^{1/2}.r_i} \cdot \frac{\sum r_i}{} \cdot y_o \qquad (3.10)$$

The procedure below was followed for each measurement of the deflection y_o, the measurable quantity of the experiment.

It was first ensured that the system was at base pressure (9×10^{-8} mbar) with the vacuum pumps operating correctly. For experiments with gases other than air the gas line was filled with a pure gas. The lamp and scale were then positioned with the mirror-scale distance set to 1088 mm. The receiver suspension was then raised from its resting position and its period timed to check the torsion fibre. The residual gas analyser and the BAG were then degassed for approximately 15 minutes and the Penning gauge switched on. The high speed rotor was then run up to speed and the system allowed to return to base pressure. It was important to start and stop the rotor with the suspension raised to avoid any vibrations affecting the silicon receiver disc. This order of events was followed so that procedures causing temporary vibrations were completed before the offset of the SRG was measured. Such disturbances may have necessitated recalibration of the SRG offset.

The pressure of the system was then raised by introducing a gas via the high precision leak valve and the RGA was used to identify and monitor the most dominant residual gases at one minute intervals. The pressure was stabilised as monitored to one decimal place by the BAG. The disc-separation was then set and the receiver damped to be quiescent. The small residual oscillation of the suspension discussed earlier was then recorded both horizontally to measure the original centre of oscillation and vertically to measure the vibration in the suspension.

The temperature was continuously recorded on a flange above the rotor by a decimal thermocouple thermometer (Fluke, 1989). The BAG and Penning gauge pressures were then recorded, as was any change in the pressure (for example from a pressure burst) during the actual measurement of the deflection. The indicated rotor speed and its current and voltage settings were also recorded.

The shutter was withdrawn from between the two discs when the light spot was at the extreme right position on the scale and the last RGA and SRG trace noted. This procedure was the easiest and most accurate for the suspensions with the longest periods. At low pressures damping of the suspension was negligible, see Chapter 2, and to an excellent approximation the induced oscillation had constant amplitude over an interval of many oscillations. In principle the initial swing of $2y_o$ (see figure 3.34) after half a period yielded the necessary measurement. For low pressures the induced oscillation was checked by recording a few consecutive oscillations.

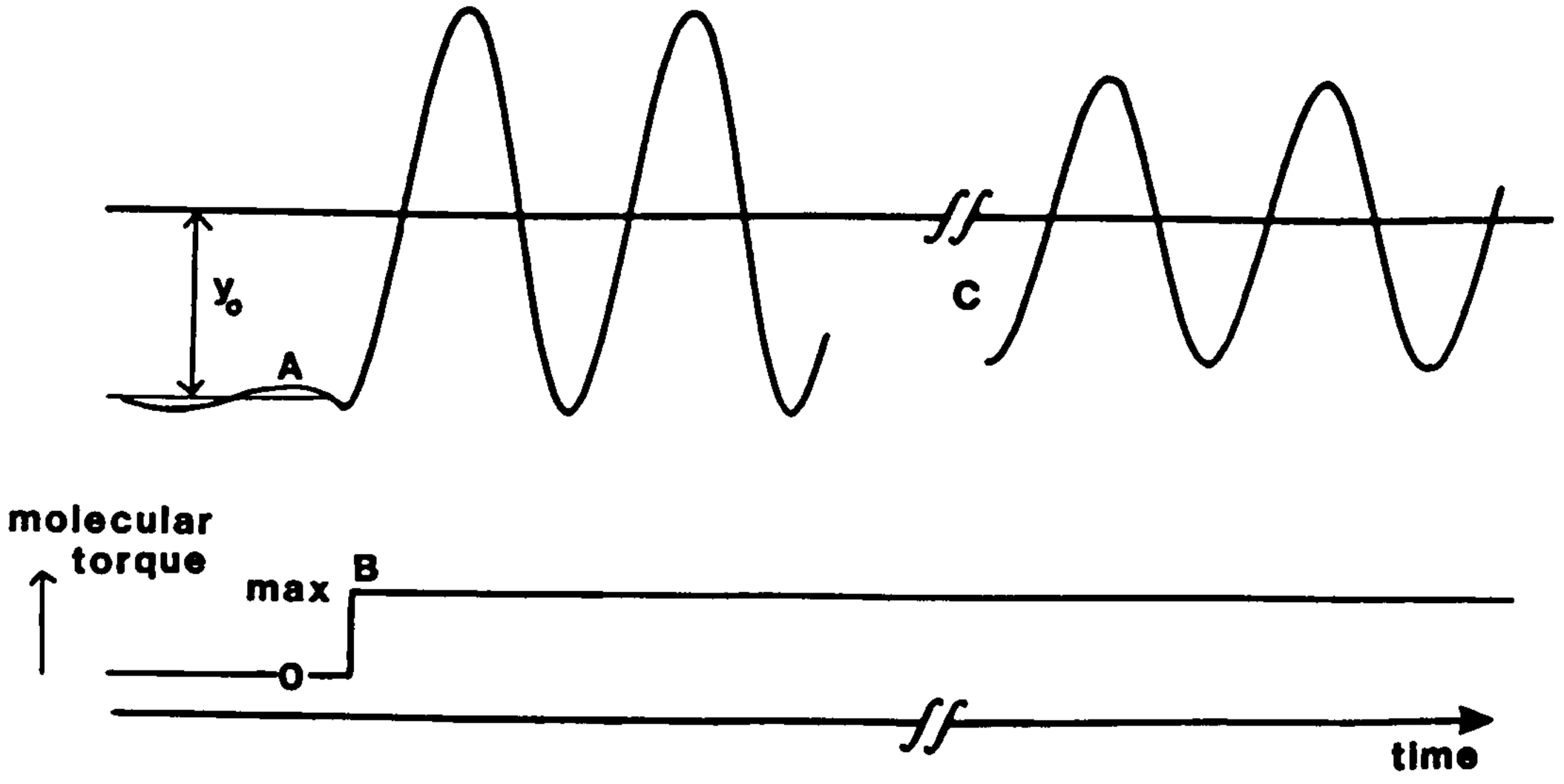

Figure 3.34 Response of the receiver to a step function of molecular torque.
A Residual oscillation; B Step function of torque delivered and C Damping after many oscillations.

The residual gas analysis was performed using the data of the RGA trace which was from the scan performed simultaneously with the measurement of the deflection. This enabled the values $\Sigma\, r_i$ and $\Sigma\, M_i^{1/2}.r_i$ to be determined where r_i is the amount of each gas relative to nitrogen. The value of P_{SRG} was measured as the mean of five consecutive readings including the one before the shutter was withdrawn. A typical log book record is shown in figure 3.35.

Date 29.4.92

Run Number	Disc Separation / mm	Last RGA plot time	Last SRG reading / x 10^{-6}	Rotor speed / krpm	Rotor Voltage / V	Rotor Current / A	BAG pressure / x 10^{-6}	Penning pressure / x 10^{-6}	Temperature / °C	Vertical motion on scale / mm	Spot position	Left	Centre	Right
54	4.27	8 minutes	1.3180	7.1	4	1.1	1.2	1.2	22.3	1	IN	400	408.5	417
											OUT	188	302.5	417
											y_o =		106 mm	

Figure 3.35 A typical log book trace for nitrogen on a 92 mm smooth silicon receiver surface. All pressures in mbar and any pressure bursts also noted. The spot position was recorded when the shutter was IN between the discs and then when the shutter was OUT.

The values of the quantities $\Sigma\, r_i$, $\Sigma\, M_i^{1/2}.r_i$, R, ω, c, T and L were all known and σ_{RDG} for the smooth receiver surface was assumed to be unity (see Chapter 1). The disc-separation t was known and the value of ε was calculated from the analytical expression given in Chapter 2. For some of the earlier work ε was calculated empirically, see Chapter 5. Thus using equation 3.10 a value of P_{RDG} could be calculated from the measured value y_o.

3.12 SUMMARY

The RDG developed is housed in a turbomolecular pumped UHV system with facilities for gas entry and residual gas analysis. A unique adaptation to a turbomolecular pump allows a 92 mm diameter metal sender disc to be rotated at controlled speeds up to 51 krpm. A silicon receiver disc of equal size is held at a variable height above it by a phosphor-bronze torsion fibre. A shield which is withdrawn from between the discs allows a step function of molecular torque to be created by molecules desorbing from the sender. The resultant deflection of the receiver is measured by a simple laser and scale apparatus. All the quantities associated with the RDG's operating equation are directly measurable hence the RDG can be used to make absolute measurements of high vacuum pressures.

CHAPTER 4

PRELIMINARY RESULTS AND ROTATING DISC GAUGE CHARACTERISTICS

4.1 INTRODUCTION

In this chapter the results of experiments performed to determine the characteristics of the rotating disc gauge (RDG) with equal sized discs and in order to test the validity of the RDG's operating equation below are reported.

$$P_{RDG} = \frac{\frac{c}{2L}}{\varepsilon\ \sigma_{RDG}\ \omega\ R^4 \left(\frac{\pi}{8000\ R_o} \right)^{1/2}} \cdot \frac{T^{1/2}}{M^{1/2}} \cdot y_o \qquad (4.1)$$

where P_{RDG} is the pressure measured with the RDG; c is the torsion constant of the fibre; L is the mirror-scale distance = 1088 mm (set); T is the absolute thermodynamic temperature; ε is the edge effect loss factor; σ_{RDG} is the tangential momentum accommodation coefficient of a gas on the receiver surface; ω is the radian frequency of the sender; R is the discs' radius = 46 mm; R_o is the gas constant; M is the relative molecular mass and y_o is the measured deflection.

The experiments are described here generally in chronological order to show the progression of work towards the ultimate aim of making pressure measurements with the RDG. The parameters varied were pressure P, the sender-receiver disc-separation t and hence ε, the sender speed ω and the relative molecular mass M.

4.2 ROTATING DISC GAUGE AND IONIZATION GAUGE COMPARISONS

From equation 4.1 it can be seen that deflection y_o is predicted to be directly proportional to pressure P where P_{RDG} is substituted by another means of pressure measurement.

The results of the first experiments are shown in figure 4.1 where deflection versus indicated hot cathode ionization gauge (IG) pressure P_{IG} is plotted on a linear scale for four values of disc-separation t.

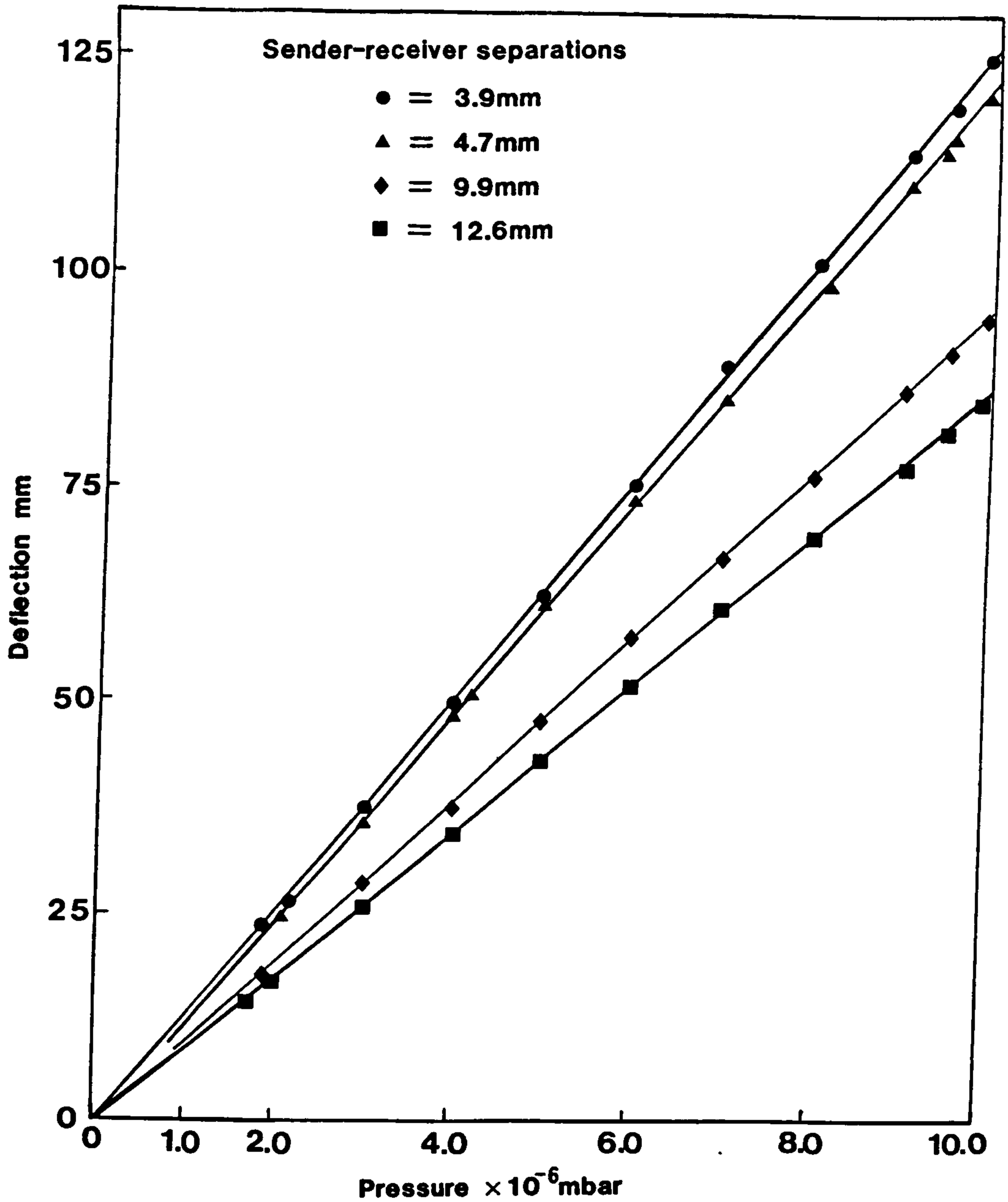

Figure 4.1 Deflection versus indicated ionization gauge pressure for air at various disc-separations.

The data was collected at a fixed sender speed of 50 krpm and the pressure varied in the range 1.0 - 9.9 $\times 10^{-6}$ mbar by the introduction of air. The data for each disc-separation were taken within a short time so that the vacuum composition was constant. The individual deflections are subject to an uncertainty of ±1 mm and for clarity these uncertainties, which are small compared to the measured deflections, are not shown. The resolution of the digital IG readings was ±0.1 $\times 10^{-6}$ mbar in the range investigated. The data were recorded using a fibre of torsion constant 6.61 $\times 10^{-7}$ Nm and at a temperature of 20 to 21 °C. The raw data have not at this stage been corrected for gas composition nor IG sensitivity factors since the vacuum composition remained constant

The full lines represent the result of a least squares fit (LSF) program to the data. The strict proportionality, within the stated experimental uncertainties is to be noted. The intersection at the origin confirms the prediction of zero deflection at 'zero' pressure. Since the IG may reasonably be expected to give a reading which varies linearly with pressure then the proportionality of the data with indicated IG pressure can be seen as a confirmation of the expected linear dependence of deflection upon pressure. As would be expected the largest deflection at a given pressure corresponds to the smallest disc-separation t where the lost torque is least.

The results of a similar experiment performed with a different fibre of torsion constant 1.465 $\times 10^{-7}$ Nm in nitrogen are shown in figure 4.2. This experiment was performed simultaneously with the first RDG/spinning rotor gauge comparison in Chapter 5 for a fixed value of t = 4.3 mm and a fixed sender speed of 30 krpm. The temperature was 23 °C. The full line again represents a LSF to the data. The strict proportionality and intersection at the origin are again to be noted and confirm that the proportionality of deflection with pressure is independent of sender speed and fibre constant. The gradient of the line is dependent upon these parameters.

In figure 4.3 the results of another experiment of deflection versus indicated IG pressure (P_{IG}) are shown. In this case the residual gas was 100% helium, the fibre used had a torsion constant of 1.470 $\times 10^{-7}$ Nm, the sender speed was 15 krpm and the temperature was 20 °C. The full line is a result of a LSF to the data.

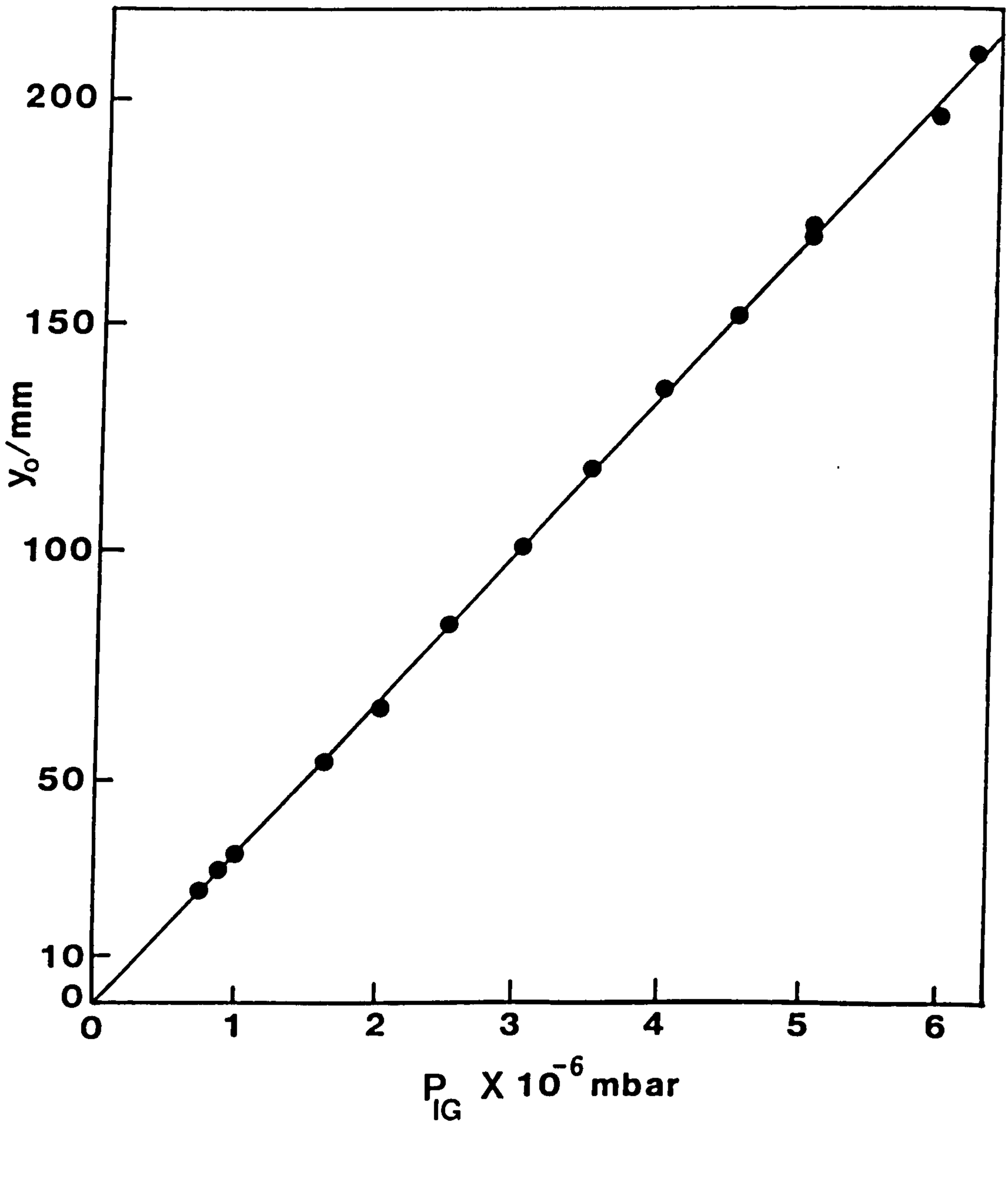

Figure 4.2 Deflection versus indicated ionization gauge pressure for nitrogen.

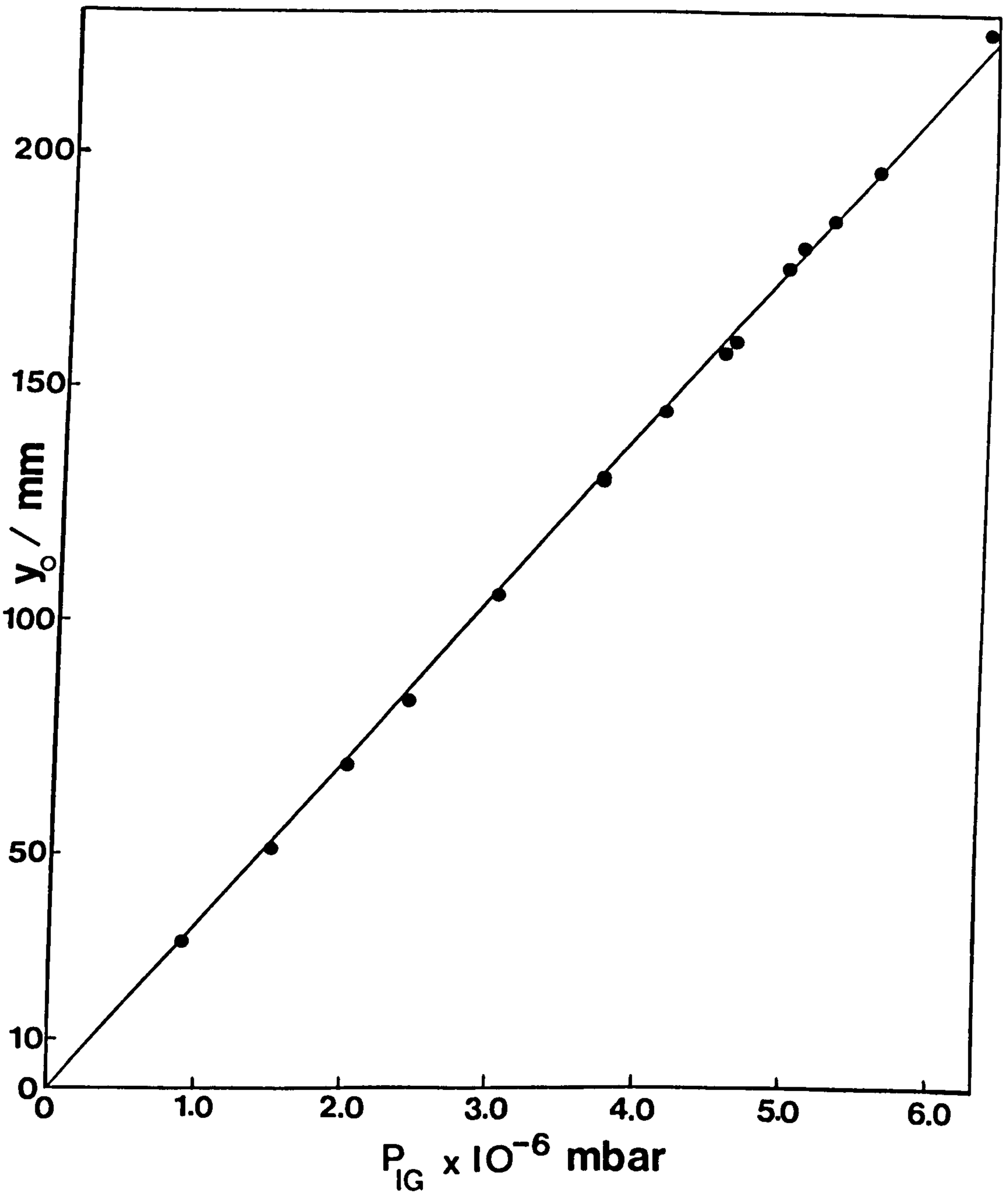

Figure 4.3 Deflection versus P_{IG} for helium.

Again the strict proportionality for this different gas species is to be noted as is the intersection at the origin. Here the P_{IG} readings have not been corrected for the sensitivity factor (typically 0.18, see below) of the gauge for helium, which would only change the gradient. Further results of deflections (computed to RDG pressure (P_{RDG}) values) versus P_{IG} are given in Chapter 6 where the relative sensitivity factors of the IG are evaluated for a range of gases by comparison of P_{IG} and P_{RDG} readings.

The results of experiments of deflection versus P_{IG} in different pressure ranges are shown in figures 4.4 and 4.5. In figure 4.4 the parameters were the same as those in figure 4.1 with a disc-separation of 4.7 mm used. The IG uncertainties are shown on this graph since proportionality is seen only within these limits. Clearly the IG uncertainty is relatively more significant for pressures near 1.0×10^{-5} mbar.

In figure 4.5 the measuring range of the experiment detailed for figure 4.2 was extended to the $1.0 - 9.9 \times 10^{-7}$ mbar range. Here under constant vacuum conditions the strict proportionality is again to be noted. The small divergence at the lower pressures is due to a greater relative proportion of hydrogen and, as above, at pressures approaching 1.0×10^{-7} mbar the uncertainty in P_{IG} becomes more significant. The proportionality is also important since the deflections measured approach zero. The relevance of this to the uncertainty in P_{RDG} and the ultimate limit of RDG pressure measurements is discussed in Chapter 5.

4.2.1 Conclusions

The experiments of deflection versus indicated IG pressure confirm the theoretically predicted linear dependence of deflection on pressure. This was true for different gases and fibre torsion constants. The results also indicated that more torque is lost from the discs' interspace as the disc-separation is increased as is expected from the theory. This effect was fully investigated as below.

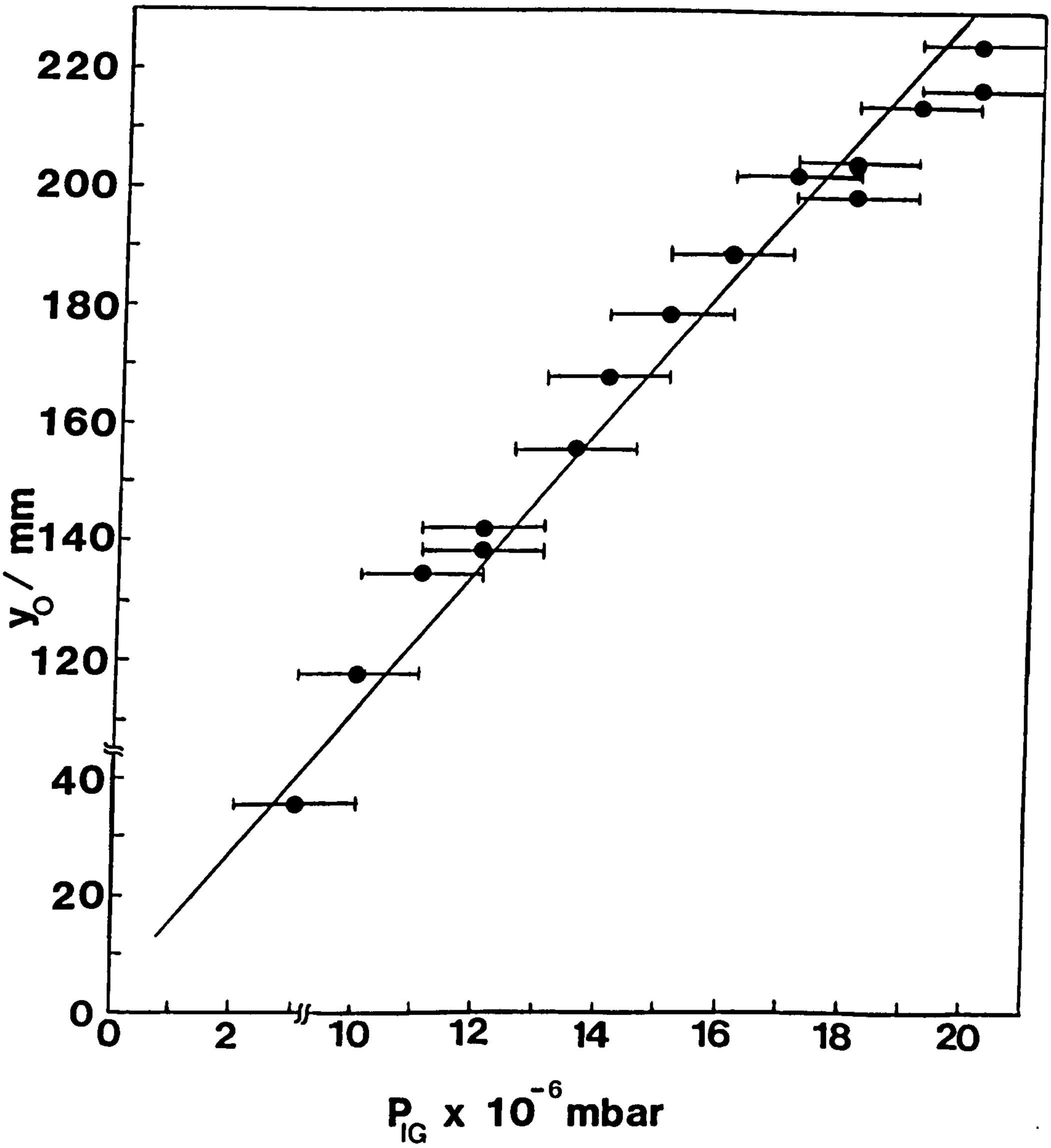

Figure 4.4 Deflection versus P_{IG} in the low 10^{-5} mbar range.

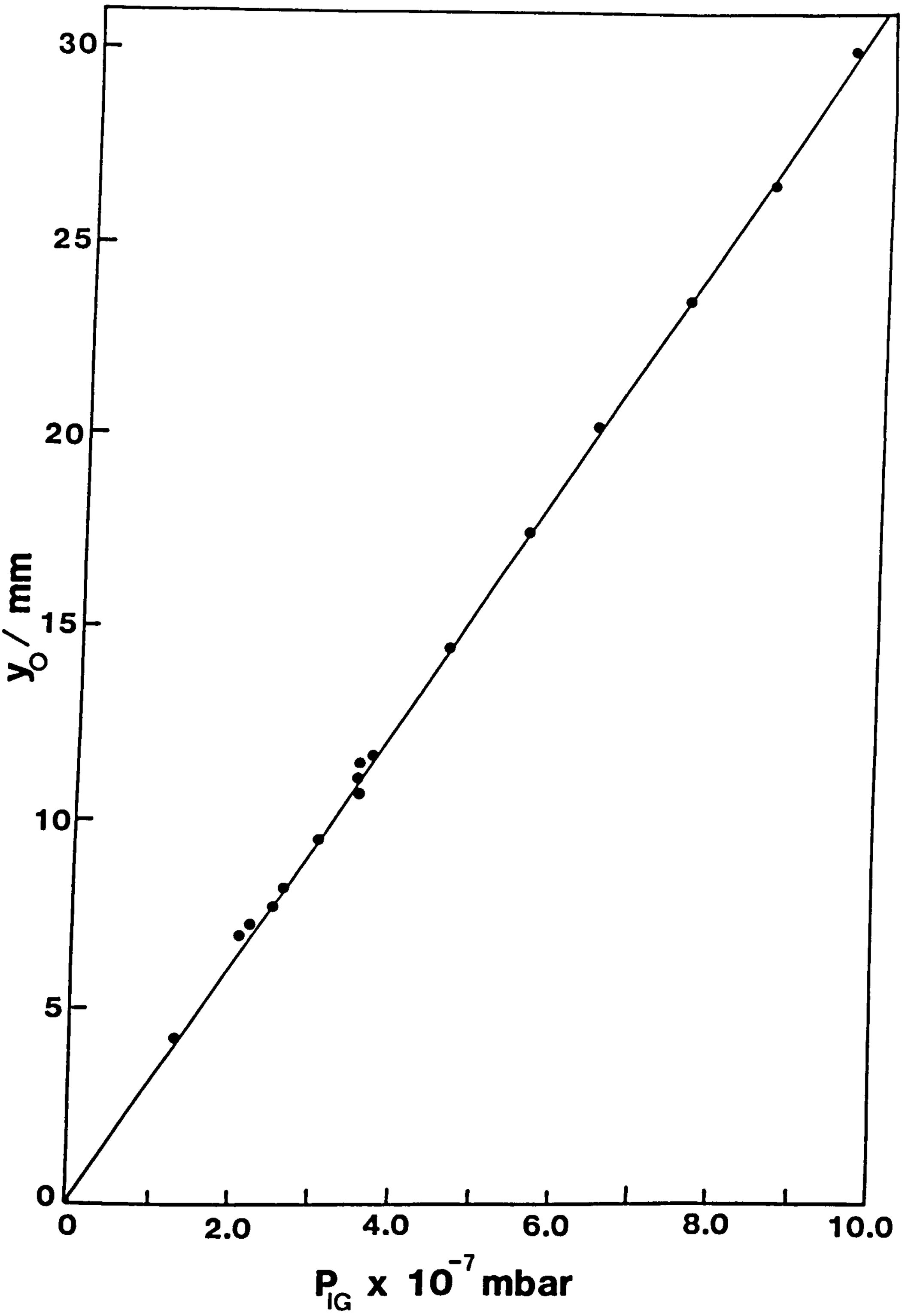

Figure 4.5 Deflection versus P_{IG} in the 10^{-7} mbar range.

4.3 EDGE EFFECT LOSSES

The edge effect loss described in Chapter 2 was investigated by measuring the deflection y_o as a function of sender-receiver separation t with all other parameters held constant. The analytical expression derived for the edge effect loss factor ε (Pert, 1993) could then be tested where

$$\varepsilon = \left[\left[1 + \left(\frac{t}{2R} \right)^2 \right]^{1/2} - \frac{t}{2R} \right]^4 \qquad (4.2)$$

In the first experiment of this type the above analysis had not been performed nor had the experiment showing a high speed fall off of deflection reported in the next section. A constant sender speed of 50 krpm was used, for maximum sensitivity, and hence the expression for ε would not hold. The data of these experiments are shown in figure 4.6. The data were recorded for the fibre of torsion constant 6.61×10^{-7} Nm at three P_{IG} values; 9.5, 6.0 and 3.0×10^{-6} mbar in air. The uncertainty in the disc-separation t was ±0.4 mm and for clarity it is not shown.

The variation of y_o with t is in each case qualitatively as would be expected. That is, as the discs become further apart the communicated torque decreases because of the increased loss of molecules out of the interspace which was discussed in Chapter 2. The full lines through the data points represents the results of quadratic least squares fits to the data. The small spread of the data is to be noted and reflects the constancy of the vacuum composition. The dashed line represents the results of Monte Carlo simulations done by Pert (1993) based on the analytical treatment of the edge effect described in Chapter 2 extended to high sender speeds. The close agreement shows the accuracy of the model. Typical values of the vacuum composition are given in table 4.1.

The shape of the curves is the same in all three cases. At a given separation the curves scale in the ratio of the P_{IG} indications i.e. in the ratio 95:60:30 = 3.17:2:1. This can be seen at the separation t = 3.44 mm where the ratio of the deflections from figure 4.6 is 122.5:77:39 = 3.14±0.08 : 1.97±0.06 : 1.0. It can be seen that at a

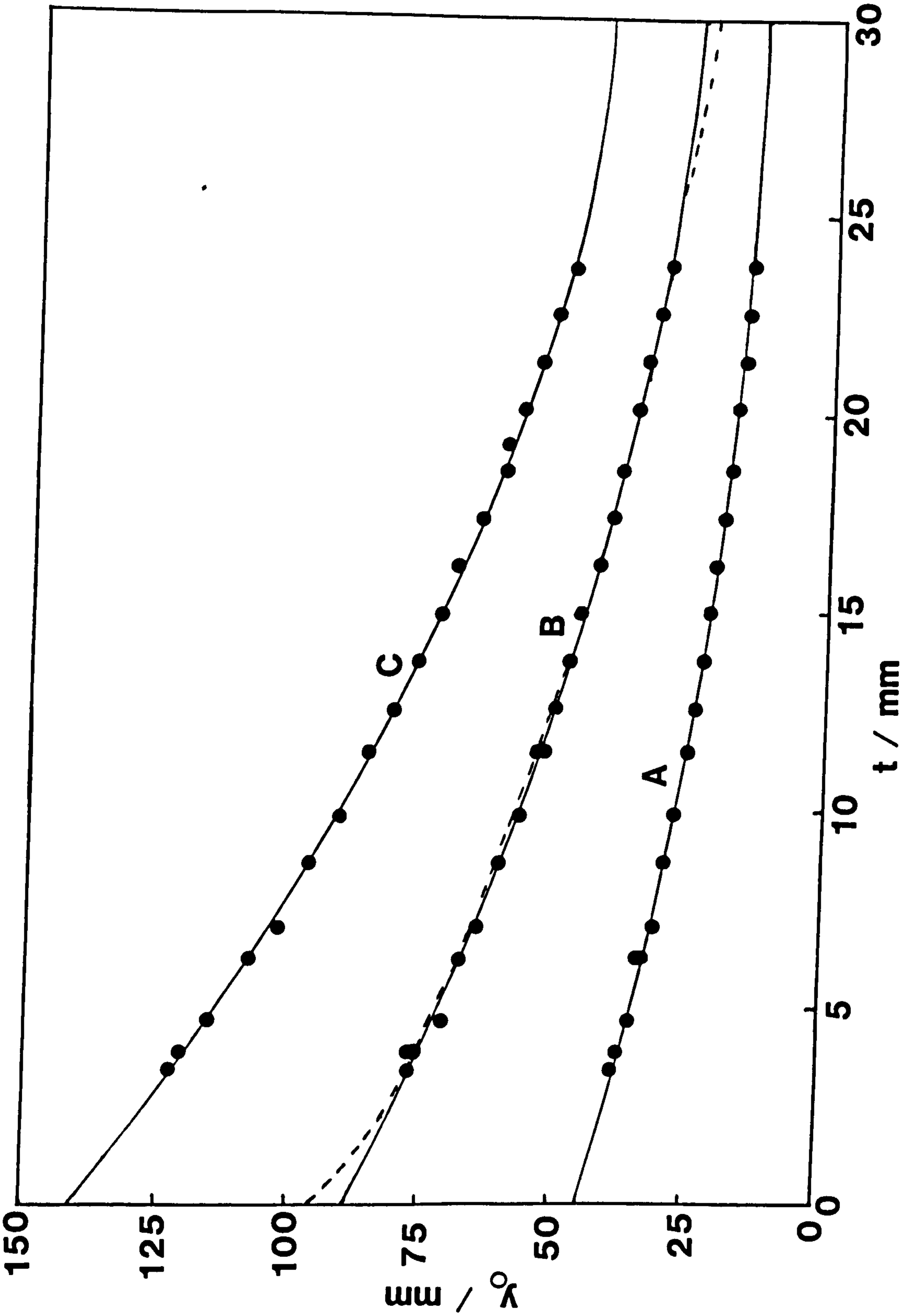

Figure 4.6 Deflection versus disc-separation in air at different pressures.
A 3.0×10^{-6} mbar; B 6.0×10^{-6} mbar and C 9.5×10^{-6} mbar. The full lines are the result of a quadratic least squares fit to the data and the dashed line is the result of a Monte Carlo simulation.

given separation the deflections which are due to the gas density in the discs' interspace scale exactly, within experimental uncertainty, with the indicated pressure measured outside the interspace in the bulk of the vacuum. Thus access of the gas to the discs' interspace is adequate for at least the separations investigated.

Gas	Relative molecular mass	IG sensitivity factor[1]	% of vacuum composition	r_i
Hydrogen	2	0.44	37.0	2.54
Helium	4	0.18	0.3	0.02
Water vapour	18	0.9	3.1	0.21
Nitrogen	28	1.0	14.6	1.0
Carbon monoxide	28	1.08	34.6	2.37
Oxygen	32	0.85	3.7	0.25
Argon	40	1.2	6.9	0.47

Table 4.1 The vacuum composition at an indicated pressure P_{IG} of 6.0×10^{-6} mbar. r_i is defined below. [1]See O'Hanlon (1989).

Measurements at separations below t = 3.44 mm were not possible due to the experimental shutter arrangement. Conductive access of the gas to the interspace would be restrictive only at very small separations.

4.3.1 Preliminary Pressure Measurements

A correction for the variety of gases present needs to be made to equation 4.1 to enable a value of P_{RDG} to be deduced. The operating equation below is for the case of N gases in the vacuum (see Chapter 2).

$$P_{RDG} = \frac{\frac{c}{2L} \quad T^{1/2}}{\varepsilon \, \sigma_{RDG} \, \omega \, R^4 \left(\frac{\pi}{8000 \, R_o} \right)^{1/2}} \cdot y_o \cdot \frac{\sum_{i=1}^{N} r_i}{\sum_{i=1}^{N} M_i^{1/2} \cdot r_i} \qquad (4.3)$$

where r_i is the partial pressure of the ith gas relative to that of

nitrogen.

The values of the quantities in this equation were listed earlier. The value of σ_{RDG} was taken as unity. Since the flat and smooth receiver surface was adsorbate covered then, from the work of Thomas (1981), this is a valid approximation and is discussed in more detail in Chapter 6. The temperature was 21.5 ± 0.5 °C.

The value the deflection would have at zero disc-separation for which ε would be unity was found by extrapolating the curves to zero separation. Here edge effect losses are zero. Table 4.2 shows the values of y_o from the intersection of the curves in figure 4.6 by using the quadratic fits to the data. By using these deflections, inserting the relevant values into equation 4.3 and correcting for vacuum composition the P_{RDG} values for each curve were calculated and are shown in table 4.2.

To compare these values to the indicated P_{IG} values the latter need correcting for vacuum composition. This was done by using the relative sensitivity factors s_i of O'Hanlon (1989) shown in table 4.1. These are typical values and a more comprehensive survey of IG sensitivity factors is discussed in Chapter 6. The true P_{IG} value is found using the equation below (see Chambers, Chew and Troup, 1992).

$$P_{IG(TRUE)} = P_{IG(INDICATED)} \frac{\sum_{i=1}^{N} r_i}{\sum_{i=1}^{N} s_i . r_i} \qquad (4.4)$$

$P_{IG(INDICATED)}$ / $\times 10^{-6}$ mbar	y_o at t = 0 / mm	P_{RDG} / $\times 10^{-6}$ mbar	$P_{IG(CORRECTED)}$ / $\times 10^{-6}$ mbar
3.0	44.6	4.7	4.4
6.0	89.0	7.4	7.3
9.5	140.9	19.4	17.3

Table 4.2 P_{RDG} and P_{IG} values corrected for vacuum composition.

There was an unknown uncertainty attached to the values of the deflections deduced at t = 0 and to the IG relative sensitivity factors. Despite this the fact that there was very good agreement between the P_{RDG} and P_{IG} values from an IG which was one of a batch whose calibration could be traced back to a standard gave great encouragement.

4.3.2 Further Edge Effect Investigations

In figure 4.7 the data of another experiment of deflection versus sender-receiver separation t is shown at indicated P_{IG} values of 5.0 and 6.2×10^{-6} mbar. The fibre used in this experiment had a torsion constant of 1.465×10^{-7} Nm and the sender speed was constant at 15 krpm. This sender speed was well within the limit of application of equation 4.2 for the analytical determination of ε. The temperature was 24 °C. The pressure was raised with nitrogen gas to approximately 50% nitrogen since there was a large residual amount of hydrogen due to the ion pump. The change in vacuum composition was negligible.

The full line represents the result of a quadratic least squares fit to the data. The dashed curve represents the analytical prediction from equation 4.2. The close agreement with the data is to be noted and confirms the theoretical analysis of the edge effect. The curves have the same shape noted in the earlier experiment. At a given separation the curves scale in the same ratio i.e. 62:50 = 1.24:1 which can be seen at t = 4.3 mm where the deflections scale as 104.5:84.5 = 1.24±0.02 : 1. By extrapolating to zero separation, correcting for gas composition and making the assumptions made earlier P_{RDG} and P_{IG} values were computed for the curve at an indicated P_{IG} value of 6.2×10^{-6} mbar. Here $P_{RDG} = 8.1 \times 10^{-6}$ mbar and $P_{IG} = 8.0 \times 10^{-6}$ mbar. Again there is close agreement.

These experiments served as a means of calibrating the edge effect factor ε of the RDG before the analytical derivation of the expression for $\varepsilon(t/R)$ was made. Originally values of ε were computed from the equations of the quadratic fits to the data. Using these equations the values of ε at each disc-separation t were calculated

where

$$\varepsilon = \frac{y_o(t)}{y_o(t=0)} \qquad (4.5)$$

The computed values of ε are shown in table 4.3 for various values of t together with those from the analytical expression of equation 4.2. It can be seen that there is very good agreement between the values of ε derived analytically and those from the quadratic fit to the data. This is also shown by the very good agreement between the analytical curve and the curve of the quadratic fit to the data in figure 4.7. The discrepancy between the quadratic fit and the analytical data at a disc-separation of 4.3 mm is $\simeq$ 1% thus the correction to the value of ε in work (Chambers, Chew and Troup, 1992 and 1992a) before the edge effect analysis was done is very small. The uncertainty in the analytical values of ε is small and is fully discussed in Chapter 5.

Disc-separation	Edge effect loss factor ε	
t / mm	Quadratic fit	Analytical
2.0	0.92	0.92
3.3	0.87	0.87
3.8	0.86	0.85
4.3	0.84	0.83
5.9	0.79	0.78
7.0	0.75	0.74
8.2	0.71	0.70
9.4	0.68	0.66
10.6	0.64	0.63
11.8	0.61	0.60
13.0	0.58	0.57
14.6	0.54	0.53
15.8	0.51	0.51
17.0	0.49	0.48
18.2	0.46	0.46
20.0	0.40	0.42

Table 4.3 Experimentally and analytically determined values of the edge effect loss factor.

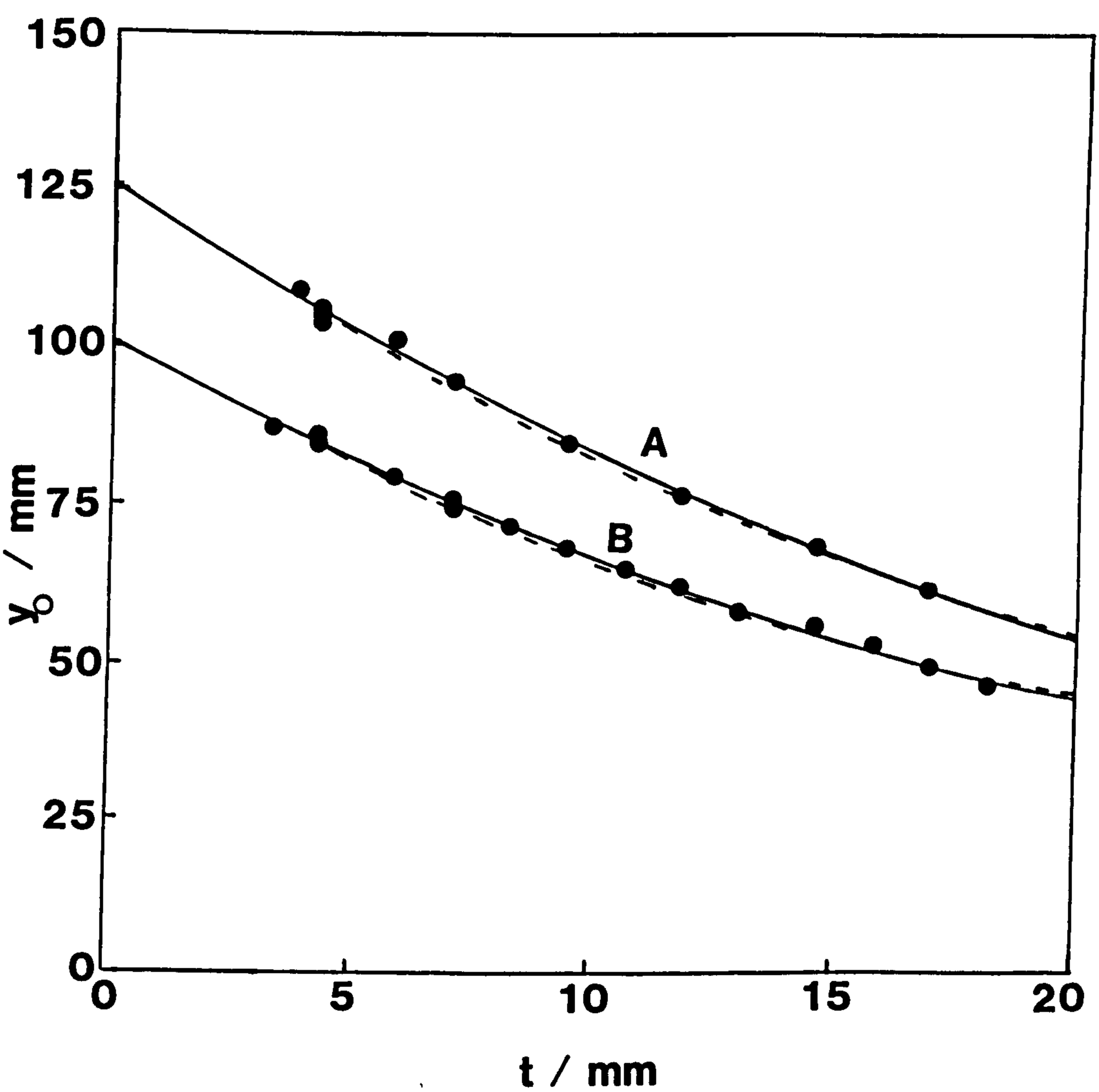

Figure 4.7 Deflection versus disc-separation for nitrogen at two different pressures. A 6.2×10^{-6} mbar and B 5.0×10^{-6} mbar. The full lines are the result of a quadratic least squares fit to the data and the dashed lines are analytical predictions.

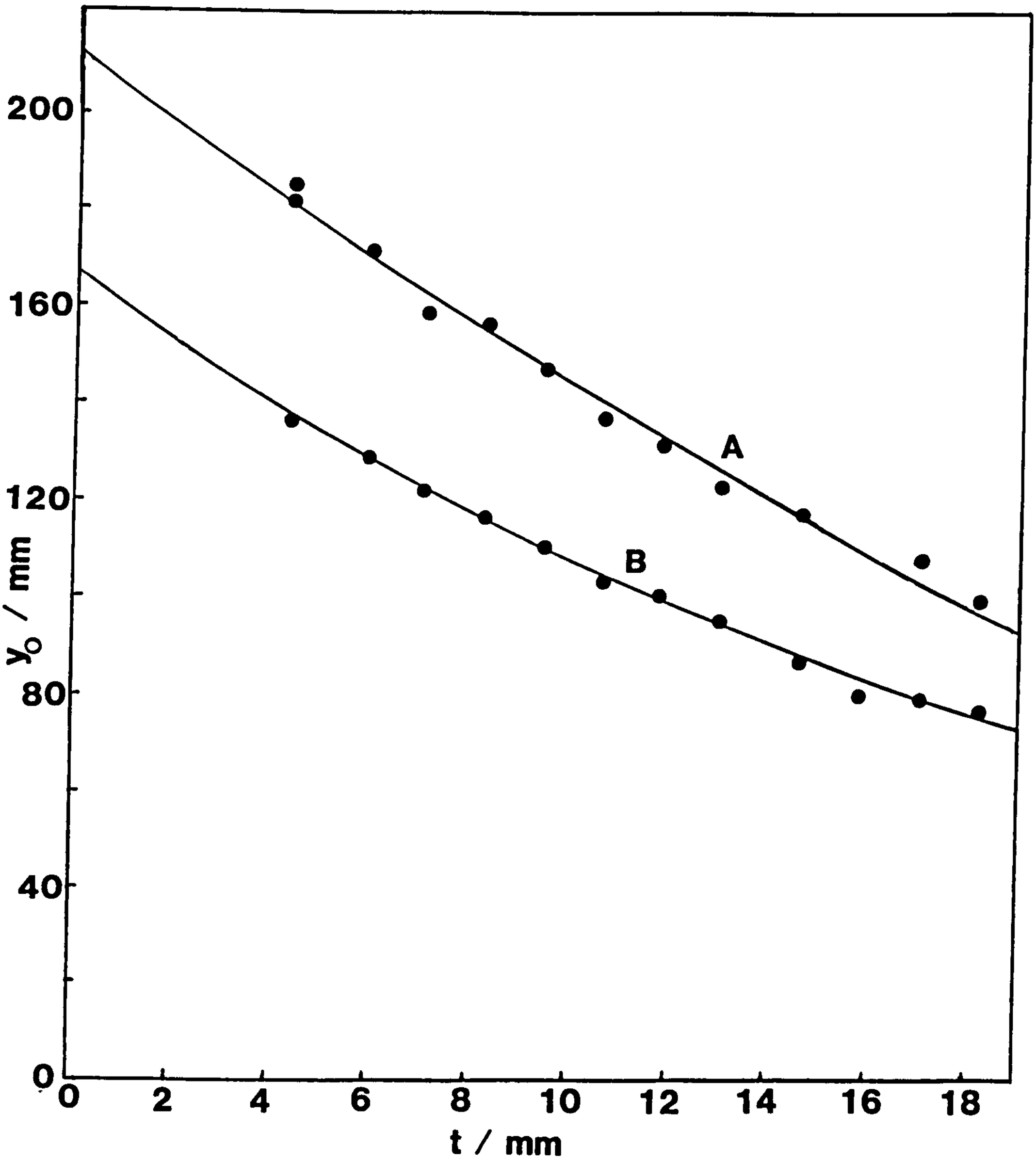

Figure 4.8 Deflection versus disc-separation in pure nitrogen at two set pressures. A 2.0×10^{-5} mbar and B 1.5×10^{-5} mbar.

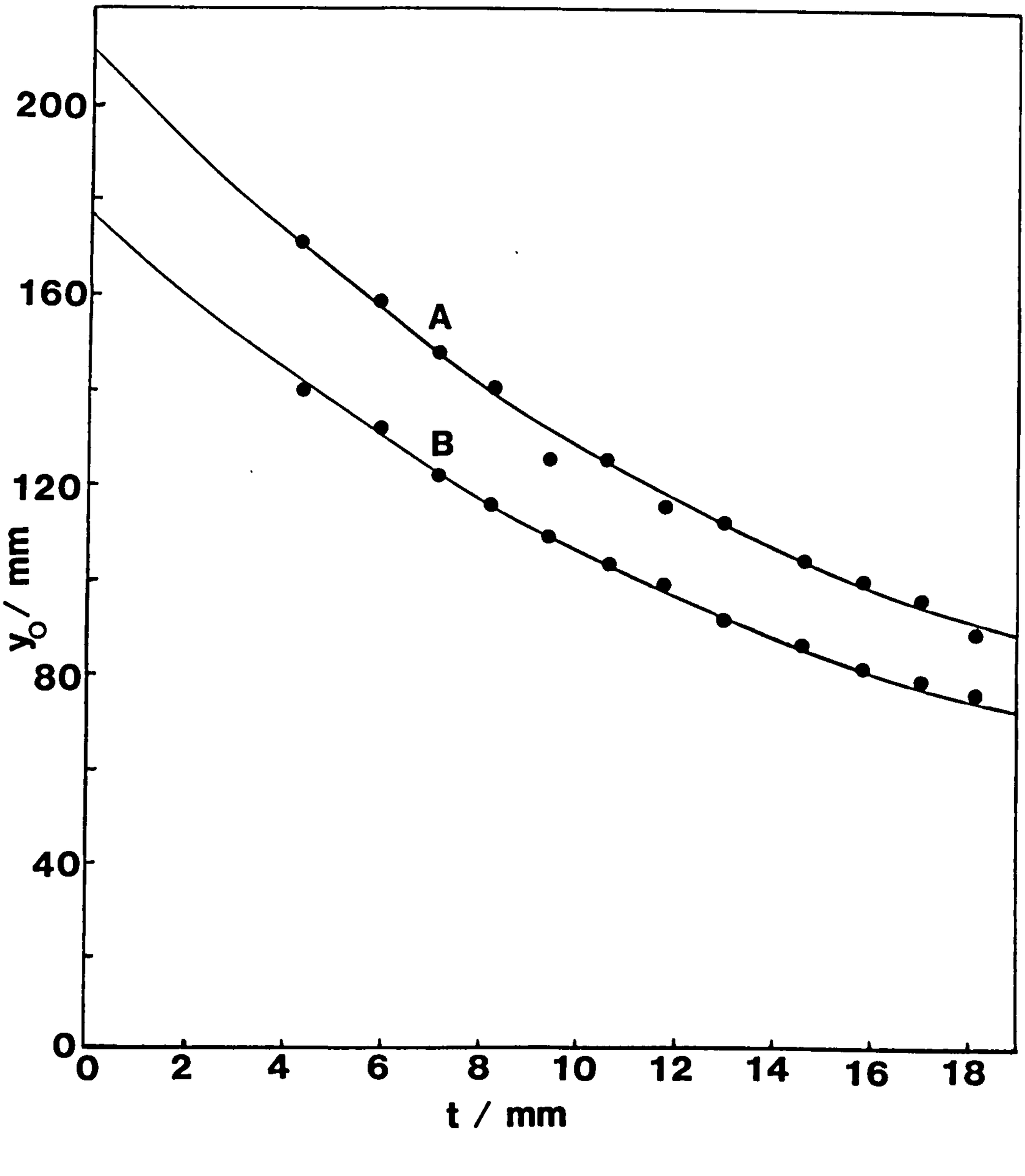

Figure 4.9 Deflection versus disc-separation in pure helium at two set pressures. A 9.0×10^{-6} mbar and B 7.5×10^{-6} mbar.

The data of deflection versus disc-separation at a fixed sender speed of 7.1 krpm for 100% nitrogen and 100% helium are shown in figures 4.8 and 4.9 respectively. The torsion constant of the fibre used in this experiment was 1.470×10^{-7} Nm and the temperature was 20 °C. In figure 4.8 the curves have the same characteristic shapes seen earlier and scale at a given separation in the ratio of the P_{IG} values i.e. 20:15 = 1.33:1. For example at a separation of 11.8 mm the deflections scale in the ratio 1.31.

The calculated values of P_{RDG} from the deflections at a separation of 4.3 mm for the curves at P_{IG} values of 1.5 and 2.0×10^{-5} mbar are 1.6 and 2.0×10^{-5} mbar respectively which again illustrates the high agreement between the IG and RDG readings.

The curves shown in figure 4.9 for helium are of the same shape as those for nitrogen. This confirms the prediction from the analysis of the edge effect in Chapter 2 that the form of the fall off of molecular torque is independent of gas species at low sender speeds. The curves also scale in the same ratio as the indicated P_{IG} values i.e. 90:75 = 1.2. For example at t = 15.8 mm the ratio of the corresponding deflections is 1.23.

By using the sensitivity factor of 0.18 for helium (O'Hanlon, 1989) the true P_{IG} values are 4.2 and 5.3×10^{-5} mbar with corresponding values of P_{RDG} of 4.4 and 5.3×10^{-5} mbar respectively calculated from the deflections at 4.3 mm. Again the very close agreement between the P_{IG} and the P_{RDG} is to be noted and shows the validity of the RDG pressure measurements in different gases. The results of further experimental comparisons, in various gases, between the RDG and the IG are given in Chapter 6.

4.3.3 Conclusions

The experiments of deflection versus sender-receiver separation show that there is very good agreement between the analytically predicted values of the edge effect loss factor and the experimental data for sender speeds where the analytical expression for ε is valid. This is for all gas types and can be taken as experimental support of the analysis.

There is also very close agreement between the experimental data and the Monte Carlo simulations at a high sender speed.

The scaling of the curves is in the same ratio as the P_{IG} indications which shows that there is adequate access for gas molecules into the discs' interspace at least for separations greater than 3 mm.

There is very good agreement between the calculated RDG and IG pressure measurements.

4.4 ROTATING DISC GAUGE PERFORMANCE UNDER VARIABLE SENDER SPEED

Although the rotor in the apparatus of Dushman (1915) was capable of speeds up to 10 krpm data at speeds up to 2 krpm only were taken. The RDG developed in this work was capable of a sender speed of 51 krpm and clearly had the capacity to considerably extend Dushman's data and to test the high speed characteristics predicted by the RDG theory. The experiments reported in this section were of deflection versus sender speed in otherwise constant conditions. They were repeated for various pressures, sender-receiver separations t and in different gases.

Figure 4.10 shows the first data recorded of deflection y_o versus sender speed ω at three different steady pressures in air as monitored by the IG. The fibre used had a torsion constant of 6.61×10^{-7} Nm, the temperature was 20.5 °C and the disc-separation was 4.7 mm. The uncertainties of ±1 mm in the deflections and ±0.1 krpm in the indicated sender speed are not shown for clarity. The full line represents the experimentally found dependence, the dashed line represents the analytical fit and the dotted line represents the Monte Carlo approximation of Pert (1993).

The linear dependence of deflection on ω anticipated in equation 4.1 is borne out by experiment up to about 35 krpm. Above this sender speed there is a discernible deviation from linearity as is predicted by the RDG theory.

In figure 4.11 more data for deflection versus sender speed is given. In this case a fibre with a torsion constant of 1.465×10^{-7} Nm was used, the temperature was 22.5 °C and the pressure was raised by

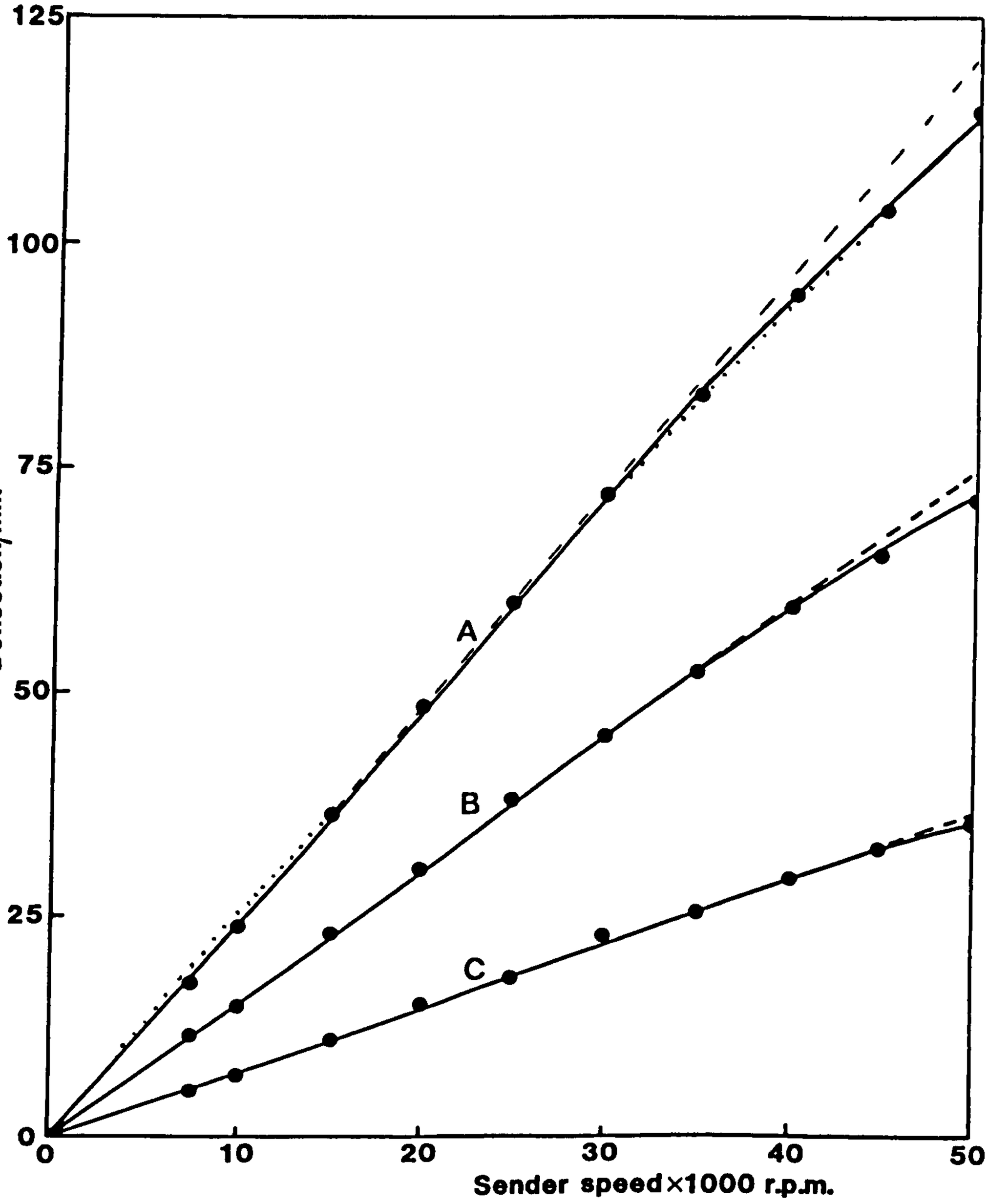

Figure 4.10 Deflection versus variable sender speed in air at three set pressures. A 9.5×10^{-6} mbar; B 6.0×10^{-6} mbar and C 3.0×10^{-6} mbar. The full line is a best fit to the experimental data, the dashed line is the analytical prediction and the dotted line is the fit from a Monte Carlo approximation.

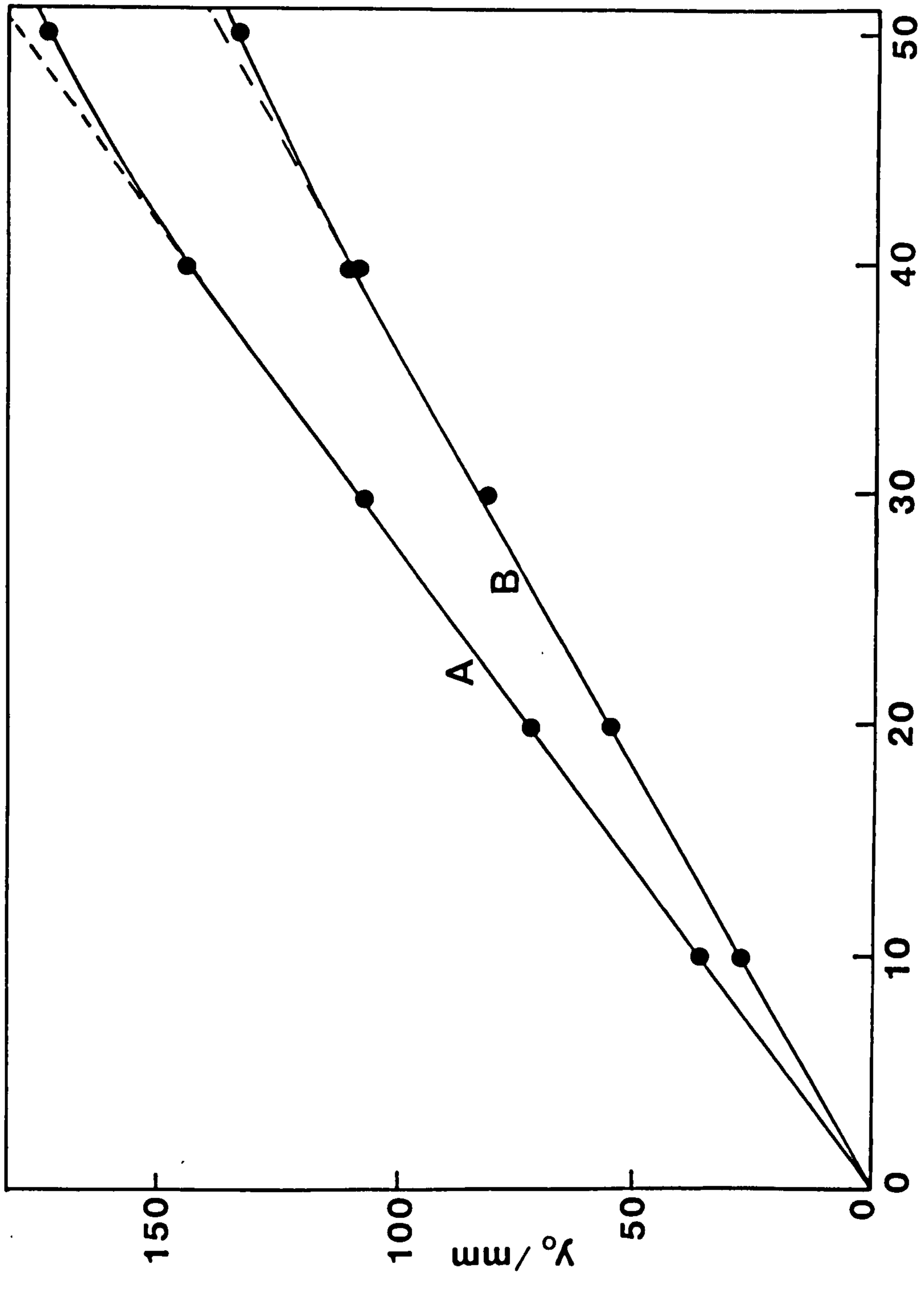

Figure 4.11 Deflection versus sender speed at two set disc-separations. A 4.3 mm and B 10.6 mm. The full line is a best fit to the experimental data and the dashed line is the analytical prediction.

nitrogen and held constant at 3.2×10^{-6} mbar. There is again a clearly detectable fall off from linearity at high sender speeds for each of the two sets of data taken at different disc-separations.

The deviation from linearity at 50 krpm can be evaluated by a comparison of the deflection produced at 50 krpm with that produced under otherwise the same conditions at a speed x by using the coefficient

$$\nu = \frac{y_o(\omega = 50)}{y_o(\omega = x)} \cdot \frac{x}{50} \qquad (4.6)$$

where a value of $\nu = 1$ represents perfect linearity and $\nu < 1$ shows a fall off from linearity at 50 krpm. From empirical determinations ν can be introduced into the RDG's operating equation to combine with ε to account for the high speed loss.

Table 4.4 shows the ν values for a comparison of the deflections at 50 krpm with those in the linear region for data shown in figure 4.10. In table 4.5 the ν values for data in figure 4.11 are given.

	Pressure / $\times 10^{-6}$ mbar		
	9.5	6.0	3.0
Sender speed ω / krpm			
35	0.97±0.02	0.96±0.02	0.97±0.05
30	0.96±0.02	0.96±0.03	0.94±0.05
25	0.96±0.02	0.94±0.03	0.99±0.06
20	0.95±0.02	0.94±0.03	0.95±0.07
15	0.95±0.03	0.93±0.04	0.95±0.09
10	0.96±0.04	0.95±0.07	0.98±0.14
7.5	0.97±0.04	0.95±0.09	0.97±0.18

Table 4.4 Values of ν at various pressures and a constant sender-receiver separation.

The uncertainty in ν is from the standard expression below where Δy_o = 1 mm and $\Delta\omega$ = 0.1 krpm.

$$\Delta\nu = \nu \left[\left(\frac{\Delta y_o}{y_o(\omega = 50)} \right)^2 + \left(\frac{\Delta \omega}{\omega = 50} \right)^2 + \left(\frac{\Delta y_o}{y_o(\omega = x)} \right)^2 + \left(\frac{\Delta \omega}{\omega = x} \right)^2 \right]^{1/2} \qquad (4.7)$$

It can be clearly seen that there is a constant fall off from linearity at high sender speed which is independent of pressure and has not been seen before. The explanations considered as the cause of this phenomenon were:

(i) At high speed the rotor is not running at its indicated speed. This was rejected since at the highest speed the rotor has the largest power intake and is therefore at its most reliable, see Chapter 3.

	Sender-receiver separation t / mm	
	4.3	10.6
Sender speed ω / krpm		
30	0.98±0.01	0.99±0.02
20	0.97±0.01	0.98±0.02
9.9	0.97±0.02	0.98±0.04

Table 4.5 Values of ν for two sender-receiver separations and a constant pressure.

(ii) The high velocity bias given to molecules at high sender speeds will cause molecules to move forward so as to miss the receiver. This adds to the loss of torque due to the Knudsen cosine distribution and was discussed in Chapter 2.

(iii) At high sender speed there is a change in the vacuum composition. This explanation can be rejected by analysis of the vacuum composition at each sender speed. Figure 4.12 shows deflection versus sender speed in nitrogen at a value of t = 5.9 mm, a pressure of 3.6×10^{-6} mbar and a temperature of 21 °C. The torsion constant of the fibre used was 1.470×10^{-7} Nm. Table 4.6 shows the values of $\sum r_i / \sum r_i . M_i^{1/2}$ which measures the vacuum composition at each sender

speed as in equation 4.3. Again fall off from linearity is seen and since it occurs with only a very small change in vacuum composition (and at a temperature equal to that in other such experiments) it can be seen that that a change in vacuum composition is not an explanation for the high speed fall off.

Sender speed ω / krpm	Vacuum composition $\sum r_i / \sum r_i.M_i^{1/2}$
7.5	0.191
9.9	0.193
15.0	0.191
20.0	0.191
25.0	0.191
30.0	0.192
32.5	0.192
35.0	0.192
37.5	0.193
40.0	0.193
42.0	0.193
44.0	0.193
46.0	0.194
48.0	0.193
50.0	0.194
51.0	0.194

Table 4.6 The vacuum composition for typical high speed fall off data.

From the theoretical analysis (see Chapter 2) of the RDG it was seen that the analytical expression for the edge effect correction factor $\varepsilon(t/R)$ in equation 4.2 held only for

$$\mu = \frac{\omega\ t}{\bar{v}} \ll 1 \qquad (4.8)$$

where t is the sender-receiver separation, ω is the radian frequency of the sender and $\bar{v}$ is the mean thermal velocity. The fall off from linearity of deflection, which is measured by ν, increases as μ

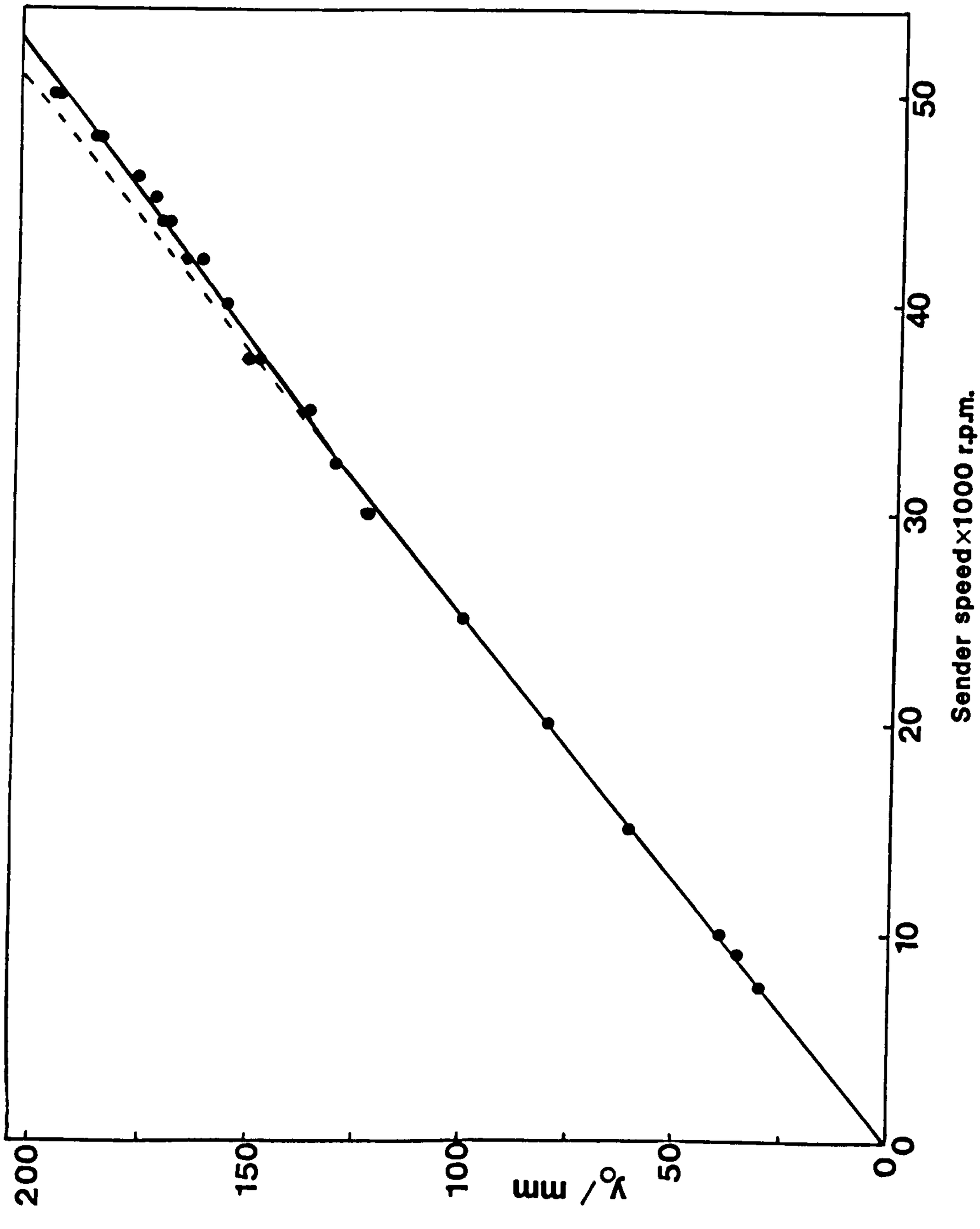

Figure 4.12 Deflection versus sender speed in nitrogen for a fixed disc-separation and a fixed pressure.

increases. Thus for a given gas species the fall off is anticipated to be greatest for the largest values of t. This is to be expected since the greater is the disc-separation the greater is the proportion of molecules which leave the sender with trajectories such that they miss the receiver. This is further discussed below.

From the options considered to be the reason for the high speed fall of and by consideration of the RDG's theory it can be seen that reason (ii) explains this phenomenon. That is at high speeds the bias velocity given by the sender to the gas molecules results in some of them moving out of the discs' interspace. The resultant loss of torque adds to the geometrical loss described earlier.

4.4.1 Effect of Disc-Separation on the High Speed Loss Effect

Table 4.7 shows values of ν for the fall off at 50 krpm in nitrogen for various disc-separations. The values were calculated from the mean of (typically) six deflections at a steady pressure. As expected it can be seen that there is a general trend for ν to decrease and hence for the fall off to increase as the separation increases. The results are not entirely conclusive since the relative change in separation is small and further experiments at larger disc-separations are needed.

Disc-separation t / mm	ν
4.3	0.95±0.01
4.7	0.96±0.05
4.8[1]	0.95±0.01
5.2[2]	0.92±0.01

Table 4.7 Values of the high speed fall off at various disc-separations.
[1]Rough silicon receiver surface used. [2]Titanium on silicon receiver surface used.

4.4.2 High Speed Fall Off Effect In Other Gases

In figures 4.13 and 4.14 data of deflection versus sender speed for helium gas are shown. Again there is a departure from linearity at high speeds for both the cases of different disc-separation and different pressures. The torsion constant of the fibre used was 1.470 ± 10^{-7} Nm.

Equation 4.8 indicates that μ is proportional to $1 / \bar{v}$ and therefore is proportional to $M^{1/2}$. This is because the mean molecular velocity decreases for higher mass molecules and thus the velocity bias of the sender is relatively more significant for them. It is therefore anticipated that the value of ν will decrease, and the fall off increase, as the molecular mass increases.

Table 4.8 shows the results of high speed fall off experiments in different gases. The value of ν is calculated for the fall off at 50 krpm. In each case the disc-separation was 4.3 mm, the torsion constant of the fibre used was 1.470×10^{-7} Nm and the temperature was constant at 19 °C. As expected the high speed fall off increases as the molecular mass of the residual gas increases.

Gas	Relative molecular mass	ν
Hydrogen	2	0.97±0.01
Helium	4	0.97±0.01
Nitrogen	28	0.95±0.01
Krypton	84	0.87±0.01

Table 4.8 The effect of increasing relative molecular mass on the magnitude of the high speed fall off.

4.4.3 Conclusions

The fall off of deflection from the linear dependence at sender speeds above 35 krpm has been observed and measured for the first time.

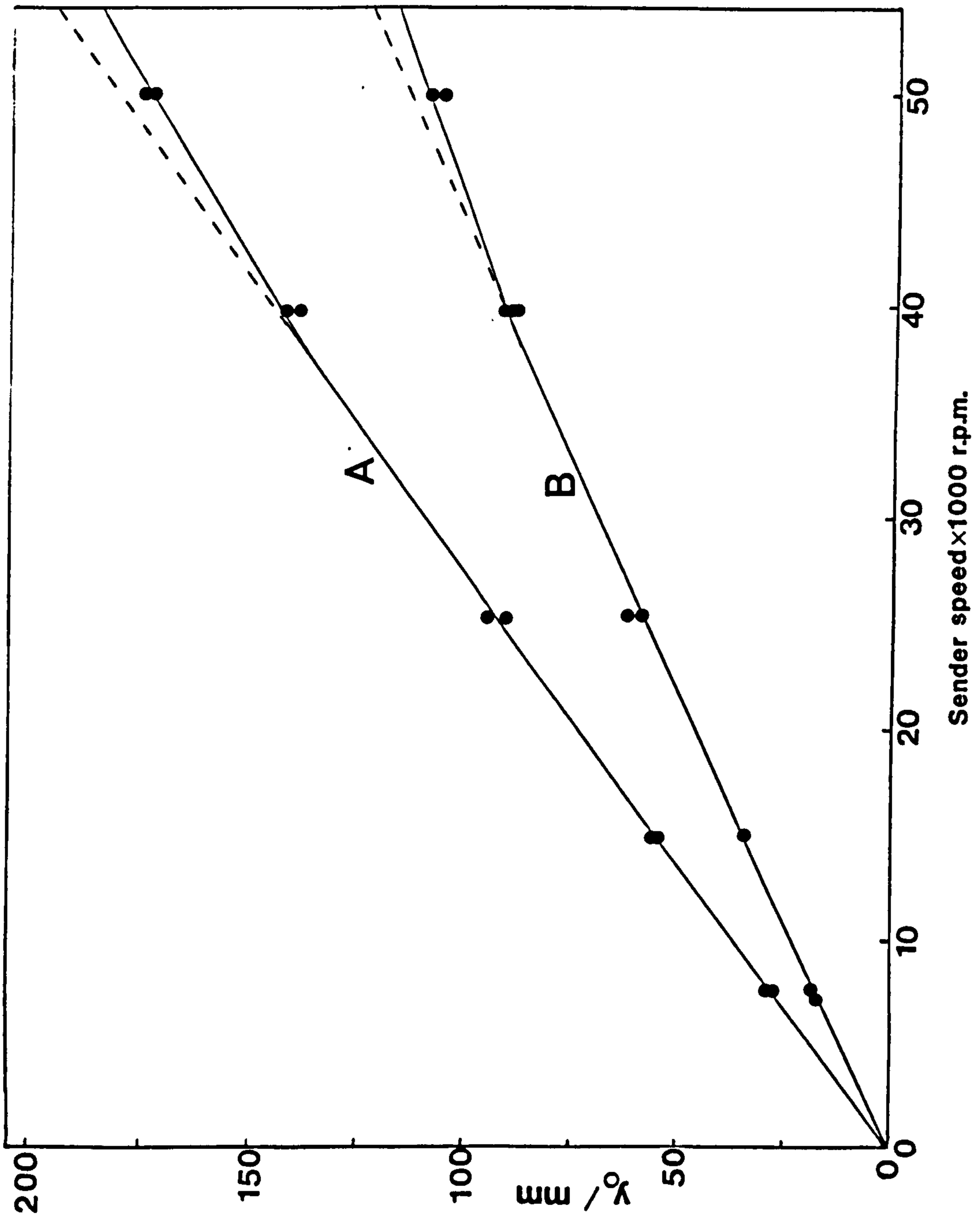

Figure 4.13 Deflection versus sender speed for helium at two set pressures. A 1.5×10^{-6} mbar and 9.9×10^{-7} mbar. Disc-separation = 4.3 mm.

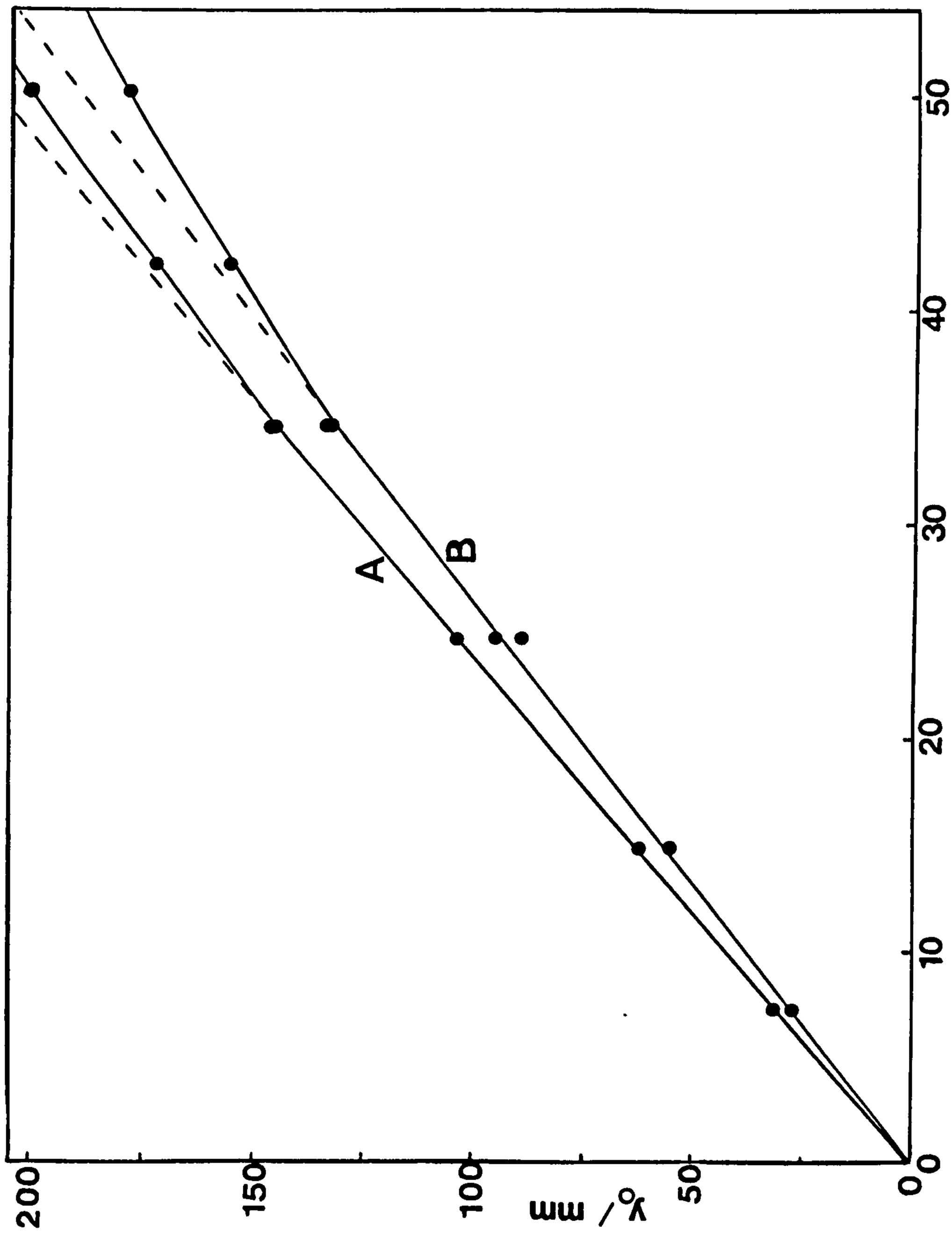

Figure 4.14 Deflection versus sender speed for helium at two set disc-separations. A 4.3 mm and B 7.1 mm. $P_{IG} = 1.7 \times 10^{-6}$ mbar.

It agrees with the theoretical prediction. The effect is due to the increased loss of molecules out of the discs' interspace from the forward motion of molecules due to the high velocity bias. The effect increases with increasing relative molecular mass in a way anticipated by theory. Further experiments at large disc-separations are needed which may necessitate changes to the apparatus.

This high speed loss effect has an important implication for pressure measurement using the RDG. Since this effect combines with the edge effect loss factor due to the Knudsen cosine distribution it must be fully accounted for in order for absolute measurements of pressure to be made using the RDG. Since the effect can only be evaluated empirically a maximum sender speed of 30 krpm was used so that the high speed effect was not present for any gas. For sender speeds at and below 30 krpm the analytically determined value of ε accounts for the edge effect loss of molecular torque and thus absolute pressure measurements can be made with the RDG.

It is also clear there will be a maximum in the deflection versus sender speed curve. Beyond this point there will be no longer an increase in deflection. Thus for the case where the high speed effect is accounted for the sensitivity of the RDG is not increased at speeds beyond this maximum point and nothing would be gained by operating at these speeds.

At the time of writing, work was in progress to calculate a universal analytical expression for the edge effect loss factor applicable for all sender speeds (Pert, 1993). Without an analytical determination of ε the RDG can not be considered to be an absolute gauge. This is further discussed in Chapter 5.

4.5 REPRODUCIBILITY OF MEASUREMENTS

In this section the results of experiments to establish the reproducibility of the measured deflections y_o are given.

Table 4.9 shows the data for an experiment performed with the pressure held constant and the vacuum composition measured in terms of the partial pressure of each gas relative to that of nitrogen r_i. The indicated IG pressure was 3.5×10^{-6} mbar, the sender speed was

30 krpm, a fibre of torsion constant 1.465×10^{-7} Nm was used, the temperature was 19 ± 1 °C and the disc-separation was 4.3 mm.

It can be seen that the measurements of deflection have a very small spread. This spread may be due to the change in the relative amount of hydrogen, the presence of which is due to ion pumping. The statistical uncertainty in the deflections was such that $\bar{y}_o$ = 119.1 ± 0.1 mm. The maximum deviation of 1.5 mm for the data when the r_i value of hydrogen had settled below 0.90 is particularly notable.

r_i							Deflection
H_2	He	CH_4	H_2O vapour	N_2	O_2	Ar	y_o / mm
1.58	0.03	0.02	0.03	1.00	0.01	0.09	118.5
1.40	0.03	0.02	0.03	1.00	0.01	0.09	119.75
1.32	0.03	0.01	0.03	1.00	0.01	0.09	119
1.18	0.02	0.01	0.02	1.00	0.01	0.09	120
1.03	0.02	0.01	0.03	1.00	0.02	0.10	120.75
0.98	0.02	0.01	0.03	1.00	0.01	0.10	121.75
0.94	0.02	0.01	0.03	1.00	0.01	0.10	119
0.87	0.02	0.01	0.02	1.00	0.01	0.09	119.25
0.86	0.02	0.01	0.02	1.00	0.01	0.09	119.75
0.86	0.02	0.01	0.02	1.00	0.01	0.09	118.75
0.86	0.02	0.01	0.02	1.00	0.01	0.09	118.5
0.82	0.02	0.01	0.02	1.00	0.01	0.09	118.25
0.81	0.02	0.01	0.02	1.00	0.01	0.09	119.5
0.83	0.02	0.01	0.03	1.00	0.01	0.09	118.5
0.84	0.02	0.01	0.03	1.00	0.01	0.09	118.25
0.80	0.02	0.01	0.03	1.00	0.01	0.09	118.75
0.80	0.02	0.01	0.03	1.00	0.01	0.09	118.75
0.81	0.02	0.01	0.03	1.00	0.01	0.09	118.75
0.80	0.02	0.01	0.03	1.00	0.01	0.09	118.75

Table 4.9 Measurements of deflection under constant conditions at a pressure of 3.5×10^{-6} mbar.

In table 4.10 data is given of the above experiment repeated at a pressure of 3.5×10^{-7} mbar at which the vacuum composition was highly constant. The measurements of deflection did not vary. This high reproducibility suggests that as long as the vacuum composition and other conditions are the same then there can be complete confidence placed in the measured values of the deflection.

r_i							Deflection
H_2	He	CH_4	H_2O vapour	N_2	O_2	Ar	y_o / mm
9.4	0.04	0.18	0.73	1.00	0.04	0.20	11.5
9.4	0.03	0.18	0.73	1.00	0.04	0.20	11.5
9.4	0.04	0.17	0.73	1.00	0.04	0.20	11.5
9.4	0.04	0.16	0.73	1.00	0.03	0.20	11.5
9.3	0.04	0.16	0.74	1.00	0.03	0.20	11.5
9.4	0.04	0.16	0.74	1.00	0.03	0.20	11.5
9.5	0.06	0.16	0.75	1.00	0.03	0.20	11.5
9.5	0.04	0.16	0.75	1.00	0.03	0.20	11.5
9.6	0.05	0.17	0.75	1.00	0.04	0.20	11.5
10.7	0.03	0.15	0.75	1.00	0.03	0.19	11.5
9.5	0.04	0.16	0.75	1.00	0.06	0.20	11.5
9.7	0.05	0.15	0.76	1.00	0.03	0.20	11.5
9.6	0.04	0.15	0.76	1.00	0.03	0.20	11.5
9.7	0.05	0.15	0.73	1.00	0.03	0.20	11.5
9.7	0.05	0.15	0.75	1.00	0.04	0.20	11.5
9.4	0.03	0.16	0.72	1.00	0.03	0.19	11.5
9.6	0.06	0.15	0.75	1.00	0.03	0.20	11.5
9.6	0.05	0.15	0.75	1.00	0.03	0.20	11.5

Table 4.10 Measurements of deflection under constant conditions at a pressure of 3.5×10^{-7} mbar.

4.6 CONCLUSIONS

The characteristics of an RDG with equal sized discs have been fully investigated and discussed for the first time. As anticipated by

theory the deflection produced is proportional to pressure. The edge effect loss of molecular torque has been measured and is in accord with the analytical expression for the loss. A fall off from linearity at high sender speeds has been seen for the first time and acts in a way predicted by theory. The sender speed should be kept at or below 30 krpm for the analytical expression for the edge effect loss factor ε in equation 4.2 to hold.

Under constant experimental conditions the deflection produced is highly reproducible. Taking full account of the characteristics of the RDG enables it to be used to measure pressure absolutely. Close agreement has been found between RDG and IG measurements of pressure. Reports of more complete comparisons of the RDG with other gauges follow.

CHAPTER 5

PRESSURE MEASUREMENT USING THE ROTATING DISC GAUGE

5.1 INTRODUCTION

In Chapter 4 it was seen that if the sender speed was kept at or below 30 krpm then the analytical expression for the edge effect loss factor ε below could be used:

$$\varepsilon = \left[\left[1 + \left(\frac{t}{2R} \right)^2 \right]^{1/2} - \frac{t}{2R} \right]^4 \qquad (5.1)$$

where t is the disc-separation and R = 46 mm is the discs' radius.

Thus the only unknown in the operating equation of the rotating disc gauge (RDG) below is σ_{RDG}, the tangential momentum accommodation coefficient of a gas on the receiver surface.

$$P_{RDG} = \frac{\frac{c}{2L}}{\varepsilon\, \sigma_{RDG}\, \omega\, R^4 \left(\frac{\pi}{8000\, R_o} \right)^{1/2}} \cdot \frac{T^{1/2}}{M^{1/2}} \cdot y_o \qquad (5.2)$$

In this equation c is the torsion constant of the fibre, L is the mirror-scale distance = 1088 mm, R_o is the gas constant, T is the absolute temperature, M is the relative molecular mass, ω is the radian frequency of the sender and y_o is the measured deflection.

In this chapter the results of an experimental comparison of the RDG with a spinning rotor gauge (SRG), performed to evaluate σ_{RDG}, are given. The uncertainties in RDG pressure measurements and the operating range and ultimate sensitivity of the RDG are then discussed.

5.2 ROTATING DISC GAUGE COMPARISON WITH A SPINNING ROTOR GAUGE

The SRG described in Chapter 3 which had recently been calibrated at the National Physical laboratory (NPL) was used as a transfer standard to compare and evaluate RDG pressure measurements (P_{RDG}). The results

of this experiment using the SRG to measure pressure simultaneously with the RDG may be regarded as a determination of σ_{RDG} for the conditions of the experiment.

5.2.1 Experimental

The fibre used had a torsion constant c = 1.465×10^{-7} Nm and a sender speed of 30 krpm, within the linear region, was used. The smooth silicon receiver surface was used. The characteristic curves of deflection versus pressure, disc-separation and sender speed for this fibre were reported in Chapter 4.

Measurements of pressure were made at a constant disc-separation of 4.3 mm. At this separation the value of ε was originally determined (see Chambers, Chew and Troup 1992a) from the quadratic least squares fits (LSF) to the curves in figure 4.7. The value was $\varepsilon = 0.84 \pm 0.02$. The value of ε determined from the above analytical expression is 0.83.

The pressure was raised into the experimental range of $1\text{-}10 \times 10^{-6}$ mbar by nitrogen. The temperature was 23 °C. Inserting the above values into the operating equation 5.2 of the RDG gives

$$P_{RDG} = 2.69 \times 10^{-8} \cdot \frac{y_o}{\sigma_{RDG}} \quad \text{mbar} \qquad (5.3)$$

using $\varepsilon = 0.84$ as was done originally. Using the analytical value of $\varepsilon = 0.83$ and the tachometer measured value of the sender speed (see Chapter 3) of 30.04 ± 0.03 krpm gives

$$P_{RDG} = 2.72 \times 10^{-8} \cdot \frac{y_o}{\sigma_{RDG}} \quad \text{mbar} \qquad (5.4)$$

The associated uncertainties in the above equations are discussed in due course.

5.2.2 Results and Discussion

Table 5.1 shows the measured deflections y_o determined at various pressures where each pressure is measured on both the SRG (P_{SRG}) and the hot cathode ionization gauge (IG). In figure 5.1 P_{SRG} is plotted against the indicated IG pressure (P_{IG}). The linearity of the least

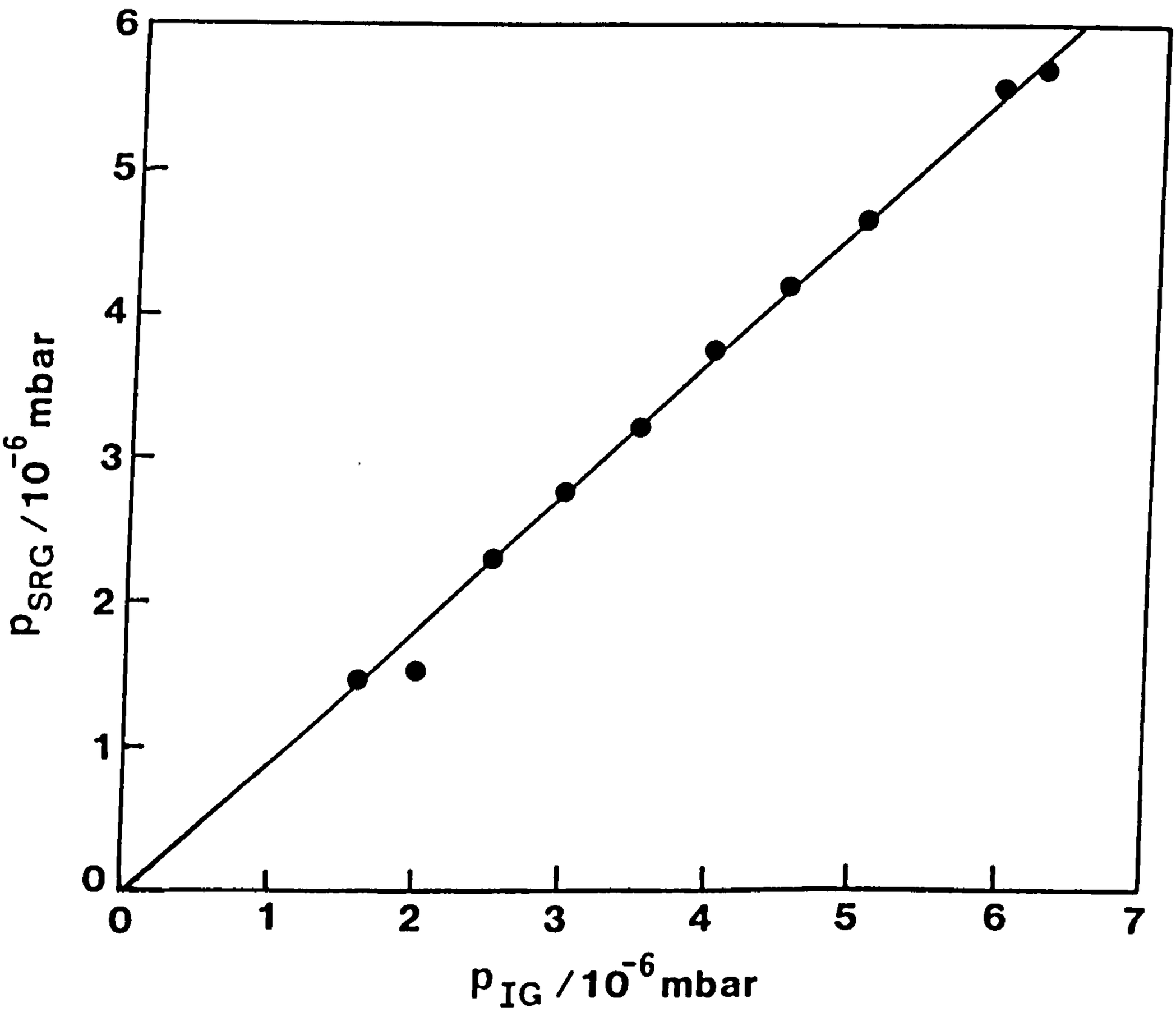

Figure 5.1 P_{SRG} versus P_{IG}.

squares fit (LSF) to the data is to be noted as is the fact that the plot passes exactly through the origin. Since it is reasonable to assume that the IG gives a reading proportional with pressure then this plot suggests that the SRG was working correctly and that the SRG offset value (2.19×10^{-5} mbar) measured at base pressure was correct. An incorrect offset would have resulted in a displacement of the plot parallel to itself.

In order to compare the pressure indications of the RDG and the SRG it was assumed that σ_{RDG} was unity. The P_{RDG} values for both means of the determination of ε is given in table 5.1 below.

Run number	P_{IG} $\times 10^{-6}$ mbar	P_{SRG} $\times 10^{-6}$ mbar	y_o mm	P^1_{RDG} $\times 10^{-6}$ mbar	P^2_{RDG} $\times 10^{-6}$ mbar
1[3]	6.2	5.66	210.25	5.67	5.72
2[4]	5.0	4.62	171.75	4.63	4.67
3	4.0	3.72	135.75	3.66	3.69
4	3.0	2.74	100.75	2.72	2.74
5[5]	2.0	1.51	65.75	1.77	1.79
6	1.6	1.45	53.5	1.44	1.46
7	2.5	2.26	83.0	2.24	2.26
8	3.5	3.19	118.5	3.19	3.23
9	4.5	4.18	152.0	4.10	4.14
10	5.0	4.61	170.0	4.58	4.63
11	5.9	5.53	196.25	5.29	5.34
12[6]	0.98	-	32.25	0.87	0.88
13	0.88	-	29.25	0.79	0.80
14	0.75	-	25.0	0.67	0.68

Table 5.1 Data of simultaneous RDG, SRG and IG pressure measurements. [1]Experimental value of ε used. [2]Analytical value of ε used. [3]Isolated measurement. [4]Onward sequence taken chronologically in one run. [5]SRG temporarily disturbed. [6]Outside recommended range of SRG.

The close agreement of the P_{RDG} values with those of P_{SRG} is to be noted. This is most strikingly illustrated in figures 5.2 and 5.3

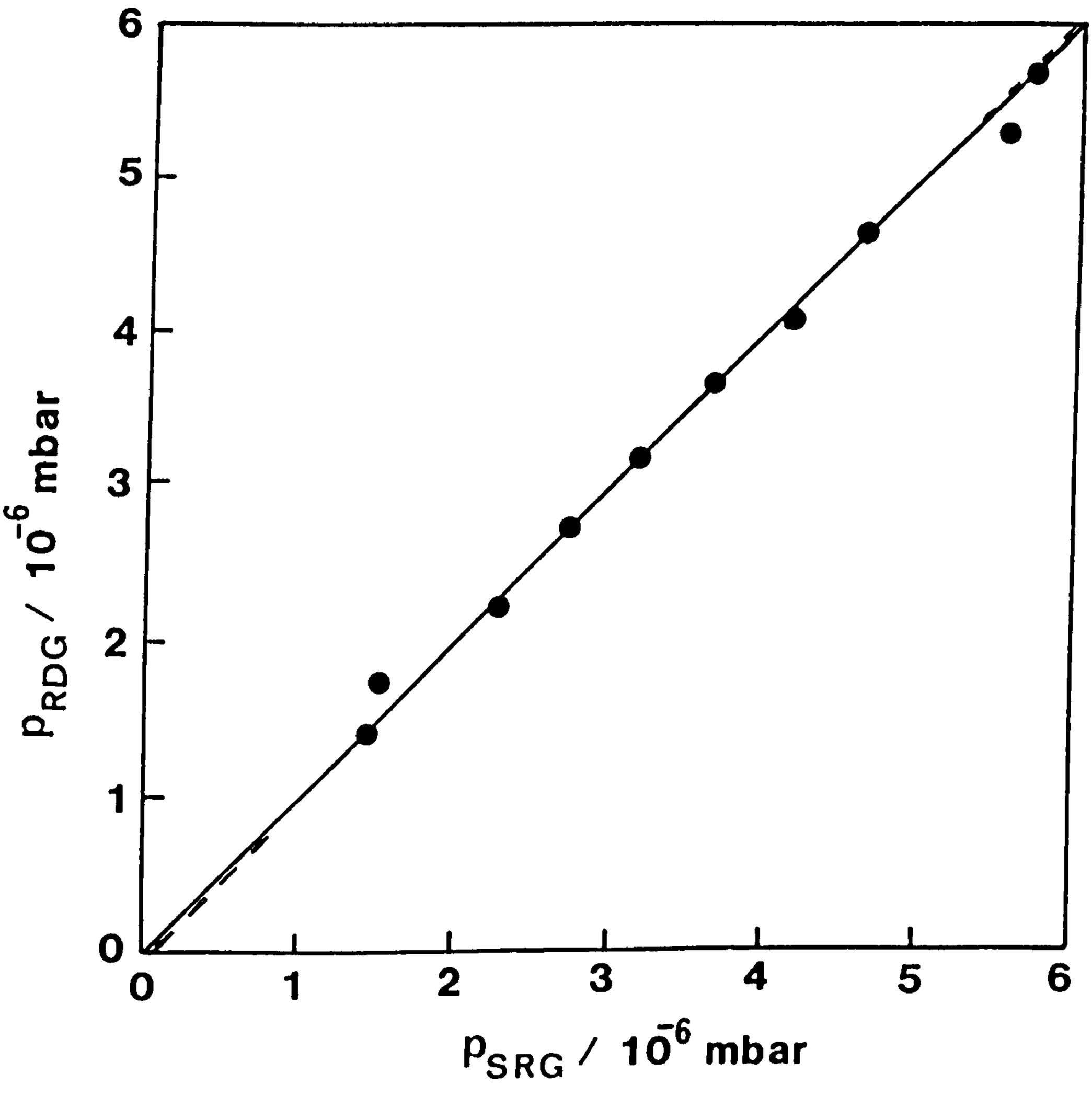

Figure 5.2 P_{RDG} versus P_{SRG} for the experimentally determined value of ε. The full line is $P_{RDG} = P_{SRG}$ and the dashed line is a least squares fit to the data.

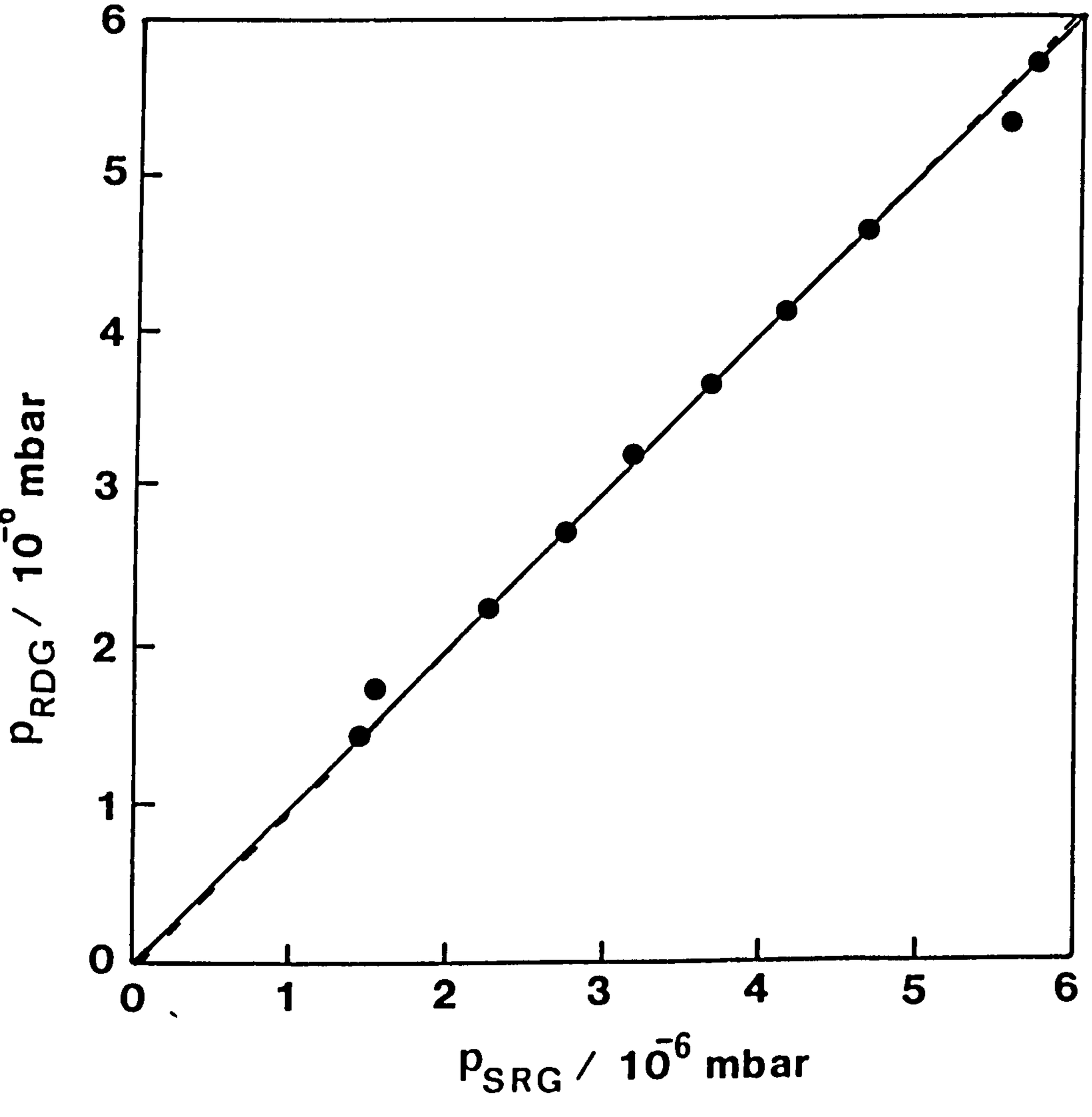

Figure 5.3 P_{RDG} versus P_{SRG} for the analytically determined value of ε. The full line is $P_{RDG} = P_{SRG}$ and the dashed line is a least squares fit to the data.

where plots of P_{RDG} versus P_{SRG} for the experimental and analytical determinations of ε are shown respectively. Complete agreement would mean that all the points would lie on the full line of $P_{RDG} = P_{SRG}$. The results of a LSF to the data are indicated by the dashed lines. The gradients of the lines from the LSF program are 1.00 ± 0.01 for figure 5.2 and 1.01 ± 0.01 for figure 5.3. These results show the high agreement between P_{RDG} and P_{SRG} data. The uncertainties are from the uncertainty of the LSF to the data. Even for this limited data set the fits give a gradient of unity and hence suggest a value of σ_{RDG} of unity.

It should be noted that the gas composition changes with pressure, nitrogen becomingly increasingly dominant at higher pressures. Corrections to the IG, SRG and RDG pressure measurements accounting for the spectrum of gases are shown in table 5.2 using the method described in Chapter 4 and the IG sensitivity factors of Leck (1989).

Corrected values		
P_{IG} $\times 10^{-6}$ mbar	P_{SRG} $\times 10^{-6}$ mbar	P_{RDG} $\times 10^{-6}$ mbar
6.8	7.34	7.44
5.3	5.77	5.73
3.9	4.11	4.12
2.6	2.32	2.75
2.3	2.46	2.47
3.3	3.56	3.55
4.5	4.73	4.78
5.7	6.05	6.00
6.4	6.55	6.57
7.5	7.92	7.64
1.3	-	1.36
1.2	-	1.32
1.1	-	1.21

Table 5.2 RDG, SRG and IG pressure values corrected for vacuum composition.

It can be seen from the operating equations 5.2 and 5.5 of the RDG and SRG respectively that the correction for vacuum composition is the same in both cases of the SRG and the RDG. This is because the dependence on molecular mass and temperature is the same for both the SRG and the RDG i.e. P_{RDG} and P_{SRG} are both proportional to $T^{1/2} / M^{1/2}$.

$$P_{SRG} = \frac{r\ \rho}{5\ \sigma_{SRG}} \left(\frac{2000\ \pi\ R_o\ T}{M} \right)^{1/2} \left(\frac{\dot{\omega}}{\omega} \right) - P_{RD} \qquad (5.5)$$

Since the SRG and the RDG were sensing the same gas and were at the same temperature no useful purpose in terms of a comparison between them is served by correcting for vacuum composition. However to make this correction the σ_{SRG} values of the constituent gases need to be known. These vary from the value of nitrogen by about 2%. This is fully discussed in Chapter 6.

5.2.3 Conclusions

The results show that the value of the tangential momentum accommodation coefficient σ for this particular combination of gases on the smooth silicon receiver surface in the $1\text{-}10 \times 10^{-6}$ mbar range is unity. This is to be expected from the work of Thomas (1981) and others (see Chapter 1) who concluded that for a smooth, highly ordered, flat and adsorbate covered surface (such as the one used in the above experiment) the value of σ is unity for all gases. Therefore based on the comparison with the SRG the RDG may be considered over at least the pressure range investigated for the particular vacuum composition as an *absolute* vacuum gauge whose operating equation 5.4 with $\sigma_{RDG} = 1$ becomes

$$P_{RDG} = 2.72 \times 10^{-8}\ y_o \text{ mbar} \qquad (5.6)$$

The results of further experiments in highly pure residual gas atmospheres to investigate the value of σ_{RDG} for a range of gases are discussed in Chapter 6.

5.3 UNCERTAINTIES IN ROTATING DISC GAUGE MEASUREMENTS

In this section the uncertainty in the RDG measurements of pressure are discussed. The systematic uncertainties associated with the values in equation 5.2 are evaluated and the other uncertainties associated with the RDG are then discussed.

5.3.1 Uncertainties From the Rotating Disc Gauge Operating Equation

From a standard uncertainty analysis (Squires, 1985) the uncertainty for the RDG's operating equation for a spectrum of gases is given below where r_i is the amount of a gas relative to that of nitrogen.

$$\Delta P_{RDG} = P_{RDG} \left[\left(\frac{\Delta c}{c} \right)^2 + \left(\frac{\Delta L}{L} \right)^2 + \left(\frac{8\Delta R}{R} \right)^2 + \left(\frac{\Delta f}{f} \right)^2 + \left(\frac{\Delta \varepsilon}{\varepsilon} \right)^2 + \left(\frac{\Delta \sigma_{RDG}}{\sigma_{RDG}} \right)^2 + \left(\frac{\Delta T}{2T} \right)^2 + \left(\frac{\Delta y_o}{y_o} \right)^2 + \left(\frac{\Delta \sum r_i}{\sum r_i} \right)^2 + \left(\frac{\Delta \sum M_i^{1/2} . r_i}{\sum M_i^{1/2} . r_i} \right)^2 \right]^{1/2} \quad (5.7)$$

The uncertainty Δc in the torsion constant c of the fibre arises from its calibration, see Chapter 3. For the fibre used in the last experiment the value of $c = 1.465 \pm 0.003 \times 10^{-7}$ Nm. This fibre was later adjusted slightly and calibrated many times and the value of $c = 1.470 \pm 0.001 \times 10^{-7}$ Nm.

The uncertainty in the mirror-scale distance L was ± 1 mm in 1088 mm. This uncertainty was kept small by careful alignment of the scale so that it was at the same height as the mirror and parallel to it. Also the radius of curvature of the scale was measured accurately to be 1088 mm and the scale was located carefully to be at this distance from the mirror on the receiver.

The uncertainty in the discs' radius R is a result of the precision of the grinding process and $R = 46.00 \pm 0.02$ mm. The uncertainty in the sender frequency was ± 0.1 krpm of the indicated speed setting. Tachometer measurements of the speed confirmed that the speed was correct and that the variation from the set speed and consequent

uncertainty was very small. For a set speed of 30 krpm the measured frequency was 500.6 ± 0.5 Hz.

The limit of measurement of temperature was such that $\Delta T = \pm 0.1$ K. During the course of any one experiment the temperature changed at most by ± 2 K and more typically by less than 1 K. The maximum uncertainty in the temperature which was measured for each deflection was ± 1 K.

The deflections y_o were measured with a maximum uncertainty of ± 1 mm. The spot size was of diameter 1 mm on a 1 mm graduated scale. This, combined with the fact that the suspension had a long period of oscillation (about 50 seconds), meant that the deflection y_o was measured with a maximum uncertainty of ± 1 mm. As the deflection became smaller this uncertainty became more significant. The range of uncertainties in y_o in the data of table 5.1 is y_o = 25.0 mm ± 4% to 210.25 mm ± 0.5%. In general the minimum deflections measured were 2 mm to 3 mm for which the value of Δy_o is 50% to 33%.

The uncertainty in ε (equation 5.1) where a typical disc-separation is t = 4.3 ± 0.4 mm is evaluated from the equation below (Squires, 1985)

$$\Delta\varepsilon = \left[\left(\frac{\delta\varepsilon}{\delta t} \Delta t \right)^2 + \left(\frac{\delta\varepsilon}{\delta R} \Delta R \right)^2 \right]^{1/2} \qquad (5.8)$$

For t = 4.3 mm the analytically determined value of ε = 0.83 ± 0.01.

For a receiver surface where σ_{RDG} is unity its associated uncertainty is zero. The uncertainty in determining the correction for the vacuum composition which appears as the last two terms in equation 5.7 is complex and depends on an unknown uncertainty in the quantitative data of the residual gas analyser. For cases where there is a single gas these last two terms become zero.

Inserting the above uncertainties and the values of their related quantities into equation 5.2 gives uncertainties in P_{RDG} as shown in table 5.3. The uncertainties are calculated for both the cases of ε determined empirically and then analytically, the latter incorporating the tachometer measured value of the sender speed.

Deflection / mm	$\pm\Delta P_{RDG}$ / %	
	$\varepsilon_{empirical}$	$\varepsilon_{analytical}$
10	10.3	10.2
100	2.7	2.1
200	2.5	1.9

Table 5.3 Uncertainties in RDG pressure measurements for various deflections.

It is clear that as the magnitude of the deflection decreases then its associated uncertainty becomes more significant. For the analytically determined value of ε the more accurately determined value of the torsion constant of the fibre gives uncertainties in the value of P_{RDG} for deflections of 200, 100, 10 and 5 mm, of ±1.8, ±2.0, ±10.2 and ±20.1 % respectively. In Chapter 4 it was seen that the deflections were highly reproducible.

The main contribution at large deflections stems from the uncertainty in ε which itself comes mainly from the uncertainty in the value of the disc-separation. It can be seen though that the uncertainty (from the RDG's operating equation) in P_{RDG} is < ±2% for a large deflection if a single gas is used. This is to be compared with the uncertainty in SRG measurements which is usually quoted as ±5% or below (Leck, 1989), see Chapter 1.

5.3.2 Additional Uncertainties

It is important to identify and evaluate systematic and random uncertainties in the measurement of P_{RDG} which are not included in the uncertainties associated with the quantities in the RDG's operating equation 5.2 discussed above.

In Chapter 3 it was recognised that the mass of the standard inertia pieces were not exactly equal to the mass of the receiver suspension. This means that there is a difference in the value of the extension of the fibre produced by the inertia pieces and the suspensions. Since

the torsion constant c is inversely proportional to the length l of the fibre then the value of c will be affected by this. For the 46 mm radius disc receiver suspension the relative change in the length of the fibre and hence in the value of c due to this effect is 1.0001 i.e. this introduces an uncertainty of ±0.01%

The affect of a change in temperature ΔT from the room temperature at which the fibre was calibrated will act to cause an extension or contraction of the fibre according to its coefficient of linear expansion α where

$$l = l_o(1 + \alpha\Delta T) \qquad (5.9)$$

l_o being the original length. The maximum value of ΔT was 4 K and α for the phosphor-bronze fibre is 1.7×10^{-5} K^{-1} (Kaye and Laby, 1992). The relative change in the length of the fibre is 1.00007 and thus this effect is negligible. The constant of the fibre, checked by repeated measurements of the period of the suspension, was highly determined.

Although the scale and mirror were very well aligned it was possible that the spot of light on the mirror was up to 4 mm from its centre. The maximum change, and hence uncertainty, in the mirror-scale distance due to this was less than ±0.04%.

The receiver suspension damping system described in Chapter 3 enabled the suspension to be made quiescent before the shutter was withdrawn. When the system was turbomolecular pumped vibrations from the high speed rotor and the pump meant that the suspension would sometimes swing. This was quantified by measuring the vertical motion of the light spot on the scale The maximum peak-to-peak vertical amplitude on the scale was 1 mm. This meant that the maximum displacement of the edge of the 46 mm radius receiver disc was 0.02 mm which is negligible compared to the uncertainty in the discs' separation.

At sender speeds below 40 krpm there was no bending of the shaft of the sender described in Chapter 3. The discs were repeatedly measured to be parallel to a high degree certainly better than 0.1 mm in 24 mm. It is difficult to quantify the uncertainty introduced by this effect. It is though likely to be small because symmetries produce

compensating effects and because the nonparallelism is small compared to the uncertainty in the separation of the discs.

The discs were measured to be coaxial to better than 0.1 mm Again symmetries would produce compensating effects to make the uncertainty of the non-coaxiality small.

In Chapter 3 it was seen that the edges of the receiver discs were slightly chipped due to the grinding process. Since these chips were uniform over the circumference no unbalancing problem resulted. The chips had the effect of increasing the local value of the tangential momentum accommodation coefficient typically by 2% (Fremerey, 1982) for such a degree of roughening. Since the area of the wafer that was chipped was very small the effect of these chips would be negligible. This was confirmed by the unity value of σ_{RDG} found for this surface from the RDG/SRG experiment described above.

At the centre of the sender disc was an indentation of 1 mm diameter. This caused a negligible ($< 10^{-6}$%) uncertainty in the analytically determined value of the molecular torque developed by the sender.

At low pressures the frictional heating of the high speed sender due to molecular impacts will be negligible. Additionally the heating of the small amount of lubricating oil at the base of the shaft would not cause any heating effects. As a result radiometric effects (Beavitt et.al., 1968) due to a temperature difference between the surfaces of the two discs were not present.

The shutter shielding the two discs could be withdrawn in less than 0.5 seconds. Since the period of the suspension was about 50 seconds then there was an almost perfect step function of torque developed.

Random vibrations such as those due to knocking the chamber caused the suspension to become disturbed. Such occurrences were easily noted by the change in the behaviour of the reflected light spot on the scale. It is interesting to note that the RDG was much less affected by such disturbances than the SRG. After such a disturbance the offset of the SRG needed recalibrating whereas no such problems were caused in the RDG.

Vibrational noise at frequencies near that of the SRG's operating frequency (about 400 Hz) would sometimes cause the SRG to be inoperable whereas the RDG was unaffected.

The effects of thermal motion can be determined by considering the receiver suspension as a classical suspension. From the equipartition theorem

$$\frac{1}{2} c \overline{\phi^2} = \frac{1}{2} k T \qquad (5.10)$$

where c is the torsion constant of the fibre, $\overline{\phi^2}$ is the mean square angular deflection of the receiver, k is the Boltzmann constant and T is the thermodynamic temperature.

This gives an equivalent nitrogen pressure for the values given earlier of 1×10^{-11} mbar.

In Chapter 1 it was seen that the limiting effect in the RDG made by Dushman (1915) was due to a torque produced by induced eddy currents in the suspension from the rotating magnetic field associated with the high speed sender. In the RDG constructed here this effect was negligible since the receiver suspension was dominantly not a conductor, the field from the sender was small and the rotor was at a large distance from the receiver. At base pressure where the molecular torque developed was negligible no deflection of the receiver was recorded indicating that no induced current effects were present.

In the theoretical derivation of the RDG's operating equation the gas number density was assumed to be the same in the discs' interspace as that outside it. The results in Chapter 4 showed this to be the case.

The assumption that the gas in the vacuum was ideal was made. For the experimental conditions of the RDG i.e. a large volume and low pressures then the equation of state of a real gas reduces to the equation of state of an ideal gas, see Roberts and Miller (1960).

Molecule-molecule collisions were ignored which is valid for the RDG at pressures below 10^{-3} mbar. At very low pressures where the molecular damping of the receiver was negligible the decrement of its

deflection was negligible over long time periods. This confirmed that damping effects from the point at which the fibre was held by the vice and the internal friction of the fibre were negligible.

5.3.3 Conclusions

The contribution to the uncertainty in a single P_{RDG} measurement from the additional uncertainties described above are small and for a deflection of 250 mm (at 1×10^{-5} mbar) the uncertainty in an RDG pressure measurement is below ±3%. The uncertainty in the deflection becomes increasingly dominant as the value of the measured deflection decreases.

5.4 RANGE OF ROTATING DISC GAUGE MEASUREMENTS

The measuring range and the ultimate sensitivity of the RDG is now discussed. With the equal sized discs configuration and the fibre of torsion constant 1.470×10^{-7} Nm it can be seen from equation 5.2 that for nitrogen with a disc-separation of 4.3 mm the expected deflection at 1×10^{-6} mbar and a sender speed of 30 krpm is 37 mm.

It is useful to establish the pressure P_{10} for which there is a deflection of 10 mm. For the conditions detailed above the value of P_{10} for nitrogen is 2.7×10^{-7} mbar. In Chapter 4 it was seen that the deflections did not deviate from the straight line plot versus pressure in the low 10^{-7} mbar range. It was also seen that by fully allowing for the small fall off of deflection at the highest sender speed the sensitivity of the RDG could be increased by approximately 70% by running the rotor at full speed (51 krpm). Thus the value of P_{10} would then be $\cong 1.6 \times 10^{-7}$ mbar. By careful repeated measurements the reproducibility data of Chapter 4 indicates that the suspension in its present form should enable measurements of 1×10^{-7} mbar with an uncertainty of ±11%.

By reducing the sender speed to its minimum (7.1 krpm), increasing the disc-separation such that $\varepsilon \cong 0.5$ and measuring the maximum deflection of 250 mm a pressure of 5×10^{-5} mbar could be measured. To measure pressures in the upper limit for which the RDG's theory holds, i.e. 1×10^{-3} mbar, a less sensitive fibre could be used with the present receiver suspension configuration. Measurements of pressure in this

upper pressure limit would need relatively trivial modifications to the RDG and are not discussed further.

It can be seen from equation 5.2 that the sensitivity of the RDG increases as the torsion constant of the suspension's fibre decreases. The fibre is limited by having to be strong enough to hold the mass of the suspension. In Chapter 3 it was seen that the torsion constant of the fibre is proportional to the shear modulus of its material and inversely proportional to its length. It can be seen from Condon and Odishaw (1967) that phosphor-bronze is a very good material providing one of the highest tensile strength : shear modulus ratios of all readily accessible materials.

Using a modified receiver such as the one used by Beavitt et.al. (1968) in their radiometer gauge it should be possible to reduce the total mass of the suspension by a factor of 10 to below 3 grammes. With the present built-in safety factor for the fibre this would enable a torsion fibre with a torsional rigidity of 1/10th of the present value to be used. These are readily available commercially (Cam Metric, 1990). The maximum length of the fibre is about twice its present (262.25 mm) length. These changes would therefore reduce the value of the torsion constant and hence the value of P_{10} by a factor of 20. The mirror-scale distance could be increased by a factor of 2.5. The minimum safe disc-separation is 3 mm for which $\varepsilon = 0.88$ which represents only a small decrease in lost torque relative to that at a separation of 4.3 mm.

A highly roughened disc could increase the tangential momentum accommodation coefficient to its maximum value of $4/\pi$, see Chapter 1. For a rough receiver surface the gauge would then need calibrating for each gas.

These changes described would give a total increase in the RDG sensitivity of $20 \times 2.5 \times 0.88/0.83 \times 4/\pi = 67.5$. Hence the value of P_{10} using a speed of 51 krpm would be $\cong 2 \times 10^{-9}$ mbar. It is likely that a more sophisticated damping system, such as the eddy current damping system of Beavitt et.al. (1968), would be needed to cancel the effects of vibrations on the more sensitive fibre.

Thus for a design used in the manner previously described careful procedures should allow measurements of pressure in the 10^{-9} mbar range for nitrogen.

These changes would mean that the period of the suspension would increase by a factor of about $2^{1/2}$ to 70 seconds. This is the maximum practicable measurement time. The period would increase and become impracticable if a more sensitive configuration was used.

5.4.1 Conclusions

With the present suspension the lower limit of pressure measurement is of the order of 1×10^{-7} mbar with a ±11% uncertainty, at 10^{-8} mbar the uncertainty would be ±100%. A change to a less sensitive fibre would enable measurements at the upper pressure limit of the RDG i.e. 10^{-3} mbar with a small uncertainty of below ±3%.

With modifications to the present RDG apparatus a lower pressure measurement limit of 2×10^{-9} mbar should be possible.

5.5 GENERAL CONCLUSIONS

The experimental data and uncertainty analysis in this chapter suggests that the RDG can be used as an absolute gauge in its present form. The measured value of the tangential momentum accommodation coefficient for a vacuum of dominantly nitrogen gas was unity on the highly ordered, smooth, flat and adsorbate covered receiver surface.

The uncertainty analysis indicates a best uncertainty of about ±3% in a single RDG measurement of 1×10^{-5} mbar. The lower limit of the RDG in its present form is about 1×10^{-7} mbar. Changes should enable pressure measurements in the 10^{-9} mbar range. Langmuir (1913) suggested a lower limit for the RDG of 10^{-7} mbar and Roth (1976) one of 10^{-9} mbar.

CHAPTER 6

ROTATING DISC GAUGE PERFORMANCE IN VARIOUS GAS ATMOSPHERES

6.1 INTRODUCTION

In this chapter the results are presented of experimental comparisons of the rotating disc gauge (RDG) with a spinning rotor gauge (SRG). The comparisons were made in pure gas atmospheres of hydrogen, helium, methane, water vapour, nitrogen, air, carbon dioxide and krypton to determine the values of the tangential momentum accommodation coefficients of these gases on the smooth silicon receiver surface used in Chapters 4 and 5. The sensitivity of the RDG, predicted in Chapter 2, for different gases was also tested which had not been done before. The universality of application of the RDG for different gases was assessed from the results of these experiments.

RDG and SRG comparisons were also made with a rough silicon receiver surface and a receiver surface of titanium grown on silicon. From these experiments the values of the tangential momentum accommodation coefficients of hydrogen, helium, water vapour, nitrogen and air on these surfaces were determined.

Simultaneous comparisons were made in these gases with the ionization gauge (IG) used previously and the relative sensitivity factors of the IG were deduced.

6.2 EXPERIMENTAL

The experimental configuration was exactly the same as that described in Chapter 5 except a fibre with a torsion constant of $1.470 \pm 0.001 \times 10^{-7}$ Nm was used. Three different receiver surfaces were used:

(i) The smooth silicon receiver surface used in Chapters 4 and 5, and described in Chapter 3 was used first. A single operating disc-separation of 4.3 mm was used for which the edge effect loss factor $\varepsilon = 0.83 \pm 0.01$.

(ii) The reverse rough side of a silicon disc was used at a fixed disc-separation of 4.8 mm for which $\varepsilon = 0.81 \pm 0.01$.

(iii) Finally a receiver surface of titanium grown on silicon was used at a fixed disc-separation of 5.2 mm for which $\varepsilon = 0.80 \pm 0.01$.

The lowest operable sender speed was used which was 7.5 krpm as indicated on the high speed rotor controller. Because of rotor drive slippage at low speeds (see Chapter 3) the sender speed was measured independently. The rotor could not be run-in properly to make tachometer measurements at low speeds. Therefore the speed was measured by taking many measurements of deflection at the nominal speed of 7.5 krpm and compared to those taken under otherwise constant conditions at 30 krpm for which the tachometer measured speed was reliable. The average indicated sender speed was measured as a frequency of 118.4 ± 1.4 Hz.

For the smooth silicon receiver surface with those parameters detailed above, and in Chapter 5, at a temperature of 293 K the working equation of the RDG becomes

$$P_{RDG} = 6.1 \times 10^{-7} \frac{y_o}{\sigma_{RDG} M^{1/2}} \text{ mbar} \qquad (6.1)$$

where M is the relative molecular mass, y_o is the deflection and σ_{RDG} is the tangential momentum accommodation coefficient of a gas on the receiver surface.

Rearranging the above enables an RDG sensitivity y_o / P to be defined viz

$$\frac{y_o}{P} = \frac{10^7}{6.1} \sigma_{RDG} M^{1/2} \qquad (6.2)$$

In the experiments reported here the sensitivities have been measured using the gases listed earlier with the pressure P measured by an SRG, and equation 6.2 tested.

6.3 PROCEDURE

The same SRG used in Chapter 5 was used again as a reference pressure standard. Its operating equation is

$$P_{SRG} = \frac{r\rho}{5\sigma_{SRG}} \left[\frac{2000\ \pi\ R_o T}{M} \right]^{1/2} \frac{\dot{\omega}}{\omega} - P_{RD} \qquad (6.3)$$

where r is the radius and ρ the density of the levitated stainless steel ball, $\dot{\omega} / \omega$ is the relative deceleration rate and P_{RD} is the residual drag offset. The value of the effective tangential momentum accommodation coefficient of the rotor σ_{SRG} was calibrated by the National Physical Laboratory (1990) to be 1.024 for nitrogen, see Chapter 3. It was not calibrated for other gases. Other workers have shown that for a range of gases the value of σ_{SRG} varies typically by ± 2% from its value for nitrogen (Comsa et.al, 1980 and Comsa et.al., 1981).

The SRG was run for more than 5 hours to ensure its stability and the residual drag was measured at base pressure. The pressure was then raised by introducing a single gas via the fine-leak valve.

Simultaneous measurements of pressure were made with the RDG and the SRG at typically 8 to 10 stable pressures in the range 0.5 to 5×10^{-5} mbar. The IG described earlier was used to monitor the stability of the vacuum.

The following gases were investigated for the smooth silicon receiver surface: hydrogen, helium, methane, water vapour, nitrogen, air, carbon dioxide and krypton whereas hydrogen, helium, water vapour, nitrogen and air were investigated for the other two surfaces. These gases provided an investigative range of relative molecular mass from 2 to 84. The experiments for nitrogen were performed repeatedly between those for other gases to ensure the same conditions before each new gas was introduced.

6.4 RESULTS AND DISCUSSION

A typical data set for one of the experiments in nitrogen using the smooth silicon receiver surface at 19 °C and assuming that σ_{RDG} is unity is shown in table 6.1 and displayed graphically in figure 6.1. The full line of the plot of P_{RDG} versus P_{SRG} is the result of a least squares fit (LSF) to the data. In this case the gradient was 1.00 and the associated uncertainty is discussed below. The small spread of

the points and the intercept at the origin is to be noted. This reflects the stability of the experimental conditions.

By inspecting equations 6.1 and 6.3 it can be seen that since the gas type is known the only unknown quantity is σ_{RDG}. In plotting P_{RDG} versus P_{SRG} a gradient of unity indicates complete agreement of the RDG and the SRG values and hence complete accommodation of tangential momentum on the receiver surface i.e. $\sigma_{RDG} = 1.0$. The LSF program was used to determine the gradients and hence the σ_{RDG} values of the plots of P_{RDG} versus P_{SRG} data. Values of σ_{RDG} below unity indicate incomplete accommodation of tangential momentum, those above unity are consistent with using a rough receiver surface.

P_{SRG} / $\times 10^{-5}$ mbar	y_o / mm	P_{RDG} / $\times 10^{-5}$ mbar
2.21	191.0	2.19
1.97	170.25	1.95
1.80	154.5	1.77
1.47	127.25	1.46
2.38	212.5	2.44
1.54	138.75	1.59
1.08	89.75	1.03
0.85	72.0	0.83
0.57	54.5	0.63
0.43	35.25	0.40
0.15	16.5	0.19

Table 6.1 A typical data set for simultaneous RDG and SRG pressure measurements in nitrogen. Each P_{SRG} value is the mean of five successive measurements.

The results of all the experiments are shown in table 6.2 and are quoted as the σ_{RDG} values of the gases on the RDG receiver surface. The experiments were repeated typically 3 times for each gas and many times for nitrogen. The uncertainty in the result of each particular experiment was calculated from equation 6.4 where

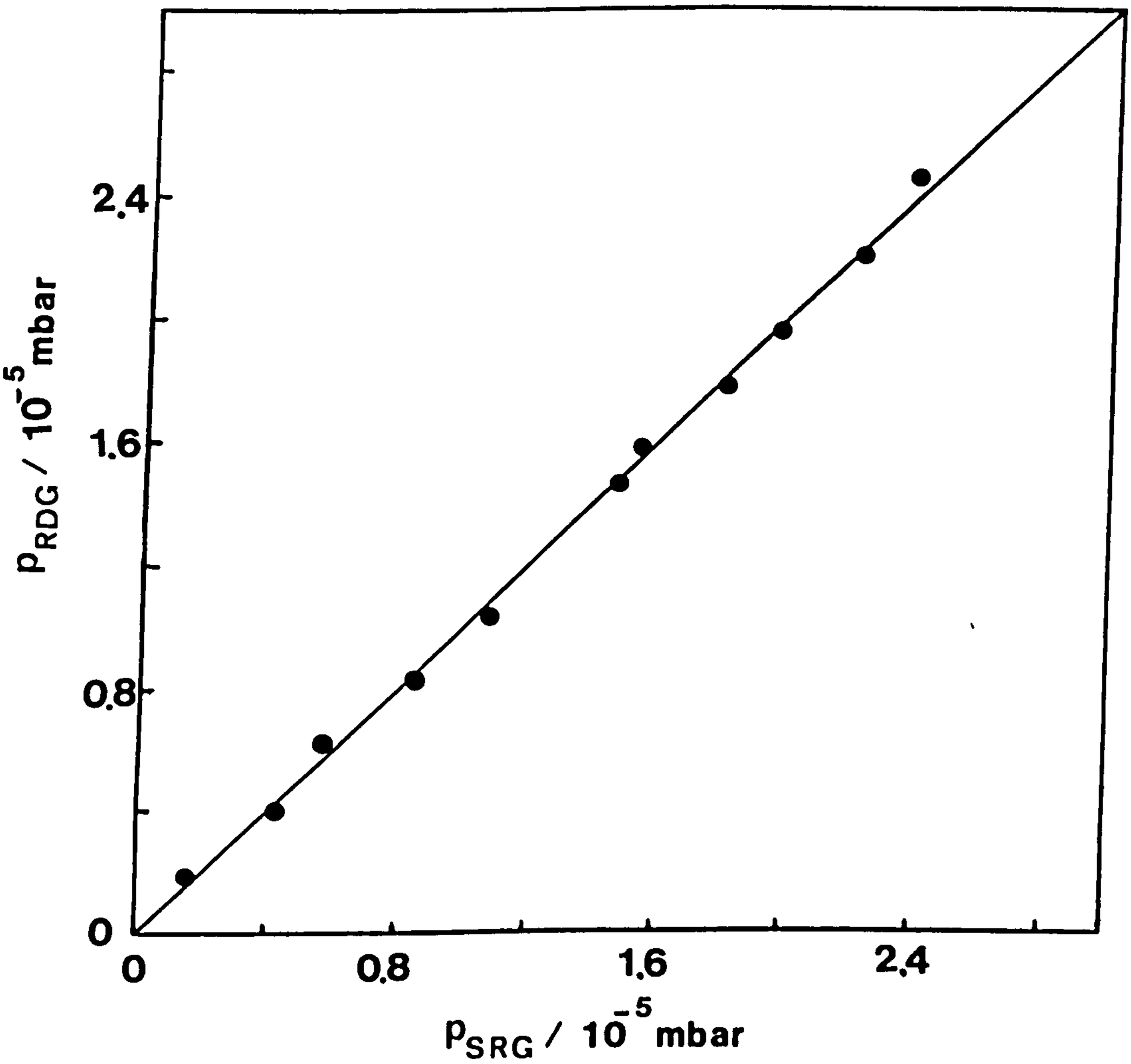

Figure 6.1 A plot of typical P_{RDG} versus P_{SRG} values for nitrogen.

$$\Delta\sigma_{RDG} = \sigma_{RDG} \left(\left(\frac{\Delta m}{m} \right)^2 + \left(\frac{\Delta\sigma_{SRG}}{\sigma_{SRG}} \right)^2 + \left(\frac{\Delta P_{SRG}}{P_{SRG}} \right)^2 \right)^{1/2} \qquad (6.4)$$

These uncertainties were calculated as a combination of the following:

(i) The uncertainty Δm in each gradient m from the LSF program where the variance (the mean square deviation) of the data points was calculated by the LSF program.

Gas	% of total	Value of σ_{RDG} of gas on		
		Smooth silicon	Rough silicon	Titanium on smooth silicon
Hydrogen	100	1.02 ± 0.12	1.04 ± 0.09	1.05 ± 0.08
Helium	96-99	0.99 ± 0.04	1.00 ± 0.06	1.00 ± 0.08
Methane	99	0.99 ± 0.03		
Water vapour	99	0.99 ± 0.04	1.02 ± 0.05	1.06 ± 0.05
Nitrogen	97	0.99 ± 0.02[1]	1.01 ± 0.06	1.02 ± 0.05
Air	80-90 (Nitrogen)	0.95 ± 0.05[1]	1.04 ± 0.05	1.04 ± 0.05
Carbon dioxide	97	0.99 ± 0.03		
Krypton	94	0.95 ± 0.04		

Table 6.2 σ_{RDG} values for various gases on different RDG receiver surfaces. [1]These experiments included one experiment at a rotor frequency of 166.3 Hz and one at 249.7 Hz.

(ii) A value of ± 2% taken as the relative uncertainty $\Delta P_{SRG}/P_{SRG}$ in the SRG measurements (Leck, 1989).

(iii) For gases other than nitrogen a ± 2% value was used as the uncertainty in the value of σ_{SRG}. This is because the SRG was only calibrated for nitrogen and from the work of Comsa et.al. (1980) and Comsa et.al. (1981) the value of σ_{SRG} varies by ±2% from its value for nitrogen for a range of gases.

The uncertainties shown in table 6.2 are a combination of the uncertainties of all the experiments for each particular gas-receiver situation. N.B. In the case of nitrogen on the smooth silicon receiver surface 15 measurements of σ_{RDG} were taken and the uncertainty calculated from their statistical distribution.

The effect of not using 100% pure gas is negligible because as noted in Chapter 5, and as seen by inspection of equations 6.1 and 6.3, P_{SRG} and P_{RDG} vary with M in the same way i.e. as $M^{-1/2}$. Also they both vary with temperature as $T^{1/2}$, the same temperature value being used for both the SRG and the RDG.

Any long term change in σ_{SRG} since calibration of the SRG is unknown. With careful use it is likely that the change is less than ± 1.5% (Dittmann et.al., 1989 and Redgrave and Downes, 1988).

With the careful procedures followed a ± 2% uncertainty in P_{SRG} is reasonable, see Leck (1989) and Redgrave and Downes (1988). For a rotor with an unknown history higher values have been quoted (American Vacuum Society, 1989).

An unknown uncertainty is introduced because of contamination of the SRG's ball before a gas is introduced. This effect gives an uncertainty below ± 1% (Redgrave and Downes, 1988). Since nitrogen was used repeatedly between experiments the same initial conditions were ensured and memory effects were therefore negligible.

Random noise effects were not present and thermal drift in the SRG avoided by stabilizing the SRG before use and by keeping the ambient room temperature constant.

6.5 ROTATING DISC GAUGE SENSITIVITY

In table 6.3 the results shown in table 6.2 for the smooth silicon receiver surface have been reexpressed as RDG sensitivities (see equation 6.2) in units of deflection per 10^{-5} mbar and are compared with the expected values which were computed assuming σ_{RDG} was unity for all the gases. The close agreement is most strikingly illustrated in figure 6.2 where the sensitivities are plotted against $M^{1/2}$ for each gas.

The full line represents the expected variation of sensitivity with $M^{1/2}$ under the assumption that σ_{RDG} is unity for all the gases. Since the experiments were performed in vacua of highly pure single gases the very good agreement (within experimental uncertainty) of the results with the predicted values confirms the $M^{1/2}$ dependence of the sensitivity of an RDG. These results considerably extend the work of Dushman (1915) who worked with air and hydrogen. It is the first direct confirmation of the predicted $M^{1/2}$ dependence of the sensitivity of an RDG.

Gas	Relative molecular mass	Sensitivity / mm / 10^{-5} mbar	
		expected	measured
Hydrogen	2.016	23.3	23.9 ± 2.9
Helium	4.003	32.9	32.6 ± 1.4
Methane	16.043	65.8	65.3 ± 2.0
Water vapour	18.015	69.7	69.2 ± 3.1
Nitrogen	28.013	86.9	86.1 ± 1.9
Air	28.611	87.9	83.9 ± 4.5
Carbon dioxide	44.010	109.0	107.9 ± 3.2
Krypton	83.800	150.4	143.2 ± 6.0

Table 6.3 Expected and measured RDG sensitivities for various gases on a smooth silicon receiver surface.

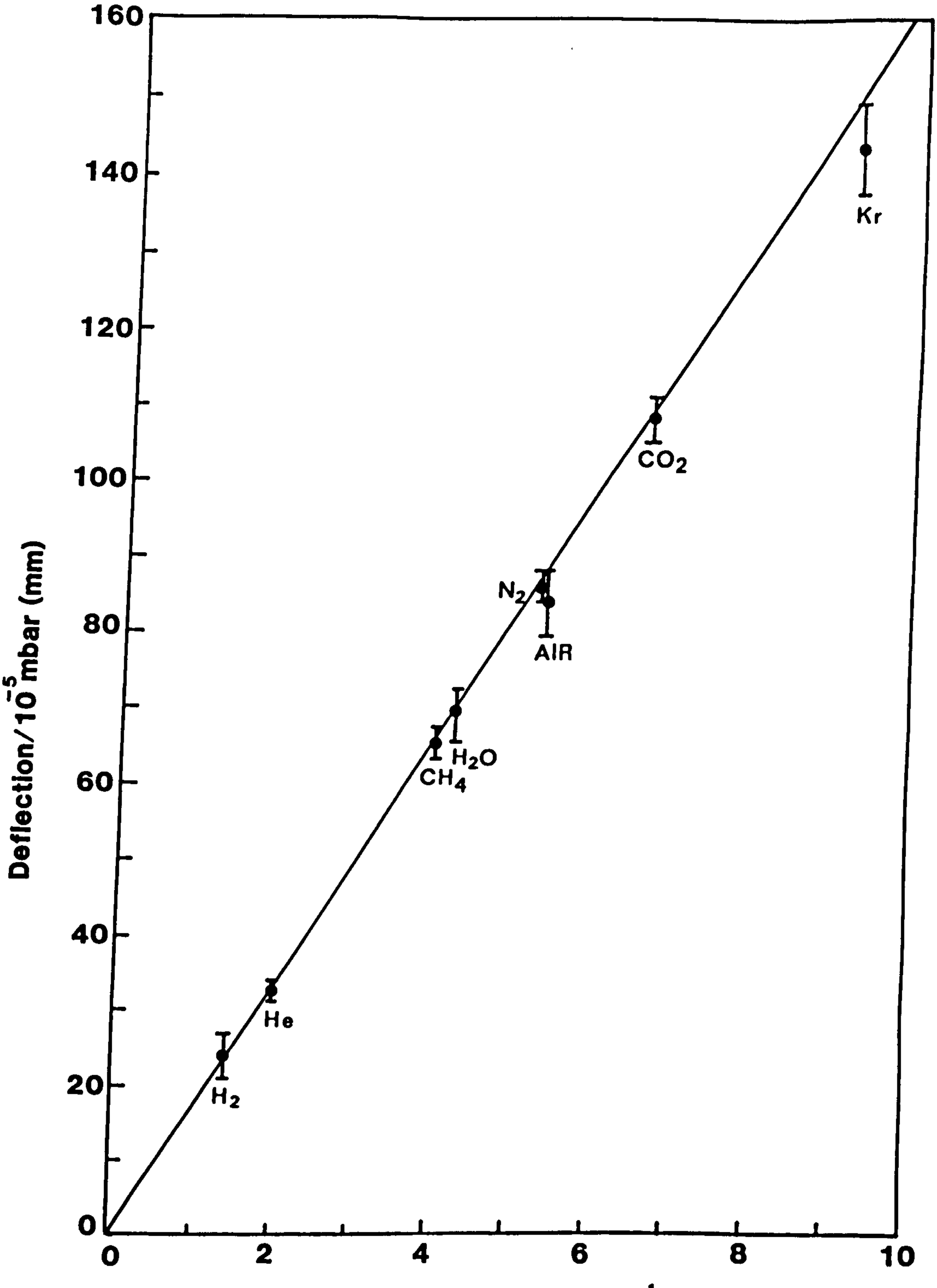

Figure 6.2 RDG sensitivity versus (relative molecular mass)$^{1/2}$ for the smooth silicon receiver surface. The full line indicates the theoretically predicted dependence.

The results indicate near perfect accommodation of tangential momentum for all the gases on the smooth silicon receiver surface i.e. they suggest that σ_{RDG} = 1.0 for all gases. However the σ_{RDG} value of krypton is lower than the other values. This may be due to the σ_{SRG} value for krypton being higher than for other gases.

Reflection high energy electron diffraction and scanning electron microscope studies confirmed that the smooth receiver surface was highly ordered, flat and smooth, see Chapter 3. Auger electron spectroscopy showed there to be an adsorbed layer of oxygen and carbon on the surface of the receiver. Other workers (Comsa et.al.,1981, Thomas, 1981 and Blankenstein 1923) have reported the same unity values of σ for all gases on smooth, flat and adsorbate covered surfaces.

The results indicating that σ_{RDG} is unity for all gases on the smooth receiver surface further support the same result (for dominantly nitrogen) found in Chapter 5.

Since σ_{RDG} is unity for all gases then all the values in the RDG's operating equation 6.1 are known. Therefore the RDG has a *universal* application for *absolute* total pressure measurement for all gases.

6.5.1 Rough Surfaces

It can be seen from table 6.2 that the value of σ_{RDG} for all gases on the rough silicon and titanium on silicon receiver surfaces is increased above unity. The values of the ratio of σ_{RDG} for the rough silicon and titanium on silicon surfaces to that of the smooth silicon surface for each gas are shown in table 6.4. These values are very accurate because the effect of the uncertainty in the value of σ_{SRG} for each gas is cancelled by the division.

Scanning electron microscopy studies (see Chapter 3) showed the smooth silicon receiver surface to be featureless on a 1 μm scale (see figure 3.17) whereas the rough silicon surface has protrusions of the order of 10 μm covering about half its surface with smaller terraces on the remainder, see figure 3.18. The titanium on silicon receiver (figure 3.19) was shown to partly be as featureless as the smooth silicon surface in places but elsewhere to have areas of protrusions (on

Gas	Ratio of $\sigma_{RDG(SURFACE)} : \sigma_{RDG(SMOOTH\ SURFACE)}$	
	Rough silicon surface	Titanium on silicon surface
Hydrogen	1.01 ± 0.13	1.02 ± 0.13
Helium	1.01 ± 0.06	1.00 ± 0.07
Water vapour	1.03 ± 0.03	1.07 ± 0.03
Nitrogen	1.02 ± 0.04	1.03 ± 0.04
Air	1.09 ± 0.03	1.09 ± 0.04

Table 6.4 Values of σ_{RDG} for two rough receiver surfaces relative to those of the smooth silicon receiver surface.

about one half of its surface) as large as those of the rough silicon surface. This was due to the non-uniform growth of titanium. Auger electron spectroscopy studies showed there to be an adsorbed layer of oxygen and carbon on both the rough silicon and titanium on silicon surfaces.

The relative increase of a few percent in the σ_{RDG} values on these rough surfaces is in accord with results reported by other workers on surfaces rough to the same scale (Fremerey, 1982).

6.6 CONCLUSIONS

The predicted $M^{1/2}$ dependence of the sensitivity of the RDG for hydrogen, helium, methane, water vapour, nitrogen, air, carbon dioxide and krypton has been confirmed experimentally. The tangential momentum accommodation coefficients σ of these gases on a flat, smooth, highly ordered and adsorbate covered silicon (111) surface have been deduced for the above gases and are close to unity. These results support the findings of other workers that $\sigma = 1$ for all gases on similarly treated surfaces. Therefore since all the values in the operating equation of the RDG are known the RDG can be considered as a *universal absolute* total pressure gauge for all gases.

Measurements of σ_{RDG} values of a few percent above unity on rough surfaces have been made for hydrogen, helium, water vapour, nitrogen

and air and are in accord with the results of other workers reported for similar surfaces. Using a rough receiver surface means that the RDG has to be calibrated for each gas.

6.7 ROTATING DISC GAUGE AND IONIZATION GAUGE COMPARISONS

The digital ionization gauge (IG) used in the previously described experiments was used primarily to monitor vacuum stability. Simultaneous measurements of IG pressures P_{IG} were taken during the RDG and SRG comparisons. All other parameters were the same as those described in the previous experiments. Since the RDG has been shown to be a universal gauge when the smooth silicon receiver surface was used then the simultaneous P_{IG} and P_{RDG} data can be used to evaluate the relative sensitivity factors of the IG for the gases listed earlier.

The relationship between the IG pressure reading $P(N_2)$ given for nitrogen and the unknown (true) pressure P(x) for a gas x (Wutz et.al., 1989) is

$$P(x) = \frac{S(N_2)}{S(x)} . P(N_2) \qquad (6.5)$$

where $S(N_2)$ is the sensitivity of the IG for nitrogen and S(x) is the sensitivity of the IG for a given gas. Normalizing the sensitivity to nitrogen gives $S(N_2) = 1$ and thus

$$P_{TRUE} = \frac{P_{INDICATED}}{\text{Relative sensitivity (S) of gas}} \qquad (6.6)$$

The IG gauge constant was given as 19 $mbar^{-1}$ for nitrogen. The relative sensitivity of the gauge for hydrogen, helium, methane, water vapour, nitrogen, air, carbon dioxide and krypton were determined as below.

6.7.1 Results and Discussion

To evaluate the relative sensitivities typically 8 to 10 P_{IG} values were plotted against simultaneous P_{RDG} measurements taken using the smooth silicon receiver surface. A typical data set is shown in table 6.5 for nitrogen and figure 6.3 shows the plot of this P_{IG} versus P_{RDG}

data.

P_{IG} / × 10^{-5} mbar	P_{RDG} / × 10^{-5} mbar
1.1	1.10
1.5	1.55
2.1	2.15
2.1	2.16
2.4	2.47
1.9	1.90
0.89	0.90
0.42	0.41

Table 6.5 Data set of simultaneous P_{IG} and P_{RDG} measurements for nitrogen.

The full line on the plot represents the result of a LSF to the data. The gradient of the line is equal to the relative sensitivity of the IG. A gradient and hence a relative sensitivity S of unity would indicate no correction to P_{IG} needed, a value of S below unity signifies a gas harder to ionize than nitrogen (for example, helium). A value above unity signifies a gas easier to ionize than nitrogen, for example carbon dioxide.

The results of all the experiments which were repeated typically three times for each gas and 23 times for nitrogen are shown in table 6.6. The values are the sensitivities relative to nitrogen. The IG was degassed and the experiment was performed repeatedly for nitrogen in between each other gas to ensure the same starting conditions for each experiment.

The uncertainty associated with each relative sensitivity factor was calculated as a combination of the uncertainty in the calculated gradient (as earlier) and a value of ± 3% taken as the uncertainty of P_{RDG}. In the case of nitrogen, helium and hydrogen many measurements were taken and the uncertainty in their S values calculated from the statistical distribution of the results.

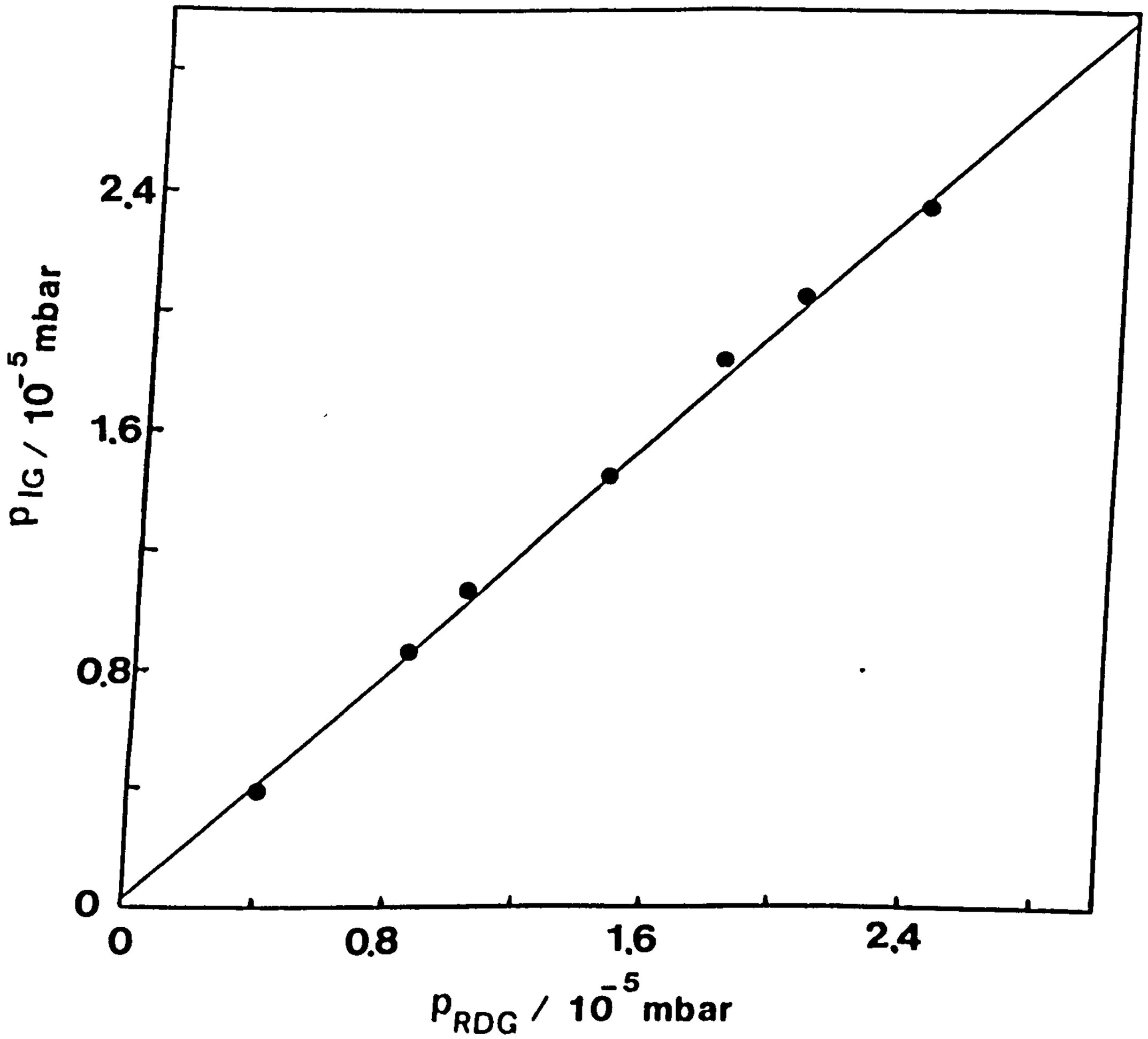

Figure 6.3 A typical P_{IG} versus P_{RDG} plot for nitrogen.

Gas	Measured value of S	S values from literature[4]
Nitrogen[1]	1.00	1.00
Hydrogen	0.396 ± 0.004	0.36 - 0.60
Helium[2]	0.20 ± 0.01	0.14 - 0.25
Methane	1.47 ± 0.07	1.40 - 1.62
Water vapour	0.85 ± 0.04	0.86 - 1.25
Air[3]	0.99 ± 0.05	0.97 - 1.00
Carbon dioxide	1.32 ± 0.04	1.30 - 1.45
Krypton	1.79 ± 0.08	1.72 - 1.94

Table 6.6 IG sensitivity factors relative to nitrogen.
[1]Includes one experiment at a sender frequency of 141.7 Hz, two at 166.3 Hz and one at 249.7 Hz. [2]Includes one experiment at a sender frequency of 249.7 Hz. [3]Includes one experiment at a sender frequency of 166.3 Hz and one at 249.7 Hz. [4]Sensitivity factors from: Vacuum Generators (1989), O'Hanlon (1989), Wutz et.al.(1989), Chambers et.al. (1989), Harris (1989), Filippelli and Dittmann (1991), Bartmess and Georgiadis (1983), Nakao (1975) and Holanda (1973).

The actual measured value of the sensitivity for nitrogen was 0.96 ± 0.01. Thus the gauge constant was in fact about 18 $mbar^{-1}$, slightly lower than the manufacturers given value. The values of the sensitivity factors relative to nitrogen are in good agreement with those recommended by the manufacturer (Vacuum Generators, 1989) and lie in the range of values determined by other workers for similar type gauges.

6.8 GENERAL CONCLUSIONS

The results of experimental comparisons of the rotating disc with a spinning rotor gauge in vacua of a range of pure gases have confirmed the theoretically predicted $M^{1/2}$ dependence of the sensitivity of an RDG for the first time.

For the flat, highly ordered, smooth and adsorbate covered silicon receiver surface the tangential momentum accommodation coefficients of various gases have been measured to be unity which is in agreement

with the results of other workers. This indicates a potential for *universal* application of the rotating disc gauge for *absolute* total pressure measurement.

Measurements of increased σ_{RDG} values on rough receiver surfaces of a few percent above unity are in accord with the results of other workers. The RDG needs to be calibrated for each gas when a rough receiver surface is used.

The relative sensitivity factors of a Bayard-Alpert ionization gauge have been measured by comparisons of it with the rotating disc gauge in a range of gases and are in agreement with the manufacturers recommended values and those of other workers.

CHAPTER 7

ROTATING DISC GAUGE CHARACTERISTICS FOR VARIOUS GEOMETRIES

7.1 INTRODUCTION

The work described so far was conducted for a rotating disc gauge (RDG) with the sender and receiver discs of the same size. The aim of the work described in this chapter was to investigate the characteristics of an RDG which had a receiver disc smaller than the sender. These characteristics are compared with those for the RDG with discs of the same size described in Chapter 4.

7.2 THEORY

The configuration of the RDG with a receiver disc smaller than the sender is shown in figure 7.1. Consider molecules leaving the sender disc within the radial distance OE which is equal to the radius R of the receiver. Due to the Knudsen cosine distribution there will be a loss of molecules out of the discs' interspace. This loss is compensated for to a certain degree by the gain of molecules, into the interspace, which leave the sender at a radial distance beyond OE. This compensating effect is not present for the RDG with the same sized discs. At high sender speeds there will be an additional loss of molecules due to the imposed bias velocity v_b as described in Chapter 2.

Molecules which leave the sender at a position P will be distributed in solid angle according to the Knudsen cosine distribution K. Molecules which leave P at angles within the angle specified by the directions PE and PO will reach the receiver to create a torque promoting rotation in the same direction as the sender. Those which leave at angles within that specified by the directions PO and PF will create a torque which opposes the receiver's rotation. The effect of these molecules which 'cross the centre' from right to left is exactly compensated by those which cross the centre from left to right, see Chapter 2. Therefore there is a net compensating effect (from molecules which come into the discs' interspace) to the loss of molecules from within it.

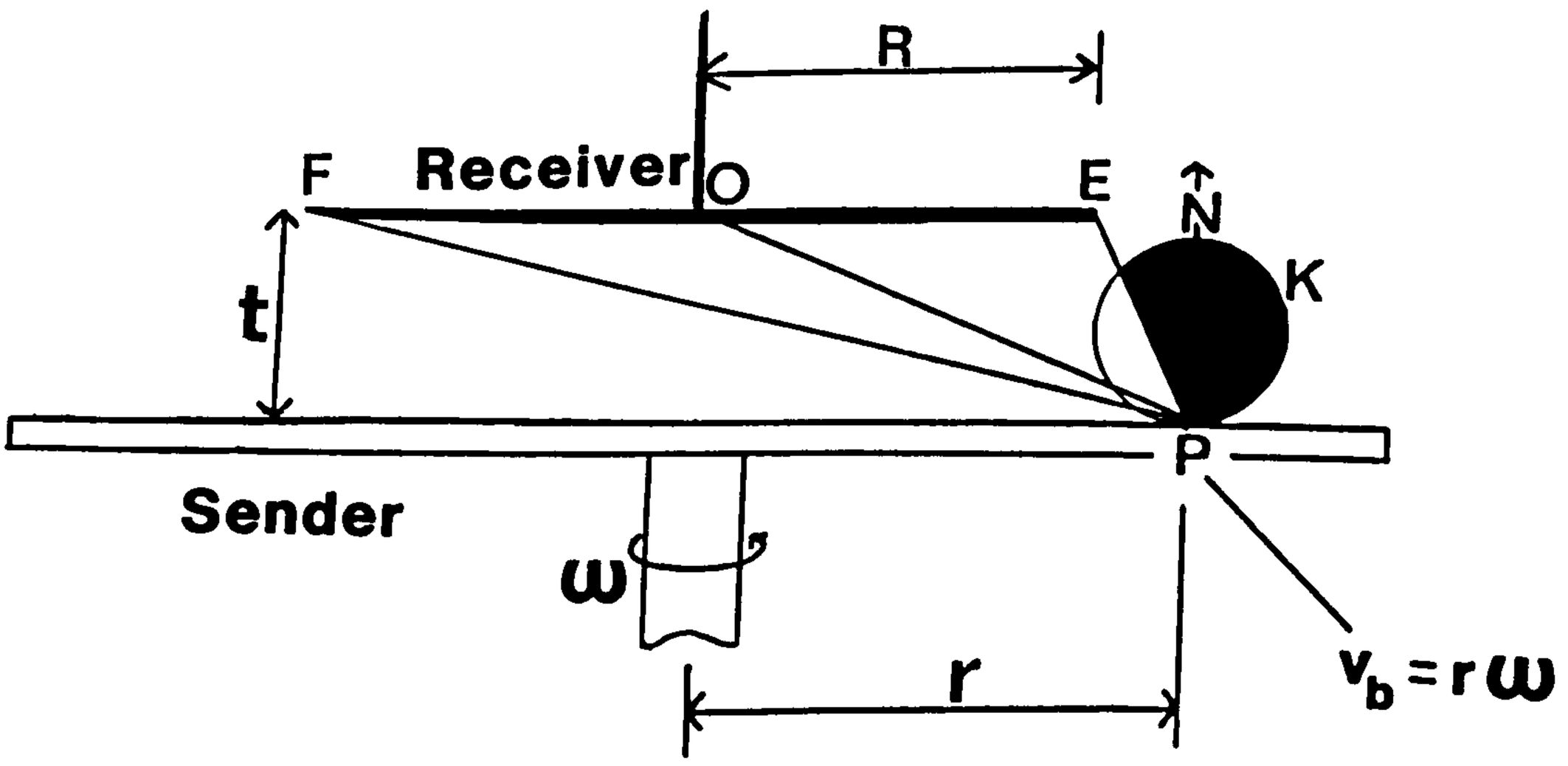

Figure 7.1 Rotating disc gauge configuration for the case of a smaller receiver disc. See text for the meaning of the symbols.

The geometrical complexities mean that a complete analysis of the configuration is much more complicated than that for equal sized discs. Since desorption from a locality at a radial distance r on the sender is on average in a direction normal N to the sender surface and because of the compensating effect described above a simplified analysis for the limit of touching discs can be made.

Because of the compensating effect a new edge effect loss factor ε' ($0 < \varepsilon' < 1$) is introduced where $\varepsilon' \to 1$ for $t \ll R$ and $\varepsilon' \to 0$ for $t \gg R$ and t is the disc-separation.

The operating equation for this changed configuration is therefore the same as that derived previously for equal sized discs in Chapter 2. However R here is the radius of the receiver and the edge effect correction factor ε' is introduced. ε' can not be determined analytically and is evaluated empirically.

$$P_{RDG} = \frac{\frac{c}{2L}}{\varepsilon' \sigma_{RDG}\ \omega\ R^4 \left[\frac{\pi}{8000\ R_o}\right]^{1/2}} \frac{T^{1/2}}{M^{1/2}} .y_o \qquad (7.1)$$

where the symbols have the previously defined meanings.

7.3 EXPERIMENTAL

Three receiver discs of diameters 84.64 mm, 78.04 mm and 70.00 mm and the same sender disc of 92 mm diameter were used. They were all ground from silicon wafers (see Chapter 3) and their smooth side was used as the receiver surface. Other experimental parameters were the same as those listed in Chapter 6. i.e. the torsion constant c of the fibre used was $1.470 \pm 0.001 \times 10^{-7}$ Nm, the mirror-scale distance L = 1088 ± 1 mm, R is the receiver radius, M is the relative molecular mass, T is the absolute temperature and y_o is the measured deflection. In Chapter 6 it was found that for the smooth receiver surfaces used σ_{RDG} is unity for all gases.

The shortest period of the receiver suspensions used was 27 seconds, sufficiently long that essentially a step function of molecular torque was developed when the shutter was withdrawn. Other approximations

and uncertainties are the same as those discussed in Chapter 5. For the smaller sized receiver discs the suspension was more affected by vibrations and harder to damp than before.

7.4 ROTATING DISC GAUGE AND IONIZATION GAUGE COMPARISONS

Figure 7.2 shows a plot of the data of deflection y_o versus ionization gauge (IG) pressure for the 84.64 mm diameter receiver disc in nitrogen at a fixed sender speed of 15 krpm. Figures 7.3 and 7.4 show data of the same experiment for the 78.04 mm and the 70 mm diameter receiver discs respectively. The linearity and the fact that the plots pass through the origin is to be noted. As expected the largest deflection at a given pressure corresponds to the smallest disc-separation where the edge effect loss is least. The same effects were seen for the RDG with the same sized discs.

For a given separation it can be seen from these three graphs that the largest deflection occurs for the largest receiver disc. This is to be expected from equation 7.1 since the torque developed and thus the receiver deflection is proportional to (receiver radius)^4.

7.5 EDGE EFFECT CHARACTERISTICS

Figure 7.5 shows data of deflection versus disc-separation t for the 84.64 mm diameter receiver disc at a fixed sender speed of 15 krpm in nitrogen. The full lines represent the results of a quadratic least squares fit (LSF) to the data. There is a clear fall off of deflection as the disc-separation increases as there was for the RDG with same sized discs. At a given separation the deflections scale in the same ratio as the indicated pressure readings as they did for the the RDG with the same sized discs. Therefore for at least the range of disc-separations investigated the conductive access to the interspace is not restrictive. By extrapolating to zero disc-separation a value of the deflection where $\varepsilon' = 1$ i.e. for zero loss of torque can be found and a value of P_{RDG} deduced. By inserting the relevant values into equation 7.1 a working equation below for the 84.64 mm diameter receiver disc can be derived for the case of $\varepsilon' = 1$. Here T = 293 K and f = 249.7 Hz.

$$P_{RDG} = 6.32 \times 10^{-8} \cdot y_o \text{ mbar} \qquad (7.2)$$

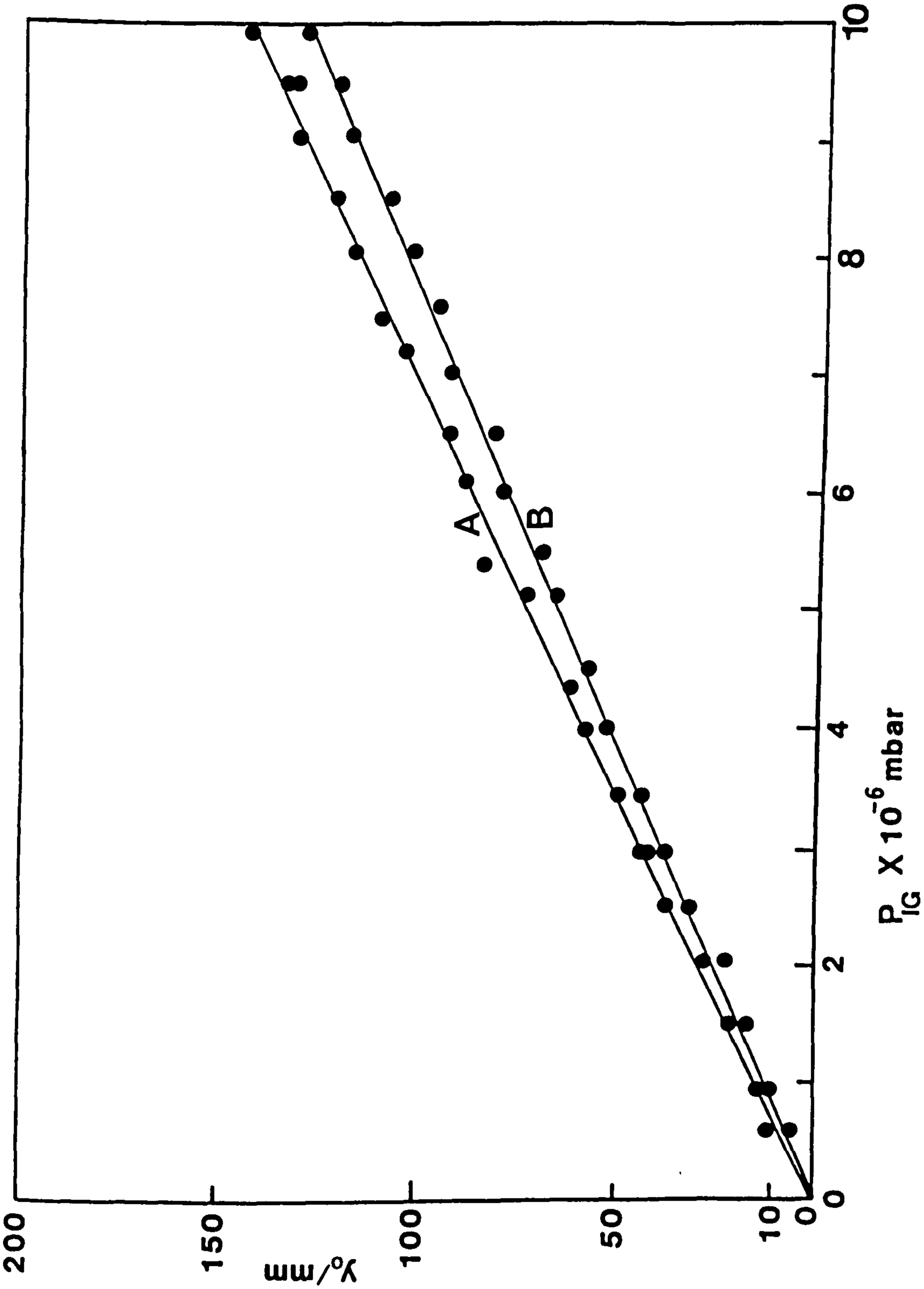

Figure 7.2 Deflection versus P_{IG} for the 84.64 mm diameter receiver disc. A t = 3.7 mm and B t = 6.5 mm.

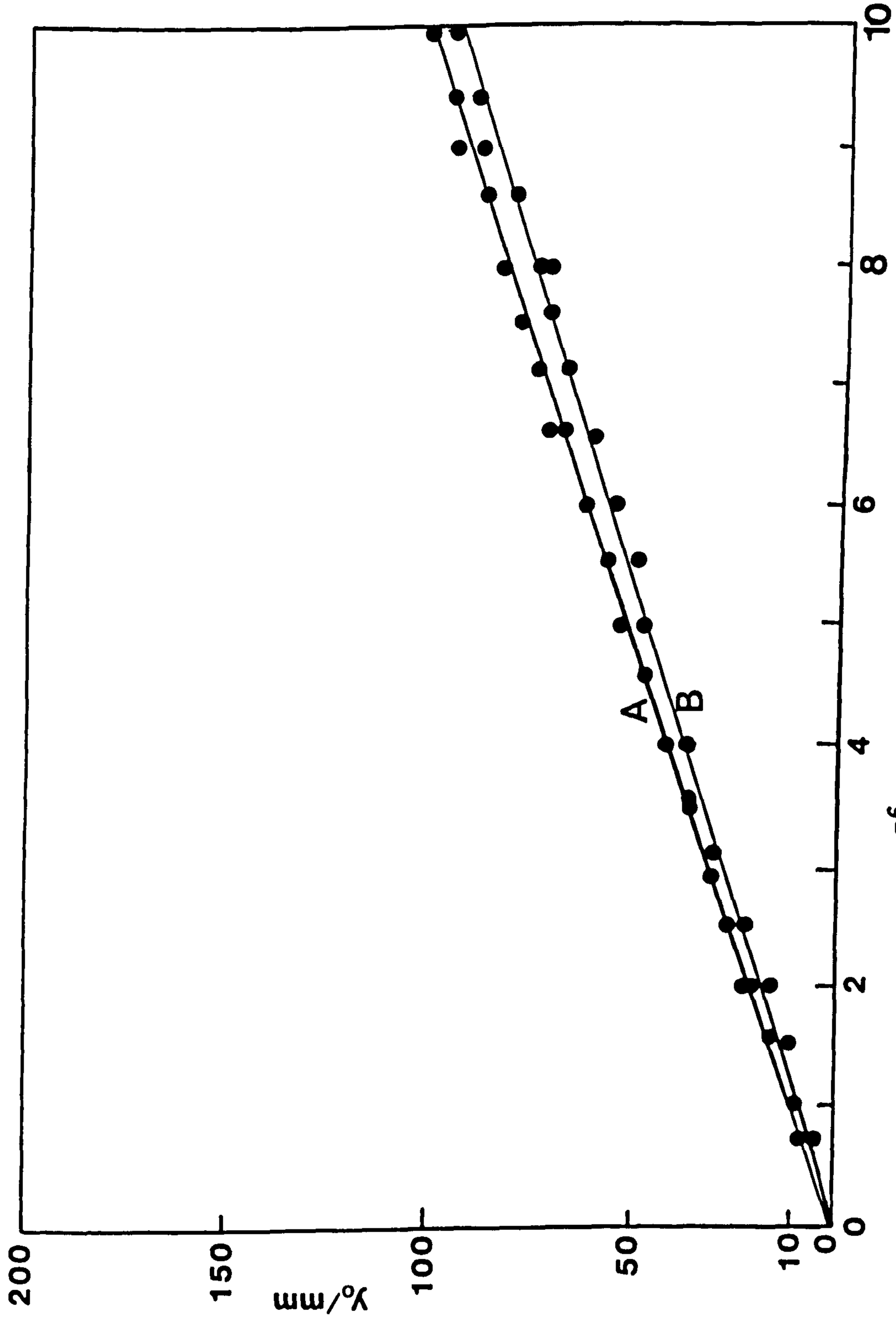

Figure 7.3 Deflection versus P_{IG} for the 78.04 mm diameter receiver disc. A t = 3.7 mm and B t = 6.5 mm.

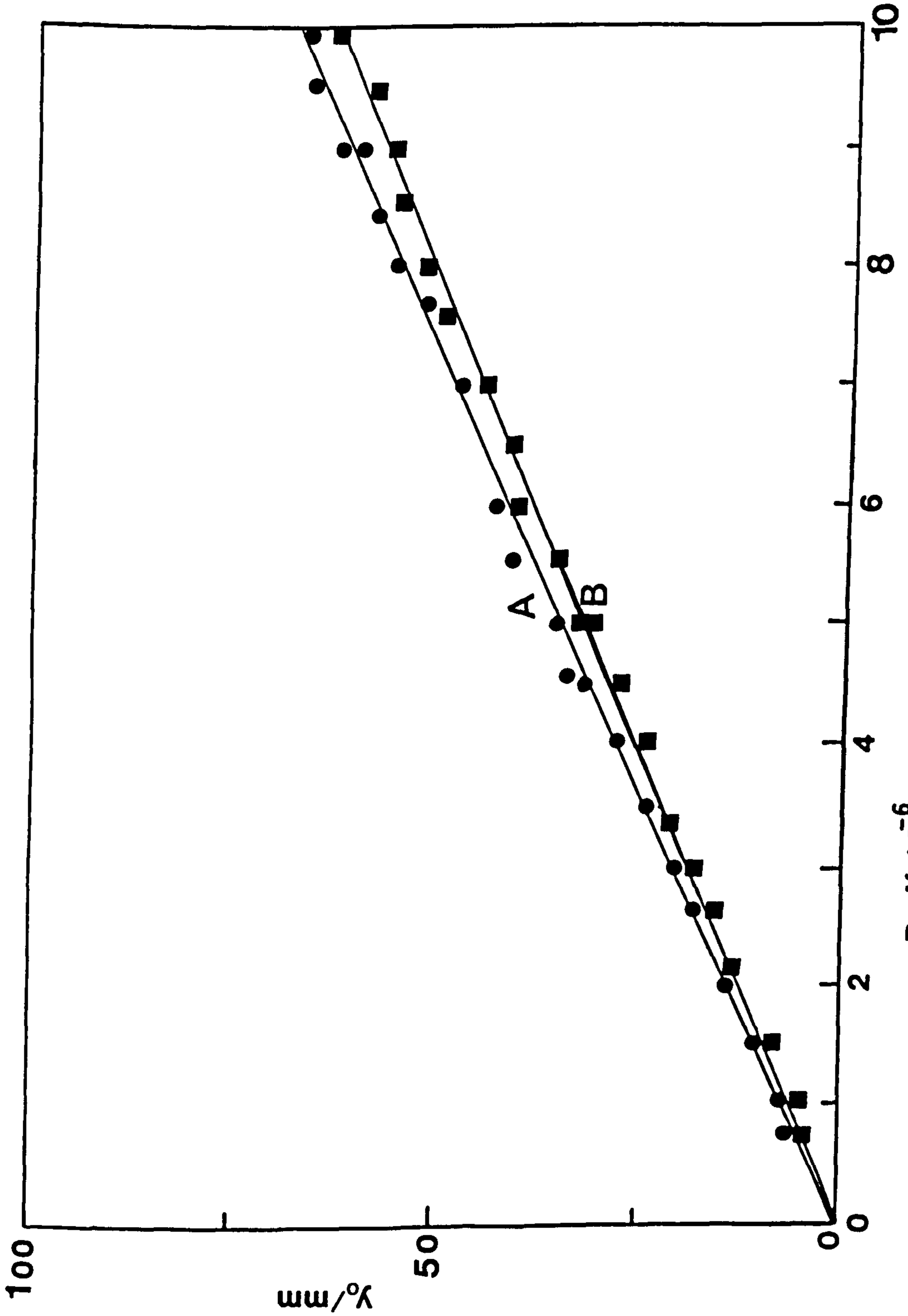

Figure 7.4 Deflection versus P_{IG} for the 70.00 mm diameter receiver disc. A t = 4.0 mm and B t = 6.8 mm.

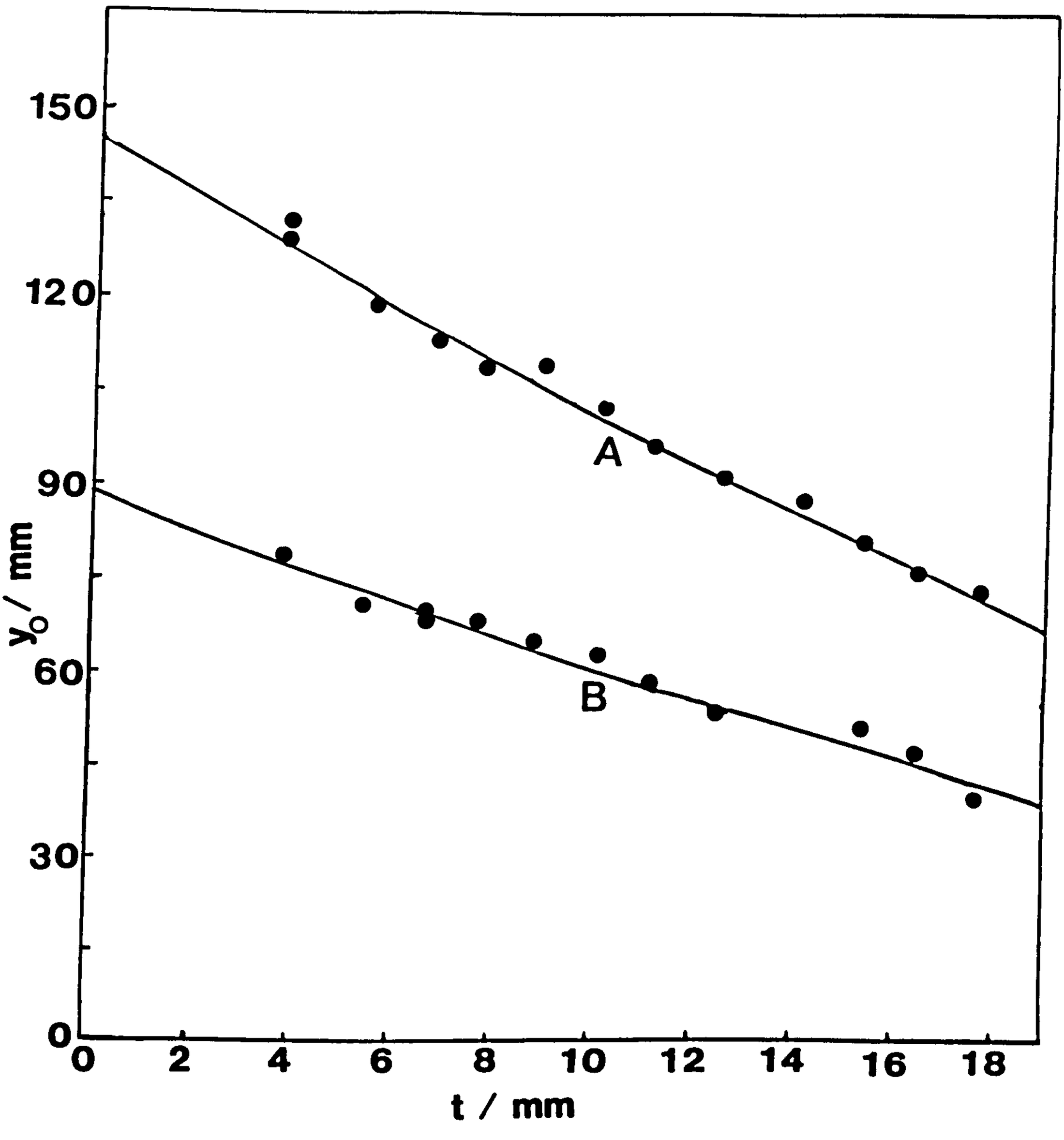

Figure 7.5 Deflection versus disc-separation for the 84.64 mm diameter receiver disc. A $P_{IG} = 9.1 \times 10^{-6}$ mbar and B $P_{IG} = 5.5 \times 10^{-6}$ mbar.

The P_{RDG} values are 9.2 and 5.6 $\times 10^{-6}$ mbar for P_{IG} values of 9.1 and 5.5 $\times 10^{-6}$ mbar respectively.

Figures 7.6 and 7.7 show data of deflection versus disc-separation for the 78.04 mm diameter and 70 mm diameter receiver discs respectively. Both sets of curves are for nitrogen and were taken at a sender speed of 15 krpm. The full lines again represent the results of a quadratic LSF to the data. It can be seen that there is a greater spread in the data as the receiver disc gets smaller which reflects the increased effect of vibrations.

The curves can be seen to become shallower and the fall off decrease as the receiver diameter decreases and again they scale in the same ratio as the indicated pressure readings. These results again show that there is adequate conductive access into the discs' interspace at least for the range of separations investigated.

The P_{RDG} values deduced from the curves for these discs, in the same manner as that described above, are shown in table 7.1.

Receiver diameter / mm	P_{RDG} $\times 10^{-6}$ mbar	P_{IG} $\times 10^{-6}$ mbar
84.64	9.2	9.1
84.64	5.6	5.5
78.04	9.5	9.4
78.04	6.1	6.0
70.00	10.1	9.9
70.00	8.5	8.0

Table 7.1 P_{RDG} and P_{IG} values for various diameter receiver discs.

It can be seen that the P_{RDG} values are greater than those of the P_{IG} by a few percent which is consistent with the measured value of the

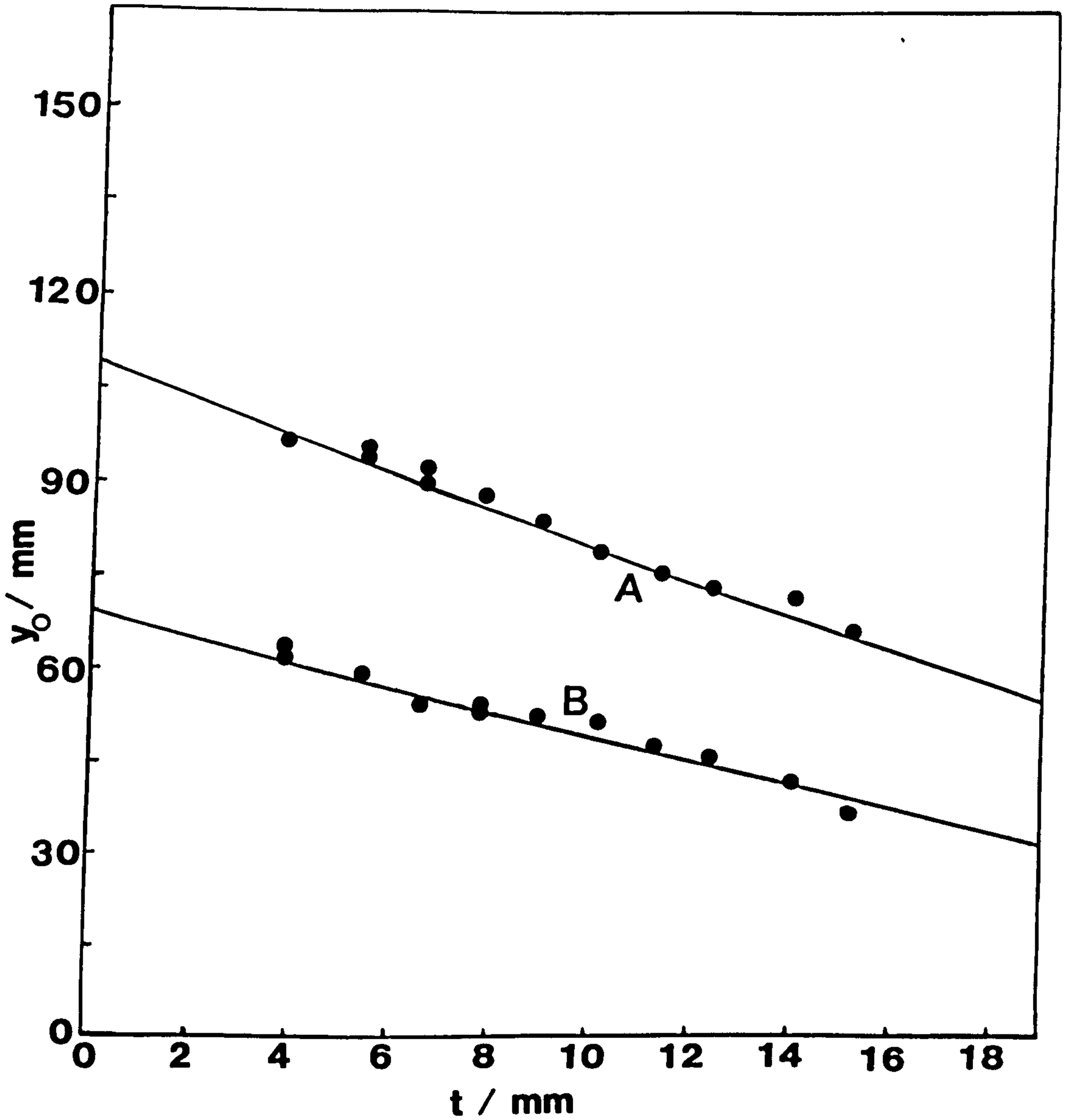

Figure 7.6 Deflection versus disc-separation for the 78.04 mm diameter receiver disc. A $P_{IG} = 9.4 \times 10^{-6}$ mbar and B $P_{IG} = 6.0 \times 10^{-6}$ mbar.

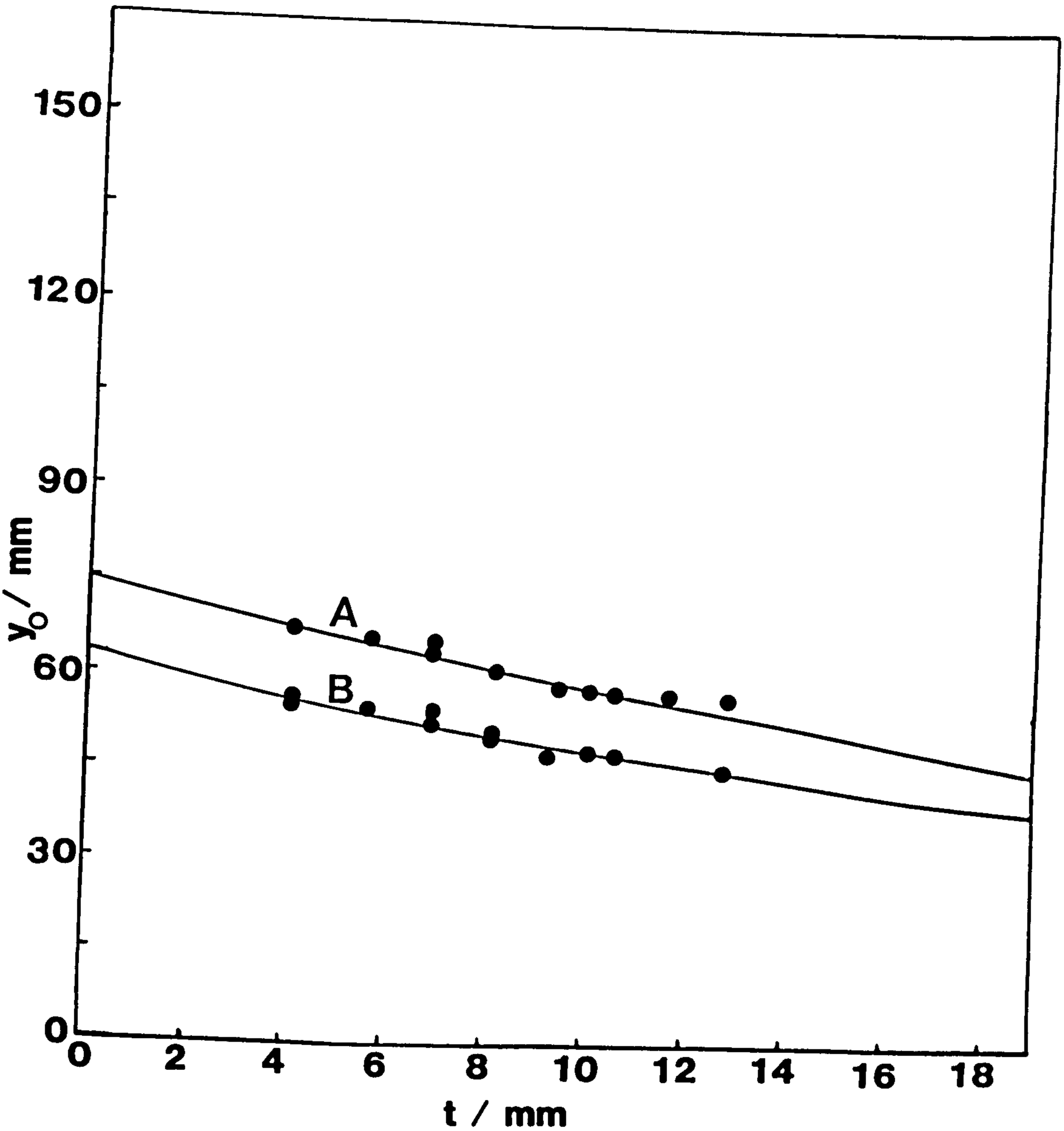

Figure 7.7 Deflection versus disc-separation for the 70.00 mm diameter receiver disc. A $P_{IG} = 9.9 \times 10^{-6}$ mbar and B $P_{IG} = 8.0 \times 10^{-6}$ mbar.

sensitivity factor of the IG for nitrogen determined in Chapter 6.

The magnitude of the compensating effect to the edge effect loss of torque described earlier is shown in table 7.2. For each receiver disc the edge effect loss factor ε' is calculated from the LSF to the curves at a value of t = 4 mm where

$$\varepsilon'_{t=4} = \frac{y_o(t=4)}{y_o(t=0)} \qquad (7.3)$$

These values of ε' are compared with the analytically derived values of ε, the value the edge effect loss factor would have for equal sized discs, from the expression below (see Chapter 2) assuming that the diameter 2R of both discs is the diameter of the receiver

$$\varepsilon = \left[\left[1 + \left(\frac{t}{2R}\right)^2 \right]^{1/2} - \frac{t}{2R} \right]^4 \qquad (7.4)$$

where t is the disc-separation.

Receiver diameter / mm	$\varepsilon_{ANALYTICAL}$	$\varepsilon'_{MEASURED}$
92.00	0.84	-
84.64	0.83	0.88
78.04	0.81	0.90
70.00	0.80	0.91

Table 7.2 Edge effect loss factors for different diameter receiver discs.

Clearly the measured edge effect loss of torque, for the case where the receiver diameter is less than that of the sender, is less than it would be for the case of equal sized discs. This is due to the compensating effect described earlier which increases as the receiver:sender diameter ratio decreases.

It can also be seen that where the sender diameter is much greater than that of the receiver the value of ε' will approach unity and no net edge effect loss will occur.

It is interesting to compare the RDG configuration used by Dushman (1915) where the receiver was 30 mm in diameter with a sender disc of about 35 mm. The disc-separation was kept below 10 mm. Despite using very low sender speeds it can be interpolated from the results in table 7.2 that there would have been an edge effect loss of torque. For the relative size of the discs used this loss of torque, which was not accounted for, would have introduced a systematic error of about 10% into Dushman's calculations.

7.6 PERFORMANCE UNDER VARIABLE SENDER SPEED

In figure 7.8 data of deflection versus sender speed at a pressure of 3.5×10^{-6} mbar in nitrogen for the 84.64 mm diameter disc is presented. The small spread of the data is to be noted as is the expected intersection at the origin. It is clear that there is a fall off of deflection at high sender speeds, deflection being proportional to sender speed up to about 35 krpm. This is the same behaviour as was seen for the same sized discs.

The results of data of deflection versus sender speed for the 78.04 mm diameter and the 70 mm diameter receiver disc is shown in figure 7.9 and 7.10 respectively. The behaviour is the same as that described above.

The fall off of deflection at high speeds can be evaluated by evaluating the quantity ν in the same way as it was in Chapter 4 for the equal sized discs where

$$\nu = \frac{y_o(\omega=50)}{y_o(\omega=30)} \times \frac{30}{50} \qquad (7.5)$$

i.e. the deflection at 50 krpm is compared to that at a speed of 30 krpm which is in the linear region of deflection versus speed. A value of ν below unity shows a fall off of deflection at 50 krpm.

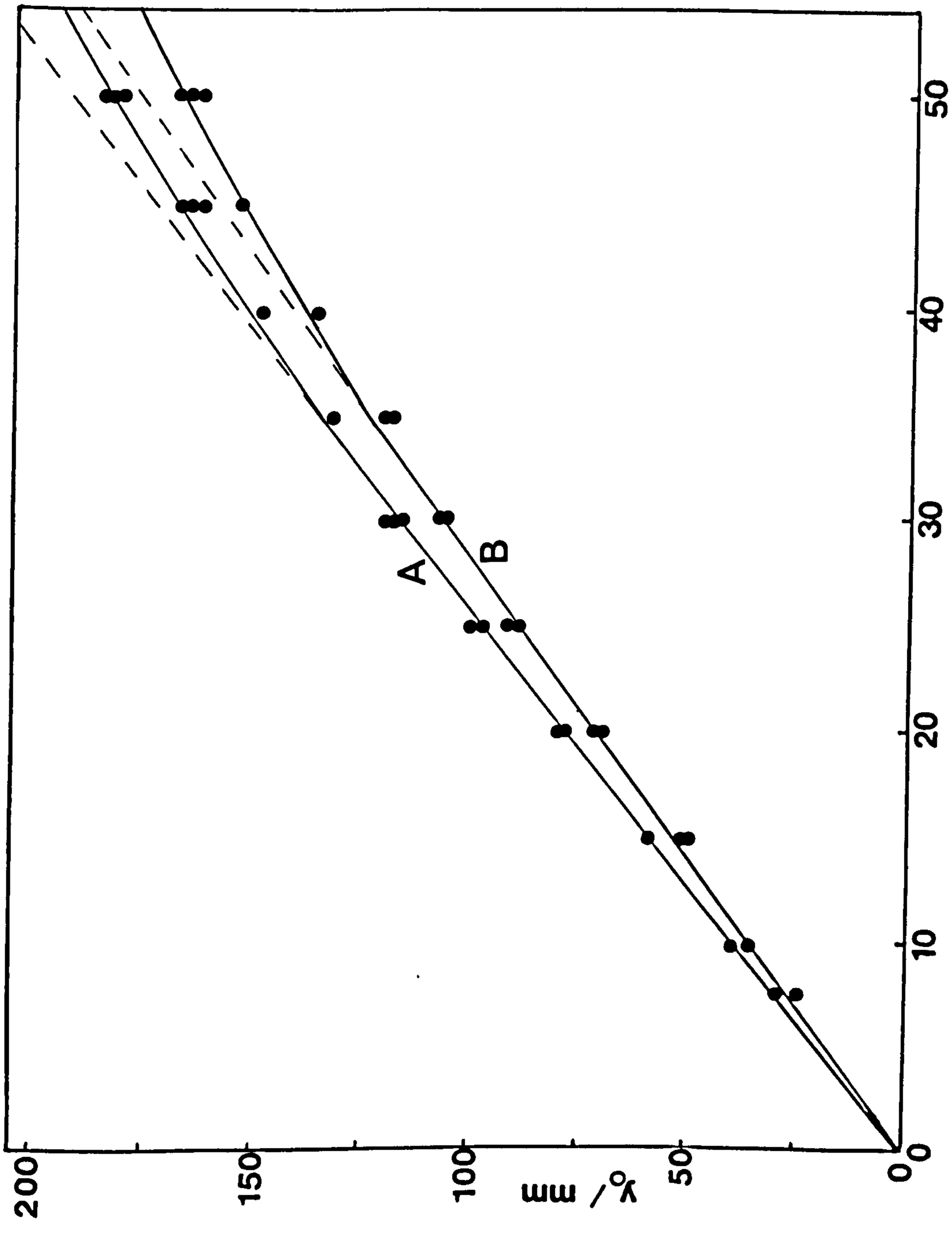

Figure 7.8 Deflection versus sender speed for the 84.64 mm diameter receiver disc. A t = 3.7 mm and B t = 6.5 mm.

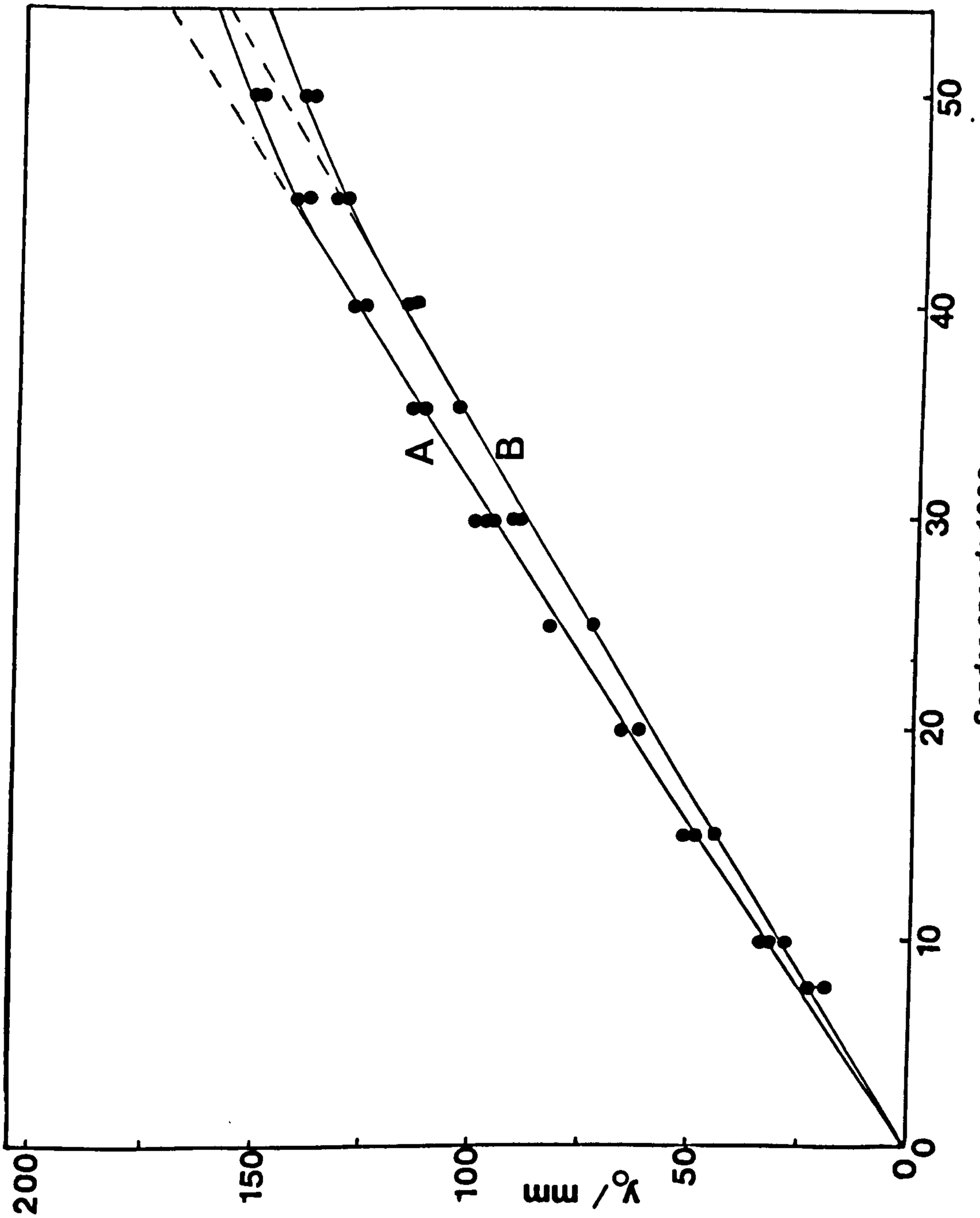

Figure 7.9 Deflection versus sender speed for the 78.04 mm diameter receiver disc. $P_{IG} = 4.0 \times 10^{-6}$ mbar. A t = 3.7 mm and B t = 6.5 mm.

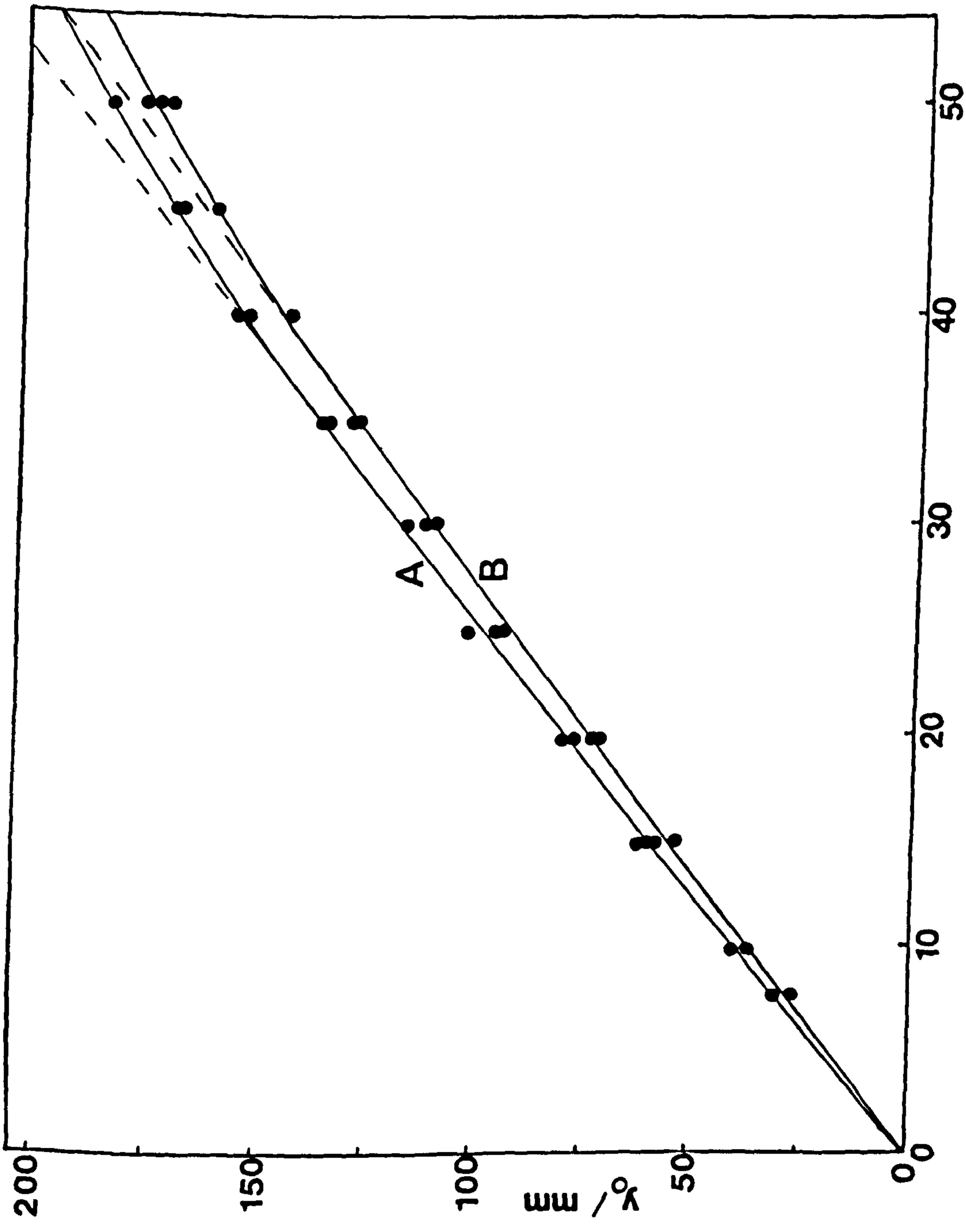

Figure 7.10 Deflection versus sender speed for the 70.00 mm diameter receiver disc. $P_{IG} = 7.0 \times 10^{-6}$ mbar. A t = 4.0 mm and B t = 6.8 mm.

Typically six measurements of deflection were made at each sender speed and the results of ν are given in table 7.3, together with a typical result in nitrogen for the 92 mm diameter receiver disc.

Receiver disc diameter / mm	Pressure $\times 10^{-6}$ mbar	Disc-separation / mm	ν
92.00	3.2	4.3	0.95 ± 0.01
84.64	3.5	3.7	0.94 ± 0.01
84.64	3.5	6.5	0.94 ± 0.01
78.04	4.0	3.7	0.93 ± 0.01
78.04	4.0	6.5	0.92 ± 0.01
70.00	7.0	4.0	0.95 ± 0.01
70.00	7.0	6.8	0.95 ± 0.01

Table 7.3 Measurements of the fall off of deflection at high sender speeds.

For a given disc diameter there is no increase seen in fall off of deflection for increasing disc-separation. This is to be expected since the relative change in disc-separation was very small.

The effect of reducing the receiver diameter on the high speed fall off of deflection is not conclusive from the data. Further experiments to investigate this are needed.

As in Chapter 4 it is to be concluded that to avoid the high speed fall off effect the sender speed should be kept below 30 krpm.

7.7 CONCLUSIONS

The characteristics of an RDG for which the receiver disc is smaller than the 92 mm diameter sender disc have been investigated experimentally for three receiver discs of diameters 84.64 mm,

78.04 mm and 70.00 mm. For each case, as expected, there was a linear increase of deflection with pressure. This is the same behaviour as was seen for the case of same sized discs. At a given pressure using the largest receiver discs and the smallest disc-separations resulted in the highest deflections.

The edge effect ε' loss of torque has been measured for each receiver disc. This edge effect is due to a loss of molecules from the discs' interspace, as is the case for same sized discs, which is combined with a compensating gain of molecules from parts of the sender beyond the discs' interspace, which does not occur for same sized discs. This compensating effect increases as the receiver diameter decreases.

At high sender speeds there is a fall off of deflection due to the velocity bias which is the same behaviour as for same sized discs. Sender speeds of 30 krpm or below should be used to avoid the need for a correction for high sender speed.

Measurements of pressure made using the RDG with a smaller receiver disc were in close agreement with those made by the ionization gauge. However since the edge effect is determined empirically the RDG in this form does not allow absolute pressure measurement. With the receiver smaller than the sender the sensitivity of the RDG is less than with equal sized discs. Therefore the best form of the RDG for pressure measurements is the equal sized discs configuration.

CHAPTER 8

CONCLUSIONS AND FUTURE WORK

8.1 CONCLUSIONS

As stated in Chapter 1 the current position of vacuum metrology is such that absolute measurements of pressure can only be made routinely at and above 1×10^{-5} mbar.

Viscosity gauges which exploit the principle of molecular drag by providing a relative motion between a surface and gas molecules are absolute gauges. Most viscosity gauges are of the decrement type whereby the decrease in amplitude of oscillation with time of a moving surface can be related to a measurement of pressure.

The rotating disc gauge (RDG) which was developed by Dushman (1915) is unique amongst viscosity gauges in that it operates from a static position. It has the important advantage of having a very short response and measurement time compared with decrement type viscosity gauges. There has not been an RDG developed in the original form since the first RDG. The RDG is in principle an absolute gauge and it was the aim of the project to develop and assess an RDG of the original design using modern day technology. In order to measure pressure absolutely the characteristics of the RDG which had not been previously reported had to be determined. It was the ultimate aim of the project to measure pressures in the high vacuum range. The technical details of the RDG developed were fully described in Chapter 3.

In Chapter 4 the measured deflection of the receiver was found to be proportional to pressure measured by a Bayard-Alpert ionization gauge (IG) in the 1×10^{-7} to 1×10^{-5} mbar range as is expected.

The edge effect loss of molecular torque due to the Knudsen cosine distribution of molecules which leave the sender and travel out of the discs' interspace was measured. Experimental measurements of this loss agreed very well with the analytical prediction when the sender speed was 30 krpm or below. At a sender speed of 50 krpm where the analytical expression for the the edge effect is not valid, the

experimental data was in good agreement with a Monte Carlo simulation. This geometrical edge effect loss was found to be the same for helium and nitrogen as is expected from the theory. At low sender speeds there is a 17% loss of torque at a typical working disc-separation of 4.3 mm.

At disc-separations above (the safe minimum) 3 mm the deflections scaled in the same ratio as the indicated pressures. This showed that there was full conductive access to the discs' interspace and therefore a reliable measurement of the vacuum was made.

Measured deflections were proportional to sender speed up to about 35 krpm. Beyond this there was a fall off from linearity. This was due to the high speed velocity bias causing the molecules to move forward out of the discs' interspace. This high speed loss of torque combines with the geometrical loss. The data for the high speed loss fitted well with a Monte Carlo simulation. The magnitude of this high speed effect was a fall off from linearity of about 4 to 5% at 50 krpm for disc-separations of 4 to 5 mm. It was expected that the fall off would increase with increasing disc-separation. The data for this were not conclusive and further experiments are necessary. These would be likely to necessitate changes to the apparatus in order to operate at significantly larger disc-separations.

Further high speed experiments showed that the magnitude of the high speed fall off increased to 13% for krypton and reduced to about 3% for hydrogen. This was expected since the mean molecular velocity decreases and hence the sender's velocity bias becomes more significant as the molecular mass M of molecules increases.

The important conclusion from this work was that for the analytical expression of the edge effect to hold for all gases and hence for absolute measurements of pressure to be made the sender speed should be kept at 30 krpm or below.

Repeated measurements of deflection under constant conditions showed extremely high reproducibility of less than 1% at a pressure of 3.5×10^{-6} mbar where the mean deflection was 119 mm. At 3.5×10^{-7} mbar the deflection was consistently measured at 11.5 mm. This gives great confidence in individual measurements of deflection.

The only non-directly determinable quantity in the operating equation of the RDG was the tangential momentum accommodation coefficient σ_{RDG} of a gas on the receiver surface. In Chapter 5 the results were given of comparisons made of the RDG with a spinning rotor gauge (SRG) in (dominantly) nitrogen to determine the value of σ_{RDG} on the highly ordered, flat, smooth and adsorbate covered silicon receiver surface. The results showed almost perfect agreement of the RDG and the transfer standard SRG which indicated a value of σ_{RDG} of unity. This agrees with unity values of σ on similar surfaces found by many other workers (for example Thomas, 1981).

The systematic uncertainties associated with quantities in the RDG's operating equation were calculated to be ±2% for a deflection of 200 mm and ±20% for one of 5 mm. Other uncertainties were harder to quantify but were all relatively small. Pressures of 1×10^{-5} mbar can be measured with an uncertainty below ±3%.

The RDG developed is capable of measuring in the range 1×10^{-7} to 1×10^{-3} mbar. Changes to reduce the mass of the receiver suspension and increase the sensitivity of the torsion fibre should enable measurements in the 10^{-9} mbar range. The suppression of vibration would be important for the more sensitive fibre.

The results of further comparisons of the RDG with the same SRG were given in Chapter 6. It was found that the values of σ_{RDG} of hydrogen, helium, methane, water vapour, nitrogen, air, carbon dioxide and krypton were unity on the smooth silicon receiver surface. The predicted (relative molecular mass)$^{1/2}$ dependence of the sensitivity of the RDG was confirmed for the first time by these experiments in the range of gases listed above. For rough silicon and titanium receiver surfaces the measured relative values of σ_{RDG} for hydrogen, helium, water vapour, nitrogen and air were a few percent above unity. For the scale of roughness of the discs the results agree with those of other workers, for example Fremerey (1982), on similar surfaces. The main conclusion to be drawn from these experiments was that by using the smooth receiver surface the RDG can be considered to be a *universal absolute* total pressure gauge. For rough receiver surfaces the RDG needs to be calibrated for each gas.

By comparison of RDG and IG measurements of pressure the relative sensitivity factors of the IG were measured as 0.40, 0.20, 1.47, 0.85, 0.99, 1.32 and 1.79 for hydrogen, helium, methane, water vapour, air, carbon dioxide and krypton respectively. These agree with the manufacturer's values (Vacuum Generators, 1989) and those of other workers.

The RDG characteristics investigated for the equal sized discs configuration were repeated for several cases where the receiver disc was smaller than the 92 mm diameter sender. The measured deflection for receiver discs of diameter 84.64 mm, 78.04 mm and 70.00 mm was proportional to pressure. The magnitude of the geometrical edge effect loss of torque was less than for the case of equal sized discs and decreased as the receiver diameter decreased. This is because there is a compensating gain of molecules into the discs' interspace from molecules which leave the sender at radial distances beyond the radius of the receiver. This compensates, to a certain degree, the loss of molecules from the discs' interspace due to the Knudsen cosine distribution. For receivers of diameter 92 mm, 84.64 mm, 78.04 mm and 70 mm the loss at a disc-separation of 4 mm was 16%, 12%, 10% and 9% respectively. Thus when the receiver is much smaller than the sender this loss tends to zero. It was again found that for the smaller receiver discs there was full conductive access to the discs' interspace. The high speed loss of torque was found to start at 35 krpm and to be of the same order as that for equal sized discs. Further experiments are needed to investigate the effect of disc-separation on the high speed loss. Since there is no analytical expression to describe the edge effect loss in unequal sized discs and since the sensitivity is lower than for equal sized discs then the equal sized discs configuration should be used for absolute pressure measurement.

In short a novel piece of instrumentation has been developed and all the initial aims of the project have been met. The RDG can be used as a *universal absolute* pressure gauge in the 1×10^{-3} to 1×10^{-7} mbar range for calibration purposes and has the potential to measure in the 10^{-9} mbar range. The work therefore considerably extends the range of primary pressure gauges and could reshape current methods of high vacuum gauge calibration.

8.2 FUTURE WORK

There are several changes and improvements to the RDG which the author would like to suggest. The lower pressure limit of the RDG was discussed in Chapter 5. The changes to the receiver suspension described in Chapter 5 would be needed to reach the ultimate sensitivity.

The present maximum measurable deflection is about 250 mm. By adapting the vacuum chamber, by placing internal mirrors or by replacing the vacuum viewport by a glass dome, greater visibility would be possible and the dynamic range of the RDG would be increased.

The method of measurement of deflection of the receiver could be changed. A technique whereby the deflection of the receiver caused a change in capacitance of two plates, one of which is fixed on the receiver, could be used to measure small deflections.

Using a torsion fibre means that the RDG has to be reset before another measurement can be made. A torque free suspension could be used to give continuous pressure measurements. Here the torsion fibre is superseded by a freely suspended receiver (above the sender) and the angular acceleration of the receiver is used to measure pressure. A magnetic suspension was developed by workers at the University of Sussex (Whorlow, 1990) but had remanent magnetism and asymmetry problems and was not pursued. For a torque free suspension using the same technique of signal measurement as the spinning rotor gauge (SRG) the sensitivity using the present receiver is theoretically five times greater than the SRG, see Appendix 1, and should therefore be able to measure high vacuum pressures. This sensitivity could be improved by reducing the moment of inertia of the receiver. In a magnetic suspension residual magnetic drag problems would be present as they are for the SRG and an electrostatic suspension would be needed to avoid this problem.

A high speed sender could be adapted from a magnetic levitation turbomolecular pump (Edwards, 1992). These pumps do not use oil lubrication for their bearings, instead they use magnetic levitation of their rotor blade stack. This would avoid the present limit to the base pressure of the vacuum system due to vapour backstreaming from

the bearing grease of the high speed rotor, see Chapter 3. The blades of an adapted turbomolecular pump could be left so that it could still function as a pump with the high speed sender disc at the top of its blade stack. It is therefore feasible to have simultaneous pumping and pressure measurement which could act as a measure of the efficiency of the turbomolecular pump.

At pressures where the mean free path is smaller than the disc-separation the RDG could be used as a classical viscometer to measure gas viscosity. The transition regime could be usefully investigated by the RDG.

In UHV a deposition source could be used to deposit different materials onto the receiver surface. Accurate measurements of the tangential momentum accommodation coefficients σ of various gases on bare surfaces and others could then be made. This would be of great interest especially in comparison to the measurements of reduced σ values on bare surfaces previously reported (Lord, 1977).

The receiver surface could be roughened to various degrees to investigate the theoretically predicted upper value of $\sigma = 4/\pi$ (Fremerey, 1982). In situ surface analysis such as auger electron spectroscopy would be useful to determine the state of the receiver surface.

The work discussed in Chapter 4 showed that the fall off of deflection with sender speed would lead to a maximum in the deflection versus sender speed plot. This could be investigated experimentally by using a higher speed sender. More experimental work is needed to investigate the predicted increase in high speed fall off with increasing disc-separation.

At the time of writing work was in progress (Pert, 1993) to derive an analytical formula to incorporate the high speed fall off effect and to produce an edge effect correction factor applicable for all speeds.

The predicted variation of RDG sensitivity with $(\text{temperature})^{1/2}$ could be investigated. At low temperatures the mean velocity of molecules will decrease and thus the high velocity bias of the sender will become more significant which would provide a parameter to the high

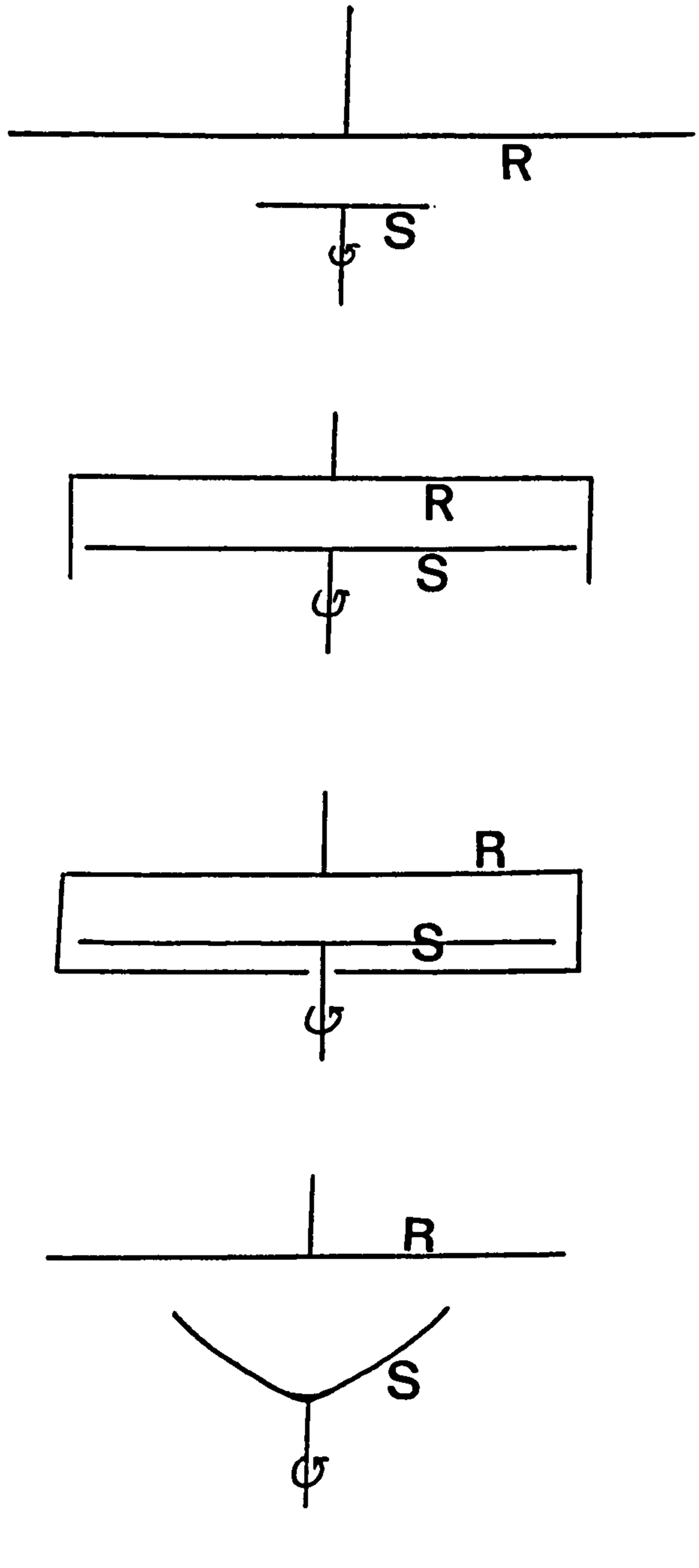

Figure 8.1 Possible rotating disc gauge geometrical variations.
R Receiver disc, S Sender disc.

speed fall off effect. Additionally the effect of varying the temperature of the receiver could be investigated by local heating or cooling of the receiver disc.

The work on the characteristics of the RDG and comparisons of it with an SRG showed that it can be classified as a *universal absolute* gauge for high vacuum pressure measurements. Clearly the RDG has potential as a means of primary pressure measurement and could be used to calibrate high vacuum gauges. This would need further confirmatory comparisons with, for example, a static expansion calibration unit. Characterizing a vacuum is the most likely industrial application of the RDG. As a marketable product a torque free suspension form of the RDG is the most likely.

The RDG could be used as a classical decrement type gauge. A measurement of deflection versus time would enable a determination of the rate of amplitude decrement of the receiver suspension and hence a measurement of pressure. The RDG could be used in the constant deflection mode suggested by Drawin (1965). This method uses the RDG to measure pressure by measuring the sender speed needed to keep the deflection or (in the case of the torque free suspension) the angular acceleration constant.

Possible variations in the sender and receiver disc sizes other than equal sized discs and the smaller receiver disc already investigated are shown in figure 8.1. These designs would constitute a means of further analysis of the edge effect and would increase the sensitivity of the RDG by increasing the molecular torque sensed by the receiver.

APPENDIX 1

TORQUE FREE SUSPENSION

Consider the case where the receiver is suspended freely above the sender. The theoretical treatment for a rotating disc gauge with equal sized sender and receiver discs is the same as that given in Chapter 2. The difference in this case is that the molecular torque G developed by the high speed sender is not measured statically, instead the torque developed is equal to the rate of change of angular momentum of the receiver:

$$G = \varepsilon\, \sigma_{RDG}\, \Omega\, R^4 \left(\frac{\pi}{8000\, R_o} \right)^{1/2} \cdot \frac{M^{1/2}}{T^{1/2}} \cdot P \qquad \text{(A1.1)}$$

$$= I\, \dot{\omega}_{RDG} \qquad \text{(A1.2)}$$

if I, the moment of inertia of the freely suspended receiver, is constant with time. $\dot{\omega}_{RDG}$ (the measured signal) is the rate of change with time of the receiver's angular velocity. The other values have their usual meanings given below.

Thus the pressure measured with the RDG is

$$P_{RDG} = \frac{I\, \dot{\omega}_{RDG}}{\varepsilon\, \sigma_{RDG}\, \Omega\, R^4 \left(\frac{\pi}{8000\, R_o} \right)^{1/2}} \cdot \frac{T^{1/2}}{M^{1/2}} \qquad \text{(A1.3)}$$

The values are: T is the absolute thermodynamic temperature (296 K at room temperature), M is the relative molecular mass (28 for nitrogen), R is the discs' radius (46 mm), Ω is the radian frequency of the sender, σ_{RDG} is unity for the smooth silicon receiver surface and ε is the geometrical edge effect loss factor. $I_{SUS} = 9.15 \times 10^{-6}$ kgm^2 for the receiver suspension described in Chapter 3. For the limit of touching discs such that the high speed fall off effect is negligible, ε is unity and the maximum sender frequency of 50 krpm is considered. Considering nitrogen and inserting the above values into equation A1.3 gives

$$\dot{\omega}_{RDG} = 5.4 \times 10^{2} \text{ P rads sec}^{-2} \qquad \text{(A1.4)}$$

where the pressure P is in mbar.

The operating equation of the SRG below (see Chapter 1) is:

$$\frac{-\dot{\omega}_{SRG}}{\omega_{SRG}} = \frac{10\ \sigma\ P}{\pi\ r\ \rho\ \bar{v}} \qquad \text{(A1.5)}$$

where $-\dot{\omega}_{SRG}\ /\ \omega_{SRG}$ is the relative deceleration rate and σ is the effective tangential momentum accommodation coefficient ($\simeq 1.0$) of the levitated ball which is typically of radius r = 2.25 mm and density $\rho = 7.8 \times 10^{3}$ kg m^{-3}. $\bar{v}$ is the mean thermal velocity, the operating frequency of the ball is a maximum of 425 Hz and P is the measured pressure.

Combining equations A1.3 and A1.5. gives

$$\frac{\dot{\omega}_{RDG}}{\dot{\omega}_{SRG}} = \frac{\pi\ \Omega\ R^{4} r\ \rho}{10\ \omega_{SRG}\ I} \qquad \text{(A1.6)}$$

For the values given earlier the relative sensitivity $\dot{\omega}_{RDG}\ /\ \dot{\omega}_{SRG} \simeq 5$. This assumes that the measurement technique is the same as for the SRG. This ratio increases as the moment of inertia of the receiver suspension decreases.

REFERENCES

Authors	Year	Location
Alexeff I.	1961	*Transactions of the AVS 8th Vacuum Symposium and the 2nd International Congress of Vacuum Science and Technology*, Volume 1, p472.
American Vacuum Society	1989	*Recommended Practice on the Use of Spinning Rotor Gauges*, September.
Anderson H.L.	1981	*Physics Vade Mecum*, AIP, New York.
Austin W.E. Leck J.H.	1972	*Vacuum* 22, 331.
Bartmess J.E. Georgiadis R.M.	1983	*Vacuum* 33 149.
Beams J.W. Young J.L. Moore J.W.	1946	*Journal of Applied Physics*, 17, 886.
Beams J.W. Spitzer D.M. Wade J.P.	1962	*Review of Scientific Instruments*, 33, 151.
Beavitt A.R. Campbell D.S. Chapman B.N.	1968	*Journal of Physics E*, 1, 45.
Bialas H.	1984	*Physics Letters*, 103A, 35.
Blakenstein E.	1923	*Physical Review*, 22, 582.
Bowden F.P. Lord R.G.	1963	*Proceedings of the Royal Society*, A271, 143.

Briggs W.E.	1954	*Vacuum Symposium Transactions - Committee on Vacuum Technology*, Pergammon Press, New York, p3.
Caburn-MDC Limited	1990	The Old Dairy, The Street, Glynde, East Sussex BN8 6SJ.
Cam Metric Ltd.	1990	Crystal Park, Tunbridge Lane, Bottisham, Cambridge CB5 9EA.
Carter G.	1972	*Vacuum*, 22, 225.
Chambers A. Fitch R.K. Halliday B.S.	1989	*Basic Vacuum Technology*, Adam Hilger, Bristol.
Chambers A. Chew A.D. Troup A.P.	1992	*Vacuum* 43, 9.
Chambers A. Chew A.D. Troup A.P.	1992a	*Journal of Vacuum Science and Technology*, A10, 2655.
Chew A.D.	1992	*Tables of Conversion Factors and SI Units* in *Procedures in Electron Microscopy*, John Wiley, Chichester.
Chew A.D. Chambers A. Troup A.P.	1993	*Vacuum*, in press.
Christian R.G. Leck J.H.	1966	*Vacuum* 16, 299.
Ciba-Geigy Plastics	1990	Duxford, Cambridge CB2 4QA.

Comsa G. 1977 *Proceedings of the 7th International Vacuum Congress and the 3rd International Conference on Solid Surfaces*, Vienna, Volume I, p157.
Fremerey J.K.
Lindenau B.

Comsa G. 1980 *Journal of Vacuum Science and Technology*, 17, 642.
Fremerey J.K.
Lindenau B.
Messer G.
Rohl P.

Comsa G. 1981 *Proceedings of the 8th International Vacuum Congress*, Cannes, Volume II, p218.
Fremerey J.K.
Lindenau B.

Condon E.U. 1967 *Handbook of Physics*, McGraw-Hill, New York.
Odishaw H.

de Boer J.H. 1968 *The Dynamical Character of Adsorption*, Oxford University Press, London.

Dittmann S. 1989 *Journal of Vacuum Science and Technology*, A7, 3356.
Lindenau B.E.
Tilford C.R.

Drawin H.W. 1965 *Vacuum*, 15, 99.

Dushman S. 1915 *Physical Review*, 5, 212.

Dushman S. 1922 *Production and Measurement of High Vacuum*, The General Electric Review, New York.

Dushman S. 1949 *Scientific Foundations of Vacuum Technique*, John Wiley, New York.

Dushman S. 1962 *Scientific Foundations of Vacuum Technique*, John Wiley, New York.
Lafferty J.M.

Edwards High Vacuum International	1989 1992	Manor Royal, Crawley, West Sussex RH10 2LW.
Eisberg R. Resnick R.	1985	*Quantum Physics of Atoms, Molecules, Solids, Nuclei and Particles*, John Wiley and Sons, New York.
English J.	1984	*Journal of Vacuum Science and Technology*, A2, 172.
Epstein P.S.	1924	*Physical Review*, 23, 710.
Evrard R. Boutry G.A.	1969	*Journal of Vacuum Science and Technology*, 6, 279.
Filippelli A.R. Dittmann S.	1991	*Journal of Vacuum Science and Technology*, A9, 2757.
Fitch R.K.	1987	*Vacuum*, 37, 637.
Fluke MFG Co. Inc.	1989	Everett, Washington, USA.
Fremerey J.K.	1971	*Review of Scientific Instruments*, 42, 753.
Fremerey J.K.	1972	*Journal of Vacuum Science and Technology*, 9, 108.
Fremerey J.K.	1980	*Proceedings of the 4th International Conference on Solid Surfaces and the 3rd European Conference on Surface Science*, Cannes, p869.
Fremerey J.K.	1982	*Vacuum* 32, 685.
Fremerey J.K.	1985	*Journal of Vacuum Science and Technology*, A3, 1715.

Gray D.E. 1982 *American Institute of Physics Handbook*, McGraw-Hill, New York.

Harbour P.J. 1965 *Journal of Scientific Instruments*, 42, 105.
Lord R.G.

Harris N.S. 1989 *Modern Vacuum Practice*, McGraw-Hill, Maidenhead.

Hiden Analytical Ltd. 1991 231 Europa Boulevard, Gemini Business Park, Warrington, Cheshire, WA5 5TN.

Hinkle L.D. 1990 *Journal of Vacuum Science and Technology*, A8, 2802.
Kendall B.R.F.

Hirata M. 1986 *Journal of Vacuum Science and Technology*, A4, 1724.
Isogai H.
Ono M.

Holanda R. 1973 *Journal of Vacuum Science and Technology*, 10, 1133.

Hotfoil Limited 1991 Coniston house, Ringway, Chapel Ash, Wolverhampton WV3 OUD.

Jitschin W. 1990 *Journal of Vacuum Science and Technology*, A8, 948.

Jitschin W. 1990 *Vacuum* 40, 293.
Migwi J.K.
Grosse G.

Kaye G.W.C. 1992 *Tables of Physical and Chemical Constants*, Longman, Harlow.
Laby T.H.

Keith J.C. 1963 *Journal of Research of the National Bureau of Standards*, 67D, 533.

Knudsen M. 1946 *The Kinetic Theory of Gases*, Methuen, London.

Langmuir I.	1913	*Physical Review*, 1, 337.
Leck J.H.	1989	*Total and Partial Pressure Measurement in Vacuum Systems*, Blackie, Glasgow.
Lichtman D.	1984	*Journal of Vacuum Science and Technology*, A2, 200.
Lindenau B.E.	1988	*Vacuum*, 38, 893.
Lindenau B.E. Fremerey J.K.	1991	*Journal of Vacuum Science and Technology*, A9, 2737.
Lord R.G.	1977	*Rarefied Gas Dynamics - Proceedings of the 10th International Symposium*, AIAA, New York, p531.
Lord R.G. Thomas L.B.	1977	*Proceedings of the 7th International Vacuum Congress and the 3rd International Conference on Solid Surfaces*, Vienna, p1229.
Madey T.E.	1984	*Journal of Vacuum Science and Technology*, A2, 110.
Masonlite P.J. and Co. Ltd.	1992	36 Second Avenue, Chatham, Kent, ME4 5AX.
McCulloh K.E.	1983	*Journal of Vacuum Science and Technology*, A1, 168.
McCulloh K.E. Wood S.D. Tilford C.R.	1985	*Journal of Vacuum Science and Technology*, A3, 1738.
Millikan R.A.	1923	*Physical Review*, 21, 217.
MKS Instruments Deutschland GmbH	1989	Schatzbogen 43, 8000 Munchen 82, Germany.

Morimura M. Nakagawa K. Nezu Y.	1974	*Japanese Journal of Applied Physics*, Supplement 2, Part 1, 135.
Mullard Limited	1965	Mullard House, Torrington Place, London WC1.
Nakao F.	1975	*Vacuum*, 25, 431.
National Physical Laboratory	1990	*Certificate of Calibration Reference 08C031/90V0682*, Teddington, Middlesex TW11 OLW.
Newman F.H. Searle V.H.L.	1965	*The General Properties of Matter*, Edward Arnold, London.
Nixon J.D. Kenney D.J.	1964	*Review of Scientific Instruments*, 35, 1721.
O'Hanlon J.F.	1989	*A User's Guide to Vacuum Technology*, John Wiley, New York.
Ono M. Hirata M. Kokubun K. Murakami H. Hojo H. Kawashima H. Kyogoku H.	1986	*Journal of Vacuum Science and Technology*, A4, 1728.
Pert G.J.	1993	To be published.
Poulter K.F.	1977	*Journal of Physics E*, 10, 112.
Radio Spares Components Ltd.	1991	PO Box 99, Corby, Northants NN17 9RS.
Redgrave F.J. Downes S.P.	1988	*Vacuum*, 38, 839.

Reich G. 1982 *Journal of Vacuum Science and Technology*, 20, 1148.

Roberts G.T. 1970 *Journal of Physics E*, 3, 806.

Roberts J.K. Miller A.R. 1960 *Heat and Thermodynamics*, Blackie, Glasgow.

Roth A. 1976 *Vacuum Technology*, North-Holland Publishing Co., Amsterdam.

Saunders S.W. Brown H.R. 1991 *The Philosophy of Vacuum*, Clarendon Press, Oxford.

Setina J. 1990 *Vacuum*, 40, 51.

Spectra-Physics Inc. 1978 1250 West Middlefield Road, Mt. View, California 94042, USA.

Squires G.L. 1985 *Practical Physics*, Cambridge University Press, Cambridge.

Steckelmacher W. 1966 *Vacuum*, 16, 561.

Steckelmacher W. 1987 *Vacuum*, 37, 651.

Taborek P. Goodstein D. 1979 *Review of Scientific Instruments*, 50, 227.

Thomas E. Leyniers R. 1974 *Japanese Journal of Applied Physics*, Supplement 2, Part 1, 147.

Thomas L.B. 1981 *Rarefied Gas Dynamics - Proceedings of the 12th International Symposium*, AIAA, New York, p83.

Thomas L.B. Lord R.G. 1974 *Rarefied Gas Dynamics - Proceedings of the 8th International Symposium*, Academic Press, New York, p405.

Truffier J.L. 1974 *Japanese Journal of Applied Physics*, Choumoff P.S. Supplement 2, Part 1, 139.

Vacuum Generators Ltd. 1989 Maunsell Road, Hastings, East Sussex TN38 9NN.

Van Dyke K.S. 1923 *Physical Review*, 21, 250.

Wacker Chemical Co. 1990 Mount Felix, Bridge Street, Walton on Thames KT12 1AS.

Wenaas E.P. 1971 *The Journal Of Chemical Physics*, 54, 376.

Weston G.F. 1979 *Vacuum*, 29, 277.

Weston G.F. 1985 *Ultrahigh Vacuum Practice*, Butterworths, London.

Whorlow R.J. 1990 University of Sussex, private communication.

Wu Y. 1966 *Annalen der Physik*, 18, 321.

Wutz M. 1989 *Theory and Practice of Vacuum Technology*,
Adam H. Vieweg, Braunschweig.
Walcher W.

Zamojski W. 1982 *Journal of Physics E*, 15, 809.

Vacuum/volume 43/numbers 1/2/pages 9 to 13/1992
Printed in Great Britain

0042-207X/92$5.00+.00

Preliminary observations of the behaviour of an absolute gauge of the rotating disc type in high vacuum

A Chambers and A D Chew, *Department of Physics, University of York, York, UK*
and
A P Troup, *Edwards High Vacuum International, Crawley, Sussex, UK*

A proposal by Langmuir for an absolute vacuum gauge exploiting the torque communicated by molecular drag between a high speed rotor and a sensor in close proximity has been further investigated experimentally. The rotor consists of a metallic disc which replaces the normal blade structure of a turbomolecular pump, and which rotates at speeds up to 50,000 rpm. The sensor is a silicon disc of matching size suspended on a torsion fibre and placed coaxially and parallel to it. Early observations in the pressure range 10^{-5}–10^{-6} mbar are reported, together with the measurement of edge effects and other phenomena.

1. Introduction

Frictional effects between gases and surfaces have long been recognised as a basis for the operation of vacuum gauges. In 1965, Drawin[1] reviewed comprehensively the development of friction-based instruments and drew attention to the rotating disc gauge (RDG) a design for which was first suggested by Langmuir[2] and implemented by Dushman[3]. More recently the spinning rotor gauge[4] has come to have an important place in vacuum measurement technology and the early promise of the RDG seems not to have been pursued. Given the advances associated with the development of turbomolecular pumps, which have enabled the routine achievement of rotation speeds of 50,000 rpm in high vacuum, we have set out to investigate further the performance of an RDG, and present in this paper some early findings on a device of this type which we have constructed.

2. Theory

The basic geometry of an RDG arrangement is shown in Figure 1. A 'receiver' disc of radius R is suspended at a height t above a 'sender' disc of the same radius, which rotates with a radian frequency Ω. At relatively high pressures where the mean free path λ in the gas is comparable with or smaller than the separation t the device would be a viscometer, dependent for its action on viscous forces. At low pressures, the region of interest here, $\lambda \gg t$, molecular flow conditions operate, i.e. molecule–surface collisions dominate gas behaviour and the coupling is by molecular drag. In the rotating reference frame of the sender disc molecules leave its surface in all directions distributed in solid angle according to Knudsen's cosine law, the circle C depicting the sphere which represents this distribution. On average molecules leave the surface perpendicularly. In the laboratory reference frame each molecule departing from locality P at radial distance r has a velocity bias $v_B = r\Omega$ superimposed on its thermal velocity and correspondingly an imposed momentum mv_B parallel to the discs and tangential to the circular motion. Molecules travel unobstructed across the interspace between sender and receiver, and the imposed momentum may be accommodated at the upper surface to produce a force and hence a torque on the upper disc. The edge of the sender disc has a speed $R\Omega$ which for $R = 4.6$ cm and $\Omega = 2\pi \times 833.3$ Hz, corresponding to 50,000 rpm, is equal to 241 m s^{-1}. Bias speeds v_B imparted to departing molecules are therefore of the order of mean molecular speeds (470 m s^{-1} for nitrogen molecules at 295 K).

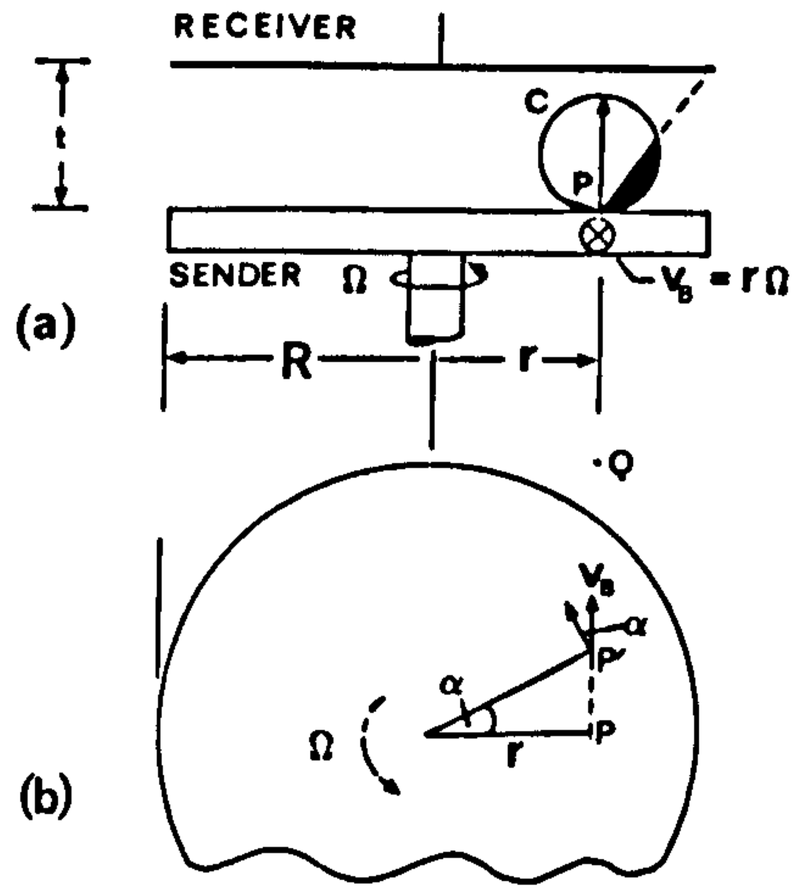

Figure 1. (a) Geometry of an RDG, side view. The shaded part of the Knudsen sphere represents loss of molecules; (b) the top view, with receiver imagined transparent. Molecule from P on sender arrives at P' on receiver. Q = miss.

The situation can be modelled by assuming that on average molecules leave perpendicularly from a particular locality P of the sender to arrive, after a time of flight across the interspace, at P' on the receiver, as shown in plan in Figure 1(b). At P', momentum $\sigma m v_B$ is given up to the receiver where σ is the tangential momentum accommodation coefficient and m is the mass of a molecule, thus creating an impulsive torque $(\sigma m v_B \cos\alpha)(r/\cos\alpha) = \sigma m v_B r$ about the centre of the receiver disc. For an annulus of width dr at radius r and a number density n of molecules with associated impingement rate $J = \frac{1}{4}n\bar{v}$, where $\bar{v}$ is the mean thermal velocity, the torque created is

$$dG = 2\pi r dr \cdot J \cdot \sigma m v_B \cdot r$$

$$= 2\pi\sigma m J \Omega r^3 dr$$

since $v_B = r\Omega$.

Ignoring (for the moment) the loss of molecules out of the interspace, a loss which of course becomes increasingly important towards the edge of the sender disc, integration of the above expression over the whole area gives a total torque

$$G = \frac{\sigma m \pi J \Omega R^4}{2}.$$

Substituting for J and using the results $n = p/kT$ and $\bar{v} = (8kT/\pi m)^{1/2}$ from kinetic theory yields

$$G = \sigma\Omega R^4 \left(\frac{\pi}{8k}\right)^{1/2} \left(\frac{m}{T}\right)^{1/2} p, \qquad (1)$$

an equation first derived by Dushman[3]. Rewriting this in terms of relative molecular mass M (=28 for N_2) leads to

$$G = \sigma\Omega R^4 \left(\frac{\pi}{8000 R_0 T}\right)^{1/2} M^{1/2} p, \qquad (2)$$

where R_0 is the universal gas constant. If more than one gas is present this equation must be modified to sum the torques from individual components so that, in an obvious notation

$$G = \Sigma G_i = \Omega R^4 \left(\frac{\pi}{8000 R_0 T}\right)^{1/2} \Sigma \sigma_i M_i^{1/2} p_i, \qquad (3)$$

with p_i being the partial pressure of gas i in the interspace. To allow for the escape of molecules referred to earlier and the consequent loss of torque (which will be referred to as the edge effect) a function $\varepsilon = \varepsilon(t/R)$ may be introduced to modify the torque expressions given so that equation (2), for example, becomes

$$G = \sigma\Omega R^4 \left(\frac{\pi}{8000 R_0 T}\right)^{1/2} M^{1/2} p \cdot \varepsilon(t/R), \qquad (4)$$

where

$\varepsilon \to 1 \quad t \ll R$ (discs very close)

and

$\varepsilon \to 0 \quad t \gg R.$

As will be described we have been able to deduce something about ε by experiment.

If the torque is to be measured statically by a torsion fibre, as depicted in Figure 2(a), then at steady state there will be a deflection ϕ such that $G = c\phi$ where c is the torque per unit twist. c may be predicted from the dimensions and elastic properties of the fibre or preferably, deduced directly from the period of torsional oscillation τ of a suspended mass of moment of inertia I using the well known result $\tau = 2\pi(I/c)^{1/2}$. The equation governing the experimental determination of pressure would therefore be

$$\sigma\Omega R^4 \left(\frac{\pi}{8000 R_0 T}\right)^{1/2} M^{1/2} p\varepsilon = c\phi. \qquad (5)$$

In this equation, the quantities Ω, R, T, c and ϕ are directly measurable. Additional knowledge of the edge effect ε, the gas type (M) and the value of its tangential momentum accommodation coefficient σ would enable an absolute determination of the pressure. In order that this should be representative of the vacuum surrounding the device requires, of course, that the disc separation be such as to allow free access of gas into the interspace.

Inserting typical numbers into equation (5), taking σ and ε to be unity, and considering nitrogen gas between 92 mm diameter discs and a rotation speed of 50,000 rpm leads to a deflection ϕ of 0.43° corresponding to a deflection of 15 mm on a scale at 1 m for a pressure of 10^{-6} mbar.

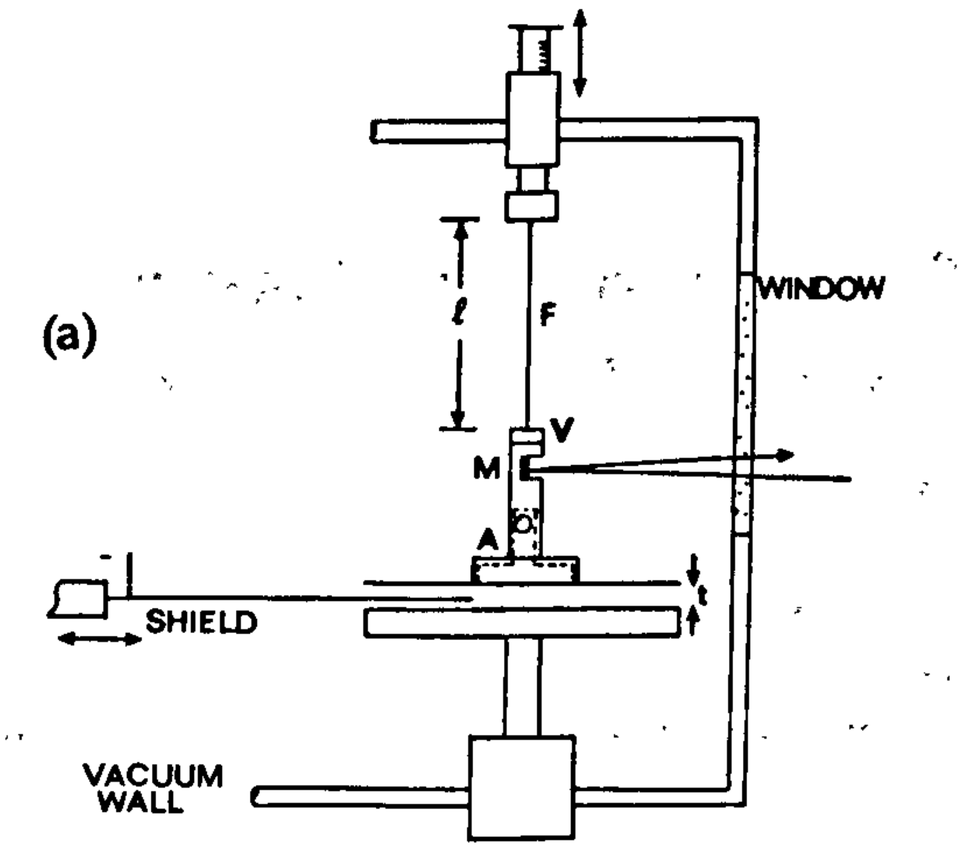

Figure 2. (a) Schematic diagram of the experimental arrangement. See text for meaning of symbols; (b) the response of the system to a step function, showing the variation of the displacement of the laser spot from quiescent position with time.

3. Experimental

The device we have constructed is shown schematically in Figure 2(a). An Edwards EXT 200 turbomolecular pump has been modi-

fied[5] by replacing its pumping blades with an aluminium alloy disc of diameter 92 mm. This constitutes the sender. It can be rotated at speeds of up to 51,000 rpm. The receiver consists of a silicon disc of the same diameter, made from a silicon wafer[6]. This is attached by a very small amount of epoxy to an aluminium piece A, hollow in part, which carries a small mirror M for the optical detection of rotation. At the top a vice V clamps the torsion fibre F. The mass of the disc plus piece A is 26.7 g and its moment of inertia 9.1×10^{-6} kg m^{-2}. The fibre F is rectangular in cross-section (0.17×0.03 mm) and made of phosphor bronze. It is of the type used typically in galvanometer suspensions and is supplied by Cam Metric Ltd[7]. Its upper support is a vice mounted on a vertical linear motion drive so that the separation t of the sender and receiver discs can be varied. The fibre length between clamps is 58.4 mm. The period of torsional oscillation of the receiver assembly on the suspension is 23.4 s.

The value of c, determined from the oscillation of a mass of simple shape and known moment of inertia comparable with that of the receiver assembly, is 6.61×10^{-7} Nm. Care is taken to ensure that the discs are parallel and concentric. A shield consisting of a flat stainless steel plate 1.5 mm thick normally separates the discs and can be moved in and out by a linear motion drive. An adjacent window of the vacuum system enables the deflection of a laser beam reflected off M to be monitored.

The system is housed in a stainless steel ion-pumped vacuum system equipped with various gauges including a hot cathode ionisation gauge[8]. Residual gas analysis is carried out with a HAL I 100 instrument[9] and a fine leak valve enables the pressure to be raised above base pressure by the ingress of atmospheric air. At present the system is not fully baked and the lubricating grease of the turbo drive restricts the base pressure to 7×10^{-7} mbar, but this proves quite adequate for preliminary investigations in the range $1\text{–}10 \times 10^{-6}$ mbar.

The technique for observing the torque on the receiver for given conditions of pressure, sender speed and sender–receiver separation is, with the sender at speed, to remove the shield from between the discs and measure the deflection of the laser spot on an exterior scale. The shield may be removed in less than 2 s so that the receiver is effectively excited by a step function. As shown in Figure 2(b) this oscillation is induced about a centre of oscillation displaced by y from the quiescent position. y is the displacement corresponding to the torque and is related to the receiver rotation ϕ by $\phi = y/2L$ where L is the mirror-scale distance, 1088 mm. At low pressures damping is very slight and to an excellent approximation the oscillation has constant amplitude over any interval of a few oscillations. In principle, as indicated in Figure 2(b), the initial swing of $2y$ after a half period yields the necessary measurement. In practice this is checked by following a few oscillations to confirm the centre of the displaced oscillation.

4. Results and discussion

Experimental data taken under various conditions are shown in Figures 3, 4 and 5. The pressures indicated are from the digital display of the hot cathode ionisation gauge and are therefore subject to an uncertainty of $\pm 0.05 \times 10^{-6}$ mbar in the range $1.0\text{–}9.9 \times 10^{-6}$ mbar.

Figure 3 shows the deflection y vs indicated pressure plotted on a linear scale for four sender–receiver separations t. Pressure is varied over a decade using the fine leak valve, so that relative gas composition changes as atmospheric gases enter the system. Pressure values are the raw data and have not at this stage

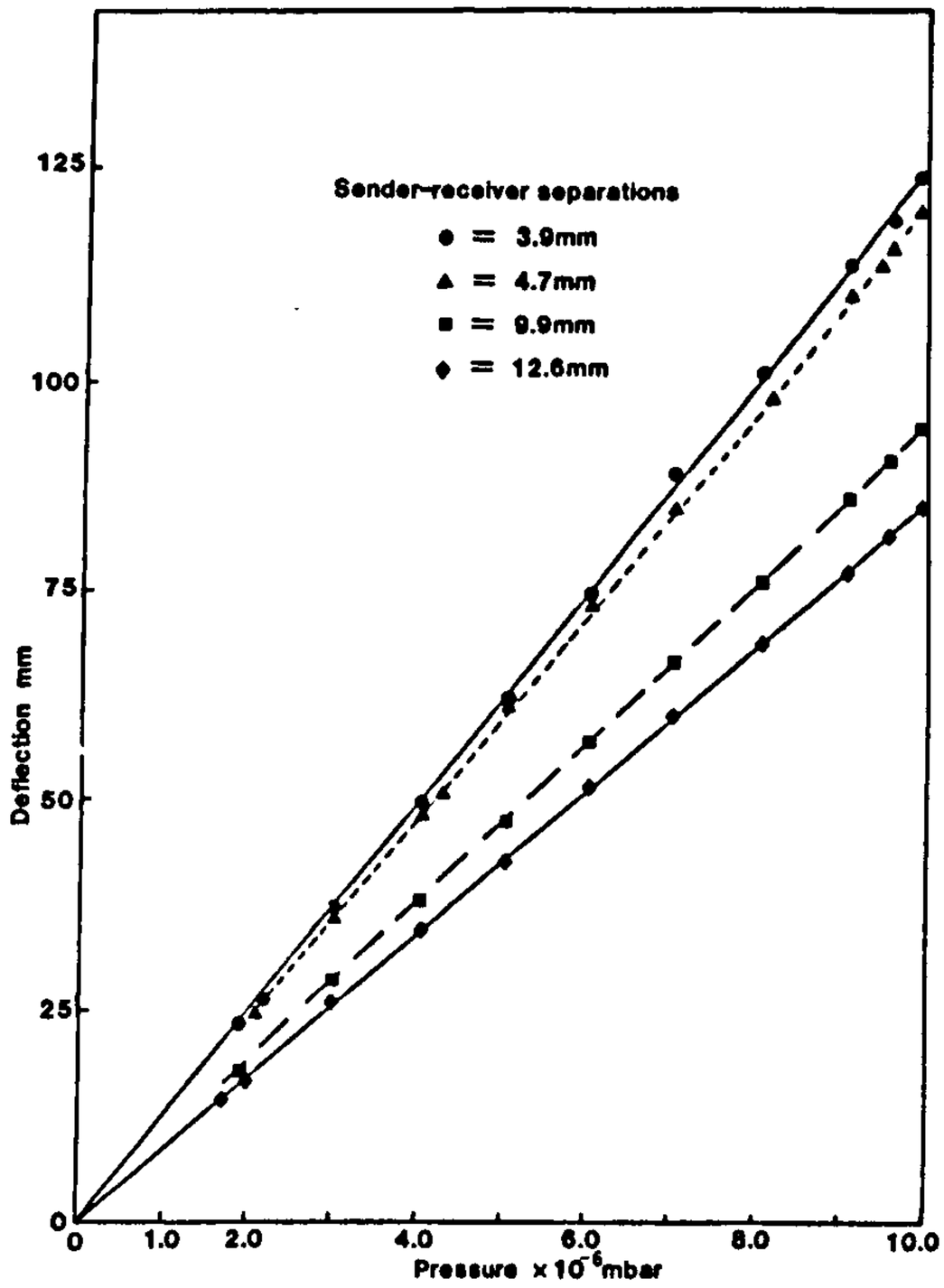

Figure 3. The dependence of deflection on gas pressure at a constant sender speed (50,000 rpm) and various sender–receiver separations.

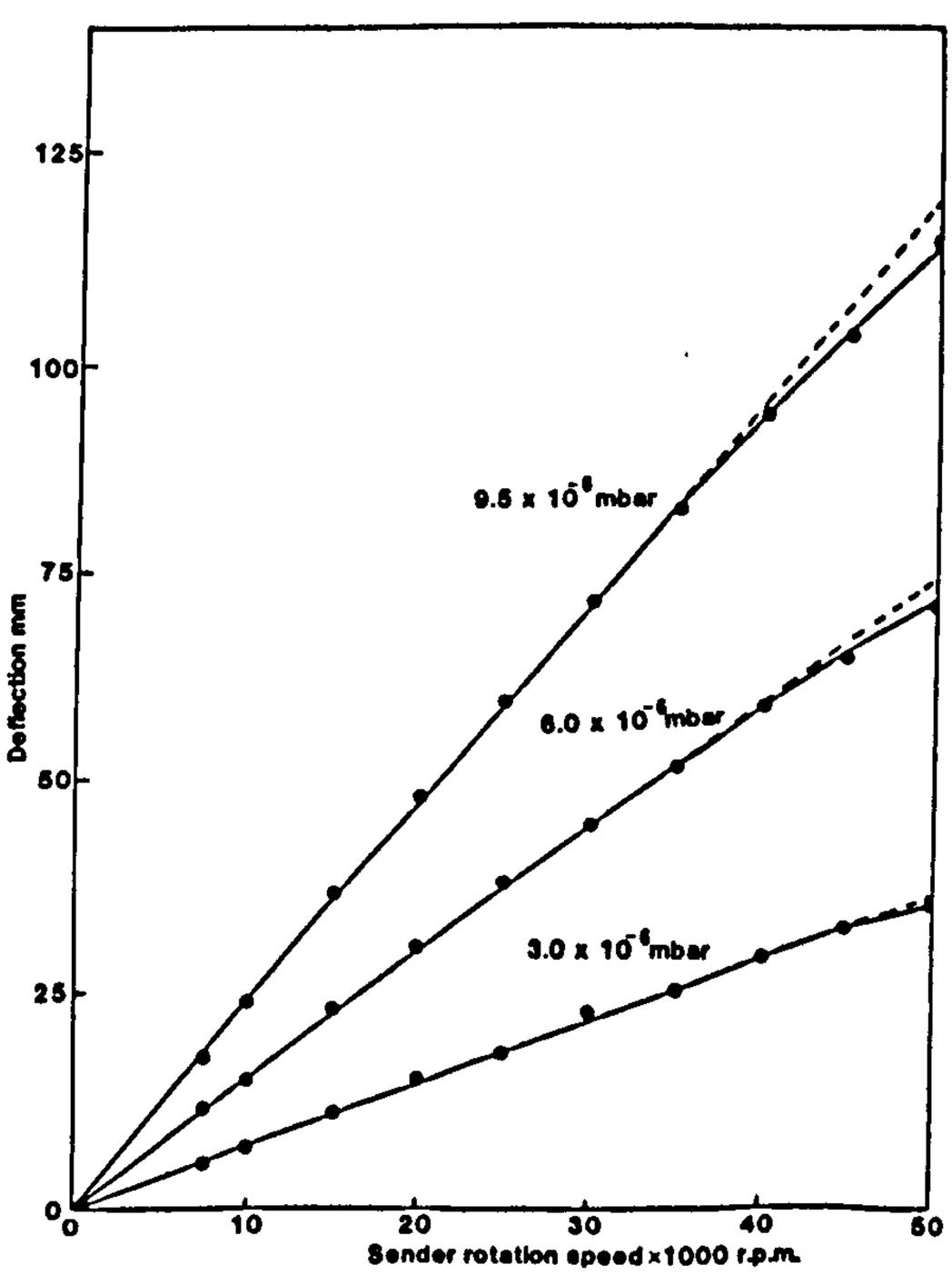

Figure 4. The dependence of deflection on sender speed at a constant sender–receiver separation (4.7 mm) and various pressures.

been corrected for the different ionisation gauge sensitivities and changing gas composition. The individual deflections y are uncertain to ± 1 mm. For clarity these uncertainties, which are small relative to the quantities displayed have not been shown. The strict proportionality, within experimental error, of deflection to indicated pressure is noteworthy. As expected the largest deflection at a given pressure corresponds to the smallest separation t where the lost torque is least. When extrapolated to low pressure the plots pass through the origin and suggest that with improvements in technique and sensitivity it should be possible to measure deflections corresponding to pressures of order 10^{-7} mbar or less.

Figure 4 shows deflections measured as a function of sender rotation speed at a fixed separation of 4.7 mm for three values of indicated pressure. The linear dependence of deflection on Ω anticipated in equation (5) is borne out by experiment up to about 40,000 rpm, above which a slight fall off from linearity becomes just discernible. This range of observed linearity considerably extends Dushman's data[3], which were limited to a maximum speed of 2000 rpm. The onset of detectable non-linearity at high speeds, which has not been observed before, is not unexpected. Inspection of Figure 1(b) shows that for molecules leaving the sender disc at or near its edge the forward velocity bias $= R\Omega$ will cause some of the forward moving molecules to miss the receiver, i.e. to pass through the plane of the receiver disc at places such as Q. Equally there will be some 'backwardly' directed molecules which now hit the receiver, but fewer (because of the Knudsen distribution) and so there is a net loss of torque. This component of loss, which will increase with speed, is a function of both speed and geometry whereas the losses out of the interspace from the sender, which were discussed earlier, are associated solely with the geometry of the arrangement. The analysis is complex and will be the subject of a future report. Centrifugal effects, in particular the possibility of centrifugal loss are not important. Even at these high speeds, the centrifugal force $mr\Omega^2$ on a molecule attached to the sender surface is less than the weakest of binding forces by many orders of magnitude.

Figure 5 shows data of deflection vs separation t at three different pressures. The variation of y with t is in each case qualitatively as might be expected. That is, the closer the plates the greater the communicated torque because of the reduced loss of molecules. The shape of the curves is precisely the same in all three cases. They scale in the ratio of indicated pressures viz 95 : 60 : 30. Since at a given separation the deflections, which are due to the gas density in the interspace, scale with the indicated pressures measured outside the interspace in the bulk of the vacuum, it is a reasonable supposition that the access of gas to the interspace is adequate. Extrapolating the curves back to zero separation then gives an estimate of what the deflection would be for zero loss, i.e. $\varepsilon = 1$. For example for the curve at the indicated

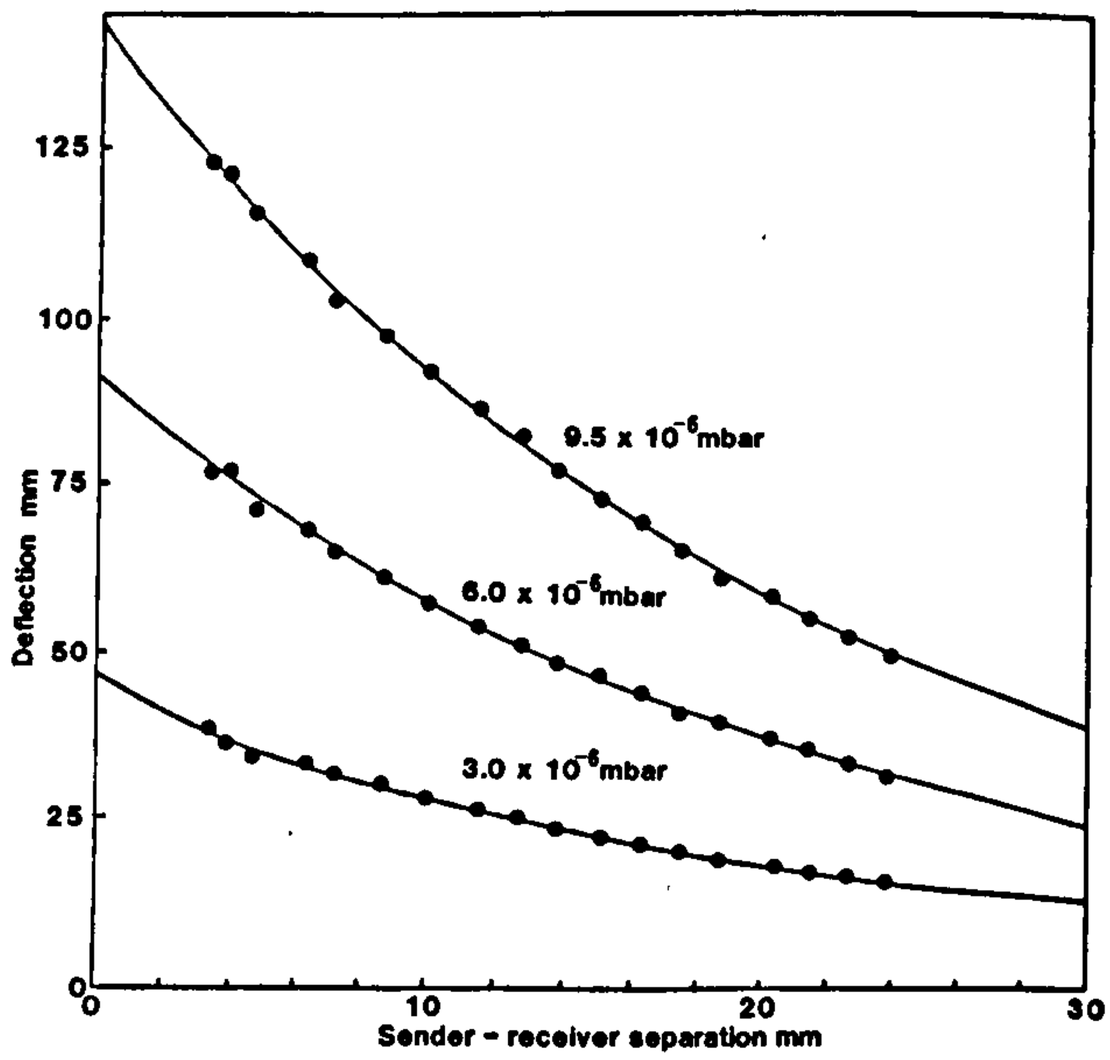

Figure 5. The dependence of deflection on sender–receiver separation at a constant sender speed (50,000 rpm) and various pressures.

pressure 6.0×10^{-6} mbar this intercept is 92 mm. We will use this result to exemplify the analysis of the data, making the simplifying assumption that $\sigma = 1$. At this indicated pressure the measured residual gas composition and partial pressure ratios to nitrogen (defined by $r_i = p_i/p_N$) are as given in Table 1, together with other relevant data.

Replacing ϕ by $y/2L$ in equation (5) and rearranging gives

$$p = \frac{c/2L}{\varepsilon\sigma\Omega R^4\left(\frac{\pi}{8000R_0T}\right)^{1/2}} \cdot \frac{y}{M^{1/2}}, \tag{6}$$

with the assumption of $\sigma = \varepsilon = 1$, $T = 295$ K and the insertion of values $\Omega = 2\pi \times 833.3$, $R = 46$ mm and $L = 1088$ mm this becomes

$$p = \beta \frac{y}{M^{1/2}}, \tag{7}$$

where $\beta = 3.2 \times 10^{-7}$ mbar mm^{-1}.

This equation predicts pressure from the displacement y caused by molecular drag of molecules of relative molecular mass M. Consider the deflection of 92 mm associated with the indicated pressure of 6.0×10^{-6} mbar. It is of interest, though not particularly meaningful, to deduce a pressure assuming that the

Table 1. Residual gas composition and other data at an indicated ionisation gauge pressure of 6.0×10^{-6} mbar together with ionisation gauge (relative) sensitivity factors taken from ref 10

Gas	H_2	He	H_2O	N_2	CO	O_2	Ar
M	2	4	18	28	28	32	40
$(M)^{1/2}$	1.41	2.00	4.24	5.29	5.29	5.66	6.32
Fractional composition (%)	37.0	0.3	3.1	14.6	34.6	3.7	6.9
r_i	2.54	0.02	0.21	1	2.37	0.25	0.47
S_i^{10}	0.44	0.18	0.9	1	1.08	0.85	1.2

residual gas consists only of nitrogen ($M = 28$). Then from equation (7) $p = 5.6 \times 10^{-6}$ mbar. That this is close to the indicated pressure is not particularly significant.

Accounting for the spectrum of residual gases and developing equation (7) with the quantities considered as partial quantities,

$$y = \sum y_i = \frac{1}{\beta} \sum M_i^{1/2} p_i$$

$$= \frac{1}{\beta} \sum M_i^{1/2} r_i p_N,$$

where p_N is the partial pressure of nitrogen.

Inserting values from Table 1 yields $p_N = 1.11 \times 10^{-6}$ mbar so that the total pressure is given by

$$p = \sum p_i = \sum r_i p_N$$

$$= 6.853 p_N = 7.6 \times 10^{-6} \text{ mbar.}$$

This is to be compared with the indicated pressure on the ionisation gauge of 6.0×10^{-6} mbar. But this indicated pressure should also be corrected for the known gas composition by allowing for the relative sensitivities, s, of the gauge for different gases. Thus

$$p_{\text{indicated}} = \sum s_i p_i = \sum s_i r_i p_N$$

and this gives, using the data of Table 1, $6.0 \times 10^{-6} = 5.64 p_N$ whence $p_N = 1.06 \times 10^{-6}$ mbar and a total pressure

$$p = \sum r_i p_N = 7.29 \times 10^{-6} \text{ mbar.}$$

The corrected ionisation gauge therefore measures the pressure as 7.3×10^{-6} mbar. The RDG measures it subject to certain assumptions as 7.6×10^{-6} mbar. No great significance can yet be attached to the pressure values deduced from the RDG; the assumptions about momentum accommodation and geometrical loss need further investigation. It is, however, encouraging that there is reasonable agreement with an ionisation gauge which is one of a batch whose calibration is traceable back to a standard. Work is in hand to model the geometrical losses computationally. It is hoped to make experimental comparisons with other gauges, including the SRG, in the near future.

5. Conclusion

We have built and characterised a molecular drag gauge of the rotating disc type, based on ideas originally proposed by Langmuir. Over a pressure range of $1\text{–}10 \times 10^{-6}$ mbar its behaviour is as predicted by a simple theory, and subject to further development, it may offer the possibility of absolute measurement of vacua at these and lower pressures. The geometrical edge effect has been measured for the first time. Computational modelling of this effect may assist the realisation of absolute measurement by allowing the use of large interspace separations which assure free access of gas.

Acknowledgements

One of us (ADC) would like to thank the SERC and Edwards High Vacuum International (EHVI) for financial support given under the CASE award scheme. Acknowledgements are also due to Mr S Fox (formerly of EHVI) who undertook adaptations to the turbomolecular pump and to the Wacker Chemical Co which donated the silicon wafers.

References

[1] H W Drawin, *Vacuum*, **15**, 99 (1965).
[2] I Langmuir, *Phys Rev*, **1**, 337 1913).
[3] S Dushman, *Phys Rev*, **5**, 212 (1915).
[4] J K Fremerey, *J Vac Sci Technol*, **A3**, 1715 (1985).
[5] Modifications carried out at Edwards High Vacuum International, Crawley, UK.
[6] Wafers (Si(111)*p*-type) supplied by Wacker Chemical Co, Walton-on-Thames, UK.
[7] Cam Metric Ltd, Cambridge, UK.
[8] Vacuum Generators Ltd (Hastings UK), Type VIG22 with Millennia IPGC controller.
[9] Hiden Analytical Ltd, Warrington, UK.
[10] J F O'Hanlon, *A User's Guide to Vacuum Technology*, p 92. Wiley, New York (1989).

Rotating disc gauge for absolute total pressure measurement in high vacuum

A. Chambers and A. D. Chew
Physics Department, University of York, York YO1 5DD England

A. P. Troup
Edwards High Vacuum International, Crawley, West Sussex RH10 2LW, England

(Received 25 September 1991; accepted 18 November 1991)

An absolute vacuum gauge exploiting molecular drag between coaxial discs, a configuration suggested by Langmuir, is being further investigated. The device operates in a range similar to that of the spinning rotor gauge. It consists of a silicon disc 92 mm in diameter suspended on a calibrated torsion fiber a few mm above a metal disc of the same size which rotates at speeds up to 50 000 rpm. Molecules leaving this rotor communicate a torque to the suspended disc by molecular drag. The angular deflection thus produced is sensed optically and is about 2° at 10^{-6} mbar. The critical factors relevant to absolute measurement, such as tangential momentum accommodation, geometry, and edge effects have been investigated and experimental comparisons with a spinning rotor gauge demonstrate that absolute pressure measurements with uncertainty better than ±5% are possible at pressures ~ 10^{-6} mbar. Measurements of similar uncertainty will be possible at 10^{-7} mbar.

I. INTRODUCTION

The measurement of pressure in the high vacuum range using devices which exploit molecular drag is possible in a number of geometries in which a gas and a surface have an imposed relative motion. Developments up to 1965 were reviewed by Drawin.[1] In the last decade particularly, there has been considerable development of the spinning rotor gauge[2] (SRG), in which pressure measurement is based on the deceleration of a levitated spinning sphere, and it has come to occupy a position of prime importance in high vacuum metrology.[3] The rotating disc gauge (RDG), suggested by Langmuir[4] in 1913, a form of which was made by Dushman[5] held out considerable promise but seems not to have been actively pursued. We have recently constructed an RDG utilizing a high speed turbomolecular pump drive, the first data from which in the pressure range 1–10 × 10^{-6} mbar has already been reported.[6] In the work presented here we have compared it with an SRG and can now justify its early promise as an absolute gauge of good accuracy for pressures at and below 10^{-6} mbar. By reducing its sensitivity, higher pressures in the molecular flow range could also be measured.

II. THEORY

It is necessary to consider molecular trajectories within an RDG in some detail, in order to justify the approximations of the analysis which lead to the governing equation of the device. The basic geometry is shown in Fig. 1(a). Above a disc of radius R which rotates at radian frequency Ω, the "sender," is suspended by one means or another at height t a "receiver" disc of the same radius. At low pressures where the mean free path λ in the gas is much greater than the sender–receiver separation t, molecular flow conditions exist and torque is transmitted to the receiver by molecular drag. Molecules desorb from a locality P at radial distance r on the sender with a bias velocity $v_B = r\Omega$ superimposed on their thermal velocity. In the sender's reference frame they are distributed in direction according to the Knudsen cosine law whose representative sphere is denoted by K in Fig. 1.

A molecule of mass m departing in the normal direction PN, because of its superimposed bias velocity v_B with respect to the laboratory reference frame, arrives at a point such as P' on the underside of the receiver as shown in Fig. 1(c), a plan view of the discs in which the receiver is imagined transparent. We imagine the receiver to be at rest. If the bias momentum mv_B is totally absorbed by the impact with the receiver an impulse mv_B is given to it in the direction shown and therefore an impulsive torque mv_Br about its center. A tangential momentum accommodation coefficient σ $(0<\sigma<1)$ may be defined to express anything less than complete accommodation $(\sigma=1)$.

For a molecule leaving P in a direction other than normal various possibilities have to be considered. Figure 1(b) shows a diametral section in which all parts of the sender (on the right hand side) are moving into the page. There are symmetrical effects which operate between certain limits and asymmetrical effects outside them. Thus in the direction PM which makes an angle θ clockwise from PN there will be a flux of molecules which arrives at the receiver with momentum mv_B at a torque arm greater than r about the center 0, but in the direction PL at θ anticlockwise from PN an equal flux will arrive at the receiver at a torque arm less than r by the same amount. The total effect is as though both fluxes left P normally to deliver torque mv_Br (or σmv_Br) per molecule to the receiver.

For molecules leaving at anticlockwise angles θ up to that specified by the direction PO the impacting molecules will create a torque promoting rotation in the same sense as that of the sender, though with a progressively smaller torque arm. For θ's beyond this the torque will oppose that rotation. However the effect of these molecules which

 0734-2101/92/042655-06$01.00

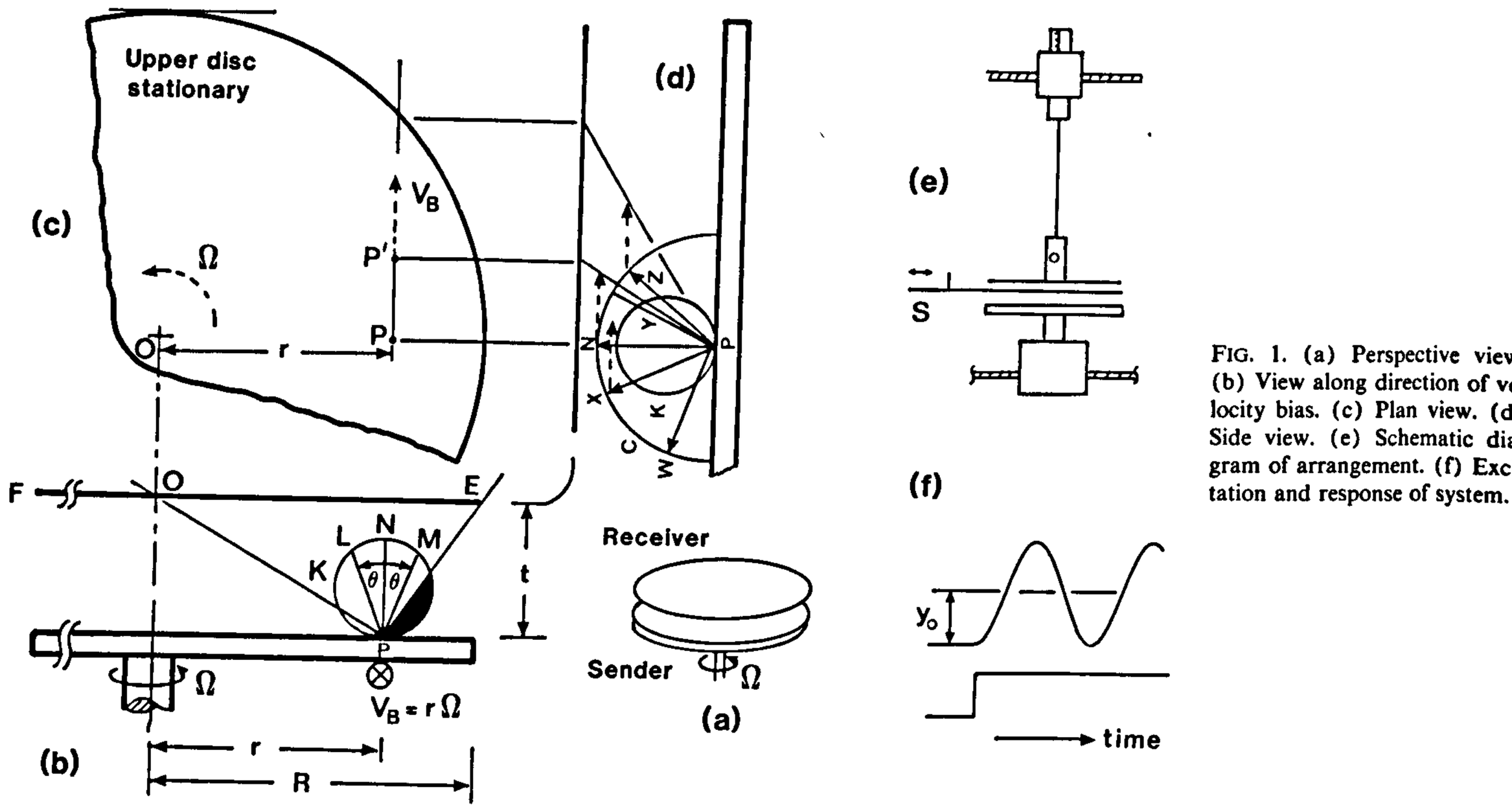

FIG. 1. (a) Perspective view. (b) View along direction of velocity bias. (c) Plan view. (d) Side view. (e) Schematic diagram of arrangement. (f) Excitation and response of system.

"cross the center" will be exactly compensated by those which similarly cross the center from the point corresponding to P at distance r on the other side. The effects therefore cancel. By similar reasoning it is clear that at even greater anticlockwise θ's from PN, at angles greater than that defined by PF to the opposite upper edge there is a loss of molecules out of the interspace, but the effect of this loss may be discounted. Had there been receiver surface at this radius to receive them, the torque would have been cancelled by a similar but opposite torque due to the flux from the other side.

The loss of molecules which desorb into solid angle at clockwise θ's greater than that specified by the line PE is of great importance. This flux is denoted by the filled in part of the Knudsen sphere K. At and near the edge of the sender disc an appreciable fraction of the molecules will be lost out of the interspace, and it is these molecules which carry the greatest bias momentum. There is therefore a considerable loss of torque. This loss, part of the "edge effect" will be further discussed in due course.

Figure 1(d) shows a side view of the arrangement at a section containing the point P. The imposed velocity bias v_B is shown by the dashed vector. K represents the Knudsen sphere and C a "velocity semicircle"—the tips of vectors drawn from P to C represent molecules which desorb with velocity v into the half space, with the flux in a given direction determined by the intersections with K. There is a complete family of semicircles such as C representing the range of molecular velocities. In any direction the distribution in velocity will be governed by the Boltzmann distribution.

Molecules leaving the sender in the normal direction PN bring momentum mv_B to the receiver surface. Those departing in direction PX bring less, those in PY more in a way which again adds to give a momentum mv_B per molecule at the upper surface, as though all molecules leave in direction PN. This symmetry again operates only within limits. Molecules desorbing in direction Z have their velocity compounded with v_B in such a way that they just reach the edge of the upper disc. For desorption from P at angles greater than this there is again lost flux, part of which is attributable to the bias velocity; correspondingly there is a gain of flux which would otherwise be lost for desorption at large anticlockwise θ's. Thus molecules desorbing in direction W just reach the receiver because of the imposed v_B.

Because of the geometrical complexities a complete analysis is not straightforward. Computational modeling is in progress and will be reported in due course. The approach which follows, based on simplified analysis with an empirical correction factor to allow for the edge effects enables the experimental data to be interpreted satisfactorily.

First imagine the plates so close together $t \ll R$ that edge losses are negligible. Because of the symmetries discussed and because, on average, desorption from a locality at r is in a normal direction, the torque transferred to the receiver from an annular ring at radius r on the sender is

$$dG = 2\pi r dr \cdot J \cdot \sigma m v_B r, \tag{1}$$

where J is the impingement rate on the upper disc corresponding to a number density n of molecules in the interspace. Kinetic theory relates J to n by the equation $J = n\bar{v}/4$ where $\bar{v} = \sqrt{8kT/\pi m}$ is the mean thermal velocity of molecules and n is related to pressure by the equation $p = nkT$. Inserting the bias velocity $v_B = r\Omega$ and integrating from $r = 0$ to $r = R$ gives a total torque

$$G=\frac{\sigma m\pi J\Omega R^4}{2}. \tag{2}$$

This equation, first derived by Dushman,[5] is the equation of perfect coupling by molecular drag between two close concentric discs. To allow for the edge effects discussed an empirical quantity $\epsilon=\epsilon(t/R)$ may be introduced where $\epsilon\to 1$ for $t\ll R$ and $\epsilon\to 0$ for $t\gg R$. Equation (2) then becomes

$$G=\epsilon\cdot\frac{\sigma m\pi J\Omega R^4}{2}. \tag{3}$$

A more practical form of the equation may be derived by substituting $J = p/\sqrt{2\pi mkT}$ from kinetic theory and introducing the universal gas constant R_0 and molar mass M to replace the Boltzmann constant k and m, respectively. The result is

$$G=\epsilon\sigma\Omega R^4\left(\frac{\pi}{8R_0T}\right)^{1/2}M^{1/2}p. \tag{4}$$

When G is measured statically by having the receiver suspended on a torsion fiber of constant c a deflection ϕ is produced at equilibrium such that $G=c\phi$. The governing equation of the device becomes

$$\epsilon\sigma\Omega R^4\left(\frac{\pi}{8R_0T}\right)^{1/2}M^{1/2}p=c\phi. \tag{5}$$

This equation offers the possibility of absolute measurement of pressure in a gas of known type if the quantities ϵ and σ are known in addition to the other directly accessible quantities. It is to be compared with the operating equation of the spinning rotor gauge, namely

$$p=\frac{r\rho}{5\sigma}\left(\frac{2\pi R_0T}{M}\right)^{1/2}\left(\frac{\dot{w}}{w}\right)-p_{\mathrm{RD}}, \tag{6}$$

where r and ρ are the radius and density of the suspended spherical rotor of the SRG, $\dot{w}/w$ is the relative deceleration rate and the term p_{RD} is the offset correction for residual drag.

III. EXPERIMENT

A. Apparatus and procedures

The RDG we have constructed has been fully described elsewhere,[6] but a recapitulation of its essential features, shown in Fig. 1(e) is appropriate. The sender is an aluminium alloy disc 92 mm in diameter attached to an Edwards EXT 200 turbomolecular pump from which the pumping blades have been removed. It can rotate at speeds of up to 51 000 rpm. The receiver is a parallel and concentric silicon disc of the same size, made from a silicon wafer, suspended by a phosphor-bronze torsion fiber with its smooth (111) face downwards. An aluminium hub carries a small mirror for the optical detection of rotation by the deflection of a laser beam, and the suspended system can be raised or lowered by a calibrated linear motion drive to vary the sender–receiver separation. The length of the fiber is 262 mm and the period of oscillation of the suspended arrangement is 49.6 s. The torsional constant c, determined by the timing of oscillations using a set of objects of accurately known moment of inertia is $c = 1.465 \pm 0.003 \times 10^{-7}$ Nm. Figure 2 is a photograph of the disc arrangement.

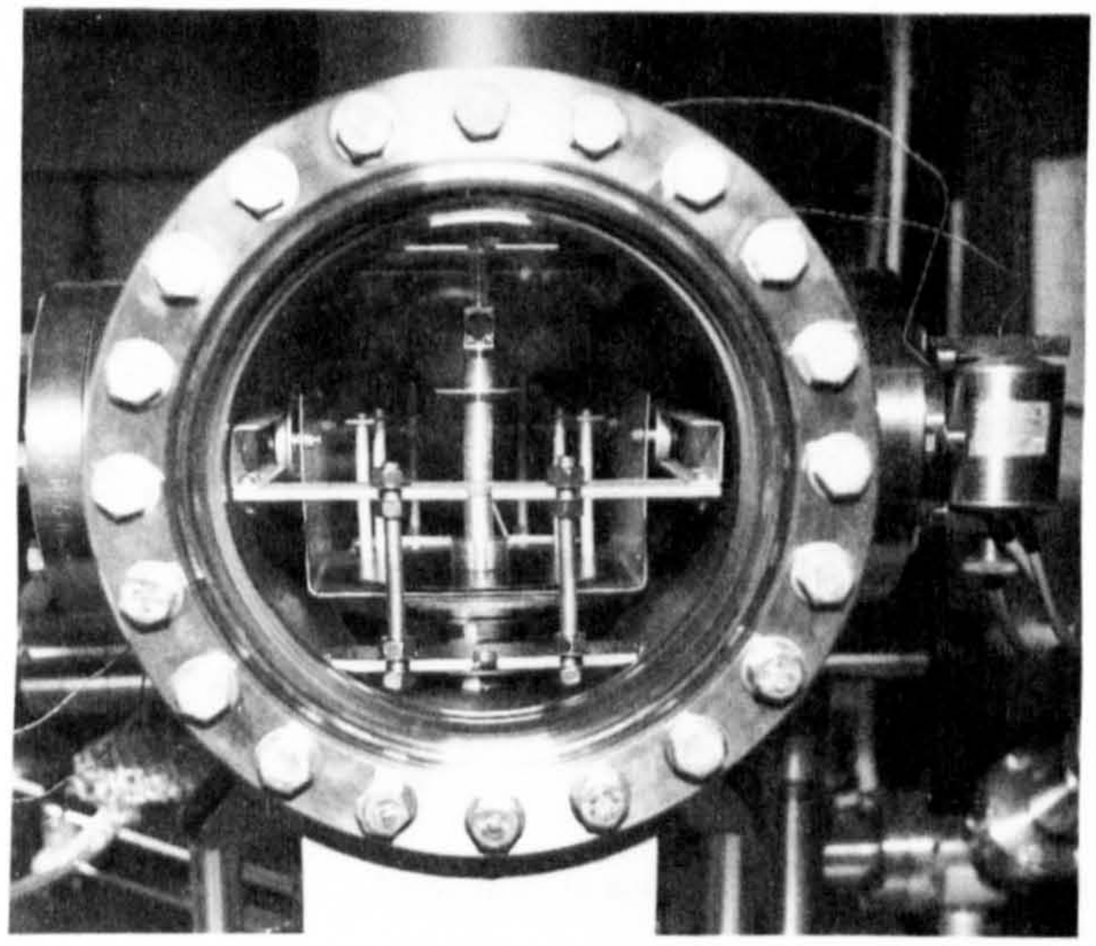

FIG. 2. The disc arrangement.

The device is housed in an ion-pumped vacuum system which also contains a hot cathode ionization gauge,[7] a residual gas analyzer,[8] a fine-leak valve for admitting dry N_2 gas and, for the purposes of this investigation a spinning rotor gauge. The SRG, an MKS Instruments Inc. type SRG-2, was calibrated at the UK National Physical Laboratory (NPL) against a generated pressure standard. Its effective tangential momentum accommodation coefficient for nitrogen is given as $\sigma_{\mathrm{effective}} = 1.024$. It is used in precise accordance with recommended manufacturer's and NPL procedures. The experiments reported have been carried out in the nominal pressure range $1\text{–}10\times10^{-6}$ mbar as read on the digital display of the uncalibrated ionisation gauge which has a resolution of 0.1×10^{-6} in the range $1.0\text{–}9.9\times10^{-6}$ mbar. The base pressure of the system is about 5×10^{-7} mbar with a residual gas composed dominantly of hydrogen and carbon monoxide.

As shown in Fig. 1(e) a shield plate S is located between the sender and the receiver. It may be withdrawn using a linear motion drive. The technique of taking the measurement is, with the suspended receiver quiescent and the sender at speed, to withdraw the shield so that the receiver is excited by a step function and set into oscillation, as shown in Fig. 1(f). The displacement y of the laser spot on a concentric curved scale at distance L is related to the rotation ϕ of the disc by $\phi = y/2L$. At low pressures the oscillation is scarcely damped and the displacement y_0 which corresponds to eventual steady deflection is quickly and easily determined, since it is the center of the induced oscillation. Substituting for ϕ in Eq. (5) leads to the following "operating" equation from which pressure may be determined

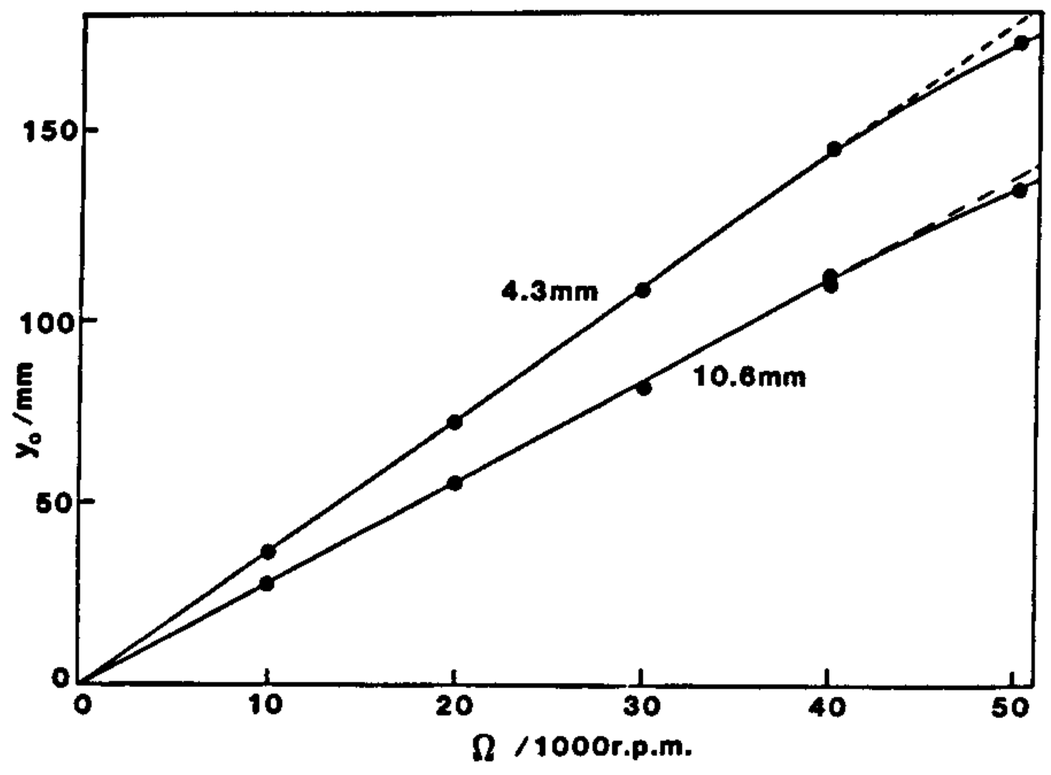

FIG. 3. Deflection as a function of rotor speed.

$$p=(c/2L)y_0\Big/\left[\epsilon\sigma\Omega R^4\left(\frac{\pi}{8R_0T}\right)^{1/2}M^{1/2}\right]. \quad (7)$$

B. Results

Three types of experiment have been carried out:

(1) The measurement of y_0 as a function of Ω at a fixed ionization gauge (IG) pressure of 3.2×10^{-6} mbar for two separations t. The data are presented in Fig. 3.

(2) The measurement of y_0 versus t at a fixed Ω of $2\pi\times250\ s^{-1}$ for two indicated IG pressures. The data are presented in Fig. 4.

(3) The measurement of deflection y_0 as a function of pressure measured by both the ionization gauge and the SRG at a fixed disc separation of 4.3 mm and fixed rotor speed of $2\pi\times500\ s^{-1}$. The pressure is varied using the fine-leak valve to admit N_2 and the data are presented in Table I.

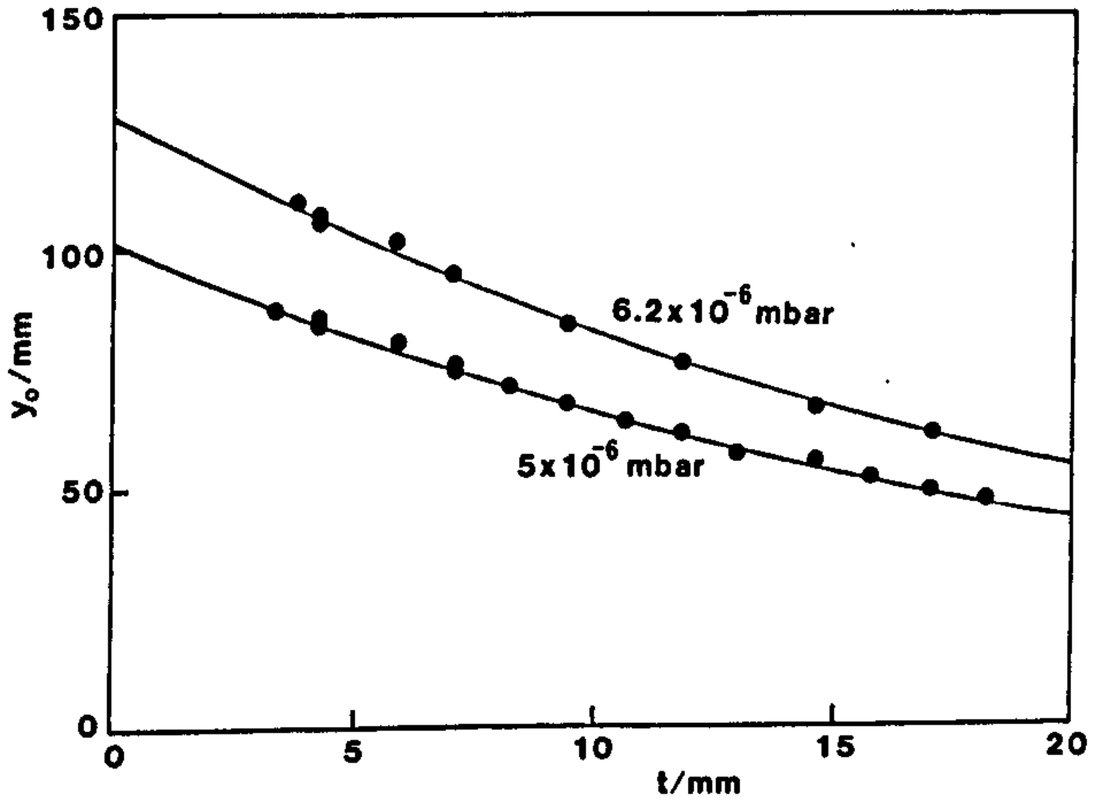

FIG. 4. Deflection as a function of sender–receiver separation.

TABLE I. Deflections y_0 and determined RDG readings at various pressures on the IG and SRG.

Footnote	P_{IG} /10^{-6} mbar	P_{SRG} /10^{-6} mbar	y_0 /mm	P_{RDG} /10^{-6} mbar
a	6.2	5.66	210.25	5.67
b	5.0	4.62	171.75	4.63
	4.0	3.72	135.75	3.66
	3.0	2.74	100.75	2.72
c	2.0	1.51	65.75	1.77
	1.6	1.45	53.5	1.44
	2.5	2.26	83.0	2.24
	3.5	3.19	118.5	3.19
	4.5	4.18	152.0	4.10
	5.0	4.61	170.0	4.58
	5.9	5.53	196.25	5.29
d	0.98	···	32.25	0.87
	0.88	···	29.25	0.79
	0.75	···	25.0	0.67

[a]Isolated measurement.
[b]Onward, sequence taken chronologically in one run.
[c]SRG temporarily disturbed.
[d]Outside recommended range of SRG.

IV. INTERPRETATION AND DISCUSSION

The data of y_0 versus Ω plotted in Fig. 3 shows exact proportionality of y_0 on Ω up to about 40 000 rpm, beyond which there is a slight fall off from linearity. This was also observed in the previously reported work.[6] It may be due to a motionally induced loss of molecules and torque rather than a purely geometrical loss and is being further investigated. For the purpose of this work, a sender speed of 30 000 rpm, well within the region of exact proportionality was chosen for the ensuing experiments. The observations verify that y_0 is proportional to Ω as Eq. (7) predicts.

The data of y_0 versus t at fixed Ω (Fig. 4) enables the edge correction factor ϵ to be estimated. The behavior is as might be expected—with increasing t there is an increased loss of molecules and therefore a decrease in the received torque. The curves have a characteristic shape noted in the earlier reported experiments. Two things should be noted. At a given separation t the deflections scale in the same ratio as the indicated ionization gauge readings. Therefore the gas density in the interspace is proportional to the gas density and hence the pressure in the space outside it. For the range of t values used the conductive access of the gas to the RDG interspace is therefore not restrictive. (Although the ionization gauge has not been calibrated it is reasonable to assume it gives a reading which is proportional to pressure. The effect of changing gas composition is slight.)

The second feature to note is that by extrapolating the curves back to $t=0$, an estimate of the lost torque and therefore the value of ϵ at a convenient value of the experimentally used separation can be obtained. Polynomial fits to the data of y_0 versus t have been carried out computationally. A quadratic best fits the data and gives a mean value of $\epsilon_{4.3}=(y_0)_{t=4.3\ mm}/(y_0)_{t=0}$ of 0.84. This ratio may be taken as the best estimate of ϵ for the t value 4.3 mm which is the sender–receiver separation used in the next

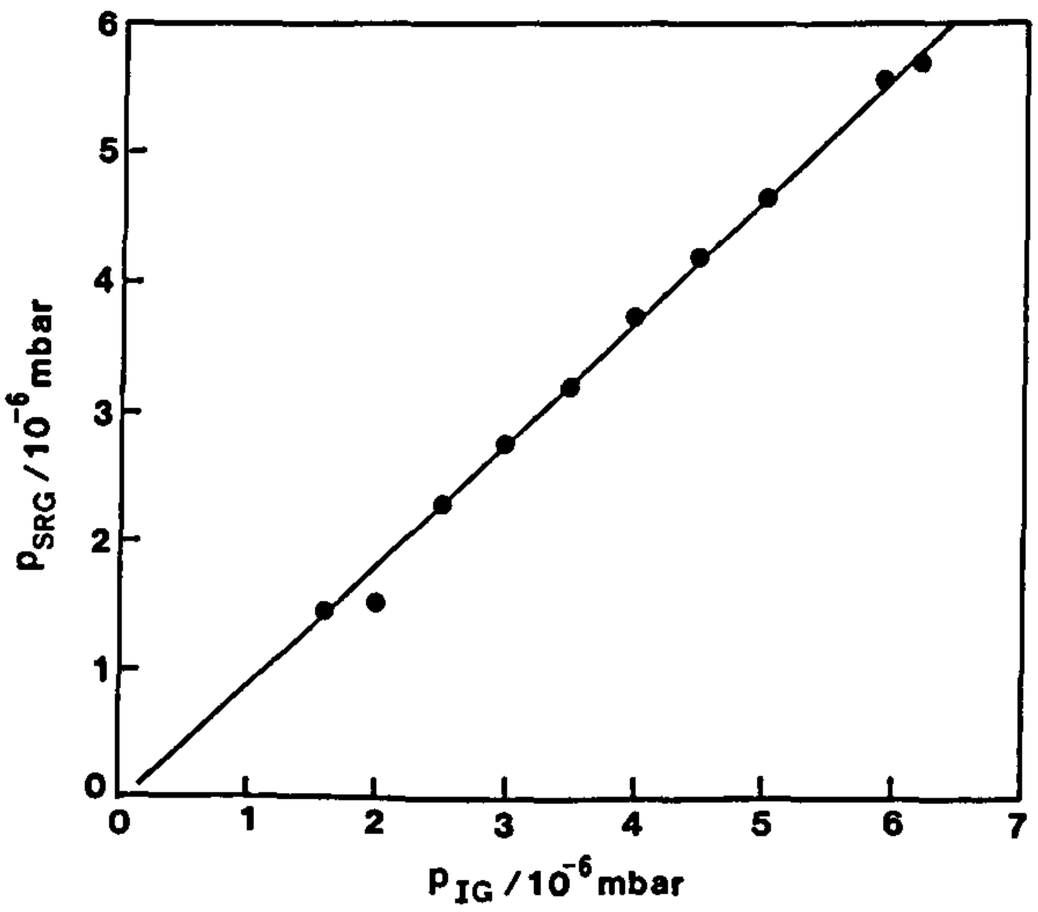

FIG. 5. SRG pressure vs IG pressure.

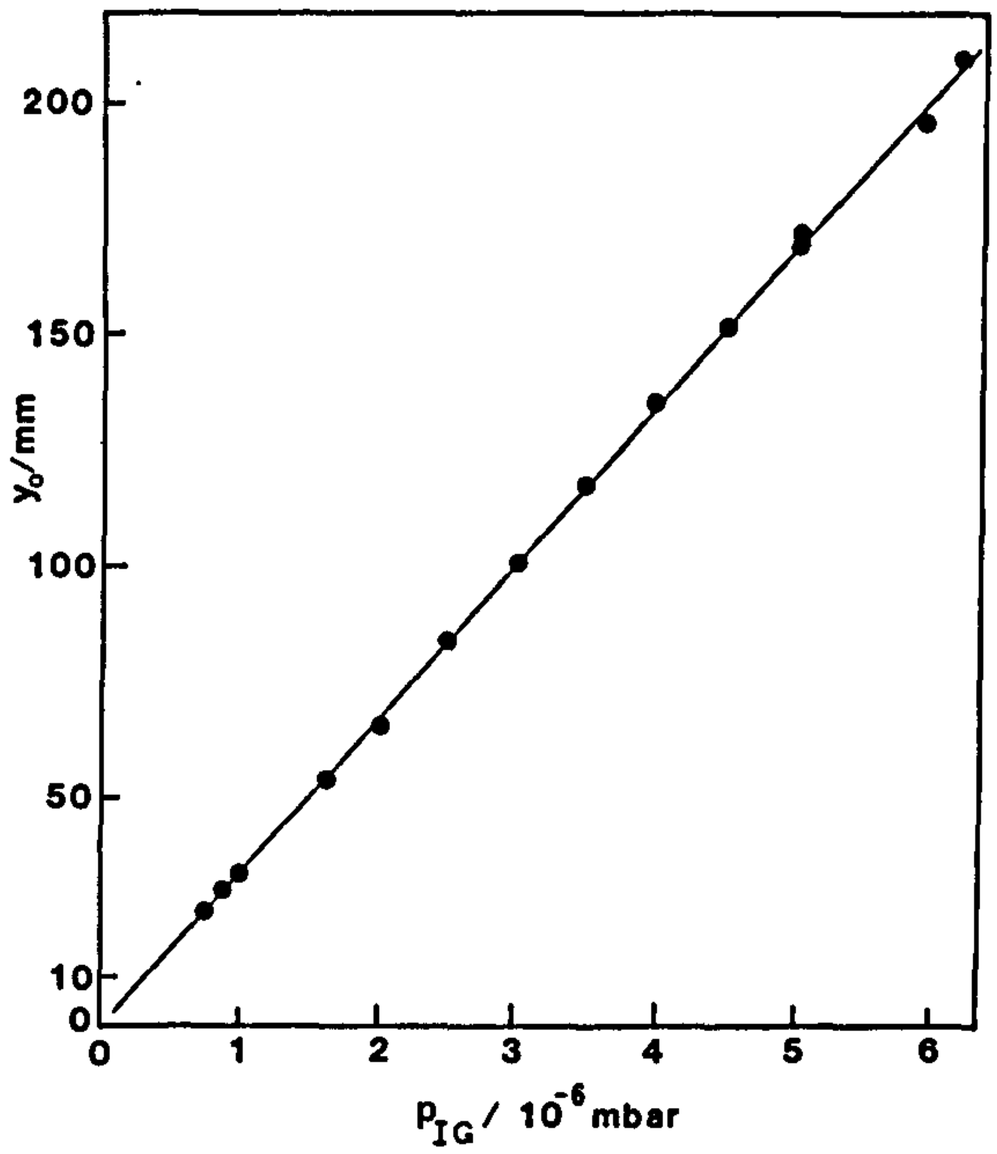

FIG. 6. Deflection as a function of IG pressure.

experiments. In Eq. (7) therefore, inserting this value of ϵ and $\Omega = 2\pi \times 500\ s^{-1}$, $R = 46.00$ mm, $L = 1088$ mm (the mirror-scale distance), c as given, $T = 296$ K and $M = 0.028$ kg for N_2 (this will be justified later) Eq. (7) becomes

$$p = 2.69 \times 10^{-8} \frac{y_0}{\sigma} \text{ mbar}. \tag{8}$$

The uncertainties inherent in this expression will be discussed in due course. If σ were known an absolute pressure determination would be possible.

The results of the next experiment using the SRG may be regarded as a determination of σ for the conditions of the experiment. Table I shows the deflections y_0 determined at various pressures where each pressure is measured on both the SRG and the uncalibrated IG. Figure 5 shows p_{SRG} plotted against p_{IG}. The linearity is to be noted and also the fact that the plot almost exactly passes through the origin. This suggests that the SRG is working reliably and that the offset subtracted in the instrument to allow for residual drag is of almost the correct value. (An incorrect offset would have displaced the plot parallel to itself.) In Fig. 6 y_0 of the RDG is also plotted against the indicated ionization gauge pressure. The strict proportionality is to be noted. We will return to this plot ultimately to discuss sensitivity.

In order to compare the pressure indications of the RDG and those of the SRG it will be assumed, as was done in the previously reported work[6] that $\sigma = 1$. With this assumption the RDG pressure values are then as given in the last column and have an uncertainty as discussed below.

The close agreement of the RDG values with the SRG values is notable and displayed most strikingly in Fig. 7 where the RDG values are plotted against the SRG values. Complete agreement would mean all points sit on the straight line corresponding to $P_{RDG} = P_{SRG}$. It should be noted that although the gas composition changes with pressure, nitrogen increasingly dominating at higher pressures, no useful purpose is served in this work by correcting the pressure indications because, as may be seen by inspecting Eqs. (6) and (7), the correction would be the same in both cases. However to make these corrections, in addition to the accurate knowledge of the gas composition, the accommodation coefficients associated with the constituent gases would need to be known. For the SRG, these vary typically,[9] by 2%.

It may be safely concluded from Fig. 7 that σ is unity on the receiver surface. This is not surprising since the silicon (111) surface is highly ordered, flat and smooth (as was checked by scanning electron microscope and reflection

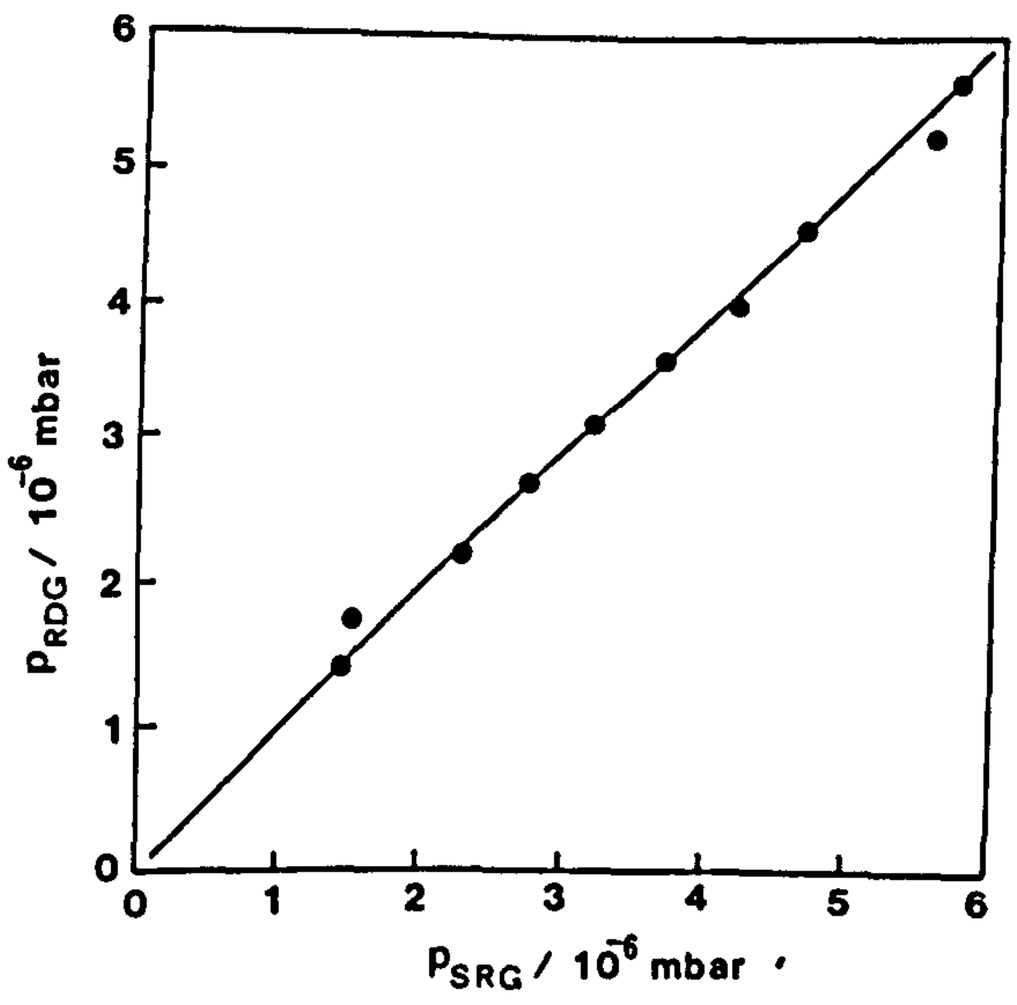

FIG. 7. RDG pressure vs SRG pressure.

high-energy electron diffraction studies). Also, since there is likely to be an adsorbed gas layer on the surface, it would be expected from the work of Thomas[10] that $\sigma = 1$. Therefore, based on the comparison with the SRG the RDG may be considered, over at least the pressure range investigated, as an *absolute* vacuum gauge whose operating equation with $\sigma = 1$ in Eq. (8) now becomes

$$p = 2.69 \times 10^{-8} y_0 \text{ mbar}. \quad (9)$$

With knowledge of the residual gas composition, allowance could be made for the $M^{1/2}$ dependence of molecular drag and a corrected true total pressure deduced as was done by procedures described in the previous work.[6]

The uncertainties associated with the quantities in Eq. (7) are as follows: $c = 1.465 \pm 0.003 \times 10^{-7}$ Nm, $L = 1088 \pm 1$ mm, $\epsilon = 0.84 \pm 0.02$, $\Omega = 2\pi \times (500 \pm 1.7)$ s^{-1}, $R = 46.00 \pm 0.02$ mm, for both sender and receiver, and $T = 296 \pm 2$ K. This gives an uncertainty in the numerical factor in Eq. (9) of $\pm 2.5\%$. Uncertainties due to nonparallelism of the discs and their possible misalignment are more difficult to quantify, but are likely to be small since symmetries will tend to produce compensating effects. The displacements y_0 can be measured with a small uncertainty of ± 1 mm because of the long period of oscillation (50 s). As the displacements become smaller this uncertainty becomes more important. The range of uncertainties in y_0 in the data of Table I is $y_0 = 25.0$ mm $\pm 4\%$ to 210.25 mm $\pm 0.5\%$. In the present investigation the small amount of vibration of the vacuum chamber due to the rotor drive has not presented a problem.

We conclude that in this pressure range absolute measurements of pressure with less than $\pm 5\%$ uncertainty are possible if a single gas is used. This is the subject of present work. SRGs are usually quoted as having an uncertainty less than $\pm 5\%$ although $\pm 14\%$ is possible.[11]

The question of ultimate sensitivity and accuracy arises. From Eq. (7) one may define a nitrogen sensitivity $S = y_0/p\Omega$. From Eq. (9) its value is 8.6×10^{-12} mm mbar^{-1} Hz^{-1}. In Fig. 6 the three displacements y_0 below 10^{-6} mbar do not deviate from the straight line plot. Using the higher speed of rotation would increase the sensitivity (see Fig. 3) by almost 66%. With an improved vacuum one can reasonably expect to be able to measure displacements ~ 10 mm with an uncertainty of ± 1 mm at worst, corresponding to measurements in the low 10^{-7} mbar range with about $\pm 11\%$ uncertainty. With the instrument in this form therefore, a relatively robust first design which does not use the most sensitive torsion fiber, absolute measurements of vacua of $\sim 1 \times 10^{-7}$ mbar are possible. It is a considerable advantage that there is no term to be incorporated in the analysis which corresponds to the residual drag of the SRG. This RDG device is however not a gauge in the "bolt-on" sense and its best future use may be to characterize a vacuum system into which "guest gauges" can be introduced for calibration.

With an optimized design, using a more sensitive torsion fiber, it should be possible to measure in the range 10^{-8} mbar though at this level, vibrational effects may become limiting. Work will be continued on this device at lower vacua to test the predictions made above.

V. CONCLUSIONS

We have built a molecular drag gauge of the rotating disc type and compared it with a spinning rotor gauge at pressures of order 10^{-6} mbar. The results show that the tangential momentum accommodation coefficient for the disc gauge is unity and hence absolute pressure measurement is possible. Pressures of order 10^{-6} mbar are measured with uncertainty less than $\pm 5\%$ and the device should be capable of measurements of similar accuracy at pressures 1 decade lower.

ACKNOWLEDGMENTS

One of us (A.D.C.) would like to thank the Science and Engineering Research Council (SERC) and Edwards High Vacuum International for financial support given under the CASE (Cooperative Awards in Science and Engineering) scheme. It is a pleasure to record thanks to B. Wilkinson who built the vacuum chamber, P. Durkin who made the receiver hub and mirror arrangement, S. Moehr who machined the silicon wafers, and the Wacker Chemical Company which donated them.

[1] H. W. Drawin, Vacuum **15**, 99 (1965).
[2] J. K. Fremerey, J. Vac. Sci. Technol. A **3**, 1715 (1985).
[3] S. Dittmann, B. E. Lindenau, and C. R. Tilford, J. Vac. Sci. Technol. A **7**, 3356 (1989).
[4] I. Langmuir, Phys. Rev. **1**, 337 (1913).
[5] S. Dushman, Phys. Rev. **5**, 212 (1915).
[6] A. Chambers, A. D. Chew, and A. P. Troup, *Proceedings of the Vacuum 91 Conference, University of Salford, UK* [Vacuum **43**, 9 (1992)].
[7] Vacuum Generators Ltd. (Hastings, UK), type VIG22 with Millennia IPGC controller.
[8] Hiden Analytical Ltd. (Warrington, UK) type HAL I 100.
[9] J. K. Fremerey, Vacuum **32**, 685 (1982).
[10] L. B. Thomas, *Rarefied Gas Dynamics* (American Institute of Aeronautics and Astronautics, New York, 1981), p. 83.
[11] American Vacuum Society Recommended Practice on the use of Spinning Rotor Gauges, September 1989.